REMOVAL OF ORGANICS IN REVERSE OSMOSIS CONCENTRATE BY ADVANCED TREATMENT

by

Nazmiye Cemre Birben

B.S. in Environmental Engineering, Yildiz Technical University, 2008

M.S. in Environmental Technology, Bogazici University, 2012

Submitted to the Institute of Environmental Sciences in partial fulfillment of

the requirements for the degree of

Doctor of Philosophy

in

Environmental Technology

Bogazici University

2020

ACKNOWLEDGEMENTS

I would like to express my greatest gratitude to Prof. Dr. Miray Bekbölet for not just being my supervisor but also for her never ending support, guidance and encouragement through my PhD. Her dedication to science influenced and inspired me strongly and facilitated me to become the researcher I am today. Sharing her experiences she had throughout her academic career and her life helped me to widen my point of view in many aspects. Her unconditional contribution, support and motivation have finally turned my PhD into a fruitful, successful, and joyful journey.

I would like to express my appreciation to the jury members Prof. Dr. İdil Arslan Alaton, Prof. Dr. Ayşen Erdinçler, Prof. Dr. Turgut Tüzün Onay, and Assoc. Prof. Dr. Hatice İnan for their valuable, supportive and kind comments.

I would like to express my special thanks to Prof. Dr. İdil Arslan Alaton and Prof. Dr. Tuğba Ölmez Hancı for providing me access to their research laboratory to conduct part of the experimental work related to my PhD.

I would like to express my appreciation to the WATERSPOUTT project, which I had a chance to work as a researcher during my PhD. Although my PhD topic and WATERSPOUTT did not have common contents, working on an international and multidisciplinary project widened my perspective as a prospective researcher for future aspects. The financial support provided by Research Fund of Bogazici University through Project No: 11081 is gratefully acknowledged.

I would like to thank everyone at the Institute of Environmental Sciences, my professors, technical and secretarial staff, my colleagues and friends. Special thanks to my dear friends Elif Hot Öç, Asu Ziylan Yavaş, Gül Geyik, Çağrı Akyol for their friendship and support. I would like to express my deepest thanks to Zeynep Akdoğan, Duygu Can Satılmış, Kübra Mert and Ayşe Seval Palteki for their valuable friendship.

I would like to specially thank Gülhan Özkösemen and Filiz Ayılmaz for their never ending help on the instrumental analysis in the laboratory. I would like to express my appreciation to Dr. Ayşe Tomruk for her support. I would like to express my gratitude to Dr. Ceyda Senem Uyguner Demirel for her valuable support and help since the beginning of this study.

Last but definitely not least, I would like to express my most sincere appreciation to my beloved family Azimet Birben, Atahan Birben, and Servet Emre Birben whose unconditional love, support, and encouragement made me the person I am today.

ABSTRACT

REMOVAL OF ORGANICS IN REVERSE OSMOSIS CONCENTRATE BY ADVANCED TREATMENT

Due to its effective and reliable purification performance, reverse osmosis technology is one of the practical and affordable ways to produce high quality recycled water. However, a major drawback of reverse osmosis is the production of concentrate usually accounting for 15-20% of the input stream containing high levels of organic pollutants some of which could be toxic and bio-accumulative. Possessing a threat to the environment, reverse osmosis concentrate (ROC) must be treated to reduce or even eliminate the negative impact associated with the presence of organic pollutants.

The main objective of this research was to investigate the applicability of homogeneous and heterogeneous advanced oxidation processes on municipal wastewater derived reverse osmosis concentrate treatment. For this purpose, reverse osmosis concentrate samples in the absence and presence of emerging contaminants were synthetically prepared with respect to physicochemical characteristics reported in the literature. Sulfamethoxazole and Carbamazepine were selected as target emerging contaminants owing to their common presence in wastewater sources. UVC/H_2O_2 and Fenton processes were selected as homogeneous advanced oxidation processes whereas solar photocatalysis by using commercially available photocatalysts as well as synthesized ones was considered as heterogeneous advanced oxidation process. Assessment of selected processes for their effectiveness on the removal of complex organic matter was presented in comparison to the sole photolytic oxidation conditions. Since molecular size distribution profiles of organic compounds in ROC plays an important role in order to assess the removal of different pollutants with respect to different molecular size fractions ROC samples were exposed to molecular size fractionation prior to and following photolytic and photocatalytic degradation processes. Expected potential risk was investigated through toxicity assessment prior to and following photodegradation and photocatalytic degradation processes. Organic fraction of reverse osmosis concentrate samples were monitored mainly by UV-vis and advanced fluorescence spectroscopic techniques in combination with PARAFAC modeling as well as organic carbon content.

ÖZET

TERS OSMOZ KONSANTRE ATIĞINDAKİ ORGANİK MADDENİN İLERİ ARITMA YÖNTEMLERİ İLE GİDERİMİ

Etkili ve güvenilir arıtma performansı nedeniyle ters osmoz teknolojisi, yüksek kalitede geri dönüştürülmüş su üretiminde pratik ve uygun fiyatlı alternatiflerden birini oluşturmaktadır. Bununla birlikte ters osmoz sisteminin en büyük dezavantajı giriş hacminin yaklaşık %15-20'si kadar üretilen, biyo-birikime ve potansiyel toksisiteye neden olabilecek olan konsantre atığının oluşumudur. İçeriğinde bulunan organik kirleticilerin varlığının çevreye yönelik tehdit oluşturması nedeniyle ters osmoz konsantre atığının giderimi ya da en azından olumsuz etkilerinin azaltılması gerekmektedir.

Bu çalışmanın temel amacı evsel atıksu arıtımından kaynaklanan ters osmoz konsantre atıklarının arıtımında homojen ve heterojen ileri oksidayson proseslerinin uygulanabilirliğinin araştırılmasıdır. Bu amaçla içerisinde öncelikli kirleticilerin olduğu ve olmadığı farklı ters osmoz konsantrea atıkları laboratuvar ortamında literatürde bulunan fizikokimysal karakterizayon parametreleri dikkate alınarak sentetik olarak hazırlanmıştır. Atıksularda sıklıkla rastlanılmaları nedeniyle Sülfametoksazol ve Karbamazepin hedef yeni kirleticiler olarak seçilmiştir. UVC/H_2O_2 ve Fenton prosesleri homojen ileri oksidayson sistemleri olarak seçilmiş olup ticari olarak elde edilebilen ve sentezlenmiş TiO_2 örnekleri varlığında solar fotokataliz prosesi ise heterojen ileri oksidasyon prosesi olarak seçilmiştir. Ters osmoz konsantre atığında bulunan organik maddelerin moleküler büyüklük dağılımları bu maddelerin giderimini anlamlandırmada önemli bir rol oynaması nedeni ile ters osmoz konsnatre atıkları fotolitik ve fotokatalitik degradasyon prosesleri öncesinde ve sonrasına moleküler büyüklük dağılımlarına ayrılmıştır. Seçilen proseslerin ters osmoz konsantre atığının organik kısmı üzerindeki etkileri organik karbon içeriği, UV-görünür bölge spektroskopisi ve Paralel Faktör Analiz modeli ile birlikte ileri floresan spektroskopisi parametreleri dikkate alınarak değerlendirilmiştir. Beklenen potansiyel riskin incelenebilmesi amacıyla proseslerin öncesinde ve sonrasında toksisite testleri gerçekleştirilmiştir.

TABLE OF CONTENTS

LIST OF FIGURES

LIST OF TABLES

LIST OF SYMBOLS/ABBREVIATIONS

Symbol	Explanation	Unit
A_{254}	Absorbance at 254 nm	cm^{-1}
E_{bg}	Band gap energy	eV
ε	Molar absorption coefficient	L/mol cm
EC_{50}	Effective concentration	mg/L
Φ	Quantum yield	
FI_{syn}	Fluorescence intensity in	
	synchronous scan mode	A.U.
Fmax	Maximum fluorescence intensity	A.U.
$H^{\bullet}$	Hydrogen radical	unitless
$HO^{\bullet}$	Hydroxyl radical	unitless
I_o	Incident photon flux	mW/cm^2
		W/m^2
		quanta/s
		Einstein/s
$^1O_2$	Singlet Oxygen	unitless
$O_2^{\bullet-}$	Superoxide radical	unitless
$HO_2^{\bullet}$	Hydroperoxyl radical	unitless
K_{ow}	Octanol-water partition coefficient	unitless
λ	Wavelength	nm
λ_{emis}	Emission wavelength	nm
λ_{exc}	Excitation wavelength	nm
λ_{max}	Maximum wavelength	nm
μL	Microliter	
μg	Microgram	
mg	Miligram	
mM	Milimolar	
pH_{zpc}	Zero point of charge	unitless
pK_a	p function of acid dissociation constant	
$R^{\bullet}$	Carbon centered radical	
SFI_{syn}	Specific Fluorescence intensity	
	in synchronous scan mode	

t_{irr}	Irradiation period	min

Abbreviation	**Explanation**
AC	Activated Carbon
AHA	Aldrich Humic Acid
ATLD	Alternating Trilinear Decomposition
AOP	Advanced Oxidation Process
BAC	Biologically Activated Carbon
BDD	Boron Doped Diamond
BET	Bruner Emmet Teller
BLLS/RBL	Bilinear Least-Squares/Residual Bilinearization
BNR	Biological Nutrient Removal
BSA	Bovine Serum Albumin
CMZ	Carbamazepine
COD	Chemical Oxygen Demand
DAN	Dissolved Ammonia Nitrogen
DOC	Dissolved Organic Carbon
DOM	Dissolved Organic Matter
ECs	Emerging Contaminants
EDCs	Endocrine Disrupting Chemicals
EDX	Energy Dispersive X-Ray
EEM	Excitation Emission Matrix
EPS	Extracellular Polymeric Substances
FMN	Flavin Mononucleotide
GAC	Granulated Activated Carbon
GC-MS	Gas Chromatography with Mass Spectrometry
GRAM	Generalized Rank Annihilation Method
HA	Humic Acid
HM	Humic Matter
HAAFP	Halo acetic Acid Formation Potential
HP-SEC	High Performance Size Exclusion Chromatography
HSs	Humic Substances
IDEA	Intermittently Decanted Extended Aeration
INH	Inhibition

LC-OCD	Liquid Chromatography Organic Carbon Detection
LED	Light Emitting Diode
MBR	Membrane Bioreactor
MCR-ALS	Multivariate Curve Resolution-Alternating Least Squares
MF	Microfiltration
MIEX	Magnetic Ion Exchange
MOC	Miscellaneous Organic Compounds
MW	Molecular Weight
MWCO	Molecular Weight Cut-off
NADPH	Nicotinamide Adenine Dinucleotide Phosphate
NF	Nanofiltration
NOM	Natural Organic Matter
NPOC	Non-Purgeable Organic Carbon
NTU	Nephelometric Turbidity Unit
OM	Organic Matter
PAC	Powdered Activated Carbon
PARAFAC	Parallel Factor
PCO	Photocatalytic Oxidation
PEC	Photoelectrocatalysis
PPCPs	Pharmaceuticals and Personal Care Products
RO	Reverse Osmosis
ROC	Reverse Osmosis Concentrate
ROC_d	Desalination Reverse Osmosis Concentrate
ROC_{ECm}	Reverse Osmosis concentrate including ECs
ROC_l	Leachate Reverse Osmosis Concentrate
ROC_m	Municipal Reverse Osmosis Concentrate
ROC_x	Industrial Reverse Osmosis Concentrate
ROS	Reactive Oxygen Species
RS	Reactive species
SEM	Scanning Electron Microscopy
SMPs	Soluble Microbial Products
SMX	Sulfamethoxazole
SUVA	Specific Ultraviolet Absorbance
SWATLD	Self-Weighted Alternating Trilinear Decomposition
TAN	Total Ammonia Nitrogen

TDS	Total Dissolved Solids
THMs	Trihalomethanes
THMFP	Trihalomethane Formation Potential
TN	Total Nitrogen
TP	Total Phosphorus
TOC	Total Organic Carbon
UF	Ultrafiltration
US	Ultrasound
UV	Ultraviolet
UVA	Ultraviolet A
UVC	Ultraviolet C
UV-DRS	Ultraviolet Diffuse Reflectance Spectroscopy
UV-LED	Ultraviolet-Light Emitting Diode
WWTP	Wastewater Treatment Plant
XRD	X-Ray Diffraction

1. INTRODUCTION

Conventionally treated wastewaters could still pose a potential risk for the receiving waters with respect to the prominence of micropollutants and other impurities with significant concentration levels. Since some of these receiving waters are also used as the feed water of drinking water treatment plants, presence of above mentioned impurities should not be expected in treated wastewater discharges. Therefore, recent interest devoted to the further treatment processes to remove such components properly in terms of water and energy sustainability. Due to its noble and reliable purification performance, membrane technology is one of the practical and affordable ways to produce high quality recycled water. Based on their pore sizes, several types of membranes are being proposed and implemented through the literature as well as industry. Microfiltration (MF) membranes have pore size between 100-1000 nm used for the removal of suspended particles, followed by ultrafiltration (UF) whose pore size varies between 5-100 nm that is able to remove bacteria and viruses. Nanofiltration (NF) membranes have pore sizes between 1-5 nm and are preferred to be used especially for the removal of dissolved particles. Last but not least, reverse osmosis (RO) membranes have pore sizes < 1 nm that enables rejection of suspended as well as dissolved components and providing high quality water (Metcalf and Eddy, 2004). Although MF and UF are more favorable than NF and RO in terms of fouling and cost factors, NF and RO are the most commonly applied options for the treatment of waters and wastewaters for providing high quality water for use. However, a major drawback of NF and RO is the production of RO concentrate (ROC) usually accounting for 15-20% of the input stream containing high levels of organic pollutants. Some of these compounds could be toxic and bio-accumulative. Possessing a threat to the environment, ROC must be treated to reduce or even eliminate the negative impact associated with the presence of organic and inorganic pollutants. Consequently, treatment and recycling municipal wastewater effluent by RO is gaining growing attention as a strategy for conserving limited fresh water resources (Figure 1.1).

In this respect, a web-based survey was conducted to provide a baseline information. Figure 1.1 presents ROC related publications throughout the literature since 2000. When the term “reverse osmosis concentrate” was searched in Google Scholar, many article papers were published since then. Moreover, number of publications was incrementally increased especially since 2010 and reached a total number of 5968 in years between 2010 and 2020. More specifically, 542 of 5968 articles were interested in municipal reverse osmosis concentrate (ROC_m), 1922 of total were about desalination

reverse osmosis concentrate (ROC_d), 1289 of total were about industrial reverse osmosis concentrate (ROC_x) and the rest (215) was focused on leachate reverse osmosis concentrate (ROC_l) respectively.

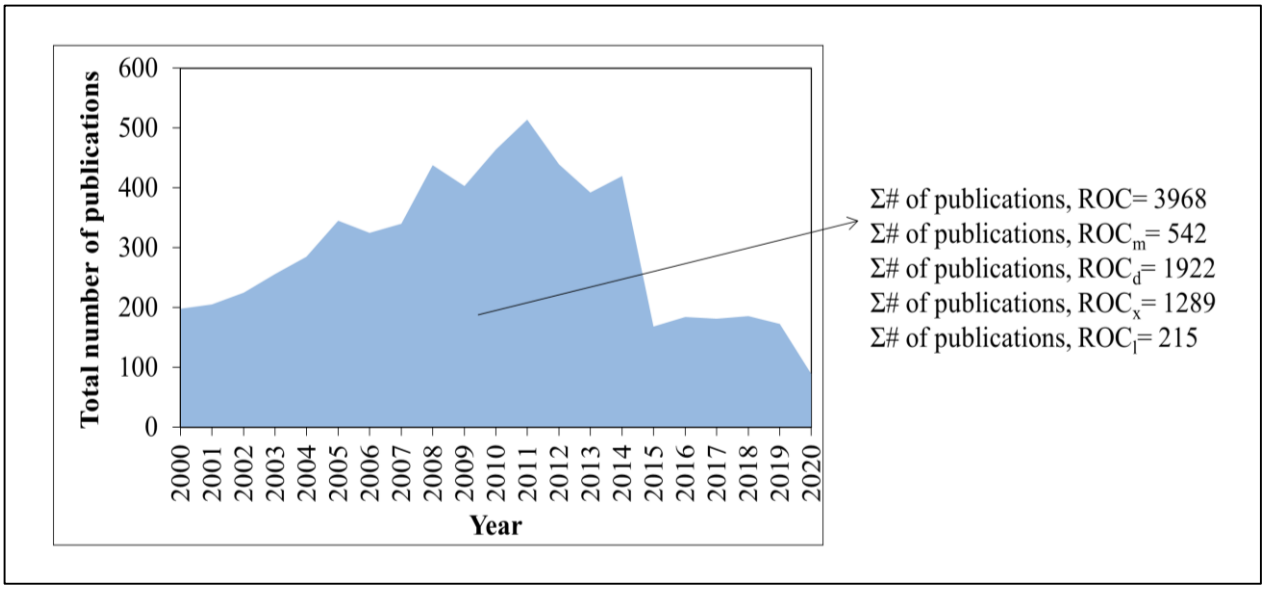

Figure 1.1. Distribution of ROC related publications throughout the literature.

Desalination is regarded one of the most important aspects of water sustainability for many countries especially for arid and semi-arid zones. Therefore, majority of the literature studies covering ROC_d could be attributed to high demand as well as application of membrane desalination processes for providing drinking water from seawater, brackish groundwater, surface water and even wastewater (Le and Nunes, 2016). Significant increase in treatment and management of ROC_x could be related to several reasons, such as removing toxic metals to provide safe disposal of wastewater due to stringent regulations (Cai et al., 2020) and potential for the recovery of metals and rare earth elements from ROC_x for reuse purposes (Le and Nunes, 2016). In addition, use of RO treatment for industry originated wastewaters enables production of high quality water that could be also used within the manufacturing process. As presented in Figure 1.1, in comparison to ROC_d (1922 publications) and ROC_x (1289 publications), ROC_m (542 publications) attained less interest through the literature which could be attributed to need of recycled water use in industrial applications as well as to the stringent regulations for the treatment of industrial wastewater effluents containing high levels of pollutants and expressing higher degree of toxicity. Among all origins of ROC, ROC_l (215 publications) gained the least interest which could be attributed to the presence of high levels of organic and inorganic constituents in ROC_l coming from landfill leachates even after treatment processes. However, management of ROC_m has also gained special interest after stringent regulations for the discharge of wastewater treatment facilities as well as need for the protection of drinking water sources that may receive wastewater treatment effluents (Arola et al., 2019; Cai et al., 2020).

2. LITERATURE REVIEW

This section was aimed to present information derived from ROC related literature studies by following a stepwise approach. First, definition, origin and sub-groups of ROC was defined and explained briefly. Among all other origins of ROC, municipal ROC was the major target of this study, therefore, the rest of the sections were focused on municipal ROC related literature. Second, as a general point of view, characterization of municipal ROC was presented in terms of its organic and inorganic constituents followed by the demonstration of concentration values of selected physical and chemical parameters derived throughout the literature. Then, treatment alternatives applied for municipal ROC and their process efficiencies were exhibited in terms of conventional treatment, either applied as pretreatment or major treatment option, as well as advanced oxidation technologies that were specified under corresponding sub-sections.

2.1. Reverse Osmosis Concentrate

Membrane treatment is a critical component of water recycling programs being implemented globally to increase limited water supplies. When removal of specific dissolved contaminants and total dissolved solids (TDS) is needed to achieve the target finished water quality, reverse osmosis treatment gets significant attention. Declining cost of membrane modules caused a dramatic increase in application of membrane processes including RO for water treatment and reuse (Adham et al, 2005). Moreover, stringent legislative restrictions on discharges from wastewater treatment plants enables membrane filtration processes, such as NF and RO as the tertiary treatment for improving quality of chemically and biologically treated wastewaters. Thus, it has been applied in a wide range of treatment facilities for several purposes, such as desalination of brackish surface and groundwater, polishing for secondary effluent of wastewater reclamation facilities and even in recycling of metal plating wastewater (Benito et al., 2002; Greenlee et al., 2009).

As a result of increasing osmotic pressure and membrane scaling issues during RO treatment, 60-70% of high-quality permeate is obtained whereas approximately 30-40% of the feeding is generated as ROC simultaneously (Westerhoff et al., 2009; Liu et al., 2012; Joo and Tansel, 2015; Arola et al., 2019). This condition is the major challenge of RO process because concentrates from RO process would contain almost all organic and inorganic constituents 6 to 7 times more concentrated than the RO feed (Solley et al., 2010; Jamil et al., 2019a and b).

Because RO is widely applied in water desalination, potable water production and more recently tertiary wastewater treatment, it would be more appropriate to differentiate ROC according to the properties of the source water as well as the treatment process. As a consequence, sources of ROC could be classified as: *i.* ROC_d: ROC coming from desalination plant brines which uses brackish water, seawater, surface water and even wastewater to produce drinking water (Charcosset et al., 2009; Lin, L. et al., 2014). *ii.* ROC_m: ROC originating from municipal wastewater treatment plants using treated municipal wastewater to obtain high quality water or to recover the nutrients (Arola et al., 2019). *iii.* ROC_x: ROC from industrial wastewater treatment that would end up with the recovery of metals and rare earth elements as well as providing high quality water to be used in the manufacturing process (Ye et al., 2018; Li et al., 2019). *iv.* ROC_l: ROC coming from treated landfill leachate for final polishing of highly polluted origin of leachate. With respect to their origins, all classifications of ROC samples could display characteristics significantly different from each other (Pérez-González et al., 2012; Umar et al., 2015; Arola et al., 2019). Majority of the ROC_x comprises wastewater originating from petrochemical wastewater treatment facilities using membrane processes. With respect to the concerns on the water scarcity and reuse purposes as well as management of pollution, treatment of ROC_m, ROC_d, ROC_x, and even ROC_l has gained special interest for the last decade. This research was mainly focused on ROC_m due to the presence of organic constituents derived from both natural as well as anthropogenic sources. Figure 2.1 presents wastewater treatment flow diagram showing in which stage ROC_m is produced. Since it is used as the final polishing step for wastewater treatment facilities, it is expected to be produced at the end of the whole process.

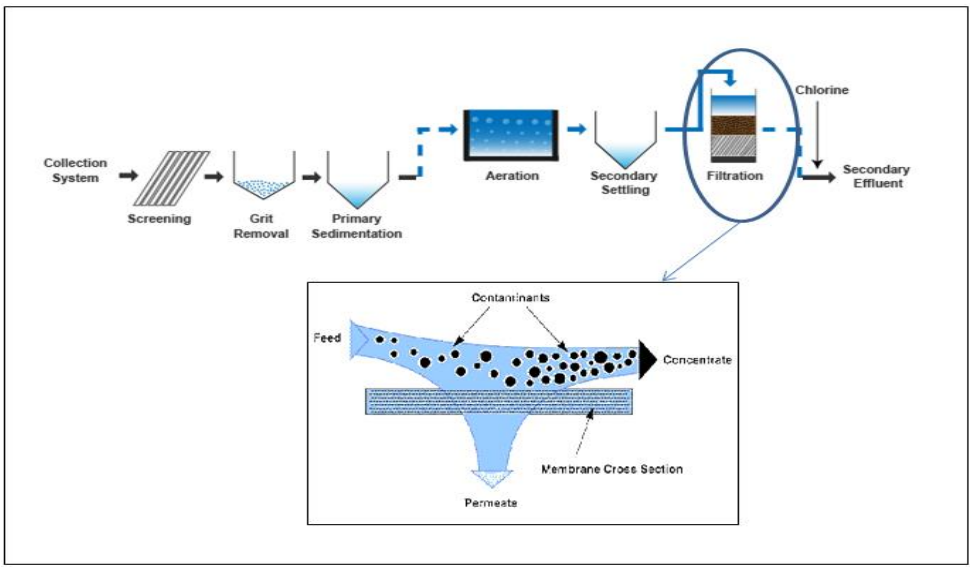

Figure 2.1. Municipal wastewater treatment flow diagram showing in which stage ROC_m is produced.

Some of the traditional ROC management methods are direct discharge to surface waters, sewer disposal, evaporation ponds, deep well injection and zero liquid discharge (Chelme-Ayala et al., 2009; Lee et al., 2009; Gabelich et al., 2011). However, all of these disposal methods are not suitable for every type of ROC. For example, direct discharge and sewer disposal cannot be used for ROC arising from municipal wastewater treatment that may be rich in toxic and/or bio-accumulative contaminants. In addition, disposal of all other types of ROC may cause many risks on the ecosystem when present at sufficient concentrations. Brines coming from desalination plants may pose a potential threat to marine ecosystems due to its high salinity, nutrients and organic content (Roberts et al., 2010; Shon et al., 2006). Development of other management options is required for inland plants without the possibility of their concentrate disposal to seawater. Various researchers focused on the review of literature studies concerning treatment alternatives for ROC management in order to find potential solutions to overcome the current situation (Umar et al., 2015; Birben et al., 2017; Arola et al., 2019; Xiang et al., 2019).

2.1.2. Characteristics of Reverse Osmosis Concentrate

Many important factors may influence quality and quantity of the ROC_m generated, such as the composition of raw water, operating parameters of the membrane process, and overall system elements (*i.e.* pre-treatment, nature of cleaning chemicals used). Membrane pore sizes and type of membrane modules are also other important factors influencing concentrate quality. Microfiltration and ultrafiltration concentrates may contain suspended solids and colloidal particles whereas only small organics and high ion concentrations are found in nanofiltration and reverse osmosis concentrates (Van der Bruggen et al., 2003; Gray et al., 2007). Moreover, variations in the types and quantity of chemicals used for periodic membrane cleaning and/or scaling/biofouling prevention procedures are other factors that may influence concentrate quality (Isaias, 2001; Ghafour, 2002). A schematic representation of ROC_m composition according to its organic and inorganic constituents was presented in Figure 2.2.

Composition of the organics present in ROC_m constitutes a wide range of groups, such as natural organic matter (NOM) mainly as dissolved organic matter (DOM) as one of the major contaminant and other miscellaneous organic compounds (MOC). MOC are composed of various refractory chemicals including pesticides, pharmaceuticals and personal care products (PPCPs), endocrine disrupting chemicals (EDCs) from public discharge, soluble microbial products (SMPs) and partially biodegraded organics from wastewater treatment plants (Ternes and Joss, 2007; Radjenovic et al.,

2008; Watkinson et al., 2007). Numerous biological materials, such as bacteria, viruses, oocysts and cell fragments could also be detected in reverse osmosis concentrates coming from wastewater treatment plants (Westerhoff et al., 2009).

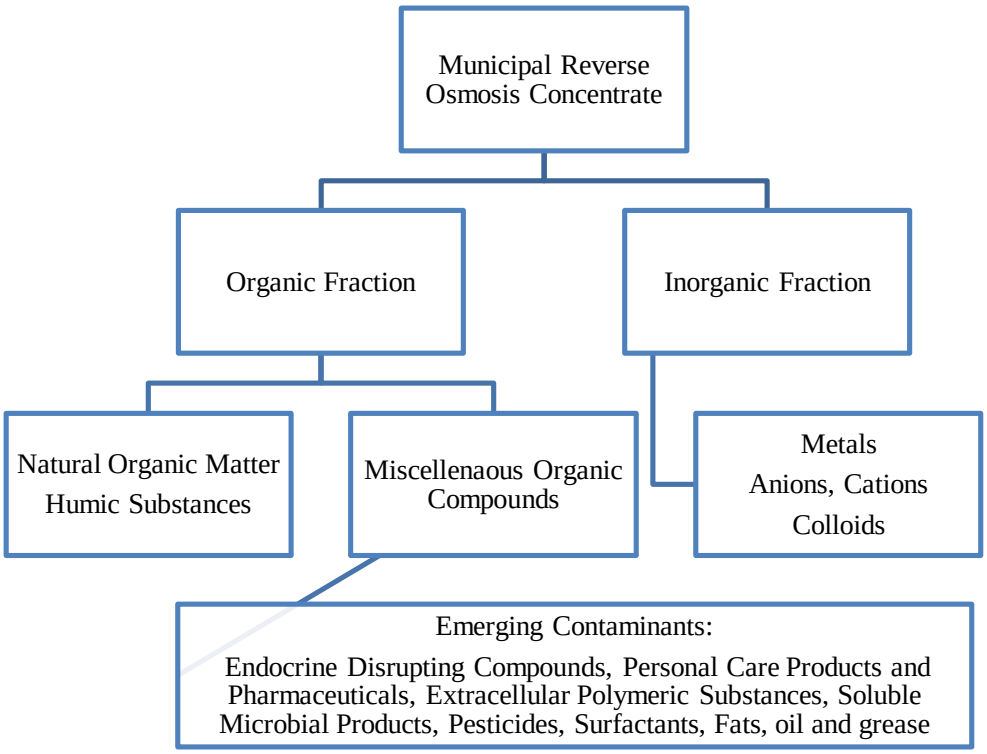

Figure 2.2. Schematic representation of ROC_m in terms of its organic and inorganic constituents.

One of the main contributors to the organic matter content of ROC_m is reported as humic substances (HSs) (Lin et al., 2014a) which is widely known as fouling agents in reverse osmosis processes and rejected within the ROC_m. Being as the major component of humic substances, effect of humic acid (HA) (as an example: commercial sample, Aldrich humic acid) on reverse osmosis membrane fouling have been investigated by Sioutopoulos and colleagues (Sioutopoulos et al., 2010a and b).

Presence of emerging contaminants (pesticides, endocrine-disrupting chemicals, pharmaceuticals and personal care products) in ROC_m is another important issue because they may have adverse ecological and health effects although they are found in low concentrations. In addition, some of those emerging contaminants are hydrophobic, bio accumulative, semi-volatile and toxic, thus reduction of such contaminants to undetectable trace levels are quite difficult. Levels of emerging contaminants present in concentrates may be affected by environmental conditions, such as temperature, pH and ionic strength (Fujioka et al., 2012).

Extracellular polymeric substances (EPS) and SMP are known to be produced from bacterial metabolism during secondary treatment and generally enter water through cell lysis, diffusion through the cell membrane and or excretion, thus such organics can be detected in municipal secondary effluents (Rittman and McCarty, 2001) and may pose a risk due to their potential toxicity (Rittman et al., 1987). Constituting the sub-fraction of soluble microbial products, proteins could be observed in secondary effluent of wastewater treatment plants. Although rejection of proteins by reverse osmosis process is applied successfully in terms of wastewater treatment purposes, deposition of proteins ends up with loss of membrane permeability, thus causes membrane fouling and produces ROC_m with protein content. Considering the fouling behavior of protein in reverse osmosis process, systematic studies on the fouling of RO membranes by proteins have been investigated (Ang and Elimelech, 2007; Li et al., 2007). Moreover, fouling behavior of protein in reverse osmosis under various physical and chemical conditions have been studied by using bovine serum albumin (BSA) as a representative of protein content coming from the feed wastewater (Mo et al., 2008; Yang et al., 2010; Wang et al., 2011).

Comprising a wide range of application in household and industrial cleaning, use of surfactants has increased substantially leading to significant concentration levels in municipal secondary effluents. Although they are able to be removed by RO process from secondary effluents, they will contribute organic fraction of ROC_m and increase its hazard potential due to their bio-resistant property and toxicity (Ikehata and El-Din, 2004). Fats, oil and grease are regarded as the third most abundant compounds in municipal secondary effluent and can be degraded biologically with a removal efficiency of 98% to 100% (Shon et al., 2006). The only exception is fatty acid originating from non-degraded fraction of lipids of the wastewater and could be removed up to 93% (Dignac et al., 2000). Other components of ROC_m could be several inorganic constituents, such as metals (Cd, Co, Cr, Cu, Fe, Mn, Mo, Ni, Pb, Zn, Si, and Al), common anions (Cl^-, NO_2^-, NO_3^-, SO_4^{2-} and PO_4^{3-}) and cations (Na^+, K^+, Mg^{2+} and Ca^{2+}) and colloids. In addition, ROC_m may also contain nitrogen (total ammonia nitrogen (TAN), dissolved ammonia nitrogen (DAN) and phosphorus compounds depending on the nutrient removal facility present in secondary treatment units of wastewater treatment plants (Kumar et al., 2007).

Some of the physical and chemical characteristics of different ROC_m reported in the literature are presented in Table 2.1. Since, this table covers characterization of almost 30 different sources of ROC_m, data was presented in terms of minimum, maximum, and average values of selected parameters for simplicity purposes (Ng et al., 2008; Badruzzaman et al., 2009; Lee et al., 2009; Westerhoff et al., 2009; Chaplin et al., 2010; Pérez et al., 2010; Radjenovic et al., 2011; Zhou et al.,

2011; Ben Abdelmelek et al., 2011; Malamis et al., 2012; Bagastyo et al., 2013; Justo et al., 2013; Lu et al., 2013; Urtiaga et al., 2013; Vendramel et al., 2013; Hurwitz et al., 2014; Lin and Li, 2014a; Lütke Eversloh et al., 2014; Umar et al., 2014; Umar et al., 2015; Badia-Fabregat et al., 2015; Ren et al., 2016; Yang et al., 2016; Xiang et al., 2017; Li et al., 2019; Arola et al., 2019). Detailed information regarding concentration values of the selected parameters for each ROC_m up to year 2017 was presented elsewhere (Birben et al., 2017). pH values of ROC_m varied between 6.9 and 8.8 which could be attributed to several factors, such as pH of the raw wastewater, chemicals used in wastewater treatment process etc. Conductivity values were found to be in the ranges of 1.97 mS/cm and 27.5 mS/cm. Among all ROC_m samples, two exceptional conductivity values (22.3 and 27.5 mS/cm) were observed for ROC_m studied by Umar and co-workers (Umar et al., 2014 and 2015). Alkalinity varied between 242 $mgCaCO_3/L$ and 1100 $mgCaCO_3/L$.

Table 2.1. Characteristics of ROC_m.

Parameter	Minimum	Maximum
Oragnic parameters		
COD, mgO_2/L	35	175
NPOC, mgOrgC/L	17	57.1
TOC, mgOrgC/L	17	31.1
A_{254}, cm^{-1}	0.42	0.80
Physical parameters		
pH	6.9	8.8
Conductivity, mS/cm	1.97	27.5
Turbidity, NTU	0.4	144
Color, Pt-Co	55	216
TDS, mg/L	1073	17400
Alkalinity, $mgCaCO_3/L$	242	1100
Inorganic parameters		
Cations, mg/L		
Na^+	203	1318
K^+	22.6	135
Ca^{2+}	47	485
Mg^{2+}	7	148
Anions ,mg/L		
Cl^-	217	5200
NO_2^-	n.d.	n.d.
NO_3^-	3.1	296
SO_4^{2-}	207	1759
PO_4^{3-}	2.4	39

Organic matter content of ROC_m was expressed in terms of gross parameters as chemical oxygen demand (COD), non-purgeable organic carbon content (NPOC), total organic carbon (TOC) and absorption at wavelength λ: 254 nm (A_{254}). COD content of ROC_m was found to be in between 35 mgO_2/L and 175 mgO_2/L and NPOC content varied between 17 mgOrgC/L and 57.1 mgOrgC/L. UV absorbance values at λ: 254 nm (A_{254}, cm^{-1}) varied between 0.42 and 0.80 cm^{-1} and taken into

consideration for the characterization of ROC_m as surrogate parameters of its organic matter content and respective NPOC content.

As common inorganic cationic constituents, Na^+, K^+, Ca^{2+} and Mg^{2+} contents of ROC_m were found to be in the following ranges of 203 to 1318 mg/L, 22.6 to 135 mg/L, 47 to 485 mg/L and 7 to 148 mg/L respectively. ROC_m was found to be rich in common anions, such as Cl^-, NO_2^-, NO_3^-, SO_4^{2-}, PO_4^{3-}. As a general trend, Cl^- concentration were reported to be between 217 mg/L and 5200 mg/L, however two of ROC_m samples displayed significantly higher Cl^- values as 8060 and 8875 mg/L which could be attributed to the origin of wastewater and/or treatment process applied in wastewater treatment facility (Umar et al., 2014 and 2015). For example, if final stage of the wastewater treatment facility includes chlorine disinfection unit, then effluent would contain residual chlorine which could end up with ROC_m. While NO_2^- was not detected in almost all ROC_m, NO_3^- content possibly coming from biological nutrient removal processes (nitrification) varied between 3.1 mg/L and 296 mg/L. SO_4^{2-} was also detected in ROC_m samples of different origins with the concentration range of 207 mg/L and 1759 mg/L whereas no significant PO_4^{3-} content (varied between 2.4 and 39 mg/L) was reported.

Table 2.2 presents emerging contaminants found in ROC_m and applied treatment methods mainly focusing on AOPs (O_3, O_3/H_2O_2, UV/H_2O_2, UV/TiO_2, electrochemical oxidation and radiolysis). While some of the studies considered only removal of ECs present in ROC_m, others preferred to deal with simultaneous removal of ECs and ROC_m via selected treatment processes. Moreover, there's only one study presented by Wei and co-workers that significantly focused on the identification of emerging contaminants present in ROC_m instead of their removal by advanced oxidation processes (Wei et al., 2015). A variety of emerging contaminants with varying concentration ranges (from 0.018 μg/L to 50 μg/L) was detected in ROC_m of different origins. Depending on their properties and target of concern, ECs could be classified into various sub-groups, such as *i.* non-steroidal anti-inflammatory drugs (diclofenac, ibuprofen, ketoprofen and naproxen), *ii.* antibiotics (sulfamethoxazole and trimethoprim), *iii.* β-blocker (propranolol), *iv.* lipid regulators (clofibric acid and gemfibrozil), *v.* antiepileptic (carbamazepine), *vi.* estrogens, and *vii.* nervous stimulant (Martín et al., 2012). Among all different types of emerging contaminants, carbamazepine, sulfamethoxazole, ibuprofen, naproxen and caffeine were found to be the most common ones present in ROC_m. Being regarded as an aromatic anticonvulsant, Carbamazepine (CMZ) is widely used to treat epileptic seizures and nerve pain, such as trigeminal neuralgia. Since CMZ removal in wastewater treatment facilities are very poor, significant portion of CMZ could be detected in wastewater treatment effluents and could reach to surface and groundwaters (Hai et al., 2018). Sulfamethoxazole (SMX) is

known as antibacterial, agent, an epitote, an anti-infective agent, a xenobiotic and a drug allergen. Due to its worldwide use as a sulfonamide antibiotic, existence of SMX in various environmental matrices has been increasing significantly (Li et al., 2020).

Table 2.2. Emerging contaminants found in ROC_m.

Reference	Experimental conditions/ECs detected
Benner et al., 2008	Ozonation with continuous quench flow system, 5-10 mgO_3/L, Q: 360 mL/h and 660 mL/h Carbamazepine, sulfamethoxazole, trimethoprim, metoprolol, clarithromycin, iomeprol, iopromide, ibuprofen, diclofenac, naproxen, acebutolol, atenolol, bisoprolol, celiprolol
Westerhoff et al., 2009	O_3/H_2O_2, 0.7 mol H_2O_2 /mol O_3, Fenton reaction, pH~3.3, 10 mM Fe^{2+} and 10 mM H_2O_2 UV/H_2O_2, 10 mM H_2O_2 and UV dose: 11.8 kWh/m^3 UV/TiO_2, TiO_2 dose: 1 and 5 g/L, UV dose: 10.4 kWh/m^3 Atrazine, caffeine, carbamazepine, cotinine, diazepam, 10evamiso, diuron, fluoxetine, hydrocodone, meprobamate, naproxen, oxybenzone, triclosan, sulfametoxazole, trimethoprim
Pérez et al., 2010	Electrooxidation by using BDD electrodes, J: 20-200 A/m^2, Q: 0.01 m^3/min Atenolol, caffeine, nicotine fenofibric acid, gemfibrozil, 10imetidine, hydrochlorothiazide, ibuprofen, naproxen, 4-acetamidoantipyrin
Radjenovic et al., 2011	Electrochemical oxidation in both batch and continuous modes by using RuO_2/IrO_2-coated titanium anodes, J: 1-250 A/m^2 Ranitidine, lincomycin, acetaminophen, diclofenac, diazinon, enrofloxacin, sulfadiazine, trimethoprim, norfloxacin, sertraline, gemfibrozil, citalopram, venlafaxine, metoprolol, hydrochlorothiazide, caffeine, atrazine tramadol, roxithromycin, diuron, carbamazepine
Ben Abdelmelek et al., 2011	Radiolysis, pulse radiation and γ radiation, 3-5 Gy per 2-3 ns pulse Gemfibrozil, naproxen, iopromide carbamazepine, ofloxacin, erythromycin, trimethoprim, venlafaxine, atenolol, metoprolol, caffeine, nalidixic acid, rohexol, N,N' diethyl-meta-toluamide, iopamidol, sulfamethoxazole, atorvastatin, lovastatin, enrofloxacin, iomeprol, sulfamerazine, sulfamethazine, sulfamethizole, famotidine, ranitidine, 5,5-diphenyl-hydantoin
Justo et al., 2013	UV/H_2O_2, λ: 254 nm, I_o: $1.5x10^{-5}$ E/s, O_3, O_3: 0.14-6.93 $mgO_3/mgTOC$, Q: 133.5 L/h Atenolol, carbamazepine, diclofenac, naproxen, 10evamisole10n, propyphenazone, codeine, paroxetine, trimethoprim, sulfamethazine, sulfametoxazole,
Urtiaga et al., 2013	Electrochemical oxidation, BDD on silicone anode and stainless steel cathode J: 20-100 A/m^2, Q: 10 L/min Atenolol, benzafibrate, caffeine, fenofibric acid, furosemide, gemfibrozil, hyrochlorothiazide, ibuprofen, ofloxacin, 4-acetamidoantipyrin, naproxen, nicotine
Hurwitz et al., 2014	Hybrid photolytic electrochemical oxidation using BDD electrodes λ: 254 nm, I_o: 8.5 mW/cm^2, J: 20 mA/cm^2, Q: 0.033 m^3/h Bromoform, chloroform, dibromochloroform, dichlorobromoform
Lütke Eversloh et al., 2014	Galvanostatic electrochemical treatment using BDD electrodes Ioprimide, iodide, iodate
Wei et al., 2015	No treatment was applied, ECs were only identified Acenaphthene, anthracene, atrazine, buthyl phthalate, caffeine, dibuthyl phthalate, diethyl phthalate, dimethyl phthalate, fluorine, Naphthalene-d8, Naphthalene, simazine, phenanthrene, 2-chloroethyl ether, 1,3-dichlorobenzene, 1,4-dichlorobenzene, 1,2-dichlorobenzene, 1,3,5-trichlorobenzene, 1,2,4-trichlorobenzene, 1,2,3-trichlorobenzene
Badia-Farbregat et al., 2015	Fungal bioreactor, *T. versicolor* pellet Ibuprofen, salicylic acid, ketoprofen, diclofenac, acetaminophen, naproxen, phenazone, codeine, oxycodone, piroxicam, xylazine propyphenazone, carbamazepine, venlafaxine, citalopram, diazepam, alprazolam, 10,11-epoxyCBZ, fluoxetine, acridone, sertraline, norfluoxetine, atenolol, sotalol, proplanolol, metoprolol, nadolol, ciprofloxacin, ofloxacin, tamsulosin, sulfametoxazole, clarithromycin, ranitidine trimethoprim, tetracyclin, metronidazole-OH, metronidazole, dimetridazole, ronidazole, valsartan, irbesartan, amlodipine, furosemide, hydrochlorotiazide, torasemide, iopromide, gemfibrozil, atorvastatin, bezafibrate, fluvastatin, thiabendazole, 10evamisole, verapamil, norverapamil, diltiazem
Jamil et al., 2016	Fixed-bed column packed with coal-based GAC, surface area: 1000±50 m^2/g Benzophenone, caffeine, carbamazepine, diazion, diclofenac, diuron, naproxen, 4-n-nonylphenol, primidone, simazine, sulfamoethoxazole, triclocarban, triclosan, verapamil
Lin et al., 2017	Bioachar and GAC adsorption, dose: 1 g/L Ibuprofen, sulfamethoxazole

Wang et al., 2017	Fe_3O_4@SiO_2@Yb_2O_3catalyzed by ozonation, catalyst dose: 0.2-1.0 g, ozone dose: 8-48 mg/min Thymol
Arola et al., 2018	Pulsed corona discharge Bisoprolol, carbamazepine, citalopram, diclofenac, furosemide, ketoprofen, metroprolol, N-N-diethyl-meta-toluamide, sotalol
Chen et al., 2020	Photoelectrocatalysis using TiO_2 nanotobe arrays Acetominophen, atenolol, carbamazepine, sulfamethoxazole, trimethoprim
Deng, 2020	Ozonation, ozone dose: 10 mg/L Carbamazepine, ketoprofen
King et al., 2020	Ozonation, ozone dose: 45-55 mg/L Atneolol, atrazine, DEET, sulfamethoxazole, tris(2-chloroethyl) phosphate

2.2. Reverse Osmosis Concentrate Treatment Technologies

Although various studies have focused on traditional ROC treatment and disposal methods or recent advances in RO technology, detailed information on concentrate treatment technologies especially minimization or removal of organics and biological constituents of concern in ROC_m are still limited. Moreover, containing the contaminants 6 to 7 times higher than the concentrations found in secondary effluents, treatment of ROC_m to an appropriate level is becoming increasingly important to enable its reuse and reduce the risk it poses to the environment by removing the contaminants of concern prior to their disposal. Therefore, treatment and management of ROC_m became a crucial part of RO based wastewater treatment technologies in order to be able to cover the concern from environmental point and resource efficiency point of view.

Physicochemical properties of the concentrate as well as the operational and design characteristics of membrane systems are the main factors on deciding methods of treatment and volume reduction of concentrate. Development of effective treatment methods involves evaluation of significant parameters, such as volume generated, concentration, characteristics of the feed water, and operational conditions. In addition, using well-verified analytical methods to detect trace amounts of contaminants, including emerging contaminants in ROC_m plays a crucial role on the determination of appropriate treatment technologies for the removal of such contaminants (Joo and Tansel, 2015). Moreover, identification of pretreatment requirements is another critical point prior to application of treatment technologies. For example, removal of ions and organics in order to prevent scaling, foaming and fouling is essential when using membrane and/or thermal treatment technologies (Pérez-González et al., 2012).

ROC_m treatment technologies comprise a wide range of alternatives from traditional treatments, such as conventional treatment methods *i.e.* evaporation and crystallization to novel technologies, such as advanced oxidation processes. Different treatment technologies have been proposed for the minimization and treatment of ROC_m in terms of physicochemical, biological and advanced oxidation processes alone or in combination. Detailed explanation related to conventional treatment technologies and advanced oxidation processes applied for ROC_m treatment were presented in the following sections.

2.2.1. Conventional Treatment Technologies

Commonly applied conventional processes for ROC_m treatment are coagulation, activated carbon adsorption, zeolite adsorption and ion exchange which have been presented in Table 2.3. Bold values in treatment process column indicates optimum chemical dose in terms of process efficiency. Table 2.3 indicated coagulation was the most frequently used conventional treatment process in which alum and ferric salts were extensively used. In most studies, coagulation performance of ferric coagulants was found to be higher than alum in terms of ROC_m removal. On the other hand, Zhou and co-workers indicated that Al^{3+} coagulants could display higher efficiency which could be attributed to the presence of large molecular weight color causing compounds indicating that the organic matter removal efficiency may depend significantly on the characteristics of ROC_m (Zhou et al., 2011; Umar et al., 2014 and 2015; Arola et al., 2019). Compared to coagulation, ion exchange and zeolite adsorption studies, the most substantial NPOC removal was attained by activated carbon adsorption whether used in granular or powder form (Dialynas et al., 2008; Zhou et al., 2011). Although activated carbon adsorption could effectively remove NPOC up to 95%, this process only enabled transfer of target compounds from one phase to another, thus adsorbed pollutants still required treatment. Moreover, presence of non-adsorbable organic fraction, such as hydrophilic organics with high molecular size fractions could make activated carbon adsorption process ineffective (Zhou et al., 2011).

Due to increased environmental awareness, reuse requirements and stringent regulations, conventional management techniques applied for ROC_m treatment would not be sufficient (Pérez-González et al., 2012; Joo and Tansel, 2015; Lazarova et al., 2013). In addition, regarding recalcitrant nature of organics present in ROC_m, conventional treatment technologies would not be able to remove such pollutants effectively they are only able to transfer these pollutants from one phase (aqueous) to another (solid), *i.e.* pollutants are encapped in flocs as chemical sludge or adsorbed on the AC. These

treatment methods create another source of waste instead of removing the target pollutants, therefore, potential environmental risk of these pollutants would be still significant. At this point, application of AOPs could be considered to fulfill the requirement of removing refractory portion of ROC_m by mineralizing them into organic acids and CO_2.

Table 2.3. Conventional treatment processes applied for ROC_m treatment.

Reference	ROC_m origin/Treatment process/Process efficiency
Dialynas et al., 2008	Pilot scale MBR Alum coagulation, dose: 0.1, 0.2, 0.3, 0.4, 1.0, 2.0 and 5.0 mM 42% NPOC removal
	$FeCl_3$ coagulation, $FeCl_3$ dose: 0.1, 0.2, 0.3, 0.4, 0.5, 1 and 2 mM 52% NPOC removal
	GAC adsorption, BET: 1250 m^2/g GAC dose: 0.1, 0.2, 0.3, 0.5, 0.75, 1.0, 1.5, 2.0, 3.0 and 5.0 g/L 91.3% NPOC removal
Bagastyo et al., 2011	BNR and MF, Two samples of different composition Alum coagulation, dose: 1.5 mM 25% for ROC_1 and 52% for ROC_2
	$FeCl_3$ coagulation, $FeCl_3$ dose: 1.48 mM 34% for ROC_1 and 38% for ROC_2
	Magnetic Ion Exchange, dose: 10mLslurry/L 24% for ROC_1 and 43% for ROC_2
Zhou et al., 2011*	Directly supplied from WWTP $FeCl_3$ coagulation, dose: 0.1, 0.2, 1.0, 1.5 and 2.0 mM 26.4%
	PAC adsorption, dose: 0.1, 0.2, 0.5, 1.0, 2.0 and 5.0 g/L 95%
	GAC adsorption, dose: 0.1, 0.2, 0.5, 1.0, 2.0 and 5.0 g/L 88%
Malamis et al., 2012	Pilot scale MBR Fixed bed column packed with natural zeolite COD removal: 17.5% to 28.4%
Umar et al., 2014*	Intermittently decanted extended aeration bioreactor UF and RO Alum coagulation, dose: 1-6 mM 29% for 1.5 mM and 16% for 3 mM
Umar et al., 2015*	Intermittently decanted extended aeration bioreactor UF and RO Alum coagulation, dose: 1-6 mM 34% for 1.5 mM 38% for 3mM
Sun et al., 2016	From municipal wastewater reclamation reverse osmosis $FeCl_3$ coagulation, dose: 100-500 mg/L, polyaluminium chloride coagulation, dose: 50-500 mg/L, GAC adsorption, dose: 4 g/L 16.9% for only $FeCl_3$ coagulation 91.8% for combined system
Chen et al., 2017	Synthetic ROC $FeCl_3$ coagulation, dose: 4 mM 64% removal of silica
Jamil et al., 2019	Combination of stromwater and biologically treated sewage effluent GAC adsorption and Purolite anion exchange resin, dose: 0.1-5 g/L GAC has higher capacity than two Purolite anion exchange resins in removing total DOC. Almost 100% humics was removed in combined system in which Purolite was followed by GAC adsorption

*Conventional treatment processes were applied as pretreatment.

2.2.2. Advanced Oxidation Technologies

Advanced oxidation processes are known to be innovative water and wastewater treatment technologies which involve the generation of hydroxyl radicals ($HO^{\bullet}$) in sufficient quantity for water purification (Glaze et al., 1987). Secondary reactions produce of highly reactive oxygen species (ROS) (*e.g.* H_2O_2, $^1O_2$, $O_2^{\bullet-}$, $HO_2^{\bullet}$) that are able to degrade even the refractory organic molecules into biodegradable compounds, and eventually mineralize them to CO_2, H_2O and inorganic anions. Among these ROS, $OH^{\bullet}$ is one of the most powerful oxidizing agent (Redox potentials: 2.80 V for $HO^{\bullet}$, 0.32 V for H_2O_2, 0.65 V for $^1O_2$, 0.94 V for $O_2^{\bullet-}$, and 1.06 V for $HO_2^{\bullet}$) and has the ability to non-selectively oxidize a wide range of pollutants effectively. Concentrates from wastewater treatment plants present higher organic matter load but lower salinity, therefore advanced treatment technologies, such as AOPs are good candidates for the degradation of resistant pollutants (Pérez-González et al., 2012). Moreover, an enhancement on the performance of biological treatment system could be achieved by incorporation of AOPs as pretreatment processes that are able to break down refractory organics into simple and biodegradable products (Zhou et al., 2011; Vendramel et al., 2013; Bagastyo et al., 2011).

A summary of AOPs applied in ROC_m treatment was presented in Table 2.4. AOPs could be classified into sub-groups of light-homogeneous AOPs, dark-homogeneous AOPs, light-heterogeneous AOPs and dark heterogeneous AOPs. Feasibility of light initiated homogeneous AOPs (UV/O_3, UV/H_2O_2 and $UV/H_2O_2/O_3$, photo-Fenton) and dark homogenous AOPs (US, O_3, US/O_3, US/H_2O_2, $US/ H_2O_2/O_3$, Fenton) were investigated. Considering all different homogeneous AOPs used in ROC_m treatment, UV/H_2O_2 system was the most prominent technology by which up to 80% NPOC removal was achieved. Heterogeneous AOPs investigated for ROC_m treatment were electro-Fenton, UV/TiO_2 photocatalysis, electrodialysis and electrochemical oxidation processes among which electrochemical oxidation displayed the superiority due to its strong potential of degrading variety of organic pollutants present in ROC_m. Being a promising treatment process, electrochemical oxidation of ROC in the presence of different electrodes has been extensively studied (Bagastyo et al., 2013; Urtiaga et al., 2013; Lütke-Eversloh et al., 2014; Hurwitz et al., 2014). On the other hand, production of trihalomethanes (THMs) as a result of electrochemical oxidation process was the major drawback of the system that is still under investigation. It could be figured out from Table 2.4 that AOPs exhibited different reacting systems although they are almost all characterized by the production of hydroxyl radicals via a non-selective oxidation pathway. Depending on the AOP used for ROC_m treatment, some of them ended up with satisfactory results for the removal of selected constituents whereas others were found to be limited regarding the complex and interrelated photo,

physical, chemical and radical mechanisms which are still inadequate in the state of knowledge of AOPs. Moreover, besides fundamental studies, more pilot and field-scale studies should be performed to determine the removal efficiencies that could be considered as dependent on both ROC_m quality conditions and operational parameters. Uncertainties related to the technical and economic effectiveness of AOPs should also be considered and interpreted.

Table 2.4. Advanced oxidation processes applied for ROC_m treatment.

Reference	Homogeneous AOPs Treatment process/Process Efficiency
Benner et al., 2008	Ozonation with continuous quench flow system, ozone dose: 5-10 mg/L 90% removal of beta blockers were achieved and Moderate bromate formation was reported.
Dialynas et al., 2008	Ultrasound, frequency: 80 kHz, 67.5 W and 135 W 29% NPOC removal at 67.5 W and 34% NPOC removal at 135 W were achieved. Energy consumption was found to be 810 kJ/mgNPOC oxidized.
Westerhoff et al., 2009	Fenton, doses: 10 mM Fe^{2+} and 10 mM H_2O_2, pH: 3.3 50% NPOC removal was achieved.
	O_3/H_2O_2, dose: 0.7 mol H_2O_2/mol ozone 75% NPOC removal at 1000 mg/L ozone dose was achieved.
	UV/H_2O_2, H_2O_2 dose:10 mM, UV dose: 11.8 kWh/m^3 40% DOC removal was achieved at pH 4 and <10% DOC removal was achieved at pH 7.
Bagastyo et al., 2011	UV/H_2O_2, H_2O_2 doses: 200, 400, 600 and 800 mg/L, I_o: 2.74x10^{-6} E/Ls Complete decolorization and breakdown of organics into smaller NOM fractions were achieved.70% and 80% NPOC removal and 30 and 80% COD removal were achieved for ROC_1 and ROC_2.
Zhou et al., 2011	UVA/H_2O_2, H_2O_2 dose: 5 mM, I_o: 7.7 mW/cm^2 Insignificant COD and NPOC removal and no change in aromaticity of the organic matter were achieved.
	UVA/O_3, O_3 dose: 0.45 and 0.58 mg/L, I_o: 7.7 mW/cm^2 28.4% NPOC removal and 15.4% COD removal were achieved. Significant decrease in 15evamisole15 of the organic matter, improvement on ecotoxicity biorefractory nature were retained.
	$UVA/H_2O_2/O_3$, H_2O_2 dose: 5 mM, I_o: 7.7 mW/cm^2, O_3 dose: 0.45 and 0.58 mg/L 25.6% NPOC removal and decrease in aromaticity of the organic matter were achieved.
	US, frequency: 20 kHz 4.9% NPOC removal, almost no change in biorefractory nature of the organic matter and very slight improvement on eco-toxicity were achieved.
	US/H_2O_2, H_2O_2 dose: 5 mM, frequency: 20 kHz 2.8% NPOC removal and no change in aromaticity of the organic matter were achieved.
	O_3, O_3 dose: 0.45 and 0.58 mg/L 21.7% NPOC removal, improvement on eco-toxicity and moderate change in biorefractory nature of the organic matter were achieved.
	US/O_3, O_3 dose: 0.45 and 0.58 mg/L, frequency: 20 kHz 27.8% NPOC removal, 16.5% COD removal, improvement on eco-toxicity and moderate change in biorefractory nature of the organic matter were achieved.
	$US/H_2O_2/O_3$, H_2O_2 dose: 5 mM, frequency: 20 kHz, O_3 dose: 0.45 and 0.58 mg/L 31.4% NPOC removal and decrease in aromaticity of the organic matter were achieved.
Ben Abdelmelek et al., 2011	γ radiation, 3-5 Gy per 2-3 ns pulse Up to 80% removal of PPCPs were achieved.
Justo et al., 2013	UV/H_2O_2, H_2O_2 dose: 0.04-0.72 mgH_2O_2/mgTOC, I_o: 1.5x10^{-5} Einstein/s 9.6% NPOC removal and 16% COD removal were achieved. Acceptable levels of elimination of pharmaceuticals required higher H_2O_2 doses.
	O_3, O_3 dose: 0.14-6.93 mgO_3/mgTOC <1% NPOC removal and 11% COD removal were achieved. Ozone resistant pharmaceuticals were detected.
Lu et al., 2013	BAC pretreatment and UVC/H_2O_2, H_2O_2 dose: 4 mM, I_o: 12.89 mJ/scm^2

	60% NPOC removal and 50%COD removal were achieved via combined treatment. No apparent toxicity was detected for both untreated and treated ROC samples.
Vendramel et al., 2013	O_3, O_3 dose: 9-11.5 mgO_3/mgNPOC 15% NPOC removal, 33% COD removal, 63% UV_{254} removal were achieved. Moderate change in biorefractory nature of the organic matter was achieved.
	UV/O_3, O_3 dose: 9-11.5 mgO_3/mgNPOC, I_o: $1.5x10^{-5}$ E/s 29% NPOC removal, 42% COD removal, 73% UV_{254} removal and significant change in biorefractory nature of the organic matter were achieved.
	H_2O_2/O_3, H_2O_2 dose: 10 mg/L, O_3 dose: 9-11.5 mgO_3/mgNPOC 37% NPOC removal, 48% COD removal, 67% UV_{254} removal and significant change in biorefractory nature of the organic matter were achieved.
	O_3/H_2O_2/UV, H_2O_2 dose: 10 mg/L, O_3 dose: 9-11.5 mgO_3/mgNPOC, I_o: $1.5x10^{-5}$ E/s 44% NPOC removal, 54% COD removal, 74% UV_{254} removal and significant change in biorefractory nature of the organic matter were achieved.
Joo, 2014	Integrated active carbon and iron activated persulfate oxidation, Fe and persulfate dose: 20 mM 80% NPOC removal, 43% TN removal, 87% TP removal and 97% NO_3^- removal were achieved.
Umar et al., 2014	UVC/H_2O_2 followed by biological treatment, H_2O_2 dose: 3 mM, I_o: 8.91 mW/cm^2 25% NPOC removal and 37% COD removal were achieved.
Ren et al., 2016	Combined Fe/Cu/air and Fenton process Up to 65% COD removal was achieved. BOD_5/COD ratio was increased from 0 to 0.26.
Yang et al., 2016	UV/H_2O_2 and UV/$S_2O_8^{2-}$ 75-80% removal of trace organics was achieved. Presence of effluent organic matter and anions were strongly scavenged $OH^{\bullet}$, therefore reduced removal efficiency.
Azaïs et al., 2017	O_3, O_3 dose: 0-74 mg/L. > 95% removal of acetaminophen and carbamazepine, 40-50% removal of atenolol.
Miralles-Cuevas et al., 2017	Solar photo-Fenton, H_2O_2 dose: 50 mg/L, Fe dose: 1 mM, I_o: 7.5 kJ/L. > 90% removal of all studied micropollutants (10–55,000 ng/L) such as caffeine, carbamazepine, naproxen and atenolol.
Weng et al., 2018	Ozonation, O_3 dose:42.4 mg/L 77% UV_{254} and 50% TOC removal were achieved.
Li et al., 2019	O_3-assisted UV-Fenton process, UV-LED, H_2O_2 dose: 15 mM, O_3 dose: 15 mg/L, Fe dose: 0.3 g/L, I_o: 12.89 mJ/scm^2. 80.4% COD removal was achieved following irradiation period of 120 min.
Lee et al., 2020	UV/H_2O_2 and UV/persulfate processes H_2O_2 and PS dose: 5 mM DOC removal efficiency of 8.4% and 25.1% were achieved via UV/H_2O_2 and UV/PS
Deng, 2020	O_3, O_3 dose: 10 mg/L ~ 20% NPOC removal was achieved. > 90% carbamazepine removal was attained.
King et al., 2020	O_3, O_3 dose: 45-55 mg/L ~ 20% NPOC removal was achieved.
Heterogeneous AOPs	
Van Hege et al., 2004	Electrochemical oxidation by using BDD, RuO_2, PbO_2, SnO_2 electrodes, J: 0.5, 1.0 and 1.5 A COD removals of 56.2%, 11.7%, 18.6% and 21.7% were achieved by using BDD, RuO_2, PbO_2, SnO_2 electrodes respectively.
Dialynas et al., 2008	Electrochemical oxidation with BDD, J: 3.6 A and 17.8 A 30% NPOC removal for 3.6A and 36% NPOC removal for 17.8 A were achieved.
Badruzzaman et al., 2009	Bipolar membrane electrodialysis and electrochlorination, J: 15-90 mA/cm^2 Production of >0.2 M mixed acid and base by electrodialysis was achieved. About 6000 mg/L concentrated hypochlorite solution was produced by electrochlorination.
Pérez et al., 2010	Electro-oxidation with BDD anode and stainless steel cathode, J: 20-200 A/m^2 100% COD removal after 8 h for 50 A/m^2, after 6 h for 100 A/m^2 and after 4 h for 200 A/m^2 were achieved. More than 92% removal of ECs was achieved.
Radjenovic et al., 2011	Electrochemical oxidation with RuO_2/IrO_2-coated titanium anodes, J: 1-250 A/m^2 25.1% NPOC removal was achieved. All persistent trace compounds were completely oxidized after applying 1.45 kAh/m^3.
Bagastyo et al., 2011a	Electrochemical oxidation with mixed metal oxide titanium coated electrodes, J: 100 A/m^2 <16% NPOC removal and >80% Color removal were achieved for all electrodes.

Bagastyo et al., 2013	Electrochemical oxidation with Ti/Pt-IrO_2, Ti/SnO_2-Sb and BDD electrodes in the presence of chloride, nitrate and sulfate salts, I: 510 mA 40%, 31% and 28% NPOC removals for Si/BDD, Ti/SnO_2-Sb and Ti/Pt-IrO_2 in the presence of NaCl were achieved. 51%, 23% and 12% NPOC removals for Si/BDD, Ti/SnO_2-Sb and Ti/Pt-IrO_2 in the presence of SO_4^{2-} were achieved. 41%, 20% and 14% NPOC removals for Si/BDD, Ti/SnO_2-Sb and Ti/Pt-IrO_2 in the presence of NO_3^- were achieved. THMFP and HAAFP were observed.
Urtiaga et al., 2013	Electrochemical oxidation with BDD, J: 20-100 A/m^2 52% NPOC removal and more than 95% ECs removal were achieved.
Hurwitz et al., 2014	Combination of photochemical and electrochemical processes, BDD electrode, I_o: 8500 $\mu W/cm^2$, J: 20 mA/cm^2 25% NPOC removal by photochemical process, 35% NPOC removal by electrochemical process and more than 80% NPOC removal by hybrid process were achieved.
Lütke Eversloh et al., 2014	Galvanostatic electrochemical treatment using BDD electrodes, I: 20 mA 96% TOC removal and up to 99% iopromidine removal after about 7.5 h were achieved.
Chen et al., 2017	Rectangular flow-through electrocoagulation reactor, mild steel electrodes, J: 8 mA/cm^2. 76-89% removal of silica with electrocoagulation.
Arola et al., 2018	Pulsed corona discharge, pulse repetition frequency: 840, pulse duration: 100 ns, amplitude: 20 kV, oxidation energy: 0, 0.3, 0.7, 1.5, 3.5 and 10 kWh/m^3 21% DOC removal and up to 92% EC removals were achieved.
Chen et al., 2020	Photoelectrocatalysis using TiO_2 nanotube arrays electrode UVA lamp, λ: 365 nm, I_o: 13.3 mW/cm^2 63% DOC removal was achieved in 180 min
Tang et al., 2020	Photoelectrocatalytic (PEC) chloride-radical (Cl%) system using WO_3[Pd- Cu/NF] electrode couples. 99.90% TN removal and 0.95% TOC removal were attained in 180 min.
Xu et al., 2020	Catalytic ozonation with Acid-washed activated carbon, nitric acid modified activated carbon, aminated activated carbon and cerium-loaded activated carbon. O_3 dose: 12.15 mg/min, H_2O_2 dose: 142 mg/L, catalysts dose: 0.2 g/L. The removal rates of p-CBA, TOC and three target pollutants (*e.g.*, tetracycline, metoprolol, atrazine) were 99.6%, 70.38%, 97.76%, 96.21% and 96.03%, respectively.

2.2.2.1. Photocatalysis. Among different AOPs, heterogeneous photocatalysis using semiconductor catalysts *i.e.* TiO_2, ZnO, Fe_2O_3, CdS, GaP and ZnS has gained specific attention due to its efficiency in degrading a wide range of equivocal resistant organics into biodegradable compounds and mineralizing to innocuous carbon dioxide and water, respectively. Therefore, heterogeneous photocatalysis is accepted to be one of the most efficient AOPs leading to total mineralization of the parent compound and its oxidation products (Ollis, 1985; Linsebigler et al., 1995; Fujishima et al., 2000). Consequently, application of photocatalysis reached numerous areas for the treatment of water, air, soil, and also in the field of environmental remediation, self-cleaning surfaces, green chemistry, green engineering, energy production, medical and biomedical applications (Pichat, 2013; Kisch, 2014; Dionysiou et al., 2016). Among all other types of organic constituents present in water and wastewater compositions, photocatalytic degradation of NOM as the major organic fraction has been widely investigated throughout the literature (Yigit and Inan, 2009; Uyguner and Bekbolet, 2005a, b, and c, Uyguner-Demirel and Bekbolet, 2011; Uyguner-Demirel et al., 2017). Various semiconductor photocatalysts have been investigated in terms of their performance, however use of TiO_2 generally gives the most desirable results because of its advantageous properties, such as good reactivity, high

chemical stability, inexpensiveness, commercial availability and low toxicity (Rajeshwar, 1995). However, the major disadvantage of TiO_2 as the photocatalysts is its wide band gap utilizing only a small portion of the solar light (< 5%). For that reason, studies have been focused on the alteration of TiO_2 by doping impurities, such as metal and non-metal species into its structure in order to make it able to harvest solar irradiation. Photocatalytic applications for ROC_m treatment throughout the literature were presented in detail in Table 2.5.

Table 2.5. Photocatalytic treatment of ROC_m.

Reference	Reactor type/Lamp specifications
Dialynas et al., 2008	Slurry type batch reactor, 9W UVA lamp, λ: 300-400 nm, I_o: $4.7x10^{-6}$ E/s TiO_2 P-25, BET: 50 m^2/g, E_{bg}: 3.01 eV, dose: 0.5-1.0 g/L. NPOC removal (50%) in 60 min was achieved. No further improvement was attained upon longer irradiation periods irrespective of TiO_2 dose.
Westerhoff et al., 2009	Slurry type batch reactor with borosilicate glass, 450W Hg vapor lamp, λ_{max}: 254 nm, I_o: 1.1 W/L TiO_2 P-25, BET: 50 m^2/g, E_{bg}: 3.01 eV, dose: 1.0-5.0 g/L. 87% NPOC removal was achieved.
	Photo-Cat® system consisted of a reactor, UV lamp, ceramic ultrafilters and automated system 75 W UV lamps, I_o: Not presented. 80% NPOC removal and removal of ECs below detection limit were achieved.
Zhou et al., 2011	Slurry type batch reactor, 9W UVA lamp, λ_{max}: 365 nm, I_o: 7.7±0.1 mW/cm^2 TiO_2 P-25, BET: 50 m^2/g, E_{bg}: 3.01 eV, dose: 1.0 g/L. 14.5% NPOC removal, 5.5% COD removal and decrease in aromaticity of the organic matter were achieved. Improvement on eco-toxicity and slight change in biorefractory nature of the organic matter were achieved.
	UVA/TiO_2/O_3, O_3 dose: 0.45 and 0.58 mg/L 52.2% NPOC removal, 29.2% COD removal and decrease in aromaticity of the organic matter were achieved. Improvement on eco-toxicity and slight change in biorefractory nature of the organic matter were achieved.
	US/UVA/TiO_2, Frequency: 20 kHz 16.7% NPOC removal, 3.4% COD removal and decrease in aromaticity of the organic matter were achieved. Improvement on eco-toxicity and slight change in biorefractory nature of the organic matter were achieved
	9W UVC lamp, λ_{max}: 254 nm, I_o: 9.1±0.1 mW/cm^2 18.6% NPOC removal, 9.9% COD removal and decrease in aromaticity of the organic matter were achieved. Improvement on eco-toxicity and slight change in biorefractory nature of the organic matter were achieved
Lin and Li, 2015	UVA lamp, λ_{max}: 365 nm I_o: 18 mW/cm^2, internally sulfated TiO_2, BET: 147 m^2/g, E_{bg}: 3.13 eV, dose: 0.1% wt Up to 77% NPOC removal was achieved following irradiation period of 6h
Lin et al., 2016	UV mercury vapor lamp, 160W Pure and Fe-doped TiO_2 mixed phase nanocomposite thin films on side-glowing optical fibers
Xiang et al., 2017	UVA lamp, λ_{max}: 365 nm, I_o: 1000 μW/cm^2 TiO_2/Zeolite composite sheet, BET: not presented, E_{bg}: not presented, dose: not presented 51% TOC removal was achieved following irradiation period of 6h
Birben and Bekbolet, 2019	Solar simulator, λ: 290-700 nm, I_o: 250 W/m^2 TiO_2, N-doped TiO_2, ZnO, and TiO_2/ZnO nanocomposite

Application of photocatalysis on ROC_m treatment has been studied addressing to TiO_2 P-25 as the commonly used commercial photocatalyst in the previous studies until 2014. Then, lab prepared TiO_2 by sol-gel method (Lin et al., 2014b) and internally sulfated TiO_2 (Lin et al., 2015) specimens have been proposed as novel photocatalysts for the treatment of ROC_m as well as ECs present in

ROC_m. Studies on photocatalytic treatment of ROC_m were found to be very limited and use of only UV (UVA and UVC) initiated photocatalytic systems were proposed. As a recent concern, application of novel synthesized photocatalysts has gained special interest. In addition to doping TiO_2 with metal or non-metal impurities, synthesis and application of nanocomposite materials, which are composed of two or more oxide surfaces, have also been proposed (Lin et al., 2016; Xiang et al., 2017). Applicability of TiO_2/zeolite nanosheet for the removal of crotamiton in ROC was presented and satisfactory results were attained (Xiang et al., 2017). However, it could be inferred from the literature studies concerning the application of photocatalysis especially using novel photocatalysts for the treatment of ROC was still found to be quite limited. Almost all of the photocatalytic treatment studies were conducted in slurry type batch reactor with varying materials, such as borosilicate glass and quartz, whereas Fe-doped TiO_2 mixed phase nanocomposite thin films were also used as immobilized photocatalysts for ROC_m treatment was also presented (Lin et al., 2016). Moreover, overall degradation efficiency of the organic matrix was expressed by extent of mineralization through organic carbon contents. Further evaluation on the removal of different organic constituents, such as NOM-like components and ECs should also be interpreted.

Referring to the previously presented information, AOPs, such as photocatalytic oxidation (PCO), ozonation (O_3), ultrasound (US) and electrolytic oxidation, have been investigated for organics removal from the RO concentrates (Dialynas et al., 2008; Benner et al., 2008; Zhou et al., 2011; Bagastyo et al., 2013). However, in most cases, these AOPs may not be enough to mineralize small fractions of the organics which are highly bio-refractory, consisting of both natural organic matter and most categories of emerging organic contaminants. Furthermore, at higher dosages of the oxidants, a larger intensity of energy input and a longer reaction time seem unable to further increase the organics removal efficiencies. As a consequence, simple AOPs would not able to substantially mineralize the organics present in the ROC_m. Coupling AOPs with other treatment technologies would be an effective alternative to achieve high organics removal efficiency.

Besides the presence of natural organic matter, due to the occurrence of MOC as composed of various refractory chemicals including pesticides, PPCPs, EDCs, SMPs and partially biodegraded organics from wastewater treatment plants, ROC_m should also be evaluated in terms of possible eco-toxic effects. It is known that, persistent emerging contaminants detected in municipal wastewater, surface water and drinking water are usually toxic to humans and have impacts on ecosystems therefore, when reverse osmosis processes successfully reject such compounds from water and wastewater, they become more concentrated than reverse osmosis influent and have higher potential of toxicity in ROC_m. In this respect, for further clarification purposes, literature studies considering

toxicity assessment of ROC_m are compiled and presented in Table 2.6. Special attention is directed to the evaluation of the toxicity data with reference to the applied AOPs details of which has been already discussed in the section 2.2.2. Irrespective of the treatment method, the most common applied toxicity method was found to be Microtox using *Vibrio fischeri* due to its recognition in the field of eco-toxicology as the standard assay for acute cytotoxicity and reveals the baseline toxicity of a targeted compounds mixture (Azaïs et al., 2017).

Table 2.6. Toxicity assessment of ROC_m using Microtox with *Vibrio fischeri*.

Reference	ROC_m composition /Treatment process/Toxicity status
Radjenovic et al., 2011	EC/ROC_m, 28 ECs as 21 pharmaceuticals and 7 pesticides Electrochemical oxidation Baseline toxicity was increased with respect to increasing applied charge
Zhou et al., 2011	ROC_m, molecular size distribution Heterogeneous PCO, O_3, US and H_2O_2 oxidation alone and/or combined 62% inhibition in raw ROC, UVA/TiO_2/O_3 reduced inhibition to 25% O_3, UVA/O_3 and US/O_3 still posed high ecotoxicity
Justo et al., 2013	EC, 11 ECs as pharmaceuticals UV/H_2O_2 and O_3 Samples did not show any non-specific toxicity before and after treatment
Lu et al., 2013	ROC_m, THMFP UVC/H_2O_2 alone or combined with Biologically Activated Carbon No apparent toxicity was detected for the untreated and treated ROC_m
Liu et al., 2012	ROC_m UVC/H_2O_2 No apparent toxicity was detected for the untreated and treated ROC_m
Lütke Eversloh et al., 2014	ROC_m, 1 EC as pharmaceutical Galvanostatic electrochemical treatment using BDD electrodes Toxicity was found to be less than 20%
Umar et al., 2016	ROC_m Coagulation, UVC/H_2O_2, and BAC treatment No toxicity was noted after sequential coagulation (using alum or ferric chloride), UVC/H_2O_2 and BAC treatment
Azaïs et al., 2017	ROC_m Ozonation More research is needed to determine the toxic potential of treated sample in relation with degradation products

Regarded as one of the most widely used bacteria toxicity bioassays, *Vibrio fischeri* toxicity method is based on bio-luminescence inhibition in the presence of toxic compounds. Referring to Table 2.2, sole ROC_m as well as ROC_m containing ECs were investigated in terms of toxic effects both prior to and following the application of AOPs. Radjenovic and colleagues investigated the contributions of 28 ECs whereas Justo and co-workers followed the toxicity originated from 11 ECs (Radjenovic et al., 2011; Justo et al., 2013). No apparent toxicity was reported for sole ROC_m (Zhou et al., 2011; Lu et al., 2013; Liu et al., 2012). In addition to *Vibrio fischeri* toxicity method, characterization and biotoxicity assessment of dissolved organic matter in ROC_m by using SOS/umu assay with *Salmonella typhimurium* TA1535/pSK1002 has been also studied and concluded that genotoxicity ROC_m could be originated mainly from hydrophilic neutral components, hydrophobic

acids and hydrophobic bases as the sub-fractions of organic matter content of ROC_m (Sun et al., 2014; 2016a and b). Moreover, bioluminescence inhibition assay using *photobacterium T3*, *Euglena gracilis* assay, and acute toxicity assay using zebrafish are other methods applied for the toxicity assessment of ROC_m following ozonation process. Cytotoxicity assays in terms of cell viability assay and intracellular reactive oxygen species measurements has also been reported as the alternative expression of toxicity of ROC_m (Weng et al., 2018).

The addition of chemicals during the treatment process further complicates the situation by changing the character of the organic and inorganic pollutants thus influencing the chemical equilibrium of the dissolved constituents (Van der Bruggen et al., 2003; Tang et al., 2013 from Zhang et al., 2018; Weng et al., 2018). Moreover, applied treatment processes for ROC_m could also change its toxicity potential with respect to transformation of organic and inorganic components. For example, upon exposure to oxidation, some of the non-toxic compounds could end up with the formation of highly toxic reaction products, whereas initially highly toxic compounds could be converted to non-toxic end products. As a consequence, toxicity assessment of ROC_m before and after treatment strategies plays a crucial role to get a further insight on the transformation of organic constituents especially emerging contaminant fraction.

3. MATERIALS AND METHODS

3.1. Materials

3.1.1. Natural Organic Matter-like Organic Matter Representative

Humic acid (HA) solution was selected as the representative of NOM-like organic fraction of ROC_m. Commercial humic acid (Sigma Aldrich humic acid, sodium salt) was used in all experiments. Stock solution of 1000 mg/L were prepared by dissolving 1.0 g humic acid in 1000 mL distilled deionized water. HA solution was kept in dark glass container to eliminate any photo-initiated reactions. Appropriate dilutions (50 mg/L and 100 mg/L) were made from the stock solution in order to prepare corresponding organic carbon content of working solutions to have approximate organic carbon content of ROC_m samples presented through the literature (Table 2.1) as given in Section 2.1.2.

3.1.2. Emerging Contaminants

According to the literature findings derived from presence of ECs in ROC_m, the most commonly found ECs were reported as sulfamethoxazole, carbamazepine, caffeine, and naproxen (Table 2.2). Therefore, sulfamethoxazole (SMX) as one of the most common active compound of antibiotics and carbamazepine (CMZ) that is known to be as an anti-epileptic drug were selected as the target ECs of ROC_{ECm} composition in order to represent real ROC_m conditions. Both SMX and CMZ was purchased from commercial suppliers (Sigma Aldrich, powder form). Working solutions of SMX and CMZ were prepared in distilled/deionized water and continuous stirring was applied over-night in order to assure complete dissolution. Initial concentration of each EC was selected as 5 mg/L for all experimental conditions.

3.1.3. Preparation of Synthetic Reverse Osmosis Concentrate Samples

3.1.3.1. Preparation of the organic matrix. Synthetic ROC_m samples were prepared according to the recipe based on the compositional variations presented in the literature (Birben et al., 2017). Commercial AHA was used in order to mimic humic matter (HM) component of ROC. Since

molecular size distribution profiles of organic matter content of ROC could be diverse, having a synthetic organic matrix with varying molecular weight compounds would represent real conditions more accurately. Therefore, two different samples were prepared according to their organic matter content and defined as ROC_{m1} and ROC_{m2}. ROC_{m1} was directly prepared by appropriate dilution (50 mg/L) of 1000 mg/L stock HA solution in the presence of other ROC constituents. On the other hand, 100 mg/L HA solution was subjected to solar photocatalysis in the presence of 0.50 mg/mL TiO_2 for irradiation period of 15 min in order to prepare ROC_{m2} which contains both non-degraded fractions as well as photocatalytically degraded fractions of 100 mg/L HA. Consequently, ROC_{m1} was composed of non-degraded fractions of HM representing medium and high molecular weight compounds whereas ROC_{m2} was composed of both non-degraded and photocatalytically degraded fractions of HM in order to obtain multicomponent organic matrix representing all molecular size fractions that could be seen in real ROC compositions (Birben et al., 2017). In addition, humic behavior in aqueous solution is considered as a good candidate for both surfactant properties and multicomponent dissolved organic matrices present in ROC composition (von Wandruszka, 2000). Consequently, HA was selected as good candidate in order to represent different variables that could be detected in real ROC samples, such as NOM-like organic matter, surfactants, *etc*.

SMX and CMZ were selected as target ECs and added as a mixture to the synthetically prepared ROC_{m1} and ROC_{m2} solutions to obtain ROC_{ECm1} and ROC_{ECm2} samples. Therefore, mixed SMX and CMZ solutions (each concentration: 5 mg/L) were prepared and added to ROC_{m1} and ROC_{m2} solutions. Thus prepared solutions designated as ROC_{ECm1} and ROC_{ECm2} were stirred over-night using magnetic stirrer to achieve complete dissolution in the absence of any actinometrically active light.

3.1.3.2. Preparation of the inorganic matrix. Aqueous solutions of common anions (Cl^-, NO_3^-, SO_4^{2-} and PO_4^{3-}) and cations (Na^+, K^+, Ca^{2+} and Mg^{2+}) in predetermined amounts were added to ROC compositions to prepare synthetic ROC_m and ROC_{ECm} solutions. Inorganic composition of ROC samples was referred to the synthetic hard water composition derived by Smith and colleagues (Smith et al., 2002). Chemicals used for the counter ions were as follows: $CaCl_2$ (Cl^- source), $CaNO_3$ (NO_3^- source), Na_2SO_4 (SO_4^{2-} source) and K_3PO_4 (PO_4^{3-} source) whereas cations were chosen as $CaCl_2$, $CaCO_3$, and $Ca(NO_3)_2$ (Ca^{2+} source), $MgSO_4$ (Mg^{2+}source), $NaHCO_3$ and Na_2SO_4 (Na^+ source), and $KHCO_3$ and KH_2PO_4 (K^+ source). Concentration values of common anions and cations were measured by analytical methods (Section 3.2.3.3) using ion chromatography and the results were validated with the expected values reported in the reference study in accordance with the results attained by the literature study.

3.1.4. Preparation of the Photocatalyst Specimens

Solar photocatalytic degradation experiments were conducted by using selected photocatalyst specimens that are either commercially available specimens or newly synthesized ones. TiO_2 Evonik P-25 and ZnO were nominated as the commercial photocatalysts, whereas N-doped TiO_2 and TiO_2/ZnO nanocomposite were proposed as lab-prepared photocatalyst specimens. Since application of N-TiO_2, ZnO, and TiO_2/ZnO nanocomposite has not been studied in the literature, these photocatalysts would bring novelty on the solar photocatalytic treatment of ROC_m. Moreover, experiments with sole TiO_2 and ZnO as well as synthesized TiO_2/ZnO nanocomposite supplied comparative evaluation of behavior and photocatalytic activity of nanocomposite and its precursors individually.

TiO_2 (Evonik P-25, 79% anatase and 21% rutile) with the primary particle size of 21 nm and surface area of 50 m^2/g and ZnO nanopowder (Aldrich) with particle size < 100 nm were used as the TiO_2 and ZnO sources of TiO_2/ZnO nanocomposite. Acetic acid (glacial, anhydrous) was purchased from Merck. All chemicals used in the experiments were reagent grade and used as received without further purification. All solutions were prepared with distilled/deionized water. TiO_2 P-25 (Evonik) and ZnO (Sigma Aldrich) were used without any modification.

N-TiO_2 was synthesized by using an incipient wet impregnation method in which urea was used as the nitrogen source and Evonik P-25 was used as TiO_2 source. 8 g TiO_2 and 10 mL urea solution were stirred for 1 h under room temperature followed by washing and centrifugation step. Following heat treatment at 378 K for 24 h, photocatalyst was calcined at 623 K for 3 h grounded and sieved. Detailed information about the preparation and characterization of N-doped TiO_2 was presented by Gurkan and co-workers and Birben and co-workers (Gurkan et al., 2012, Birben et al., 2015).

TiO_2 (Evonik P-25, 79% anatase and 21% rutile) with the particle size of 21 nm and surface area of 50 m^2/g and ZnO nanopowder (Aldrich) with particle size < 100 nm were used as the TiO_2 and ZnO sources of TiO_2/ZnO nanocomposite. TiO_2/ZnO nanocomposite was prepared by the following simple sonolytic method: 2.5 g TiO_2, 2.5 g ZnO, 20 mL distilled/deionized water, and 1.5 mL acetic acid were grounded in agate mortar for 10 minutes. The mixed oxides were diluted by the addition of 180 mL deionized water and then sonicated in an ultrasonic bath with 35 kHz frequency for 10 min. Following mixing step, composite suspension was filtered, heat-treated at 378 K for 24 h to eliminate water, calcined at 773 K for 1 h and grounded. This methodology was modified from the synthesis method used by Wang and colleagues (Wang et al., 2009). Detailed information about the modified

preparation technique as well as characterization of the photocatalyst was presented elsewhere (Turkten and Bekbolet, 2020). Physicochemical and photochemical properties of all photocatalyst specimens are presented in section 4.2 in Table 4.3.

3.2. Methods

Methodology of this study was followed by a stepwise approach to identify and explain all experimental work, analytical methods applied as well as data evaluation tools for clarification purposes. First, all treatment process related reactors used in the experiments were classified and presented in detail in terms of their irradiation source that are either UVC irradiation initiated reactors or simulated solar irradiation initiated reactors under "Reactor configurations" subheading. Then, all applied treatment processes were presented in a broader perspective with all of their specific experimental conditions in detail. In a similar manner of reactor configurations, treatment processes were also given depending on irradiation source of the reactor as UVC irradiation initiated processes (UVC photodegradation, UVC/H_2O_2, photo-Fenton processes) and solar irradiation initiated processes (solar photodegradation and solar photocatalytic degradation processes). Analytical methods used for the characterization of samples were presented in "analytical methods" subheading comprehensively.

3.2.1. Reactor Configurations

3.2.1.1. UVC light initiated reactor. UVC photodegradation experiments were performed at room temperature in a 600 mL capacity, cylindrical quartz batch photoreactor located in the center of an octagonal reaction chamber consisted of 14 UV-C lamps (I_o: 8W each, λ_{max}: 254 nm) located on the reactor walls. Schematic representation of UVC reactor was presented in Figure 3.1.

Figure 3.1. UVC irradiation initiated reactor configuration.

3.2.1.2. Solar light initiated reactor. Solar light initiated reactor is consisted of ATLAS Suntest CPS+ solar simulator equipped with an air cooled Xenon lamp (I_o: 250 W/m^2 and emission spectrum range between λ_{range}: 300-800 nm) as the light source (Ref.56052371, Atlas). Schematic representation of solar simulator was presented in Figure 3.2.

Figure 3.2. Solar irradiation initiated reactor configuration (Atlas Suntest CPS+).

3.2.2. Treatment Processes

3.2.2.1. UVC photodegradation process. UVC photodegradation experiments were performed at UVC light initiated reactor explained in Section 3.2.1.1. 500 mL of sample was exposed to UVC irradiation for t_{irr}: 0-90 min with 20 min intervals.

3.2.2.2. UVC/H_2O_2 process. UVC/H_2O_2 experiments were conducted by using the same reactor configuration given in UVC photodegradation experiment (Figure 3.1). According to the literature studies performed on UVC/H_2O_2 treatment of ROC_m, which have similar organic carbon content of this study, optimum H_2O_2 concentration was selected as 3 mM (Umar et al., 2014 and 2015) from the range of 1-6 mM. All ROC samples were exposed to UVC/H_2O_2 process for irradiation period of 60 min. After each experiment, residual H_2O_2 was quenched with stoichiometric amount of catalase in order to terminate the reaction of H_2O_2 prior to analyses.

3.2.2.3. Fenton and photo-Fenton processes. Photo-Fenton experiments were conducted by using UVC light initiated reactor specified in Figure 3.1. Optimum H_2O_2 concentration and Fe^{2+} concentration was reported 1:1 molar ratio through the literature (Westerhoff et al., 2009) and selected as 3 mM for all experiments. Fenton experiments were also performed in same reactor configuration under the same experimental conditions as a control experiment. All ROC samples were exposed to Fenton and photo-Fenton processes for following reaction period of 60 min. After each experiment, catalase was used to quench residual H_2O_2 in order to terminate the reaction and pH was increased to

neutral value in order to precipitate Fe^{2+}. Then samples were filtered through 0.45 μm acetate membrane filters prior to analyses.

3.2.2.4. Solar photodegradation process. Solar photodegradation experiments were performed by using solar light initiated reactor as explained in Section 3.2.1.2 (Figure 3.2). 150 mL Pyrex reaction vessels were used. 50 mL of each sample was exposed to simulated solar irradiation for reaction periods of 20, 40, 60, and 90 min. Volume correction was done by distilled/deionized water in order to eliminate the evaporation loss. Continuous stirring was provided during the whole reaction by magnetic stirrer.

3.2.2.5. Solar photocatalytic degradation process. Solar photocatalytic degradation experiments were performed with the same ATLAS Suntest CPS+ solar simulator as used in solar photodegradation experiments. With respect to the results attained from preliminary experiments carried out with solar photocatalytic degradation of sole HA sample, optimum photocatalyst concentration was selected as 0.25 mg/mL. All ROC samples were subjected to irradiation for reaction periods of 20, 40, 60, and 90 min. Volume correction was done by distilled/deionized water in order to eliminate the evaporation losses. Continuous stirring was provided during the whole reaction by magnetic stirrer. Following photocatalytic degradation process, all samples were filtered through 0.45 μm membrane filters as explained in ultrafiltration section (Section 3.2.3.4) in order to remove the photocatalyst particles from the reaction medium both for terminating the reaction and to prepare clear transparent solution for the UV-vis and fluorescence spectroscopic as well as for organic carbon analyses.

3.2.3. Analytical Methods

3.2.3.1. Characterization of the photocatalyst specimens. Vast number of studies targeted application of semiconductor photocatalysis with respect to its potential application in a wide spectrum and therefore came up with the idea of synthesis and use of new photocalaysts. Consequently, development of various characterization techniques simulated in order to get a further insight on the properties of new materials (Zhang et al., 2019). TiO_2, N-TiO_2, ZnO, and TiO_2/ZnO are characterized in terms of their physical structure (SEM), elemental composition (EDX), crystallographic properties (XRD), band structure expressed as band gap energy (UV-DRS), and surface stability expressing adsorptive interactions given as Brunauer-Emmett-Teller (BET) surface area.

Scanning electron microscope in combination with Energy dispersive X-ray analysis (SEM/EDX). Surface morphologies of the photocatalysts were assessed by Scanning Electron Microscope (SEM)

in combination with Energy Dispersive X-ray analysis (ESEM-FEG/EDX Philips XL-30) operating at 20 kV using sample powders supported on carbon tape.

X-ray powder diffraction (XRD). The X-ray powder diffraction (XRD) patterns were recorded on a Rigaku-D/MAX-Ultima diffractometer using Cu Kα radiation (λ=1.54 Å) operating at 40 kV and 40 mA and scanning rate of $2^{o}min^{-1}$. Crystallite size (d) was determined (Eq. 3.1) using the Scherrer equation:

$$d = \frac{0.9\,\lambda\,180}{\left(\Pi\ FWHM_{hkl}\cos\theta\right)} \tag{3.1}$$

where; $FWHM_{hkl}$ is the full width at half maximum of an hkl peak at θ value (Alexander and Klug, 1950, Schrerrer, 1918).

Ultraviolet diffuse reflectance spectroscopy (UV-DRS). Band gap energies of the photocatalysts were determined using UV-DRS spectra (Perkin Elmer Lambda 35 spectrometer equipped with an integrating sphere assembly using $BaSO_4$ as the reference material) and calculated through the use of the Kubelka-Munk formula (Kubelka and Munk, 1931) (Eq. 3.2) as given below;

$$F® = (1\text{-}R)^2/2R \tag{3.2}$$

Where R is the reflectance read from the spectrum. Using the Tauc relationship by plotting $[F® h\nu]^n$ vs hν, where hν is the photon energy and n = ½, band gap energy (eV) was deduced from the extrapolation of the Tauc's linear portion to the photon energy axis.

Specific surface area determination with Brunauer-Emmett-Teller method. For the specific surface area determination, nitrogen adsorption/desorption isotherm was obtained at liquid nitrogen temperature 77 K using Quantachrome Nova 2200 e automated gas adsorption system. The specific surface areas were determined using multi-point Brunauer-Emmett-Teller BET analysis.

3.2.3.2. Characterization of organic matter. Organic matter characterization prior to and following each process was followed by monitoring changes in UV-vis and fluorescence spectroscopic parameters as well as organic carbon content expressed as Non-Purgeable Organic Carbon (NPOC). Detailed information about the characterization of organic matter is presented below.

UV-vis absorption spectroscopy. UV-vis absorption spectra were recorded in the 200-600 nm wavelength range using Perkin Elmer Lambda 35 UV-vis double beam spectrophotometer employing Hellma quartz cuvettes of 1.0 cm optical path length. Organic matter was characterized by specified UV-vis parameters. Absorbance values at 436 nm ($Color_{436}$), 365 nm (UV_{365}), 280 nm (UV_{280}) and 254 nm (UV_{254}) were recorded prior to and following each processes. $Color_{436}$ represents color forming moieties coming from humic substances. Humic compounds are known to be rich in phenols and quinones and since phenols and quinones are assumed to be the major groups responsible for the absorption above 350 nm (Del Vecchio and Blough, 2004), absorption above 350 nm could be assigned to phenols and quinones in humic compounds. UV_{280} and UV_{254} indicates aromatic groups with differing properties as well as with various activities. Moreover, UV_{254} could be also considered as a surrogate parameter for DOC (Uyguner-Demirel and Bekbolet, 2011).

Providing quantitative measure of aromatic content per concentration of organic carbon content, $SUVA_{254}$ defined as the UV_{254}/NPOC (L/mg m) was also calculated. It is very well known that $SUVA_{254}$ is regarded to be proportional to both molecular weight and the aromaticity of humic substances. $SUVA_{254} > 4$ refers to the presence of hydrophobic and aromatic organic fractions whereas $SUVA_{254} < 4$ indicates presence of highly hydrophilic and lower molecular weight organic fractions (Edzwald, 1985). NPOC normalized aromatic moieties giving absorbance at 280 nm were also expressed as $SUVA_{280}$ (L/mg m) and evaluated for all samples. $SUVA_{365}$ was also calculated in a similar fashion as the ratio of the UV_{365} absorbing species to NPOC. ($SCoA_{436}$, L/mg m) was defined as $Color_{436}$/NPOC to signify organic carbon normalized color forming moieties (Uyguner-Demirel and Bekbolet, 2011).

Fluorescence spectroscopy in combination with PARAFAC modeling. Fluorescence spectra were recorded by using a Perkin Elmer LS 55 Luminescence Spectrometer equipped with a 150 W xenon arc lamp and a red sensitive red photomultiplier tube. Both synchronous scan mode and Excitation Emission Matrix (EEM) scan mode were used for the characterization of organic matter present in ROC (Sen-Kavurmaci and Bekbolet, 2014; Bekbolet and Sen-Kavurmaci, 2015). Synchronous scan mode was performed in excitation wavelength range of 200-600 nm with the bandwidth of $\Delta\lambda$: 18 nm between the excitation and emission monochromators.

EEM fluorescence contour-plots were constructed based on the fluorescence data recorded in the excitation wavelength range of 200-500 nm with 10 nm steps and emission wavelength in the range of 200-600 nm with 0.5 nm steps. EEM fluorescence contour-plots were plotted as fluorescence intensity with respect to emission and excitation wavelengths by using Matlab 2013a. Fluorophoric

regions were elucidated according to the regional speciation defined previously (Sen-Kavurmaci and Bekbolet, 2014). PARAFAC modeling was conducted using EEM fluorescence data and DOMFluor Toolbox in Matlab 2013a according to the recommended procedure (Stedmon and Bro, 2008).

Non-Purgeable organic carbon. Organic carbon content was expressed as non-purgeable organic carbon excluding inorganic carbon contents and measured by Shimadzu TOC-VWP Total Organic Carbon Analyzer calibrated by using potassium hydrogen phthalate. Calibration range were selected as low range: 0-5 mg/L and high range: 0-25 mg/L.

3.2.3.3. Characterization of inorganic matter. In addition to organic matter characterization of the samples, inorganic constituents of the samples were monitored by following analytical methods. Alkalinity measurements were performed according to the methodology presented in Standard Methods (2320 Alkalinity, 2320 B. Titration Method) (Standard Methods, 2012). Dionex ICS-3000 ion chromatography was used for the determination of common anions both in the absence and presence of HM (upon appropriate dilution). Common cations were measured according to Standard Methods by using Perkin Elmer Aanalyst 300 Atomic Absorption Spectrometry (Standard Methods, 2012). Total dissolved solids (dried at 180ºC, 2-57) were determined with respect to the methodology outlined in Standard Methods (2450 C, Total Dissolved Solids) (Standard Methods, 2012).

3.2.3.4. Molecular size fractionation by ultrafiltration. Prior to and following photolytic and photocatalytic degradation processes, the organic fraction present in all ROC samples were exposed to sequential fractionation. An Amicon stirred cell ultrafiltration unit (Amicon Corp. Model 8050) with Millipore YM series cellulose membrane filters were used for the molecular size fractionation procedure. Continuous stirring and constant operating pressure by pure nitrogen gas were applied throughout the process. Prior to ultrafiltration step, all samples were filtered through 0.45 μm Millipore cellulose acetate membrane filters. Consecutively, samples were fractioned into nominal molecular weight cutoffs of 100 kDa, 30 kDa, 10 kDa, 3 kDa and 1 kDa.

3.2.3.5. Assessment of toxicity. Potential toxicity of samples prior to and following treatment was followed by using BioTox™ test kit (Aboatox Oy, Finland; *V. fischeri* code 1243-500) in accordance with the ISO 11348-3:2007 protocol (ISO 11348-3:2007). The method is based on inhibition of luminescent marine bacteria *V. fischeri*. Following an incubation period of 30 minutes, luminescence measurements were performed and toxicity was expressed as inhibition percentages (INH, %) as calculated by the decrease in luminescence measured in comparison to baseline conditions. Prior to toxicity procedure, salinity content was adjusted to 2% and pH of samples were adjusted to 7.0-7.5.

4. RESULTS AND DISCUSSION

4.1. Characterization of the Samples

4.1.1. Physicochemical and Photochemical Properties of Selected Emerging Contaminants

Physicochemical and photochemical properties of SMX and CMZ were presented in Table 4.1. It could be deduced from Table 4.1 that although target emerging contaminants seemed to have almost comparable molecular weight (SMX: 253 g/moL and CMZ: 236 g/moL), they are significantly differed from each other in terms of molecular structure, solubility properties, ionic state, and photochemical properties that could influence their reaction mechanisms during the treatment processes.

Table 4.1. Physicochemical and photochemical properties of SMX and CMZ.

Parameters		
Name	Sulfamethoxazole	Carbamazepine
Abbreviation	SMX	CMZ
Molecular structure	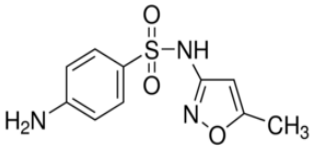	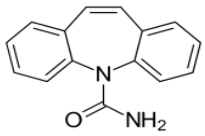
IUPAC name	4-Amino-N-(5-methylisoxazol-3-yl)-benzenesulfonamide	5H-dibenzo[b,f]azepine-5-carboxamide
Molecular formula	$C_{10}H_{11}N_3O_3S$	$C_{15}H_{12}N_2O$
Molecular weight, g/mol	253	236
Molar absorption coefficient, L/mol cm	$1.65\text{-}1.71x10^4$	$2.5x10^4$
Molar absorption coefficient, L/mol cm*	$1.82x10^4$	$2.08x10^4$
λ_{max}, nm	265	285
K_{ow}	0.89	2.47
pK_a	pK_{a1}: 1.6, pK_{a2}: 5.7	13.9
Water solubility, mg/L	610	17.7

*determined molar absorption coefficient with the principle of Beer-Lambert Law from equations 4.2 and 4.5.

SMX molecule has a total number of 29 bonds of which 18 of them are non-H bonds and 13 of them are multiple bonds. In addition, SMX has one five membered and one six membered rings. Moreover, it has various functional groups, such as amine, sulfonamide, and isoxazole which play crucial role on the degradation mechanism of SMX via either chemical or photochemical processes.

The CMZ molecule holds a total number of 32 bonds. 20 of them are non-H bonds, 14 of them are multiple bonds, 2 double bond(s). In addition, presence of 12 aromatic bonds, 2 six-membered

rings, 1 seven-membered ring, 2 eleven-membered rings indicate the complexity and aromaticity of the compound (Mol-Instincts, A Fundamental Chemical Database based on Quantum Mechanics & QSPR, https://search.molinstincts.com/guide/guide.ce). In addition, tricyclic nucleus composed of two benzene rings coupled with a nitrogen atom and a side chain ($CONH_2$) linked by the nitrogen atom of the central nucleus also express complexity of CMZ in comparison to SMX.

pH dependent ionic state of SMX and CMZ display importance on the understanding of physicochemical interactions under the reaction conditions. SMX has two pK_a values as pK_{a1}: 1.6 and pK_{a2}: 5.7. When pH value of the reaction medium is less than pK_a value of SMX, it would be stable in its protonated form, particularly at free $–NH_2$ group. At higher pH values, -NH- group displays acidic properties and able to donate the proton (Farías et al., 2003). On the other hand, pK_a of CMZ is 13.9 indicating that CMZ is mostly found in protonated form under almost all pH dependent conditions.

Concentration dependent UV-vis absorption spectra of SMX and CMZ were displayed in Figure 4.1A and B by which the characteristic sharp peaks at λ: 265 nm for SMX and at λ: 285 nm for CMZ were noticeably observed. The absorption of a monochromatic beam of light by homogeneous absorbing system is described by the well-known Beer-Lambert Law. The commonly applied version of the law for photochemical studies is as follows:

$$I/I_o = 10^{-\varepsilon cl} \tag{4.1}$$

Where I_o represents the light energy (or number of quanta) of strictly monochromatic light incident per unit of time at the front of a column of a single absorbing species of concentration c, mol/L; I is the energy per unit time transmitted through the column of the solution, l path length in cm units; and ε is molar extinction L/mol cm, defined as constant for a given pure absorbing species at given wavelength and is a measure of the probability that the quantum molecule interaction will lead to absorption of the quantum (Calvert and Pitts, 1966).

Based on λ_{max} of each EC as SMX (265 nm) and CMZ (285 nm) derived from the UV-vis absorption spectra presented in Figure 4.1A and B, absorbance values recorded at their respective wavelength values were plotted against corresponding concentration values of SMX and CMZ expressed as either mg/L or mM and the results were presented in Figure 4.2A and B. The plots attained expressed linear relationships (R^2=0.999) revealing equations (Equations 4.2 and 4.3) that were used for the determination of the concentration of each EC. Furthermore, these equations were

used for the elucidation of SMX and CMZ prior to and following UVC and solar photodegradation as well as solar photocatalytic degradation processes.

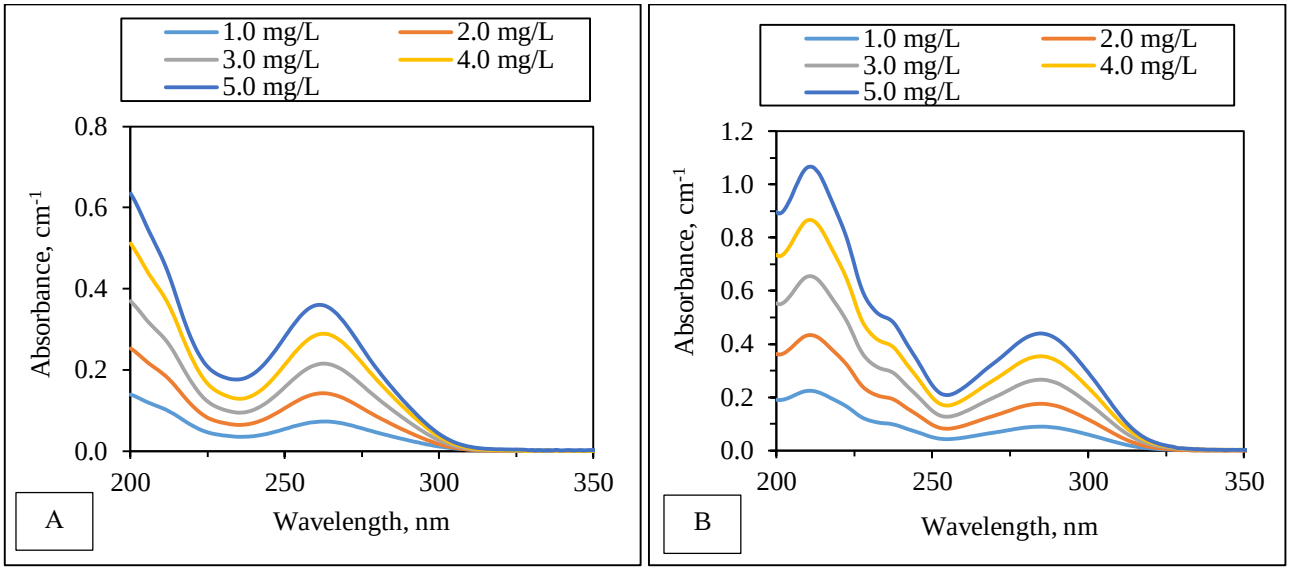

Figure 4.1. Concentration dependent UV-vis absorption spectra of SMX (A) and CMZ (B).

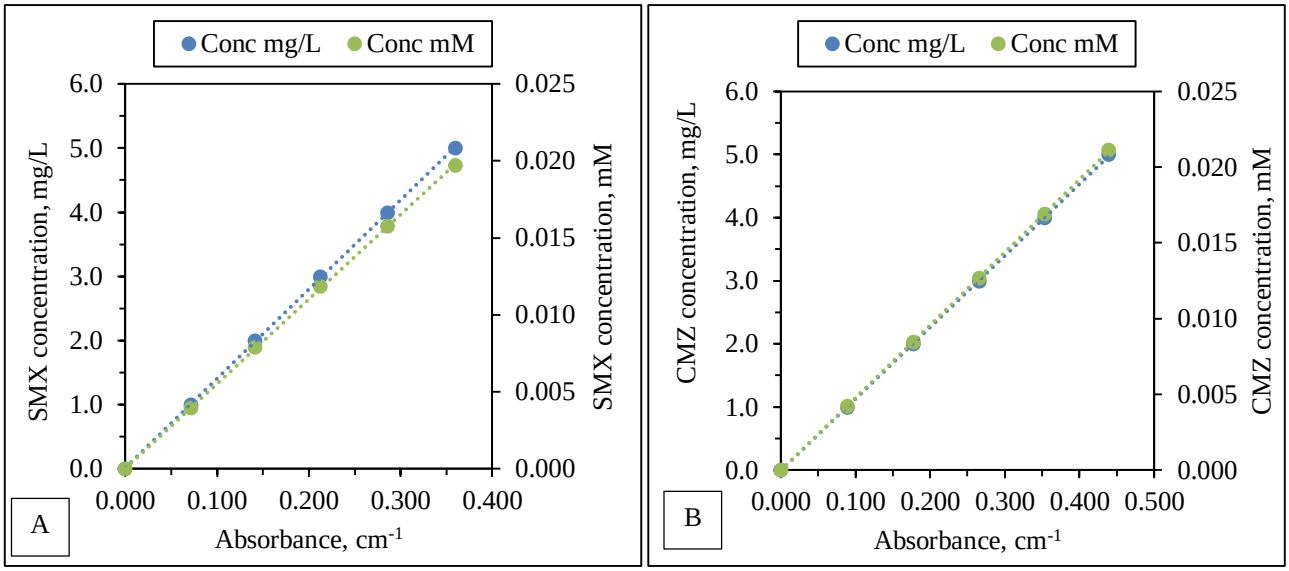

Figure 4.2. Absorbance vs concentration graphs for SMX (A) and CMZ (B).

Absorbance values at λ_{max}: 265 nm were recorded and plotted against corresponding SMX concentrations (0-5 mg/L and 0-0.020 mM) as presented in Figure 4.2A. Relationship between absorbance and concentration values of SMX revealed the linear formula as follows:

$$SMX_{conc}\ (mM) = 5.5x10^{-2}\ (Abs) + 4.97x10^{-5} \qquad R^2 = 0.999 \qquad (4.2)$$

$$SMX_{conc}\ (mg/L) = 13.9\ (Abs) + 1.32x10^{-3} \qquad R^2 = 0.999 \qquad (4.3)$$

In addition, slope of the linear formula was used for the determination molar extinction coefficient of SMX as ε: 1.82 L/mol cm according to Beer-Lambert Law. Determined molar absorption coefficient of SMX was found to be correlated well within the results attained through the literature in the range of ε: 1.64-1.71 L/mol cm (Canonica et al., 2008; Baeze and Knappe, 2011; Carlson et al., 2015). In addition to absorbance vs concentration graph, SMX concentration versus NPOC contents was also plotted in order to determine the relationship between NPOC contents and concentration of SMX revealed the following equation:

$$SMX_{conc}\ (mg/L) = 2.1\ (NPOC, mgOrgC/L) - 9.11x10^{-2} \qquad R^2 = 0.998 \qquad (4.4)$$

This linear equation will be used for the determination of concentration dependent approximate NPOC values of samples under photodegradation and photocatalytic degradation processes. Further evaluation of the NPOC results were proceeded by comparison of theoretical carbon content, which was calculated from molecular formula of SMX, versus analytically measured carbon content of prepared SMX solutions with respect to increasing concentration values. Consequently, theoretical and measured carbon content of the samples displayed proximate results with the recovery percentage in the range of 95-98%.

Absorbance values at λ_{max}: 285 nm were recorded and plotted against corresponding CMZ concentrations (0-5 mg/L and 0-0.021 mM) as presented in Figure 4.2B. Relationship between absorbance and concentration values of CMZ revealed the linear formula as follows:

$$CMZ_{conc}\ (mM) = 4.81x10^{-2}\ (Abs) - 4.33x10^{-5} \qquad R^2 = 0.999 \qquad (4.5)$$

$$CMZ_{conc}\ (mg/L) = 11.4\ (Abs) - 6.31x10^{-4} \qquad R^2 = 0.999 \qquad (4.6)$$

In addition, the slope of the linear formula was used for the determination molar extinction coefficient of CMZ as ε: 2.08 L/mol cm according to Beer-Lambert Law. Determined molar absorption coefficient of CMZ was found to be correlated well within the results attained through the literature (Doll and Frimmel, 2003; Lam and Mabury, 2005; Pereira et al., 2007). In addition to absorbance vs concentration graph, CMZ concentration versus NPOC contents was also plotted in order to determine relationship between NPOC contents and concentration of CMZ revealed the following equation:

$$CMZ_{conc}\ (mg/L) = 1.27\ (NPOC, mgOrgC/L) + 0.104 \qquad R^2 = 0.999 \qquad (4.5)$$

These linear equations will be used for the determination of concentration dependent approximate NPOC values of samples under photolytic and photocatalytic degradation processes. Precision of the preparation of standard CMZ solutions were checked by comparing theoretical carbon content as well as analytically measured carbon content of samples with respect to corresponding concentration values. Recovery percentage in the range of 94-97% was achieved for organic carbon calculated versus organic carbon measured indicating precision and validation on the preparation of standard solutions.

4.1.2. Characterization of Synthetically Prepared Reverse Osmosis Concentrate Samples

Physicochemical characterization of all ROC samples were presented in Table 4.2. Initial individual NPOC contents of SMX and CMZ were 2.6 mg/L and 3.9 mg/L respectively. Contribution of each ECs on carbon content of ROC_{ECm} samples could be verified by NPOC (mgOrgC/L) measurements expressing ROC_{m1}= 14.3 mg/L, ROC_{m2}= 23.2 mg/L, ROC_{ECm1}= 19.2 mg/L and ROC_{ECm2}= 28.5 mg/L. Moreover, NPOC contents of all ROC samples revealed proximate results as have been presented in the literature in Table 2.1. $SUVA_{254}$ and $SUVA_{280}$ values indicated high aromaticity in all ROC samples indicating the presence of large molecular weight components.

Concentrations of alkalinity, Ca^{2+}, Mg^{2+}, NO_3^-, and PO_4^{3-} in synthetic ROC samples were found to be the within the ranges given in real ROC samples, whereas TDS, Na^+, K^+, Cl^-, and SO_4^{2-} contents were found to be considerably lower in synthetic ROC samples. The reason could be attributed to different origins of municipal wastewater sources of real ROC samples. Since real ROC samples contains effluents of municipal wastewater discharges, it is expected to have higher concentration of solids. In addition, post chlorination step in municipal wastewater treatment processes is expected to contribute to the chlorine content of ROC samples. Higher concentrations of Na^+, K^+, and SO_4^{2-} in real municipal ROC samples could be attributed to the chemicals used in wastewater treatment processes.

It could be inferred from Table 4.2 that most of the physical and chemical parameters of synthetically prepared ROC samples displayed close results within the concentration values of real ROC samples although expressing distinct differences in OM composition as presented in Table 2.1 (NPOC values in the ranges of 17-57.1 mgOrgC/L and TOC values in the ranges of 17-31.1 mgOrgC/L). Moreover, measurement of common anions by IC was validated in the presence of HM by expressing proximate results even in the presence of different humic components.

Table 4.2. Physicochemical and spectroscopic characterization of ROC samples.

Parameters	ROC samples			
	ROC_{m1}	ROC_{m2}	ROC_{ECm1}	ROC_{Ecm2}
Organic Carbon Content, mgOrgC/L				
NPOC	14.3	23.2	19.2	28.5
Specified UV-vis parameters, cm^{-1}				
$Color_{436}$	0.311	0.442	0.252	0.385
UV_{365}	0.595	0.899	0.505	0.809
UV_{280}	1.24	2.01	1.47	2.17
UV_{254}	1.44	2.34	1.75	2.57
Specific UV-vis parameters, L/mg m				
$SCoA_{436}$	2.18	1.92	1.31	1.35
$SUVA_{365}$	4.16	3.87	2.63	2.84
$SUVA_{280}$	8.71	8.66	7.68	7.61
$SUVA_{254}$	10.1	10.1	9.13	9.01
Common anions, mg/L				
Cl^-	45.6±0.79			
NO_3^-	5.38±0.37			
SO_4^{2-}	57.9±0.33			
PO_4^{3-}	2.56±0.061			
Common cations, mg/L				
Na^+	11.7±0.37			
K^+	4.18±0.27			
Ca^{2+}	68.2±1.1			
Mg^{2+}	9.69±0.11			
Other parameters				
TDS, mg/L	102	162	235	280
Alkalinity, $mgCaCO_3/L$	355	347	361	368

Spectroscopic evaluation of ROC samples was done by considering UV-vis absorption scan spectra (Figure 4.3A) as well as fluorescence spectra (Figure 4.3B) recorded in synchronous scan and EEM scan modes as presented in Figure 4.5 designated as contour-plots.

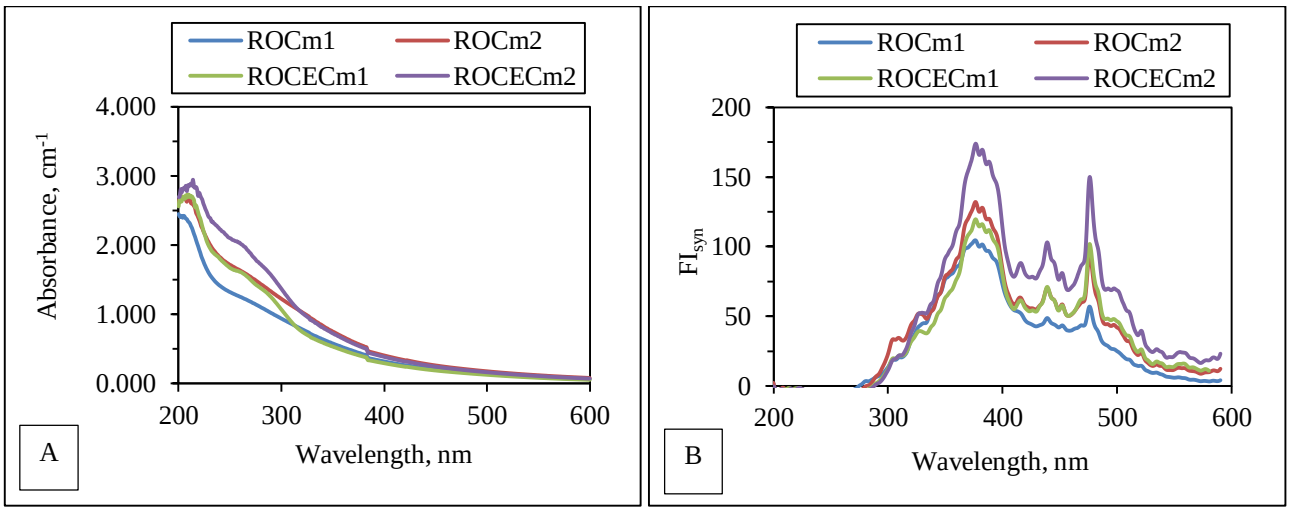

Figure 4.3. UV-vis absorption spectra (A) and synchronous scan fluorescence spectra (B) of ROC_m and ROC_{ECm} samples.

UV-vis absorption spectra of ROC samples displayed humic matter type featureless and monotonous decreasing trend with respect to increasing wavelength in the region of 200-600 nm. On the other hand, in accordance with the NPOC results indicating contribution of ECs in ROC_{ECm} samples, UV-vis absorption spectra of ROC_{ECm1} and ROC_{ECm2} were evidently showed the presence of ECs by giving shoulders in between wavelength regions of 250 nm and 300 nm which were not detected in ROC_{m1} and ROC_{m2} samples. These shoulders could be related to UV-vis absorption spectrum of SMX (λ_{range}: 190-310 nm, λ_{max}: 265 nm) and CMZ (λ_{range}: 190-340 nm, λ_{max}: 285 nm). Depending on the spectral regions given by synchronous scan fluorescence spectroscopy, regional expression of different components could be classified as follows: λ_{range}: 260-302 nm could be regarded as aromatic amino acids and some other volatile acids containing highly conjugated aliphatic structures being too hydrophobic for back elution from the sorbents with base, λ_{range}: 302-340 nm corresponding to naphthalene and its derivatives, λ_{range}: 340-370 nm related to are polycyclic aromatics with three to four fused benzene rings, λ_{range}: 370-420 nm referring to polycyclic aromatics with approximately five fused benzene rings, λ_{range}: 420-487 nm influence of polycyclic aromatics consisting of about seven fused benzene rings also the most common lignin descriptors give fluorescence within this region (Peuravuori et al., 2002). Synchronous scan spectra of all ROC samples displayed two characteristic sharp peak at 380 nm and 477 nm which could be related to the humic-like components (Uyguner and Bekbolet, 2005a and b) and a moderate peak at 440 nm. Moreover, in the presence of ECs fluorescence intensities of ROC_{ECm1} and ROC_{ECm2} were found to be higher than ROC_{m1} and ROC_{m2} which could be attributed to the presence of six membered rings of SMX and CMZ that could contribute to the fluorescence intensity at around λ_{range}: 370-420 nm and seven membered ring of CMZ to the fluorescence intensity at wavelength region of λ: 420-487nm.

Organic matter exhibits fluorescence in excitation wavelength range of λ_{exc}~200-500 and emission wavelength range of λ_{emis} ~ 280-600 nm. Fluorophoric centers could be described as humic-like fluorescence (λ_{exc}: 220-470 nm, and λ_{emis}: 380-580 nm), fulvic-like (λ_{exc}: 220-250 nm, and λ_{emis}: 380-580 nm), aromatic proteins I (λ_{exc}: 220-250 nm and λ_{emis}: 280-332 nm), aromatic proteins II (λ_{exc}: 220-250 nm and λ_{emis}: 332-380 nm), and microbial by-products (λ_{exc}: 250-470 nm and λ_{emis}: 280-380 nm (Coble, 1996; Sen-Kavurmaci and Bekbolet, 2014) (Figure 4.4).

Figure 4.5 revealed that both humic-like and fulvic-like fluorophoric regions could be visualized for all ROC samples. Lower intensities of the samples could be attributed to the presence of medium and high molecular size fractions of humic-like matter that has the tendency to mask all other fluorophores with lower molecular size fractions as a result of internal quenching effect of humic macromolecules.

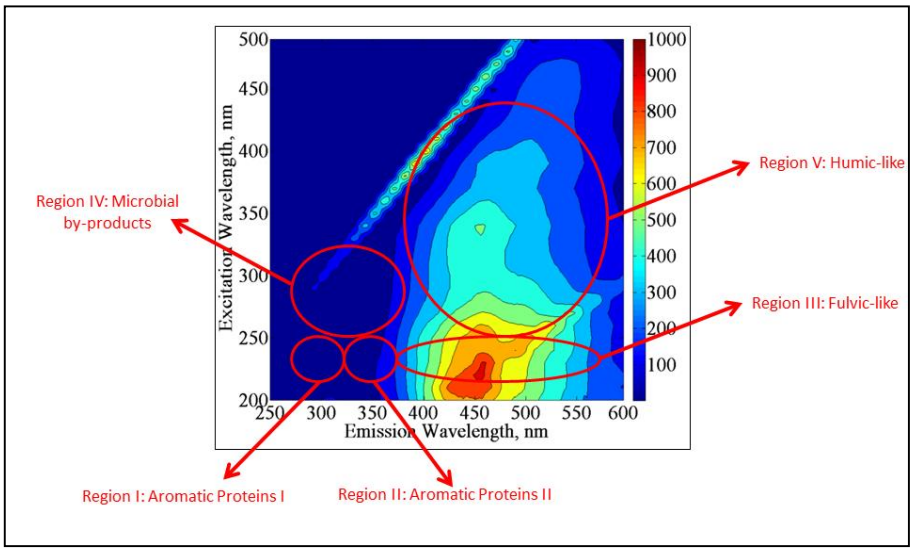

Figure 4.4. Regional representation of fluorophores by EEM fluorescence spectra.

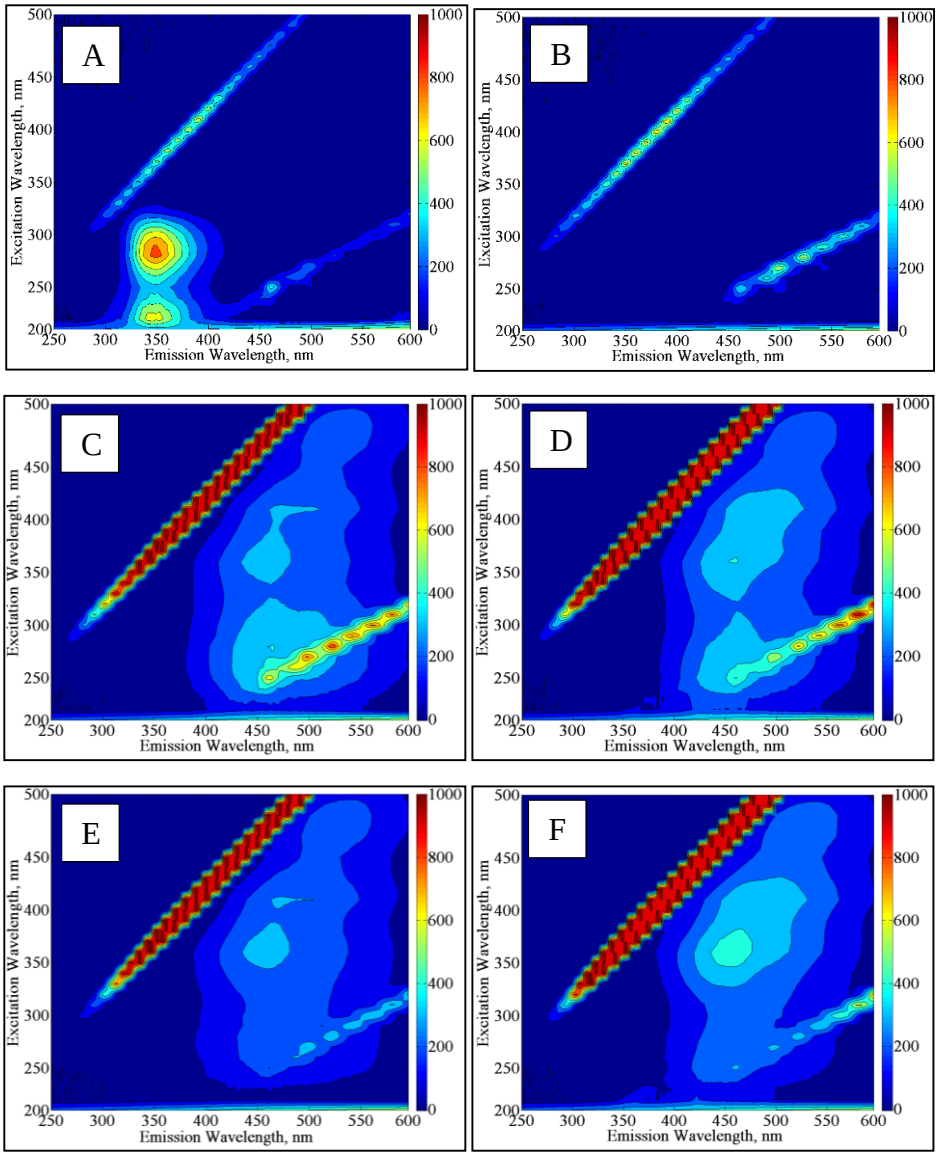

Figure 4.5. EEM fluorescence contour-plots of ECs and ROC samples (A: SMX, B: CMZ, C: ROC_{m1}, D: ROC_{m2}, E: ROC_{ECm1}, F: ROC_{ECm2}).

Although these fluorophores could be attributed to the origin of dissolved organic matter, disappearance and/or formation of new fluorophores indicates the significance of EEM fluorescence spectral features under oxidative and non-oxidative conditions. Regional representation of these fluorophores were presented previously in Figure 4.4. Based on this regional distribution of the EEM fluorescence contour-plots related to the OM remaining ROC composition was characterized prior to and following each processes. EEM fluorescence contour-plots of ECs and ROC samples prior to all applied processes were presented in Figure 4.5.

Under natural conditions, CMZ is not fluorescent in solution but can only be transformed into a fluorescent compound via a photochemical reaction under strong acidic conditions (Brittain, 2016). On the other hand, it could also be attained from Figure 4.5 that SMX exhibits fluorescence maxima in the Ex/Em wavelength region of 210/350 nm and 290/350 nm which correspond to the regions of Aromatic Proteins I and II (Sen-Kavurmaci and Bekbolet, 2014). Previous literature studies revealed that protein-like fluorophoric region could be regarded as representative of various ECs and therefore could be followed by EEM fluorescence contour-plots in water and wastewater composition (Ben Abdelmelek et al., 2013; Sgroi et al., 2017). Although these fluorophoric regions are expected to be observed in the presence of ROC_{ECm1} and ROC_{ECm2} due to presence of SMX for its fluorescent properties, they were shielded by humic-like fluorophores. The reason could be attributed to the masking effect of humic-like and fulvic-like fluorophores on components giving fluorescence in Protein I and II regions (Wang et al., 2015).

4.2. Characterization of the Photocatalysts

4.2.1. XRD Diffactogram

X-ray diffractograms of the catalysts were examined in the range 20-70° (2θ) following MDI-JADE6 library. Figure 4.6 displayed the XRD patterns of TiO_2, N-TiO_2, ZnO and TiO_2/ZnO nanocomposite. The XRD diffractogram of TiO_2 revealed the presence of both anatase and rutile phases without any impurity diffraction peaks. 0.5% N-TiO_2 diffractogram consisted of typical peaks of anatase and rutile. No existence of any new nitrogen dopant-related peaks were detected indicating no reactions between N anions and TiO_2 to form new crystalline phase peaks (Gurkan et al., 2012). The crystallite sizes were calculated from diffraction plane (1 0 1) of anatase and diffraction plane (1 0 1) of anatase zincite. The anatase crystallite size was found to be as 20.74 nm for zincite crystallite and 38.74 nm for TiO_2/ZnO nanocomposite. The average crystallite sizes of TiO_2, 0.5% N-TiO_2, and

ZnO were determined as 22.3, 18.8 and 58 nm respectively (Karunakaran et al., 2011; Birben et al., 2016). Besides, ZnO diffractogram indicated the presence of zincite phases only. Both anatase and rutile peaks of TiO_2 and zincite peaks of ZnO were observed via diffractogram of TiO_2/ZnO. This finding implied that TiO_2/ZnO consisting of only TiO_2 and ZnO. The diffractogram of TiO_2/ZnO revealed that the most intense peak at $2\theta=25.38^o$ is the characteristic (1 0 1) anatase peak of TiO_2 and $2\theta=36.34^o$ is the characteristic (1 0 1) zincite peak of ZnO. Other TiO_2 anatase diffractions of (0 0 4), (1 1 2), (2 0 0), (1 0 5) and (2 1 1) appeared at 37.90^o, 38.68^o, 48.06^o, 54.02^o and 55.16^o (2θ), respectively. Moreover, the peaks located at 27.50^o and 36.15^o (2θ) responded to (1 1 0) and (1 0 1) as the planes of rutile phase respectively.

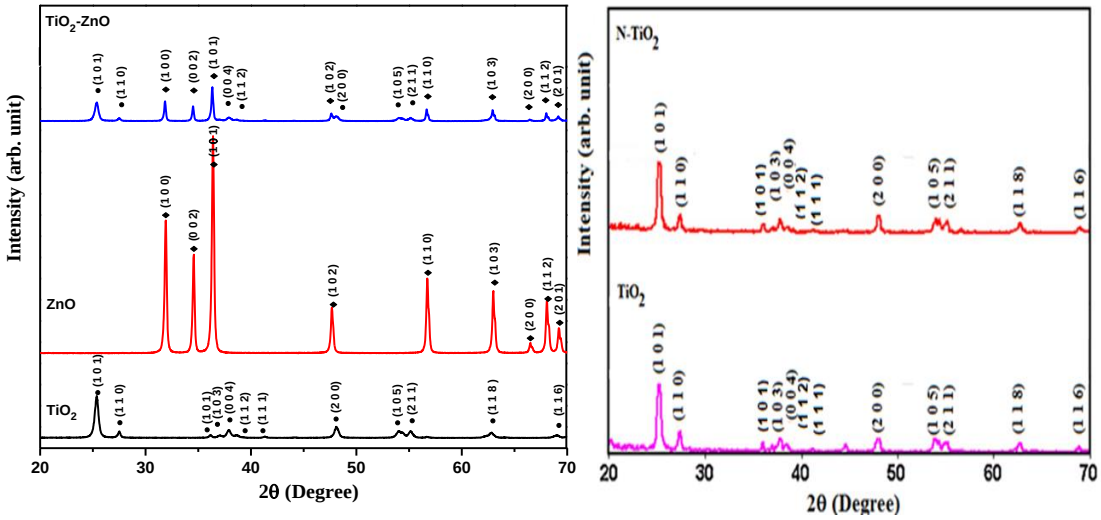

Figure 4.6. XRD diffractograms of TiO_2, N-TiO_2, ZnO, and TiO_2/ZnO nanocomposite.

Upon presence of zincite peak of ZnO, 2θ angles of 31.86^o, 34.50^o, 47.64^o, 56.68^o, 62.92^o, 66.44^o, 68.02^o and 69.16^o corresponded to the crystalline planes of (1 0 0), (0 0 2), (1 0 2), (1 1 0), (1 0 3), (2 0 0), (1 1 2) and (2 0 1) of ZnO. In the diffractogram of TiO_2/ZnO, the peaks at $2\theta=36.15^o$, 37.01^o, 41.35^o, 62.78^o and 69.12^o and corresponded to (1 0 1), (1 0 3), (1 1 1), (1 1 8) and (1 1 6) TiO_2 peaks were disappeared. Furthermore, TiO_2/ZnO nanocomposite exhibited lower intense peaks than TiO_2 and ZnO.

4.2.2. SEM

Surface morphologies of all photocatalysts specimens were evaluated by SEM micrographs as presented in Figure 4.7. TiO_2 was consisted of small, spherical particles whereas the micrograph of ZnO indicated mostly quasi-spherical particles and the average particle sizes were in nanometer scale.

Particle size of ZnO was found to be greater than the particle size of TiO_2, whereas TiO_2/ZnO expressed higher particle size than TiO_2 and ZnO. The reason could be attributed to the sonication step involving in the synthesis process of TiO_2/ZnO enabling particle size reduction and the efficient dispersion of the particles (Parsons, 2006). The texture characteristics of both TiO_2 and ZnO was clearly observed in SEM micrograph of TiO_2/ZnO displaying the combination of regular and very well defined spherical particles of TiO_2 and quasi-spherical particles of ZnO. On the other hand, SEM micrograph of N-TiO_2 displayed slightly agglomerated particles with larger particle size than TiO_2.

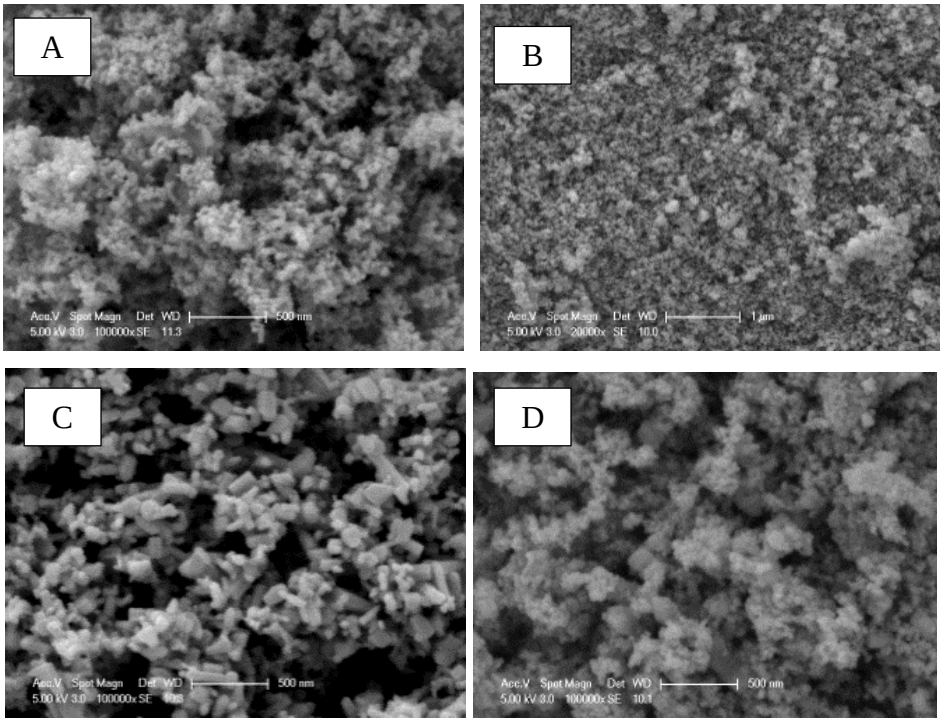

Figure 4.7. SEM micrographs of A: TiO_2 (Birben et al., 2015), B: N-TiO_2 (Birben et al., 2015), C: ZnO (Birben et al., 2017), and D: TiO_2/ZnO (Birben and Bekbolet, 2019).

With respect to the results attained from analytical characterization of all photocatalyst specimens, an overall representation of the physicochemical and photochemical characteristics of TiO_2, N-TiO_2, ZnO, and TiO_2/ZnO were presented in Table 4.3.

Table 4.3. Physicochemical and photochemical characterization of the photocatalysts.

Photocatalyst specimen	Band gap eV	Wavelength nm	Crystallite size nm	BET m^2/g	pH_{ZPC}
TiO_2	3.21	388	22.3	57	6.25
N-TiO_2	2.79	479	18.8	55	6.23
ZnO	3.31	375	33.1	31	8.96
TiO_2/ZnO	2.97	418	38.7	37	7.69

Doping TiO_2 with nitrogen caused a red shift on the band gap value of N-TiO_2 whose photoactivity was shifted to visible light region (λ: 479 nm). Although its' both precursors (TiO_2 and ZnO) are photocatalytically active under UVA irradiation, TiO_2/ZnO nanocomposite revealed a narrow band gap value in comparison to TiO_2 and ZnO, therefore its photoactivity was shifted to visible light irradiation region. The reason could be attributed to distinct redox energy levels of valence and conduction band values of ZnO and TiO_2 enabling inhibition of recombination of electron-hole pairs by interfacial charge transfer (Lan et al., 2019).

Primary crystallite sizes of the photocatalyst specimens were calculated by using Scherer equation (Equation 3.1., in Section 3.2.1.2) and could be expressed by the following order; N-TiO_2<TiO_2<ZnO<TiO_2/ZnO. Nitrogen doping (18.8 nm) reduced the crystallite size of TiO_2 (22.3 nm) whereas TiO_2/ZnO exhibited comparatively higher crystallite size value (38.7 nm) in comparison to sole TiO_2 and ZnO (33.1 nm).

Due its surface oriented mechanism, the adsorptive interactions between the substrate and photocatalsyts play a crucial role to get further understanding on the photocatalytic degradation mechanism. Therefore, surface area of the photocatalysts specimens were determined in order to assess interactions between the substrate and the photocatalsyst. Surface are of the commercial photocatalyst TiO_2 was found to be 57 m^2/g indicating accordance with the widely reported data (55±15 m^2/g) whereas ZnO revealed surface area value of 31 m^2/g. Moreover, nitrogen doping did not cause any alteration on surface area of N-TiO_2 which revealed almost the same surface area with TiO_2 as its precursor. On the other hand, surface area of TiO_2/ZnO nanocomposite was found to be lower than TiO_2 and higher than ZnO. Consequently, surface area values of the photocatalyst specimens were found to be in reducing order of TiO_2>N-TiO_2>TiO_2/ZnO>ZnO.

Since surface interactions play a crucial role on the mechanism of photocatalytic degradation process, ionic state of the photocatalysts should also be evaluated in terms of their zero point of charge (pH_{ZPC}). Zero point of charge determination is based on the pH dependent measurement of zeta potential of photocatalyst specimens. pH value at which zeta potential equals to zero is regarded as pH_{ZPC}. It could be inferred from Table 4.3 that no significant difference was attained between pH_{ZPC} values of TiO_2 and N-TiO_2 specimens indicating nitrogen doping or procedure applied for nitrogen doping did not cause any substantial change. On the other hand, TiO_2/ZnO displayed distinctly different pH_{ZPC} value in comparison to its precursors as TiO_2 and ZnO.

4.3. UVC Irradiation Initiated Processes

This section focused on the application of UVC irradiation initiated processes for ROC_m and ROC_{ECm} treatment. Reactor configuration and its properties for the application of UVC irradiation initiated processes were presented in section 3.2.1.1. Incident photon flux of the UVC irradiation source was found to be $1.80x10^{17}$ quanta/sec (Appendix A). A systematic and stepwise approach was followed in order to assess influence of UVC irradiation either alone or UVC irradiation in the presence of oxidizing agents, *i.e.* H_2O_2 and Fe on the degradation of organics present in ROC samples. First, ECs and ROC samples were exposed to UVC photodegradation process to evaluate only light initiated reactions, then UVC/H_2O_2 system was used for the treatment of ROC samples in order to examine the influence of ROS. Finally, photo-Fenton process was applied to understand beneficial or detrimental effect of Fe in the presence of H_2O_2 and UVC irradiation. Moreover, in order to reveal background information for photo-Fenton reactions, Fenton process was also assessed to understand reactions between H_2O_2 and Fe in the absence of irradiation. Process efficiency of each system was followed by observing changes in specified and specific UV-vis and fluorescence spectroscopic parameters as well as organic carbon contents.

4.3.1. UVC Photodegradation Processes

4.3.1.1. UVC photodegradation of ECs. Time dependent UV-vis scan spectra of UVC photodegradation of SMX and CMZ were presented in Figure 4.8. Significant differences were attained between UVC photodegradation profiles of SMX and CMZ virtually depending on their chemical properties. Characteristic sharp peak of SMX at λ_{max}: 265 nm was totally disappeared following irradiation period of 40 min. On the other hand, following UVC photodegradation, the characteristic sharp peak of CMZ at λ_{max}: 285 nm was still evident. With respect to the changes in maximum absorbance values of SMX at λ: 265 nm and CMZ at λ: 285 nm, equivalent concentration values were calculated by using the equations 4.3 and 4.6 respectively.

Photochemical reactions of SMX and CMZ under UVC irradiation was evaluated in terms of removal rates as well as quantum yields. The efficiency and the nature of a photochemical reaction could be understood by the assessment of the term quantum yield as following equation:

$$\Phi_\lambda = \frac{dn(M)/dt}{\Phi_P^{abs}} \quad (4.6)$$

Where, Φ_λ refers to quantum yield, dn(M)/dt corresponds to number of n of reactant molecules M consumed per unit time, and Φ_P^{abs} represent number of photons absorbed during this period (Oppenländer, 2002). Consequently, quantum yield values for UVC photodegradation of SMX and CMZ were determined by above given equation using their UVC photodegradation rates (R, L/mg min) and incident photon flux of the UVC irradiation initiated reactor (I_o, quanta/sec).

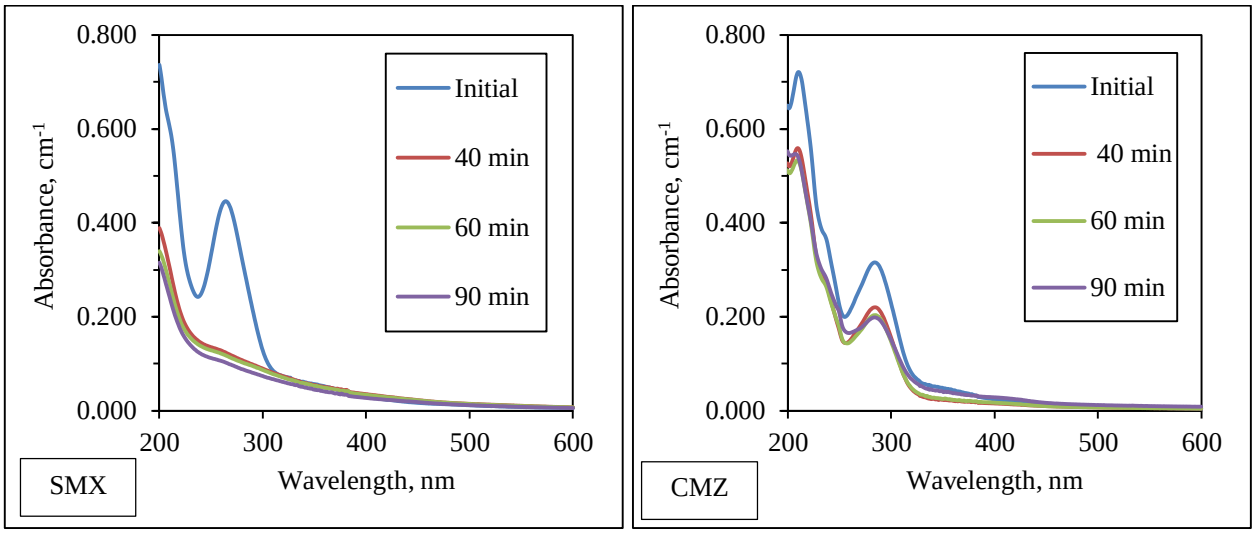

Figure 4.8. Time dependent UV-vis absorption spectra of SMX and CMZ upon UVC photodegradation (I_o: $1.80x10^{17}$ quanta/s).

With respect to the results attained from UV-vis absorption spectra of UVC photodegradation of SMX, rapid removal could be observed even after irradiation period of 40 min by which characteristic sharp peak of SMX at λ: 265 nm was almost disappeared. Following irradiation period of 90 min, up to 80% SMX removal was achieved via UVC photodegradation as observed in previous literature studies (Kim et al., 2015). Reduction in SMX concentration under UVC irradiation followed an exponential decay with respect to increasing irradiation period and therefore fit into Pseudo first-order kinetic model expressing kinetic constant (k, min^{-1}) as $1.61x10^{-2}$ min^{-1}, half-life value of 43 min and removal rate as $10.1x10^{-2}$ mg/L min. In addition, primary quantum yield of UVC photodegradation of SMX was found to be 0.022 displaying good agreement with the results attained through the literature revealing quantum yield values in the range of 0.023-0.033 (Canonica et al., 2008; Baeza and Knappe, 2011; Carlson et al., 2015).

As a result of UVC photodegradation process, fast removal of SMX could be achieved within a very short period of time as has been reported by various researchers (Kim and Tanaka, 2009; Nasuhoglu et al., 2011; Lekkerkerker-Teunissen et al., 2012; Martinez-Costa et al., 2018). Rapid degradation of SMX under UVC irradiation could be attributed to several reasons in terms of its

chemical and photochemical properties. When exposed to UVC irradiation, compounds with sulfonyl (R-SO_2-R) groups tend to separate from the compound as a results of breakage of bond between -SO_2- and its side atoms. Moreover, UVC induced cleavage of C-S bond and N-O bond of the five-membered ring ended up with the removal of these compounds (Sugimori, 1998). Another important parameter on efficient SMX removal is its higher quantum yield (Zhou and Moore, 1994; Andreozzi et al., 2003; Carlson et al., 2015; Yang et al., 2017; Luo et al., 2018). pH of the reaction medium is also another crucial parameter influencing SMX degradation which is strongly dependent on the state of ionization (pK_a: 5.6) (Zhou and Moore, 1994). With respect to the pH value of most of the aquatic environments varying in between 6-8, SMX is expected to be more stable due to its deprotonated form therefore it would be degraded easily under natural pH conditions (Luo et al., 2018).

UVC photodegradation of SMX in aqueous media may undergo various reaction pathways including producing intermediates and eventually ending up with the generation of final products. Upon exposure to UVC irradiation, one of the most predominant reactions will be rupture of N-O bond causing rearrangement of isoxazole ring forming a five membered oxazole ring namely 4-amino-N-(5-methyl-2oxazolyl) benzenesulfonamide that is known to be one of the most common transformation by-products of SMX (Zhou and Moore, 1994; Alharbi et al., 2017). The reactive diradical which is formed via UVC induced cleavage of N-O bond of SMX then may undergo recyclization to produce intermediates, such as 2H-azirine, whose hydration generates other intermediates. 3-amino-5-methyl-isoxaole could be formed via free radical reaction initiated by δ-fission (Zhou and Moore, 1994). According to previous literature studies, the most common photodegradation by-products of SMX are found to be sulfanilic acid, 3-amino-5-methylisoxazole, aniline, (Zhou and Moore, 1994; Kim and Tanaka, 2009; Nasuhoglu et al., 2011; Alharbi et al., 2017; Yang et al., 2017; Martinez-Costa et al., 2018). In addition to these transformation by-products various transformation intermediates of SMX that have not been matched with any identified compound was also presented throughout the literature by explaining their possible formation mechanisms (Zhou and Moore, 1994; Nasuhoglu et al., 2011; Niu et al., 2013; Alharbi et al., 2017; Yang et al., 2017; Martinez-Costa et al., 2018). It could be concluded that major by-product formation pathway for SMX degradation is based on the breaking of sulfonamide bond, and/or attack of hydroxyl radicals either generated via photodegradation of SMX or added to the reaction medium (Martinez-Costa et al., 2018).

Formation and accumulation of these intermediates in the reaction medium could be followed by monitoring changes in carbon content of the solution. Following UVC irradiation of 90 min, more than 80% SMX removal was achieved whereas under the same conditions, organic carbon removal

was around 65%. Additionally, irradiation time dependent changes of organic carbon content were measured while corresponding theoretical carbon content of remaining SMX concentration was determined. It was concluded that measured carbon content of the samples (0.83 mg/L for t_{irr}: 90 min) were found to be slightly higher than the expected carbon content (0.68 mg/L for t_{irr}: 90 min) which could be attributed to the formation of photodegradation by-products of SMX. Moreover, slight increase in carbon content indicates that photodegradation intermediates of SMX may show resistance to photodegradation and tend to remain in the reaction medium as final products, therefore retard organic carbon reduction (Nasuhoglu et al., 2011). It's been previously reported that following prolonged UVC irradiation period, *i.e.* 6 hours, complete removal of SMX was achieved, however, its common by-products, such as sulfanilic acid and 3-amino-5-methylisoxazole were still present in the reaction medium (Nasuhoglu et al., 2011). Being regarded as the most common phototransformation by-products of SMX, sulfanilic acid absorbs irradiation from 249 nm to 256 nm with λ_{max}: 253 nm, 3-amino-5-methylisoxazole absorbs irradiation in the wavelength region between 224 nm and 232 nm with λ_{max}: 228 nm and aniline absorbs from 210 nm to 250 nm with λ_{max}: 225 nm. Therefore, with respect to the absorbance spectra of these by-products, sulfanilic acid is found to be prone to UVC photodegradation, whereas 3-amino-5-methylisoxazole and aniline tend to show resistance to UVC photodegradation. As a result of SMX removal organic carbon content of reaction medium is expected to decrease. However, production and accumulation of transformation by-products in the reaction medium would contribute to carbon content with respect to their resistance to photodegradation. Previous literature findings also indicated that even after prolonged irradiation periods of UVC photodegradation process, *i.e.* 6 hours, complete removal of SMX was achieved, whereas only 24% COD removal was attained which could be attributed to resistance of photoproducts of SMX, which are sulfanilic acid and 3-amino-5-methylisoxazole, to UVC photodegradation (Nasuhoglu et al., 2011).

UV-vis absorption spectrum of CMZ (Figure 4.1) indicated that it absorbs irradiation in wavelength region of 190-340 nm with λ_{max}: 285 nm. Exposing to either UVC (λ_{max}: 254 nm) or solar irradiation (λ: 290-700 nm), CMZ could undergo photodegradation that would have ended up with the production of reaction intermediates. Following UVC irradiation period of 90 min only 37% CMZ removal was attained. In accordance with the attained removal efficiency of CMZ, UV-vis absorption spectra revealed that characteristic sharp peak (λ_{max}: 285 nm) of CMZ is still evident indicating that UVC photodegradation of CMZ was found to be quite insignificant under natural conditions. As a result of exposure to UVC irradiation, CMZ removal efficiency was found to be in the range of 10-20% throughout the literature (Vogna et al., 2004; Kim et al., 2009; Rosario-Ortiz et al., 2010). Reduction in CMZ concentration under UVC irradiation followed an exponential decay with respect

to increasing irradiation period and therefore fit into Pseudo first-order kinetic model expressing kinetic constant (k, min^{-1}) as $5.02x10^{-3}$ min^{-1}, half-life ($t_{1/2}$, min) value of 139 min and removal rate as $1.92x10^{-2}$ mg/L min. In addition, primary quantum yield of UVC photodegradation of CMZ was found to be 0.0004 displaying good agreement with the results attained through the literature revealing quantum yield values in the range of 0.0002-0.0006 (Chiron et al., 2006; Pereira et al., 2007).

Resistance of CMZ to UVC photodegradation could be attributed to its chemical structure that contains amide bonds ($RCONR_2$) known to be less susceptible to UVC photodegradation. Therefore, efficient removal of CMZ under UVC irradiation would require prolonged irradiation periods or ROS attack (Kim, 2009). Since low quantum yield values ($\Phi << 1$) indicate almost no net chemical transformation as a result of deactivation, fluorescence, or other processes (Calvert and Pitts, 1966), susceptibility of CMZ to UVC photodegradation could be attributed to its low quantum yield that limits photo-initiated reactions (Chiron et al., 2006; Pereira et al., 2007). Moreover, another reason of resistance to UVC photodegradation could be related to its heterocyclic structure with two six membered rings, one seven membered ring and one eleven membered ring which require high energy for breakdown of chemical bonds.

With respect to exposure to UVC irradiation, CMZ undergoes various direct or indirect reactions and subsequently generates transformation by-products. Hydroxylation of CMZ at the 10 position would give a radical intermediate that evolves to give 10,11-epoxycarbamazepine. As a result of epoxide ring opening, generated labile species, such as 1-(2-benzaldeyhe)-(1H,3H)-quinazoline-2,4-dione known as quinazoline derivatives, or would undergo facile ring contraction to give acridine-9-carbaldehyde or acridone-N-carbaldehyde. Further decomposition of acridine-9-carboxaldehyde via cleavage of aldehyde group and $CONH_2$ lateral chain yields acridine known as the most common transformation by-products of CMZ (Vogna et al., 2004; Chiron et al., 2006; Kosjeck et al., 2009; Donner et al., 2013; Alharbi et al., 2017). In addition, being regarded as another common transformation by-product of CMZ, acridone formation is expected either by further hydroxylation step with loss of $CONH_2$ lateral chain or further oxidation of acridine via indirect photolysis (Chiron et al., 2006). Consequently, the major mechanisms of occurrence of phototransformation by-products of CMZ are direct photolysis and/or indirect photolysis that ends up with the formation of free radicals from the parent compound in the absence of any oxidant.

Further evaluation of photodegradation and photomineralization of CMZ was followed by organic carbon content of the samples. For this purpose, organic carbon content of samples was

measured instrumentally following photodegradation process while theoretical carbon content of remaining CMZ concentration in solution were also calculated for the same samples. Upon exposure to UVC photodegradation, reduction of organic carbon content was expected, however if phototransformation products of CMZ are not prone to photodegradation then they tend to remain in the reaction medium and therefore contribute to the carbon content with almost no change. Surprisingly, results revealed that measured carbon content of the samples were found to be lower than the expected carbon content indicating an additional mechanism contributing to mineralization. 10-hydroxycarbamazepine gives maximum absorption at λ: 270 nm, acridine gives primary maxima at λ: 260 nm and one secondary maxima at λ: 350 nm, and acridone gives one primary absorption maxima at λ: 254 nm and one secondary maxima at λ: 380 nm. UV-vis absorption spectra of all CMZ derived phototransformation by-products overlap with the maxima of UVC lamp therefore, upon UVC photodegradation of CMZ, formation as well as photodegradation of acridine, acridone, and 10-hydroxycarbamazepine are expected to occur concurrently which could be the reason of reduction in carbon content of reaction medium.

4.3.1.2. UVC photodegradation of ROC samples. Since both ECs (SMX, λ_{max}: 265 nm and CMZ, λ_{max}: 285 nm) and UV absorbing centers of HM were susceptible to UVC radiation, all ROC samples were exposed to irradiation using UVC lamp (λ_{max}: 254 nm) in order to elucidate the reactions occurring among all components of ROC samples either individually or depending on matrix conditions. Reaction time dependent degradation profiles of ROC_m and ROC_{ECm} via UVC photodegradation were followed by considering changes in specified and specific UV-vis parameters, fluorescence features in synchronous scan mode and EEM mode, and organic carbon contents expressed as NPOC. Time dependent UV-vis absorption scan spectra of ROC_m and ROC_{ECm} samples upon UVC photodegradation were presented in Figure 4.9. As a general trend, UV-vis absorption spectra of humic matter are expected to display a broad, featureless and monotonously decaying profile in the wavelength region of 200-600 nm (Uyguner-Demirel and Bekbolet, 2011). Time dependent UV-vis absorption spectra of ROC_{m1} and ROC_{m2} displayed the expected humic matter-like trend with respect to increasing UVC irradiation periods. On the other hand, ROC_{ECm1} and ROC_{ECm2} revealed shoulders in UV-vis absorption spectra in the wavelength region of 230-300 nm due to the characteristic sharp peaks of SMX (λ: 265 nm) and CMZ (λ: 285 nm). Upon exposure to UVC irradiation, noticeable reduction in these shoulders were attained with respect to increasing irradiation periods indicating photodegradation of SMX and CMZ present in ROC_{ECm1} and ROC_{ECm2}. In order to get a further insight on the reactions occurring in the absence and presence of ECs, specified UV-vis parameters related to λ_{max} of SMX and CMZ were assessed in ROC_m and ROC_{ECm} samples. Upon exposure to UVC photodegradation for 90 min, 32% UV_{265} and UV_{285} removals were

attained for ROC_{m1}, whereas under the same conditions only 8% UV_{265} and 2% UV_{285} removals were achieved for ROC_{ECm1}. Similarly, ROC_{m2} revealed 20% removal of UV_{265} and UV_{285} but in the presence of ROC_{ECm2} 8% UV_{265} and 2% UV_{285} removals were observed. Removal efficiencies attained in the presence of ROC_{m1} and ROC_{m2} are related to aromatic compounds present in humic structure, however, in the presence of ROC_{ECm1} and ROC_{ECm2}, absorbance values in these wavelengths are related to both aromatics of humic matter and ECs. Significant reduction of UV_{265} and UV_{280} removals indicate competition between HM and ECs for harvesting UVC irradiation.

As a result of UVC photodegradation process following t_{irr}: 60 min, ROC_{m1} revealed removal efficiencies of 30% for $Color_{436}$, 29% for UV_{365}, 26% for UV_{280}, 25% for UV_{254}, and 13% NPOC whereas ROC_{ECm1} displayed removal efficiencies as 10% for $Color_{436}$, 4% for UV_{365}, 2% for UV_{280}, 9% for UV_{254}, and 4% for NPOC. Under the same experimental conditions, ROC_{m2} displayed removal percentages as 15% for $Color_{436}$, 14% for UV_{365}, 13% for UV_{280}, 13% for UV_{254}, and 8% for NPOC. On the other hand, following UVC irradiation period of 60 min, $Color_{436}$, UV_{365}, UV_{280}, UV_{254}, and NPOC removal efficiencies for ROC_{ECm2} were found to be 8%, 3%, 2%, 6%, and 2% respectively. Removal of specified UV-vis parameters were found to be higher than the mineralization extent of ROC_{m1} and ROC_{m2} which could be attributed to the rapid removal of UV absorbing moieties present in samples. In other words, insignificant change in organic carbon content could be referred to inefficient photomineralization of carboxylic groups into inorganic carbon (Umar et al., 2014; Zhang et al., 2019). Hindering effect of ECs on UVC photodegradation profiles of ROC_{ECm} samples could be clearly visualized by significant reduction achieved for the removal of specified UV-vis parameters as well as organic carbon content. $Color_{436}$, UV_{365}, UV_{280}, UV_{254} removal efficiencies of ROC_{ECm1} and ROC_{ECm2} were found to be three times lower than the results attained for ROC_{m1} and ROC_{m2}. Mineralization extent of ROC_{ECm1} and ROC_{ECm2} expressed as NPOC removal efficiency was also reduced to half of the values attained for ROC_{m1} and ROC_{m2}.

Being regarded as an important parameter referring to the aromaticity of the organics, UVC photodegradation of ROC_m and ROC_{ECm} samples were assessed in terms of their $SUVA_{254}$ values. Since majority of the aromatic rings are corresponding to humic-like compounds in ROC_m and ROC_{ECm} composition, the photodegradation of aromatic rings could be mainly deduced to the photodegradation of humic-like compounds (Helms et al., 2014; Zhang et al., 2019). Following UVC irradiation period of 60 minutes, $SUVA_{254}$ values were reduced to 8.66 L/mg m for ROC_{m1} and 9.48 L/mg m for ROC_{m2} from initial values of 10.1 L/mg m and 10.8 L/mg m corresponding to approximately 12-14% reduction on the aromaticity of the samples, whereas under the same experimental conditions, 60 min of UVC irradiation period reduced $SUVA_{254}$ values from 8.64 L/mg

m to 8.42 L/mg m for ROC_{ECm1} and from 8.87 L/mg m to 8.61 L/mg m for ROC_{ECm2} showing almost insignificant change (< 5%) indicating eminence of hydrophobic, high molecular weight organic compounds with higher aromaticity. Previous literature studies were also reported insignificant change in the aromaticity of samples upon exposure to UVC photodegradation process (Westerhoff et al., 2009; Zhou et al., 2011). In addition to $SUVA_{254}$, $SUVA_{280}$, $SUVA_{365}$, and $SCoA_{436}$ were also taken into consideration on the assessment of UVC photodegradation of ROC samples. Upon exposure to UVC photodegradation for t_{irr}: 90 min, $SUVA_{280}$ values reduced from 8.71 L/mg m to 7.42 L/mg m for ROC_{m1} and from 9.21 L/mg m to 8.69 L/mg m for ROC_{m2}, whereas a slight increase from 7.16 L/mg m to 7.44 L/mg m for ROC_{ECm1} and from 7.49 L/mg m to 7.59 L/mg m for ROC_{ECm2} was attained. In the presence of all ROC samples, $SCoA_{436}$ values displayed slight reduction for all ROC samples as follows: from 2.18 L/mg m to 1.72 L/mg m for ROC_{m1}, from 2.03 L/mg m to 1.62 L/mg m for ROC_{m2}, from 1.25 L/mg m to 1.20 L/mg m for ROC_{ECm1}, and from 1.33 L/mg m to 1.19 L/mg m for ROC_{ECm2}.

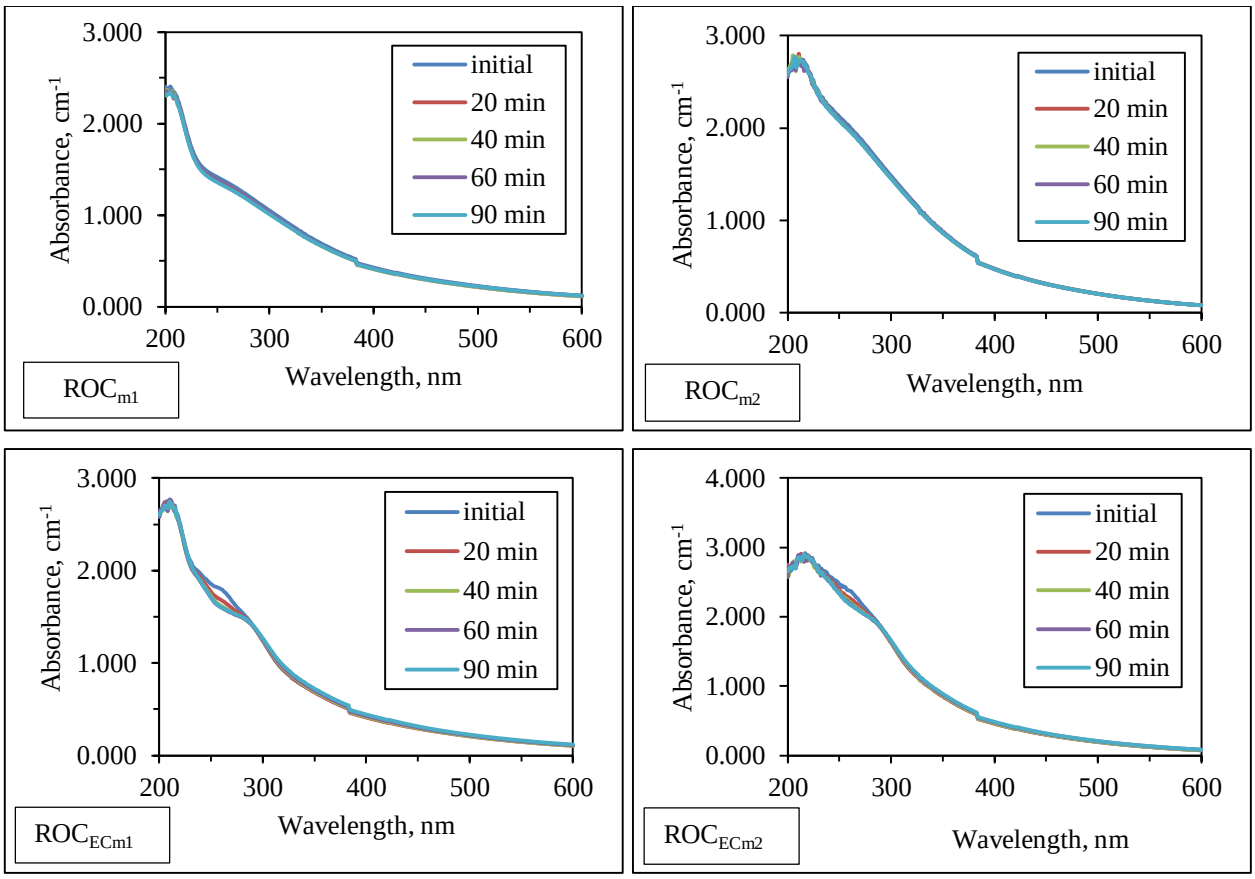

Figure 4.9. Time dependent UV-vis absorption spectra of ROC_m and ROC_{ECm} upon exposure to UVC photodegradation (I_o: 1.80×10^{17} quanta/s).

The major reactions on UVC photodegradation of ROC_{m1} and ROC_{m2} are expected to be photodegradation of humic matter to a limited extent depending on the susceptibility of its functional

groups, such as aromatic rings, carboxylic groups, and phenolic groups to photodegradation. In addition to above mentioned reactions occurring during photodegradation process, direct and/or indirect photolysis, which is defined as the reaction between photochemically generated reactive species and substrate, of ECs as well as their reaction intermediates also take place for ROC_{ECm1} and ROC_{ECm2}. It has been previously reported that SMX is prone to UVC photodegradation (Zhou and Moore, 1994; Nasuhoglu et al., 2011; Alharbi et al., 2017). Although susceptibility of CMZ is not as much as SMX due to its lower quantum yield and chemical structure containing amide groups, it is also expected to face photodegradation with much lower extent in comparison to SMX that could be attributed to formation of reactive species as a result of UVC photolysis (Chiron et al., 2006; Lekkerkerker-Teunissen et al., 2012; Ali et al., 2018). Therefore, upon exposure to UVC photodegradation, immediate degradation of parent compounds and formation of their reaction intermediates would take place. Consequently, since there are more competitors for reactive species, *i.e.* parent compounds (SMX and CMZ) and their reaction intermediates, reduction on the removal efficiencies of humic parameters could be expected.

UVC photodegradation of ROC_m and ROC_{ECm} samples were assessed via fluorescence spectroscopy in synchronous scan and EEM modes. Irradiation time dependent changes in synchronous scan spectra of ROC_m and ROC_{ECm} samples upon exposure to UVC photodegradation were presented in Figure 4.10, while EEM fluorescence contour-plots of ROC_m and ROC_{ECm} samples prior to and following UVC photodegradation with t_{irr}: 40 min and 90 min were displayed in Figure 4.11.

Following solar photodegradation period of 90 min, 27% and 26% reduction in FI_{syn} was achieved for ROC_{m1} and ROC_{m2}, whereas 20% and 24% reduction was obtained for ROC_{ECm1} and ROC_{ECm2} indicating that presence of ECs almost caused no change in FI_{syn} values at λ: 470 nm In addition to insignificant changes attained for FI_{syn} values of ROC_m and ROC_{ECm} samples, NPOC normalized values of FI_{syn} namely SFI_{syn} revealed removal efficiencies of 15% for ROC_{m1}, 20% for ROC_{m2}, 14% for ROC_{ECm1} and 18% for ROC_{ECm2} indicating irrelevant changes were attained with respect to varying compositions of organic matter in ROC samples.

On the other hand, second characteristic sharp peak at 380 nm displayed gradual increase with respect to increasing irradiation periods for ROC_{ECm1} and ROC_{ECm2} whereas ROC_{m1} and ROC_{m2} revealed general trend of decreasing fluorescence intensity in relation to irradiation periods. The reason could be attributed to transformation of higher molecular weight humic components giving fluorescence intensity at λ: 470 nm into lower molecular weight humic-like or fulvic-like

components. Another possible mechanism could be related to the interactions between ECs and/or their photodegradation products expressing properties as humic-like and fulvic-like components. In accordance with the findings attained in specific and specified UV-vis parameters, aromatic core of organic fraction in ROC_m and ROC_{ECm} samples were still evident even after UVC irradiation period of 90 min. Results were found to be meaningful compared to literature findings presented for UVC photodegradation profiles of humic-like matter mainly using HA as the representative of NOM (Uyguner-Demirel and Bekbolet, 2011; Helms et al., 2014; Zhang et al., 2019) as well as ROC samples (Westerhoff et al., 2009; Zhou et al., 2011; Umar et al., 2014 and 2015).

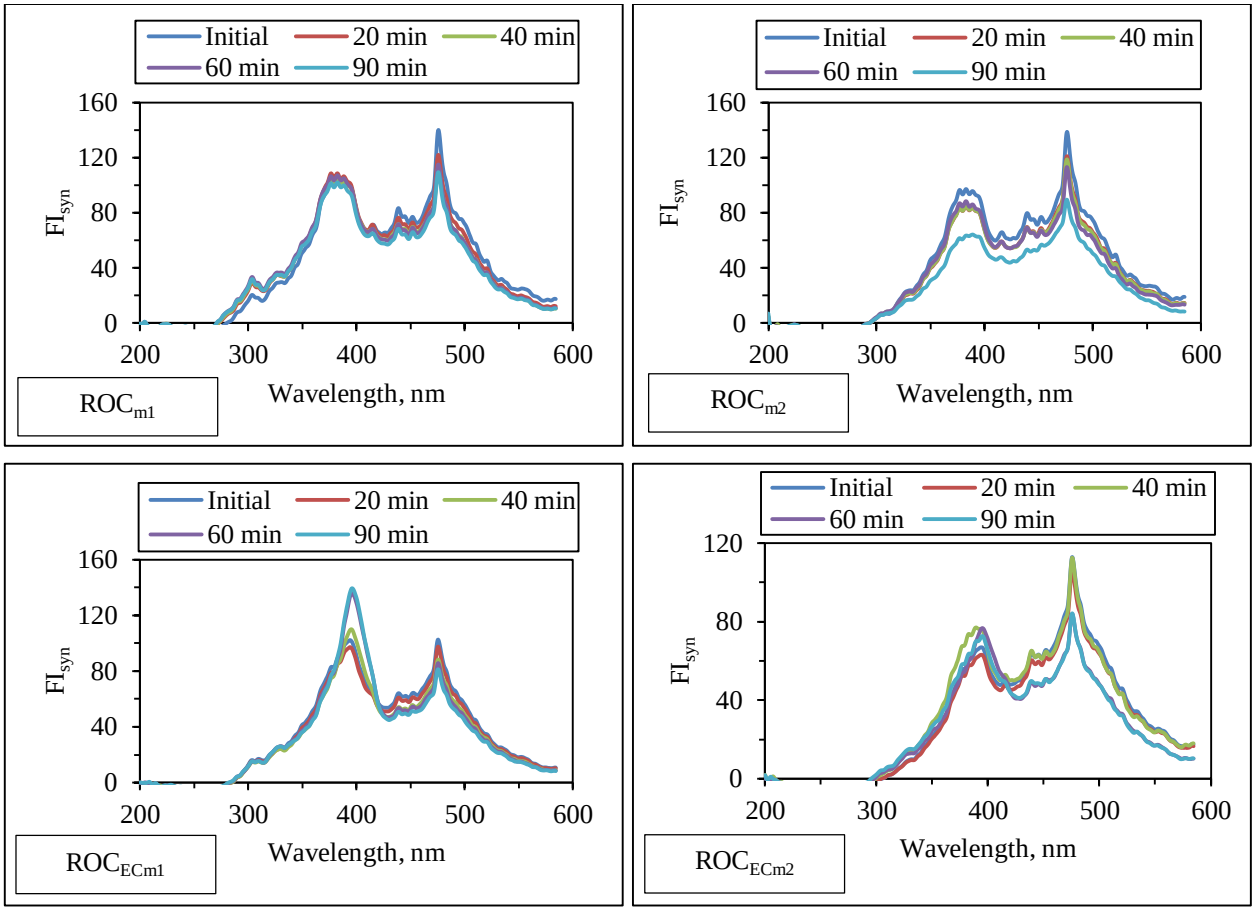

Figure 4.10. Synchronous scan fluorescence spectra of ROC_m and ROC_{ECm} upon UVC photodegradation (I_o: 1.80×10^{17} quanta/s).

Upon exposure to UVC photodegradation for irradiation period of 40 min, negligible difference in the fluorescence intensity of peaks in humic-like and fulvic-like regions were attained for all ROC samples which could also evidenced by the minor mineralization extents (NPOC removal< 10%). In this respect, considerable amount of NPOC was still present as the organic matrix in the reaction medium quantified as follows: 12.7 mg/L for ROC_{m1}, 20.8 mg/L for ROC_{m2}, 19.5 mg/L for ROC_{ECm1}, and 28.2 mg/L for ROC_{ECm2}.

Prominence of significant amount of NPOC indicates the presence of humic macromolecules with highly saturated aromatic structure which enables inter and/or intramolecular bonding and self-quenching within other humic components and therefore revealing lower fluorescence intensities even in the presence of high concentrations (Chen et al., 2003). On the other hand, slightly noticeable differences in shape and intensity of fluorophores were attained for ROC_{m1} and ROC_{ECm1} following t_{irr}: 90 min in comparison to t_{irr}: 40 min. In the presence of same organic matrix, presence of ECs significantly influenced shape, related to regional distribution of fluorophores and intensity of fluorophores for ROC_{m1} and ROC_{ECm1}, which differed from each other in terms of humic-like and fulvic-like fluorophores, whereas almost no difference was attained between ROC_{m2} and ROC_{ECm2}. The reason could be attributed to potential formation of humic aggregates in the presence of ROC_{m2} and ROC_{ECm2} causing light attenuation of HM, therefore reduced photodegradation efficiency (Šmejkalová and Piccolo, 2008).

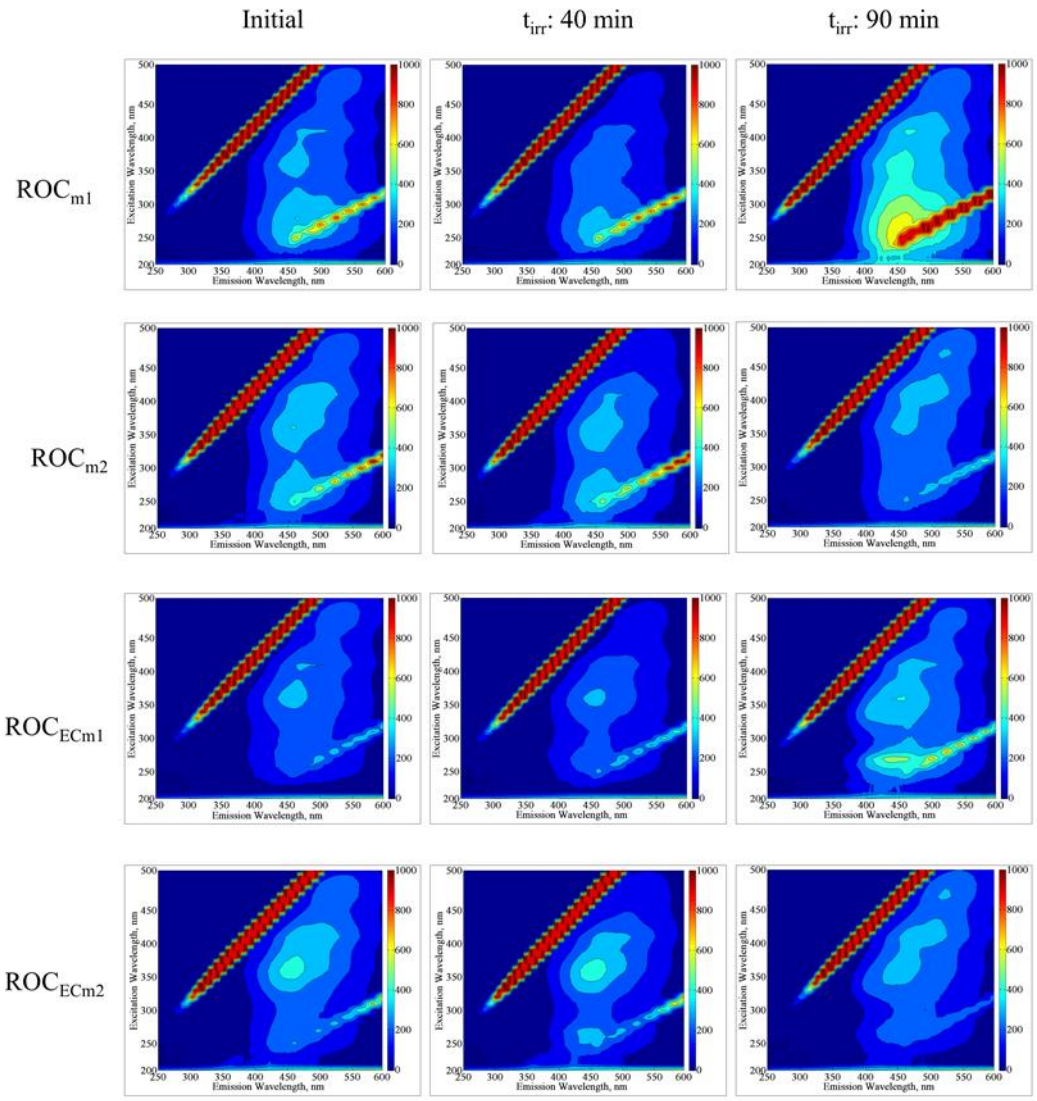

Figure 4.11. EEM fluorescence contour-plots of ROC_m and ROC_{ECm} prior to and following UVC photodegradation (I_o: $1.80x10^{17}$ quanta/sec, t_{irr}: 40 min and 90 min).

4.3.2. UVC/H_2O_2 Process

UVC/H_2O_2 process is based on the generation of hydroxyl radicals through photolysis of H_2O_2 as the auxiliary oxidant under UVC light irradiation. Homolitic cleavage of chemical bond present in H_2O_2 leads to the formation of hydroxyl radicals as depicted by the following reaction:

$$H_2O_2 + h\nu\ (\lambda: 253.7\ nm) \rightarrow HO^{\bullet} + HO^{\bullet} \quad (4.7)$$

Photolysis of H_2O_2 at λ: 253.7 nm in 0.1 N perchloric acid gives the quantum yield of 1.00 at 25°C which is independent of concentration of peroxide in the range of $4.5x10^{-7}$ to 1M and light intensity in the range of $5x10^{-4}$ Einstein/L min. The extinction coefficient of H_2O_2 at λ: 253.7 nm is determined as 19.6 L/mol s (Lay, 1989). Hydroxyl radicals proceed in a non-selective reaction pathway to attack organic molecules, such as HM in a non-specific manner and converting them into lower molecular weight compounds as carboxylic acids and aldehydes and eventually transforming them via mineralization into innocuous carbon dioxide (Backlund, 1992; Wang et al., 2000).

Previously reported results attained for UVC/H_2O_2 treatment of ROC_m giving same characteristics of ROC samples used in this study from the literature was revisited. According to the results attained from these studies, optimum H_2O_2 concentration was found to be in the ranges of 3-4 mM (Lu et al., 2013; Umar et al., 2014 and 2015) selected from experimental range of 1-6 mM. Therefore, H_2O_2 dose of 3 mM was selected as the working dose within the scope of this study. Consequently, all ROC samples were exposed to UVC irradiation in the presence of 3 mM H_2O_2 with an irradiation period of 60 min. Removal of OM present in ROC samples were assessed in terms of specified and specific UV-vis and fluorescence spectroscopic parameters both in synchronous scan and EEM modes as well as NPOC contents as presented in Figure 4.12.

Impact of ECs on UVC/H_2O_2 treatment of ROC samples could be explained by the assessment of the results attained for ROC_m and ROC_{ECm} in terms of the removal of specified and specific UV-vis parameters as well as NPOC contents. Following 60 min of UVC/H_2O_2 treatment, ROC_{m1} ended up with the removal efficiencies of 85% for $Color_{436}$, 83% for UV_{365}, 78% for UV_{280}, 76% for UV_{254}, and 14% for NPOC, whereas ROC_{ECm1} revealed the following removal efficiencies as 11% for $Color_{436}$, 5% for UV_{365}, 17% for UV_{280}, 14% for UV_{254}, and 8% for NPOC. Following irradiation period of 60 min, ROC_{m2} revealed removal efficiencies of 74% for $Color_{436}$, 75% for UV_{365}, 73% for UV_{280}, 72% for UV_{254}, and 11% for NPOC, whereas ROC_{ECm2} revealed the following removal efficiencies as 8% for $Color_{436}$, 6% for UV_{365}, 12% for UV_{280}, 11% for UV_{254}, and 6% for NPOC.

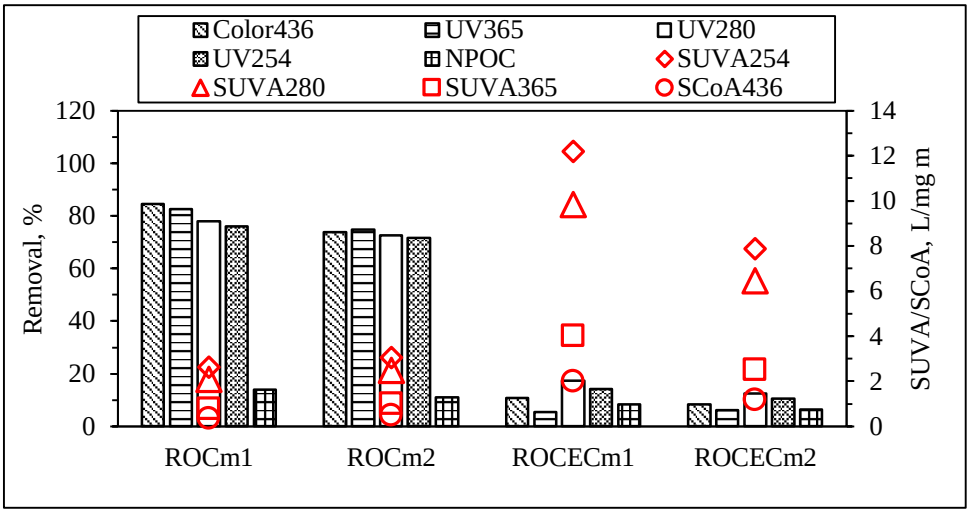

Figure 4.12. Comparative removal efficiencies of ROC_m and ROC_{ECm} in terms of specified ($Color_{436}$, UV_{365}, UV_{280}, and UV_{254}) and specific ($SCoA_{436}$, $SUVA_{365}$, $SUVA_{280}$, and $SUVA_{254}$) UV-vis parameters and NPOC via UVC/H_2O_2 (I_o: 1.80x10^{17} quanta/s, H_2O_2 conc.: 3 mM, t_{irr}: 60 min).

It could be clearly observed that presence of H_2O_2 boosted removal of specified UV-vis parameters in all ROC samples in comparison to UVC photodegradation. The reason could be attributed to the role of different mechanisms in photodecomposition of OM, which could proceed either via direct photochemical reactions or via indirect processes with the involvement of photochemically produced ROS (Zafiriou, 1983; Zafiriou et al., 1984; Cooper et al., 1989; Blough and Zepp, 1995). In the dominance of direct photochemical reactions, only chromophoric portion of the DOM is broken down, whereas indirect photochemical reactions allow photodecomposition of non-chromophoric material. Reactions between $HO^{\bullet}$ and organic compounds rely on two basic mechanisms: *i.* hydroxylation, defined as the addition of H atom, generally to an aromatic ring, and *ii.* $H^{\bullet}$ abstraction. Both of the mechanism are capable of transforming high molecular aromatic components into low molecular weight acids. Hydroxylation of aromatic moieties enables the ring opening of precursor material followed by the formation of mono- and diacids (Gopalan et al., 1994; Lanzalunga et al., 2000). Moreover, both of the mechanisms are capable of breaking aromatic ring to produce hydroxycyclohexadienyl radicals**.** A carbon centered radical ($R^{\bullet}$) could form when $H^{\bullet}$ abstraction from an unsaturated C-C bond occurs. Then, $R^{\bullet}$ reacts with O_2 to form $O_2^{\bullet}$ and subsequent decomposition to a carboxylic acid (Goldstone et al., 2002).

In the presence of ROC_{m1} and ROC_{m2}, $HO^{\bullet}$ tends to attack to the humic-like and fulvic-like components as well as to the other inorganic constituents, however, in the presence of ROC_{ECm1} and ROC_{ECm2}, there would be various targets for $HO^{\bullet}$ to attack, such as humic-like and fulvic-like components, inorganic contents, and ECs as well as their transformation by-products. Following 60

min treatment with UVC/H_2O_2 process, disappearance of SMX and CMZ could be clearly visualized by UV-vis absorbance of ROC_{ECm1} at which shoulders related to SMX (λ_{range}: 190-310 nm, λ_{max}: 265 nm) and CMZ (λ_{range}: 190-340 nm, λ_{max}: 285 nm) were no longer observed.

Previous literature studies indicated that upon exposure to UVC/H_2O_2 process, from 80% to complete removal of SMX and CMZ could be achieved either in the absence or presence of other water and wastewater constituents (Nasuhoglu et al., 2011; Lekkerkerker-Teunissen et al., 2012; De la Cruz et al., 2013; Yang et al., 2017). Additionally, concomitant generation and removal of their direct or indirect photo-transformation by-products were also expected. Since removal of ECs and their transformation by-products dominated the removal preference of hydroxyl radicals, noticeable reduction on the removal efficiencies of specified UV-vis parameters were attained for ROC_{ECm1} and ROC_{ECm2} in comparison to ROC_{m1} and $ROC_{m2.}$ Additionally, evidence of aromatic core of humic matter could be understood by assessing specified UV-vis parameters as $SUVA_{254}$, $SUVA_{280}$, $SUVA_{365}$, and $SCoA_{436}$. Following UVC/H_2O_2 process for 60 min, $SUVA_{254}$ of ROC_{m1} and ROC_{m2} were reduced to 2.64 L/mg m and 3.05 L/mg m from initial $SUVA_{254}$ values of 9.46 L/mg m and 9.51 L/mg m indicating transformation of hydrophobic and aromatic core of humic matter into more hydrophilic lower humic fractions. However, under the same experimental conditions, 60 min of UVC irradiation reduced $SUVA_{254}$ values from 13.0 L/mg m to 12.2 L/mg m for ROC_{ECm1} and from 8.26 L/mg m to 7.89 L/mg m for ROC_{ECm2} showing almost insignificant change therefore indicating prominence of high degree of aromaticity and high molecular weight organic compounds.

UVC/H_2O_2 derived $HO^{\bullet}$ non-selectively attack to ECs and their UVC originated or ROS attack originated transformation by-products which avoids degradation of humic matter present in the solution matrix, therefore, in the presence of ECs, aromaticity referring to the humic matter is still evident for ROC_{ECm1} and ROC_{ECm2} even after reaction period of 60 min at which only 14% and 11% UV_{254}, 17% and 12% UV_{280}, 8% and 6% NPOC removal efficiencies were attained. Another reason could be attributed to the molecular weight distribution of organic components presented in ROC_m and ROC_{ECm} samples. Although both HM and ECs have aromatic rings within their structures, HM presents higher degree of aromaticity and complexity with respect to its higher molecular weight. Increasing molecular weight may cause aggregation of DOM which enables inner reaction sites inaccessible for $HO^{\bullet}$ attack, therefore in the presence of both HM and ECs, $HO^{\bullet}$ would preferentially react with ECs with respect to its available reaction sites to $HO^{\bullet}$. Presence of $HO^{\bullet}$ originated from AOPs could enhance SMX degradation to some extent, however, since the major mechanism of SMX degradation is based on photodegradation process, contribution of $HO^{\bullet}$ to SMX removal efficiency could be limited to with an enhancement of 10-15% by increasing oxidant concentration or UV dose

as has been previously reported through the literature (Nasuhoglu et al., 2011; Lekkerkerker-Teunissen et al., 2012; De la Cruz et al., 2013). On the other hand, $HO^{\bullet}$ significantly enhances formation as well as removal of transformation by-products of SMX originated from UVC photodegradation process (Nasuhoglu et al., 2011; Lekkerkerker-Teunissen et al., 2012; De la Cruz et al., 2013; Yang et al., 2017). For example, being regarded as two of the most common photodegradation by-products of SMX, 3-amino-5-methylisoxazole and sulfanilic acid could also be produced via another pathway with the involvement of $HO^{\bullet}$ in addition to direct photodegradation mechanism (Lam and Mabury, 2005).

Upon use of UVC/H_2O_2, more than 90% CMZ removal could be achieved following irradiation period of 30 min (Lekkerkerker-Teunissen et al., 2012). In case of UVC/H_2O_2 system, CMZ oxidation would start initially with $HO^{\bullet}$ attack to the aromatic structure causing hydroxylation and followed by further formation of hydroxylated compounds. Formation of acridine and its derivatives could also be attained within a short time following t_{irr}: 30 min. Although lower yields of acridine formation could be related to minor CMZ degradation via UVC/H_2O_2 process, significance of $HO^{\bullet}$ attack to acridine (k: $5.8x10^9$ L/mol s) indicates compatibility of this reaction intermediate with decomposition of parent compound (Vogna et al., 2004). The most common reaction by-products of CMZ are 10,11 epoxycarbamazepine, hydroxycarbamazepine, acridine-9-carboxaldehyde upon application of UVC/H_2O_2 process (Vogna et al., 2004; Lekkerkerker-Teunissen et al., 2012). Consequently, in the case of ROC_{ECm1} and ROC_{ECm2}, $HO^{\bullet}$ consuming fractions would be both humic-like and fulvic-like components originating from ROC, SMX and CMZ as the ECs as well as their photo-initiated and $HO^{\bullet}$ attack initiated reaction intermediates which could explain significant reduction of mineralization extent in ROC_{ECm1} and ROC_{ECm2} compared to ROC_{m1} and ROC_{m2}.

UVC/H_2O_2 treatment for the removal of organics in ROC_m (DOC_i: 40 mgOrgC/L) in the presence of 10 mM H_2O_2 with I_o: 11.8 kW h/m^3 at pH 7 ended up with only <10% DOC removal (Westerhoff et al., 2009). Umar and colleagues were focused on UVC/H_2O_2 treatment of municipal ROC samples by using 3 mM H_2O_2 at pH 5 and results were evaluated in terms of removal of DOC, COD, Color and UV-vis absorbance at 254 nm (A_{254}). Following an irradiation period of 60 min, <20% DOC removal was attained whereas up to 70% A_{254} removal and up to 80% Color removal were observed (Umar et al., 2014). Another study of UVC/H_2O_2 treatment of ROC_m (DOCi: 47.5 mgOrgC/L) was performed with H_2O_2 concentration of 4 mM and I_o: 12.89 mJ/s cm^2 between pH values of 7.8-8.4. Following irradiation period of 30 min, 50% Color removal, 61% UV_{254} removal, and only 15% DOC removals were attained (Lu et al., 2013).

Considering similar organic carbon contents of ROC samples presented in literature studies (Table 2.1) and in our studies (Table 4.2), having closer results indicated the possible response of UVC/H_2O_2 process to the removal of organics in municipal ROC samples which could be concluded as fast removal of UV absorbing centers of organic fractions in ROC, but very limited extent of mineralization. The faster reduction of specified UV-vis parameters could be attributed to breakdown of bonds in chromophoric moieties within the major fragments and/or bulk of the original molecules remaining unbroken (Umar et al., 2014). Moreover, overall $HO^{\bullet}$ scavenging factor is expected to be considerably higher due to presence of common anions and alkalinity which would reduce overall mineralization extent of ROC samples.

Complete removal of SMX, CMZ and their photo-transformation products could mainly be achieved in the presence of hydroxyl radicals. Main removal mechanism of SMX is based on UV photodegradation process which could be slightly enhanced by the addition of H_2O_2 to the system (González et al., 2009; Alfonso-Oliveras et al., 2016; Yang et al., 2017; Martinez-Costa et al., 2018) whereas CMZ removal could be enhanced significantly via UVC/H_2O_2 system in comparison to UV photodegradation alone (Pereira et al., 2007; Deng et al., 2013; Miralles-Cuevas et al., 2017). Therefore, removal of ECs and their photo transformation by-products has the ability to lessen the overall mineralization extent of ROC_{ECm1} and ROC_{ECm2} in comparison to ROC_{m1} and ROC_{m2}.

In addition to specified and specific UV-vis parameters and organic carbon contents, further evaluation regarding changes in all fluorophoric components at their specific regions present in ROC_m and ROC_{ECm} were followed by fluorescence EEM features. EEM fluorescence contour-plots of ROC_m and ROC_{ECm} samples prior to and following UVC/H_2O_2 process were presented in Figure 4.13.

Following UVC/H_2O_2 treatment of ROC samples for t_{irr}: 60 min, in accordance with the attained organic carbon removal results, humic-like and fulvic-like fluorophores were slightly present with lower intensities for ROC_{m1} and ROC_{m2} whereas they were still prominent for ROC_{ECm1} and ROC_{ECm2}. Moreover, emergence of protein-like fluorophores in Aromatic Proteins I (Ex/Em: 220-250/280-332 nm) and Aromatic Proteins II (Ex/Em: 220-250/332-380 nm) was observed for ROC_{ECm2} which could be attributed to presence of SMX giving peaks (Ex/Em: 210-250/350 nm) in these regions (Ben Abdelmelek et al., 2013; Sgroi et al., 2017). Since protein-like fluorophores were known to be components with comparatively lower molecular size fractions (1-5 kDa), they could be masked by higher molecular size fraction components, such as humic-like and fulvic-like fluorophores therefore depending on the composition of the organic matrix they could not be visualized by EEM fluorescence spectra clearly (Wang et al., 2015).

On the other hand, another reason of not observing protein-like fluorophores in ROC_{ECm1} could be attributed to complete removal of ECs that could give no more fluorescence intensity. Previous literature studies indicated up to 90% removal of SMX and CMZ could be achieved via UVC/H_2O_2 process following t_{irr}: 30 min (Vogna et al., 2004; Lekkerkerker-Teunissen et al., 2012). In the presence of ROC_{ECm1}, organic matter composed of medium and high molecular size humic-like fluorophores that are able to shield fluorophores originated from ECs, whereas comprising medium and lower molecular size humic-like and fulvic-like fluorophores, SMX derived fluorophores giving maxima at Ex/Em: 210-290/350 nm could be clearly seen in the presence of ROC_{ECm2}.

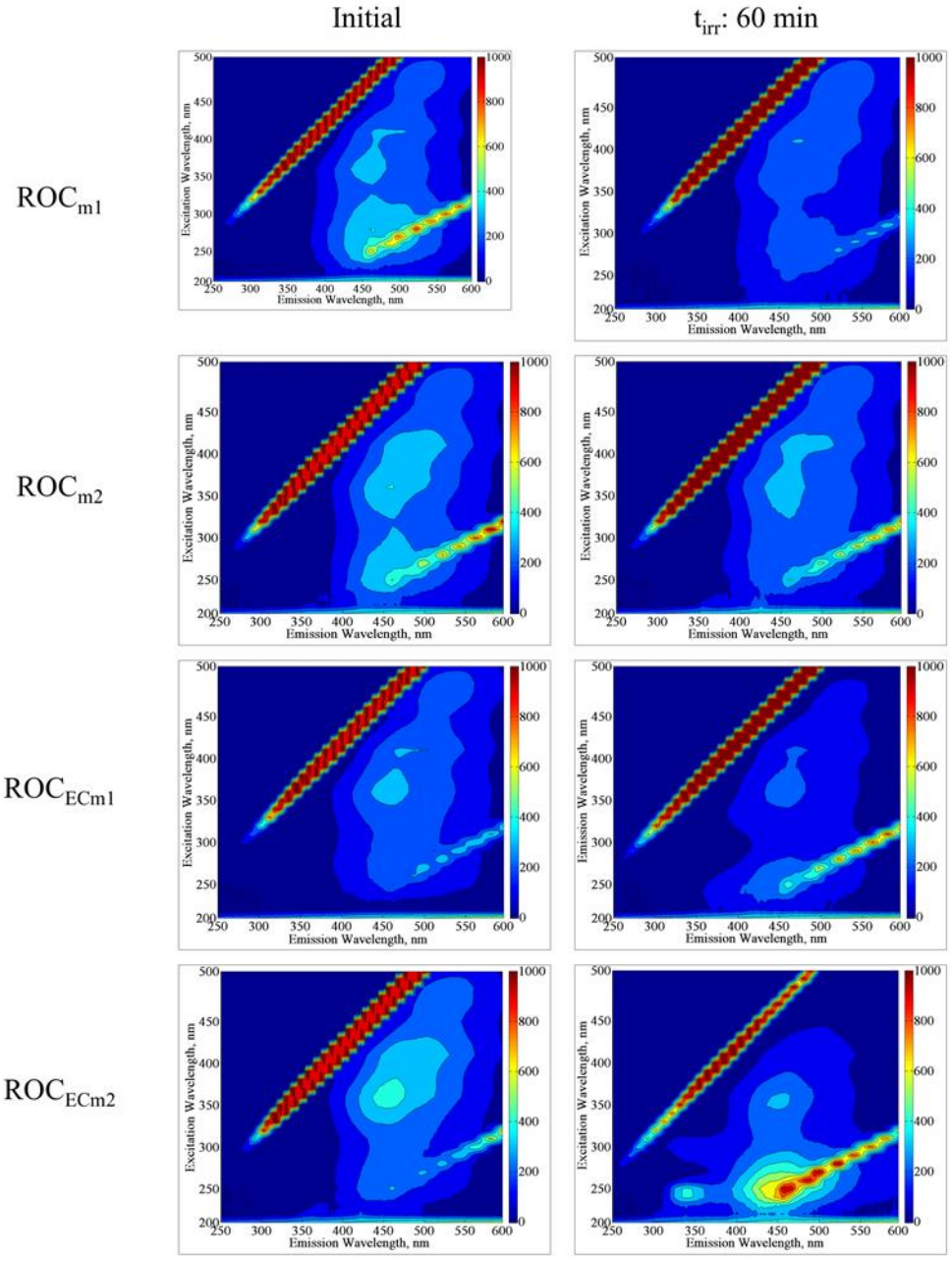

Figure 4.13. EEM fluorescence contour-plots of ROC_m and ROC_{ECm} upon UVC/H_2O_2 process (I_o: $1.80x10^{17}$ quanta/sec, H_2O_2 conc.: 3 mM, t_{irr}: 60 min).

4.3.3. Fenton and photo-Fenton Processes

Conventional dark-Fenton process is based on the use of one or more oxidizing agents, such as hydrogen peroxide and/or oxygen, and a metal salt or oxide as the catalyzer. Photo-Fenton process includes exposure to irradiation that could be either sunlight or an artificial source that are able to enhance the removal of contaminants via oxidation and reduction cycle of Fe by which a range of free radicals can be generated (Fenton, 1894; Faust and Hoigné, 1990; Pignatello, 1992; Hermosilla et al.,2009).

Under acidic conditions and in the presence of H_2O_2, dissolved Fe (II) is oxidized to Fe (III) and ended up with the generation of highly reactive hydroxyl radicals ($HO^{\bullet}$) spontaneously (Reaction 4.8). Other possible reactions which may take place between the species in Reaction 4.8 is presented in reactions 4.9-4.13 by excluding other species that may be present in the reaction medium.

$$Fe^{2+} + H_2O_2 \rightarrow Fe^{3+} + HO^{\bullet} + OH^{-} \quad (4.8)$$

$$Fe^{3+} + H_2O_2 \rightarrow Fe^{2+} + HO_2^{\bullet} + H^{+} \quad (4.9)$$

$$Fe^{2+} + HO^{\bullet} \rightarrow OH^{-} + Fe^{3+} \quad (4.10)$$

$$H_2O_2 + HO^{\bullet} \rightarrow HO_2^{\bullet} + H_2O \quad (4.11)$$

$$Fe^{2+} + HO_2^{\bullet} + H^{+} \rightarrow Fe^{3+} + H_2O_2 \quad (4.12)$$

$$Fe^{3+} + HO_2^{\bullet} \rightarrow Fe^{2+} + O_2 + H^{+} \quad (4.13)$$

Fenton reaction can proceed without the influence of light and highly efficient in the pH range of 2-4 with an optimum value of 2.8 (Pignatello, 1992). As a result of the generation of highly reactive oxygen species, Fenton process enables complete degradation of various organic compounds into CO_2, H_2O, and organic ions (Kang and Kwang, 2000; Neyens and Baeyens, 2003; Pignatello et al., 2006).

$$Fe^{3+} + H_2O + h\nu\ (\lambda\text{: 180-400 nm}) \rightarrow Fe^{2+} + H^{+} + HO^{\bullet} \quad (4.14)$$

When Fenton reaction takes place under irradiation (UVC and UVA) with suitable wavelength region of λ: 180-400 nm, formation of hydroxyl radicals or ferryl species are catalyzed by Fe (III) and this reaction is named as photo-Fenton process (Reaction 4.14).

This reaction is then followed by above mentioned Fenton reactions (reactions 4.8-4.13). During photo-Fenton reaction, an iron cycle between +2 and +3 oxidation states occurs which is known to be one of the contributors to HO• generation. Hydroxyl radical production depends on the availability of irradiation of suitable wavelength as well as H_2O_2. Theoretically, two moles of HO• is generated per mole of H_2O_2 by the combination of reaction 4.6 and reaction 4.12.

With respect to the literature findings dealing with Fenton and photo-Fenton treatment of ROC, the optimum experimental conditions were found to be 1:1 ratio of Fe^{2+}/H_2O_2 (Table 2.4 and references cited therein). Therefore, in accordance with the experimental conditions selected in UVC/H_2O_2 experiments, 3 mM of Fe^{2+} (in the form of $FeSO_4$) and H_2O_2 with 1:1 ratio was selected for Fenton and experiment for reaction period of 60 min. In a similar manner with UVC/H_2O_2 experiments, removal efficiencies were followed by UV-vis and fluorescence spectroscopic parameters as well as NPOC contents. Removal efficiencies of the specified and specific UV-vis parameters and NPOC contents of ROC samples were presented in Figure 4.14.

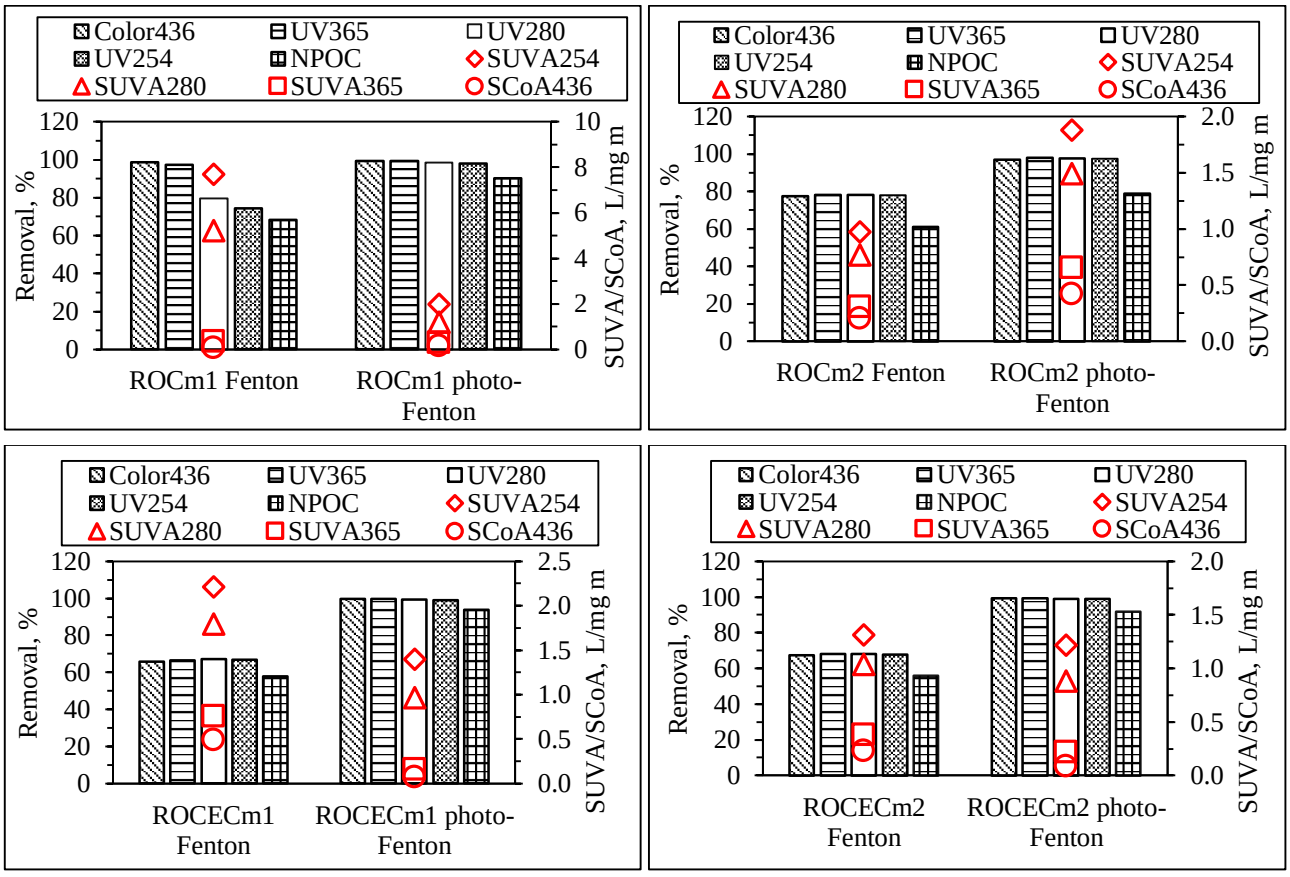

Figure 4.14. Removal efficiencies of ROC_m and ROC_{ECm} in terms of specified ($Color_{436}$, UV_{365}, UV_{280}, UV_{254}) and specific ($SUVA_{254}$, $SUVA_{280}$, $SUVA_{365}$, and $SCoA_{436}$) UV-vis parameters as well as NPOC upon Fenton and photo-Fenton processes (I_o: $1.80x10^{17}$ quanta/sec, Fe^{2+} conc.: 3 mM, H_2O_2 conc.: 3 mM, t_{irr}: 60 min).

Following Fenton reaction period of 60 min ROC_{m1} ended up with the removal efficiencies of 99% for $Color_{436}$, 97% for UV_{365}, 80% for UV_{280}, 74% for UV_{254}, and 68% for NPOC, whereas ROC_{ECm1} revealed the following removal efficiencies as 66% for $Color_{436}$, 67% for UV_{365}, UV_{280}, and UV_{254}, and 58% for NPOC. Fenton reaction ended up with removal efficiencies of 78% for $Color_{436}$, UV_{365}, UV_{280}, and UV_{254}, and 61% for NPOC for ROC_{m2}, whereas ROC_{ECm2} revealed the following removal efficiencies as 67% for $Color_{436}$, 68% for UV_{365}, UV_{280}, and UV_{254}, and 56% for NPOC. In a similar trend attained for UVC/H_2O_2 process, presence of ECs strongly influenced removal of selected parameters by lowering their removal efficiencies in ROC_{ECm1} and ROC_{ECm2} via Fenton process. Under acidic conditions, Fenton reaction generated highly reactive oxygen species (ROS) tend to attack to organic constituents of ROC samples, such as humic matter and ECs. Degradation of humic-like components would transform them into lower molecular size constituents via ROS attack, whereas in the presence of SMX and CMZ, ROS are expected to deal both with the parent compounds as well as their reaction intermediates. (Zhou and Moore, 1994; Lam and Mabury, 2005; Alharbi et al., 2017).

In addition to its susceptibility to photodegradation, $HO^{\bullet}$-mediated photoproducts of SMX could be observed via Fenton reactions that are able to generate $OH^{\bullet}$. Many products formed by direct photolytic means also formed in solutions where $HO^{\bullet}$ was generated with a non-photochemical source. In addition to direct photolysis, $HO^{\bullet}$ may provide another pathway leading to the production of 3-amino-5-methylisoxazole (Lam and Mabury, 2005). Upon exposure to Fenton process, hydroxylation of CMZ could end up with the formation of hydroxycarbamazepine and epoxycarbamazpeine as the reaction intermediates. Further attack of $HO^{\bullet}$ enables the formation of dihydroxycarbamazepine and carbamazepine-o-quinone. Ring opening of these intermediates is then followed by the generation of short-chain organic acids, such as maleic, malonic, acetic, and formic acid which are finally oxidized to oxalic acid and to CO_2 (Monsalvo et al., 2015). Degradation of all these intermediates requires additional oxidants to be converted to final products. Therefore, reduction of removal efficiencies for ROC_{ECm1} and ROC_{ECm2} could be attributed to these reactions consuming additional $HO^{\bullet}$ than ROC_{m1} and ROC_{m2}. Consequently, significant reduction of removal efficiencies of specified and specific UV-vis parameters as well as organic carbon content of ROC_{ECm1} and ROC_{ECm2} could be attributed to additional consumption of ROS for the removal of ECs as well as their reaction intermediates.

Applicability of Fenton process on the removal of organics in municipal reverse osmosis concentrate (DOC_i: 19.2 mg/L) has been investigated previously through the literature (Table 2.4, Section 2.2.2). Both Fe^{2+} and H_2O_2 concentration values were selected as 10 mM corresponding to

1:1 ratio at pH 3.3. Following reaction period of 60 min, 50% DOC removal was achieved (Westerhoff et al., 2009). Although there was limited number of publications considered Fenton reaction for the treatment of organics in ROC, reported outcome indicated meaningful proximity within the results attained in this study.

Following photo-Fenton reaction period of 60 min, ROC_{m1} ended up with the removal efficiencies of 99% for $Color_{436}$, UV_{365}, and UV_{280}, 98% for UV_{254}, and 90% for NPOC, whereas ROC_{ECm1} revealed the following removal efficiencies as complete removal for $Color_{436}$ and UV_{365}, 99% for UV_{280} and UV_{254}, and 94% for NPOC. Photo-Fenton reaction revealed removal efficiencies of 97% for $Color_{436}$, 98% for UV_{365}, UV_{280}, and UV_{254}, and 79% for NPOC for ROC_{m2}, whereas ROC_{ECm2} revealed the following removal efficiencies as 99% for $Color_{436}$, UV_{365}, UV_{280}, and UV_{254}, and 92% for NPOC. In the presence of all ROC samples, significant enhancement of removal efficiencies of specified and specific UV-vis parameters as well as NPOC contents were attained for photo-Fenton process in comparison to Fenton process. More than 98% removal of specified UV-vis parameters and up to 94% NPOC removal efficiencies were achieved. Assessment of photo-Fenton process for ROC treatment was found to be limited to its application on industrial ROC samples (ROC_x) through the literature. It was concluded that 60% COD removal and complete COD removal were achieved by the application of Fenton and photo-Fenton processes for ROC samples originated from papermill wastewater respectively (Hermosilla et al., 2012).

It could also be concluded that photo-Fenton system is able to reduce the gap between removal efficiencies of ROC_m and ROC_{ECm} samples attained in UVC/H_2O_2 as well as Fenton processes. The reason could be attributed to several factors: *i.* additional $HO^{\bullet}$ formation as a result of UVC photolysis of H_2O_2, *ii.* cycle of Fe (II) between the +II and +III oxidation states that are able to catalyze the formation of hydroxyl radicals or ferryl species in the presence of UVC irradiation (Parsons, 2004), and *iii.* UVC photodegradation of ECs could be regarded as another additional mechanism in photo-Fenton system that enhances overall removal efficiency. It has been previously reported that major removal mechanism of SMX is based on photodegradation process which could be enhanced by 15-20% more with the contribution of ROS (Nasuhoglu et al., 2011; Lekkerkerker-Teunissen et al., 2012; De la Cruz et al., 2013). Consequently, presence of UVC irradiation in photo-Fenton process triggered overall process efficiency irrespective of the organic matrix composition of ROC origin in comparison to Fenton process. It is very well known that Fenton and Fenton-like processes give low effectiveness in the degradation of ECs requiring very high concentrations of the iron species to achieve significant removal which could be overcome by applying UVC or solar irradiation in the absence/presence of iron salts, such as $FeSO_4$ and $FeCl_3$ (Martinez-Costa et al., 2018).

Further evaluation of organic constituents in ROC samples with respect to Fenton and photo-Fenton processes were done by the assessment of fluorescence spectroscopic properties. EEM fluorescence contour-plots of ROC_m and ROC_{ECm} samples prior to and following Fenton and photo-Fenton processes as presented in Figure 4.15.

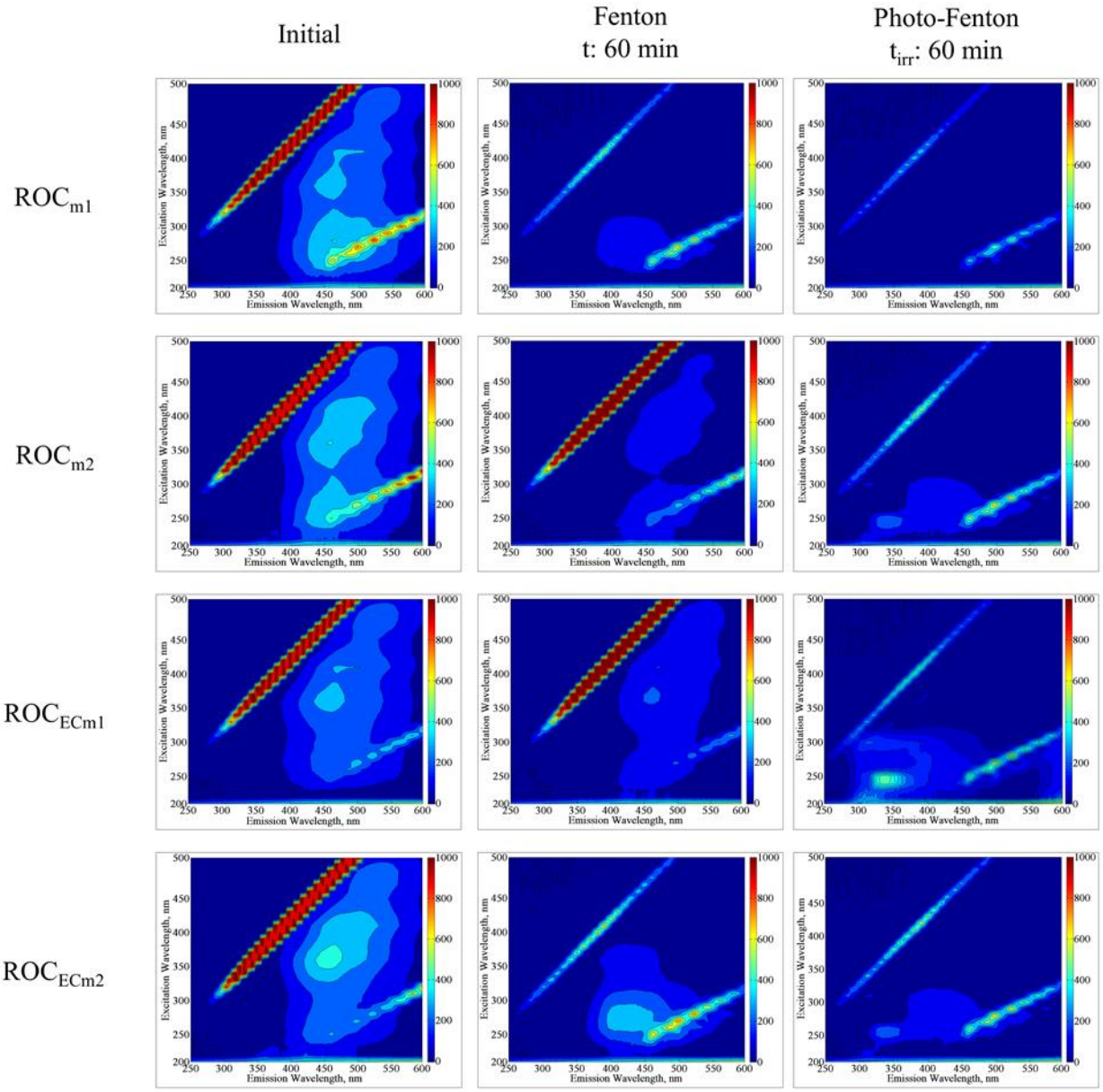

Figure 4.15. EEM fluorescence contour-plots of ROC_m and ROC_{EC} prior to and following Fenton and photo-Fenton processes (I_o: 1.80×10^{17} quanta/sec, Fe^{2+} conc.: 3 mM, H_2O_2 conc.: 3 mM, t: 60 min).

Upon exposure to Fenton process for 60 min, humic-like fluorophores were almost completely disappeared for ROC_{m1} and ROC_{ECm2}, however they were still evident for ROC_{m2} and ROC_{ECm1}. In addition, emergence of new fulvic-like fluorophores were attained for ROC_{ECm2} indicating

transformation of high molecular weight humic-like fluorophores into lower molecular weight fulvic-like compounds as a result of ROS attack. Following irradiation period of 60 min, disappearance of humic-like fluorophores was observed for all ROC samples via photo-Fenton process, whereas fulvic-like fluorophores with considerably lower intensity were still present for all ROC_{m1}, ROC_{m2}, and ROC_{ECm1}. Both humic-like and fulvic-like fluorophores were still evident in ROC_{ECm2} even after reaction period of 60 min. Emergence of protein-like fluorophores were clearly observed for ROC_{ECm1} which could be attributed to the presence of ECs whose fluorophores were masked by humic-like and fulvic-like fluorophores. When humic-like and fulvic-like fluorophores were removed from the reaction medium, their masking effect was eliminated therefore, protein-like fluorophores could be visualized clearly as observed for ROC_{ECm1} in Figure 4.10.

Although similar trend was expected to outcome for EEM fluorescence contour-plot of ROC_{ECm2}, protein-like fluorophores could not be seen due to prominence of humic-like and fulvic-like fluorophores that were camouflaged protein-like fluorophores as reported by Wang and colleagues (Wang et al., 2015). Following irradiation period of 60 min via photo-Fenton reaction, all humic-like, fulvic-like and even protein-like fluorophores were disappeared which could be attributed to the removal of specified UV-vis parameters (almost complete removal) as well as organic carbon contents (> 90% removal) that are related to all organic components, such as humic-matter and ECs in all ROC samples. Previous literature findings indicated that addition of iron (II) into UV/H_2O_2 system is expected to show insignificant improvement on the removal of ECs (Ali et al., 2018; Martinez-Costa et al., 2018).

Removal of all humic-like and fulvic-like fluorophores and occurrence thereby the presence of protein-like fluorophores could be regarded to the mechanism of photo-Fenton process by which no significant enhancement of EC removal was attained. Since main removal mechanism of SMX is based on UV photodegradation by which up to 95% SMX removal could be achieved, photo-Fenton process would only enhance overall SMX removal by 5-10% (Martinez-Costa et al., 2018). Therefore, photo-Fenton reaction has the tendency to improve overall mineralization extent via photo-Fenton originated hydroxyl radical attack to the organic matrix mainly to the humic-like and fulvic-like components present in reaction medium (De la Cruz et al., 2013). Another reason could be attributed to the competition between ECs and H_2O_2 for harvesting irradiation leading to light initiated reactions. Due to its λ_{max} (254 nm) and quantum yield (Eq. 4.7), H_2O_2 would absorb majority of the incident light making inadequate portion of light available for SMX. Therefore, fluorescence intensity attained for regions Aromatic Proteins I and II could be attributed to evidence of SMX or its fluorescent reaction intermediates that were still present with respect to their insufficient removal.

4.4. Solar Irradiation Initiated Processes

This section covers the application of solar light initiated processes on ROC_m and ROC_{ECm} treatment. All experiments were performed by using solar reactor configuration as presented and explained in Section 3.2.1.2. Evaluation of solar photodegradation and solar photocatalytic degradation processes for ROC_m and ROC_{ECm} treatment were taken into consideration. Solar photocatalytic degradation experiments were carried out using TiO_2, N-TiO_2, ZnO, and TiO_2/ZnO as the commercially available as well as synthesized photocatalysts. Influence of selected processes on the degradation profiles of ROC_m and ROC_{ECm} samples were evaluated in terms of specified and specific UV-vis parameters, fluorescence spectroscopic parameters, and organic carbon content as reported previously for other treatment processes.

4.4.1. Solar Photodegradation Processes

4.4.1.1. Solar photodegradation of ECs. Time dependent UV-vis absorption spectra of SMX and CMZ upon solar photodegradation process were presented in Figure 4.16. Although SMX gives maximum absorbance at around λ_{max}: 265 nm as the characteristic peak, solar photodegradation processes caused a slight shift of λ_{max} (± 9 nm) with respect to increasing irradiation period which could be attributed to the formation of phototransformation by-products of SMX as sulfanilic acid and sulfanilamide that give absorbance in this wavelength regions along with SMX (Willach et al., 2018). Under the same experimental conditions, characteristic sharp peak of CMZ at λ_{max}: 285 nm was still evident and displayed almost no change with respect to increasing solar irradiation periods. With respect to the changes attained in λ_{max} values of SMX at λ: 265 nm and CMZ at λ: 285 nm, corresponding concentration values were calculated by the equations 4.1 and 4.3.

Solar photodegradation of SMX ended up with only 22% removal of parent compound as well as 7% organic carbon removal following irradiation period of 90 min. SMX removal rate was found to be 0.0182 mg/L min for solar photodegradation whereas it was determined as 0.101 mg/L min for UVC photodegradation indicating superior efficiency of UVC irradiation in comparison to solar irradiation on the removal of SMX. The reason could be attributed to UV-vis absorption spectrum of SMX (Figure 4.1) that it absorbs irradiation from 190 nm up to 315 nm with λ_{max}: 265 nm, which is in accordance with the output of UVC lamp (λ_{max}: 254 nm) and slightly covering the irradiation supplied by the solar simulator ($\lambda_{rang}\varepsilon$: 290-700 nm). In addition, due to having monochromatic source of light at lower wavelength, energy supplied by the UVC lamp (I_o: $1.80x10^{17}$ quanta/sec) is expected

to be considerably higher than that of solar simulator (I_o: $1.73x10^{16}$ quanta/sec) therefore, UVC irradiation would be more efficient for breaking chemical bonds in selected ECs (Abellán et al., 2007; Gonzales et al., 2009; Nasuhoglu et al., 2011; Martinez-Costa et al., 2018). Although SMX removal under solar irradiation was found to be limited in comparison to UVC photodegradation process, similar photodegradation intermediates of SMX that were attained under UVC irradiation could also be observed under solar irradiation conditions. Sulfanilic acid, 3-amino-5-methylisoxazole and its hydroxylated analogues have been detected as phototransformation products of SMX under simulated solar light and presented in previous literature studies (Lam and Mabury, 2005; Niu et al., 2013; Gmurek et al., 2015). Additionally, as observed in UVC photodegradation experiments, solar photodegradation of SMX ended up with limited organic carbon removal which could be related to generated photoproducts that are less susceptible to solar photodegradation (Abellán et al., 2007). Moreover, another reason could be attributed to the UV-vis spectral features of photoproducts giving λ_{max} values in the wavelength region of 200-260 nm that does not lay within the spectral region of Xenon lamp in solar simulator (λ: 290-700 nm).

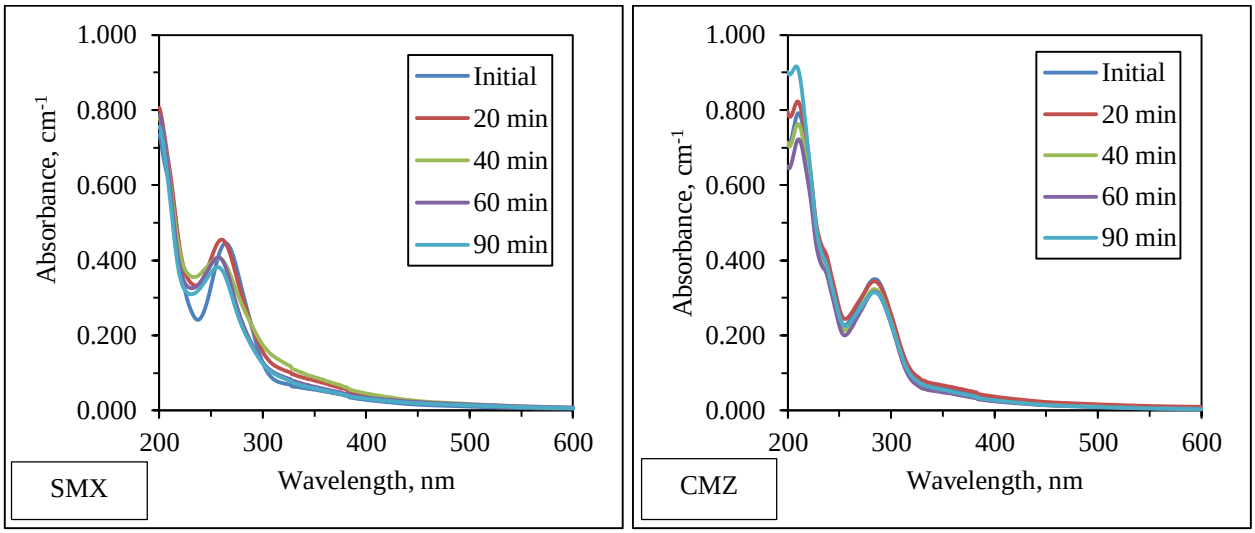

Figure 4.16. Time dependent UV-vis absorption spectra of SMX and CMZ upon exposure to solar photodegradation process (I_o: $1.73x10^{16}$ quanta/s).

Solar photodegradation of CMZ revealed 11% removal of parent compound and 16% removal of organic carbon content following irradiation period of 90 min indicating that CMZ has limited susceptibility to solar photodegradation as to UVC photodegradation as also reported by Achilleos and colleagues (Achilleos et al., 2010). CMZ removal rate was found to $4.9x10^{-3}$ mg/L min for solar photodegradation whereas it was determined as $1.89x10^{-2}$ mg/L min for UVC photodegradation indicating superior efficiency of UVC irradiation in comparison to solar irradiation on the removal of CMZ. The reason could be attributed to UV-vis absorption spectrum of CMZ (Figure 4.1) that it

absorbs irradiation from 200 nm up to 335 nm with λ_{max}: 285 nm which does not overlap with the maximum irradiation supplied by UVC lamp (λ_{max}: 254 nm) and slightly overlapping with the irradiation supplied by solar simulator (λ: 290-700 nm). Moreover, as has been mentioned in UVC photodegradation section (Section 4.3.1.1), CMZ is not prone to photodegradation with respect to its chemical and photochemical properties. Efficient degradation of CMZ could be achieved in the presence of reactive species or applying prolonged irradiation periods as reported by Kim (Kim, 2009). Upon exposure to simulated solar light, CMZ undergoes several reaction pathways to produce various intermediates which are also observed in UVC photodegradation process. Being regarded as one of the most common reaction intermediates of CMZ, 10,11-epoxycarbamazepine is expected to form via direct or indirect means in sunlit natural surface waters (Vogna et al., 2004; Lam and Mabury, 2005). Rearrangement of 10,11-epoxycarbamazepine would ended up with the formation of 9-acridinecarboxaldehyde whose further reactions give acridine and acridone respectively as previously explained in detail in Section 4.3.1.1 with respect to the results derived from previous literature findings (Lam and Mabury, 2005; Petrovic and Barceló, 2007; Calisto et al., 2011).

4.4.1.2. Solar photodegradation of ROC. All ROC samples were subjected to solar irradiation. Time dependent UV-vis absorption spectra of ROC_m and ROC_{ECm} samples exposing to solar photodegradation process are displayed in Figure 4.17. Removal efficiencies of the specified UV-vis parameters as well as NPOC contents of all ROC samples upon exposure to solar photodegradation process for t_{irr}: 90 min were presented in Table 4.4.

Table 4.4. Removal of specified UV-vis parameters as well as NPOC contents of ROC_m and ROC_{ECm} upon solar photodegradation process for t_{irr}: 90 min (I_o: $1.73x10^{16}$ quanta/s).

ROC sample	Removal, %				
	$Color_{436}$	UV_{365}	UV_{280}	UV_{254}	NPOC
ROC_{m1}	15	14	11	9	11
ROC_{m2}	6	5	4	3	6
ROC_{ECm1}	6	5	4	3	12
ROC_{ECm2}	9	8	5	4	7

Following solar photodegradation period of 60 min, ROC_{m1} revealed following removal efficiencies of 15% for $Color_{436}$, 14% for UV_{365}, 11% for UV_{280}, 9% for UV_{254}, and 11% NPOC whereas ROC_{ECm1} displayed following removal efficiencies as 6% for $Color_{436}$, 5% for UV_{365}, 4% for UV_{280}, 3% for UV_{254}, and 12% for NPOC. Under the same experimental conditions, ROC_{m2} displayed removal percentages as 6% for $Color_{436}$, 5% for UV_{365}, 4% for UV_{280}, 3% for UV_{254}, and

6% for NPOC. On the other hand, $Color_{436}$, UV_{365}, UV_{280}, UV_{254}, and NPOC removal efficiencies for ROC_{ECm2} were found to be 9%, 8%, 5%, 4%, and 7% respectively.

Overall removal efficiencies of specified UV-vis parameters and organic carbon content were found to be lower than the results attained for UVC photodegradation process. Since aromatic carbon absorbs energy in the wavelength region of 240-280 nm (Westerhoff et al., 2001), it does not overlap within the spectral range of solar simulator (λ_{range}: 290-700 nm) which could be the reason of lower removal efficiency under solar irradiation conditions. In addition, due to complex and high aromatic structure of humic substances present in ROC composition, prolonged irradiation periods, *i.e.* 6 hours are required for the breakdown of conjugated aromatic rings. However, organic and inorganic constituents of ROC_m and ROC_{ECm} samples are able to drive various photoinduced transformations. The major reactions on solar photodegradation of ROC_{m1} and ROC_{m2} are as follows: *i.* photodegradation of functional groups of DOM, such as aromatic rings, carboxylic groups, and phenolic groups, *ii.* formation of reactive species (RS) originating from direct (reaction 4.1) or indirect photolysis (reactions 4.2 and 4.3) of anions, such as NO_3^- (Zepp et al. 1987; Neta et al., 1988; Mack and Bolton, 1999), SO_4^{2-}, CO_3^{2-} (Neta et al., 1988), and Cl^- (Saran et al., 1999; Chiron et al., 2006) via below given reactions are also other major reaction pathways occurring during solar light initiated processes:

$$NO_3^- + h\nu\ (\lambda > 290\ nm) + H^+ \rightarrow HO^\bullet + NO_2^\bullet \quad (4.15)$$

$$Cl^- + HO^\bullet \leftrightarrow ClOH^{\bullet-} \quad (4.16)$$

$$CO_3^{2-} + HO^\bullet \rightarrow HO^\bullet + CO_3^{\bullet-} \quad (4.17)$$

$$HSO_4^- + HO^\bullet \rightarrow H_2O + SO_4^{\bullet-} \quad (4.18)$$

As a result of anion derived reactive species, photodegradation and photomineralization of humic-like components present in ROC_{m1} and ROC_{m2} were observed via the changes attained in specified UV-vis parameters and NPOC contents. On the other hand, in the presence of ROC_{ECm1} and ROC_{ECm2}, direct and/or indirect photolysis of ECs as well as their reaction intermediates also take place together with the reactions 4.13-4.16. Consequently, hindering effect of ECs on solar photodegradation of ROC could be clearly visualized by significant reduction attained for the removal of specified UV-vis parameters. $Color_{436}$, UV_{365}, UV_{280}, UV_{254} removal efficiencies of ROC_{ECm1} and ROC_{ECm2} were found to be three times lower than the results attained for ROC_{m1} and ROC_{m2}. On the other hand, organic carbon removal efficiencies of ROC_{ECm1} and ROC_{ECm2} was found to be almost the same values attained for ROC_{m1} and ROC_{m2}. UV-vis absorbance ratios at specified wavelengths, such as E2/E3 defined as the ratio of absorbance values at λ: 254 nm to λ: 365 nm would give

information about the changes attained in molecular weight of OM (Peuravuori et al., 1997; Del Vechhio et al., 2002; Helms et al., 2008; Sharpless et al., 2014). Upon exposure to solar photodegradation, E2/E3 ratio of ROC_{m1} and ROC_{m2} tend to increase slightly which could be attributed to slight photodegradation of conjugated aromatic rings present in humic structure as a result of reactions with reactive species originated from direct and/or indirect photolysis of anions. On the other hand, in the presence of ROC_{ECm1} and ROC_{ECm2} E2/E3 ratios were slightly decreased with respect to increasing irradiation period indicating presence of aromatic rings even after exposure to solar photodegradation as previously reported by Mostafa and Rosario-Ortiz (Mostafa and Rosario-Ortiz, 2013).

Moreover, it has been previously reported that presence of Fe has a significant effect on photodegradation and photobleaching of DOM under acidic conditions which could be the reason of enhancement in removal efficiencies of all parameters via photo-Fenton process irrespective of ROC samples (Porcal et al., 2014). Furthermore, enhancing effect of Cl^- on Fe(III)-induced photoreactions for the removal of CMZ could be regarded as another important factor. As a result of charge transfer reactions induced by Fe(III) colloids, Cl^- is able to oxidized to $Cl^{\bullet}$/ $Cl_2^{\bullet-}$ as follows:

$$\equiv Fe^{III}\text{-}OH + Cl^- + h\nu \rightarrow Fe^{2+} + OH^- + Cl^{\bullet} \quad (4.19)$$

$$Cl^- + Cl^{\bullet} \leftrightarrow Cl_2^{\bullet-} \quad (4.20)$$

The radical $Cl_2^{\bullet-}$ is capable of CMZ degradation faster than Fe(III) colloids in the absence of Cl^-. By this way, limitation to the photodegradation of organic substrates by Fe (III) colloids could be overcome by photogenerated co-oxidant $Cl_2^{\bullet-}$ (Chiron et al., 2006).

Another impact of Cl^- could be attributed to the formation of different transformation by-products. Upon exposure to photo-Fenton reaction under acidic conditions, in addition to common reaction intermediates of CMZ, that are known to be 10-hydroxycarbamzepine, hydroxyacridine-9-carboxaldehyde, acridine, and acridone, presence of Cl^- and Fe (III) could come up with the formation of different by-products, such as chloro-10-hydroxycarbamazepine and its further oxidation intermediates (Chiron et al., 2006). Since ROC_{ECm} contains significant amount of Cl^-, formation of these by-products are also expected in photo-Fenton treatment of ROC_{ECm}. Reduction on NPOC removal efficiencies of ROC_{ECm1} and ROC_{ECm2} in comparison to ROC_{m1} and ROC_{m2} could be attributed to formation of these additional by-products that tend to scavenge ROS, therefore hinders overall organic carbon removal efficiency.

Moreover, absorbing a large portion of photons, DOM is regarded as a potential photosensitizer. It has been previously proposed and reported that singlet oxygen, superoxide ion/hydroperoxyl radicals, hydroxyl radicals and organic peroxy radicals can be generated in natural waters under natural sunlight condition (Zafiriou and True, 1979; Zepp et al., 1981; Zepp et al., 1985; Haag and Hoigné, 1984 and 1986; Cooper et al., 1988; Hoigné et al., 1989; Cooper et al., 1989; Vaughan and Blough, 1998). Therefore, efficient removal of NPOC even in ROC_{ECm1} and ROC_{ECm2} could be related to additional removal of parent compounds (SMX and CMZ) as well as their phototransformation intermediates with the contribution of photosensitizing effect of DOM. With respect to the results attained in previous literature studies, presence of DOM could enhance removal of other organic micropollutants which could be attributed to presence of reactive species derived from photosensitizing effect of DOM present in reaction medium (Andreozzi et al., 2003; Pereira et al., 2007; Matatmoros et al., 2009; Dong et al., 2015).

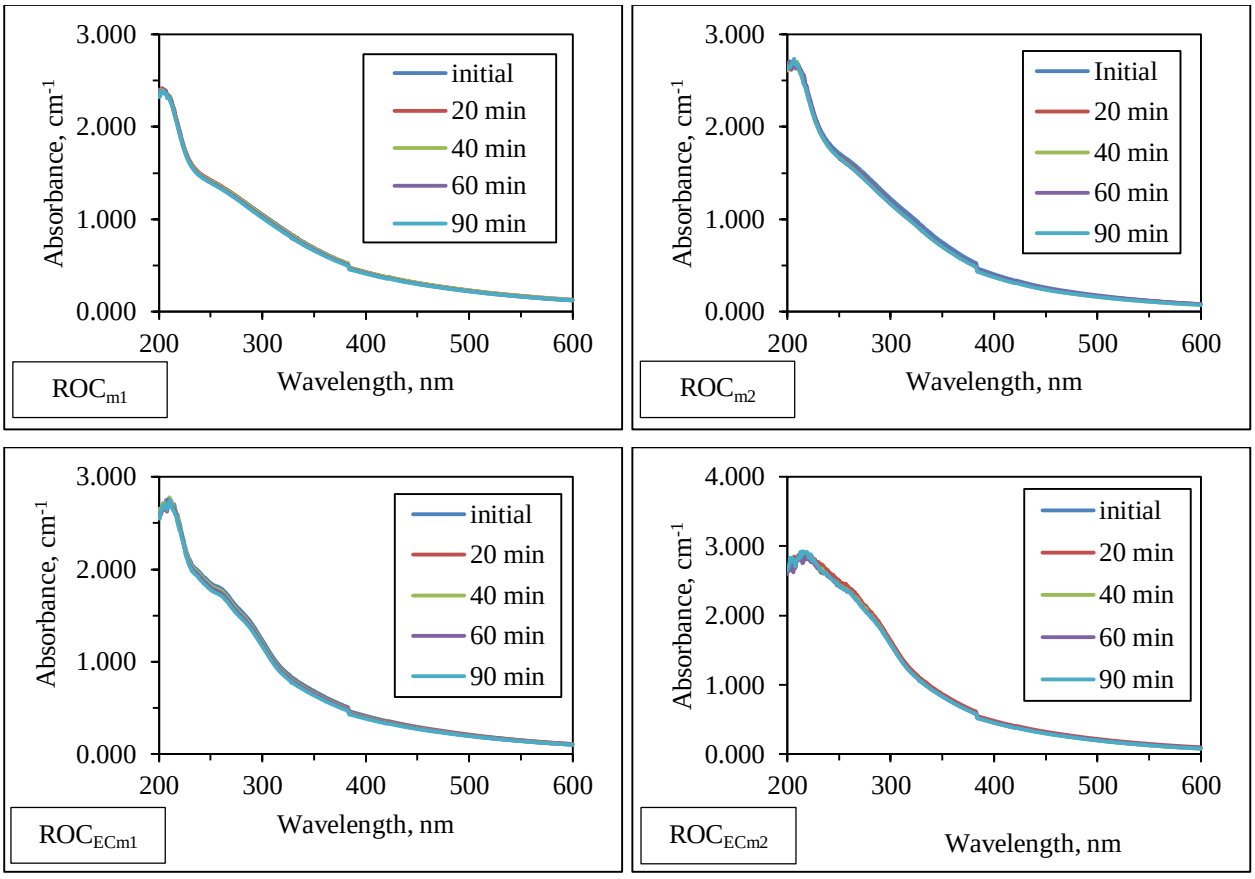

Figure 4.17. Time dependent UV-vis absorption spectra of ROC_m and ROC_{ECm} upon solar photodegradation (I_o: $1.73x10^{16}$ quanta/s).

Further spectroscopic evaluation of ROC_m and ROC_{ECm} samples with respect to solar photodegradation was assessed in terms of fluorescence spectroscopy acquired in synchronous scan mode and EEM modes as presented in figures 4.18 and 4.19 respectively. Time dependent

synchronous scan fluorescence spectra of ROC_m and ROC_{ECm} samples displayed slight intensity changes. Characteristic humic-like peaks at λ_{emis}: 380 nm and λ_{emis}: 470 nm were reduced with respect to increasing solar irradiation periods whereas shape of the peaks did not change significantly. Presence of various functional groups could either cause a decrease (*i.e.* carboxyl) or increase (*i.e.* amine and hydroxyl) in fluorescence intensity of the samples as a result of electron withdrawing or donating properties of these functional groups (Westerhoff et al., 2001; Świetlik and Sikorska, 2004). Reduction of intensities could be related to the break-up of molecules into smaller fragments.

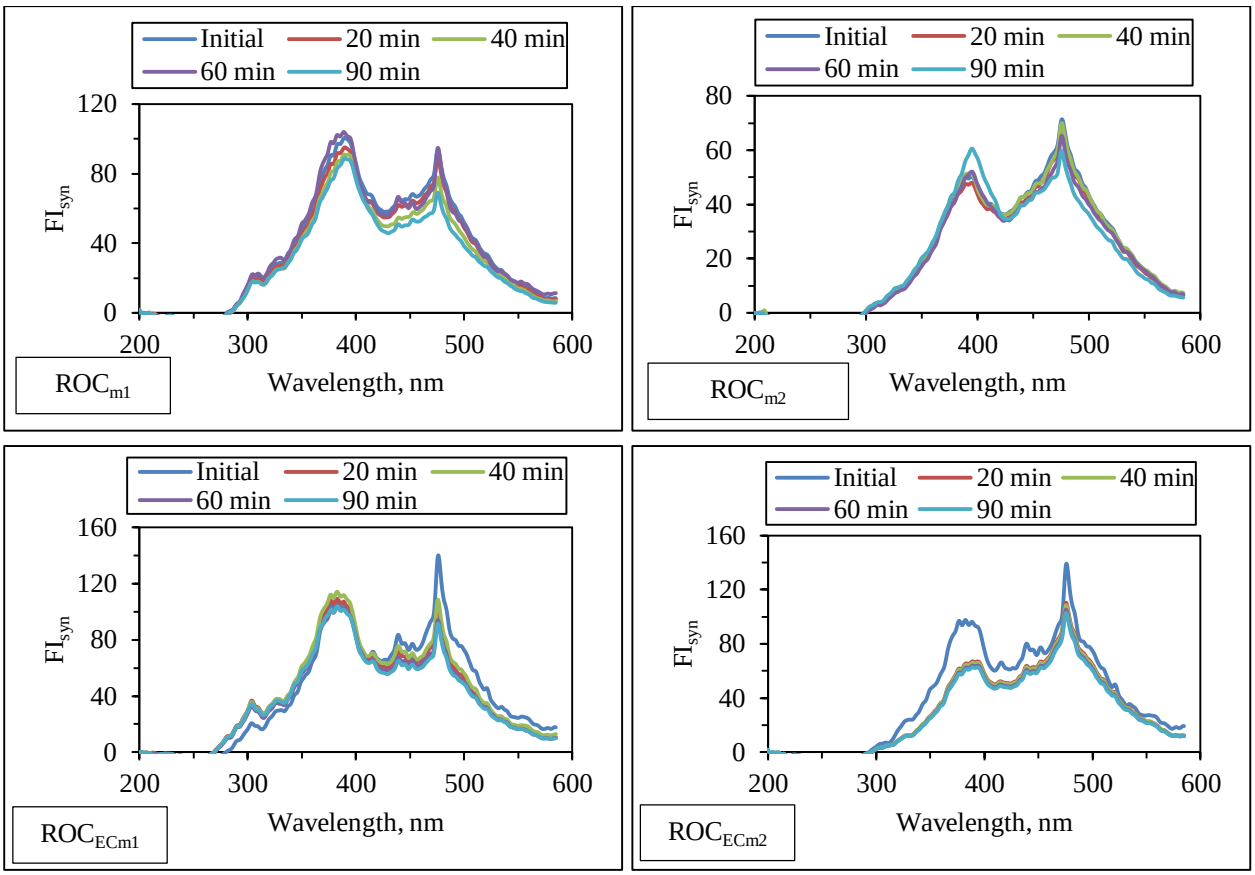

Figure 4.18. Time dependent synchronous scan fluorescence spectra of ROC_m and ROC_{ECm} upon exposure to solar photodegradation (I_o: $1.73x10^{16}$ quanta/s).

Following solar photodegradation period of 90 min, 28% and 16% reduction in FI_{syn} was achieved for ROC_{m1} and ROC_{m2}, whereas 26% and 16% reduction was obtained for ROC_{ECm1} and ROC_{ECm2} indicating that presence of ECs did not cause any substantial change in FI_{syn} values corresponding to humic specific region (λ_{emis}: 470 nm) due to presence of humic-like components with higher degree of aromaticity and high molecular weight in this region. However, NPOC normalized values of FI_{syn} namely SFI_{syn} revealed removal efficiencies of 18% for ROC_{m1}, 6% for ROC_{m2}, 12% for ROC_{ECm1} and 3% for ROC_{ECm2} indicating that under the same experimental conditions, changes in organic carbon content revealed distinct trend than the changes attained for

fluorophores representing high molecular weight humic-like components. On the other hand, second characteristic sharp peak at 380 nm displayed gradual increase with respect to increasing irradiation periods for ROC_{m1} and ROC_{m2}. The reason could be attributed to transformation of higher molecular weight humic compounds giving fluorescence intensity at 470 nm into lower molecular weight humic-like or fulvic-like compounds by the contribution of RS produced by solar photolysis of anions present in ROC composition (Uyguner and Bekbolet, 2005a, b, and c; Uyguner-Demirel and Bekbolet, 2011).

Emergence of new humic-like and fulvic-like fluorophores could be noticeably observed for EEM fluorescence contour-plots of ROC_{m1}, ROC_{m2}, and ROC_{ECm1} upon exposure to solar photodegradation (Figure 4.18). The reason could be attributed to phototransformation of larger molecular size humic-like fluorophores into lower molecular size humic-like fluorophores and/or into lower molecular size fulvic-like fluorophores via attack of anion derived reactive species (Sen-Kavurmaci and Bekbolet, 2015).

Even following photodegradation period of 90 min, significant amount of NPOC (12.38 mg/L for ROC_{m1}, 17.51 mg/L for ROC_{m2}, 19.89 mg/L for ROC_{ECm1}, and 23.2 mg/L for ROC_{ECm2}) is still present in all ROC samples indicating eminence of high molecular weight humic compounds with higher degree of aromaticity. Therefore, presence of humic compounds with their highly substituted aromatic structures causes inter and/or intramolecular bonding and self-quenching ending up with lower fluorescence intensities. Moreover, since high molecular weight humic macromolecules are still evident even prolonged irradiation periods, they tend to mask SMX related fluorophores which give maxima at Ex/Em: 210-290/350 nm with respect to lower molecular size of these fluorophores (1-5 kDa).

Upon exposure to solar photodegradation for t_{irr}: 90 min, SFI_{syn} values were reduced from 6.60 to 5.45 for ROC_{m1}, from 4.85 to 4.57 for ROC_{m2}, from 3.42 to 2.38 for ROC_{ECm1}, and from 2.23 to 2.17 for ROC_{ECm2}. Since SFI_{syn} values represents NPOC normalized fluorescence intensities at λ_{emis}: 470 nm, change in this parameter reveals alterations, *i.e.* removal and/or production of humic-like fluorophores under oxidative and non-oxidative conditions. The most noticeable changes in SFI_{syn} were attained for ROC_{m1} and ROC_{ECm1} which could be attributed to transformation of high molecular weight humic fluorophores into lower ones. On the other hand, ROC_{m2} expressed lower SFI_{syn} removal efficiency in comparison to ROC_{m1} and ROC_{ECm1} indicating the most irrelevant change in humic fluorophores. The observed change in shape and intensity of EEM contour-plot of ROC_{ECm2} was attributed to almost no change in SFI_{syn} representing no alteration in humic fluorophores.

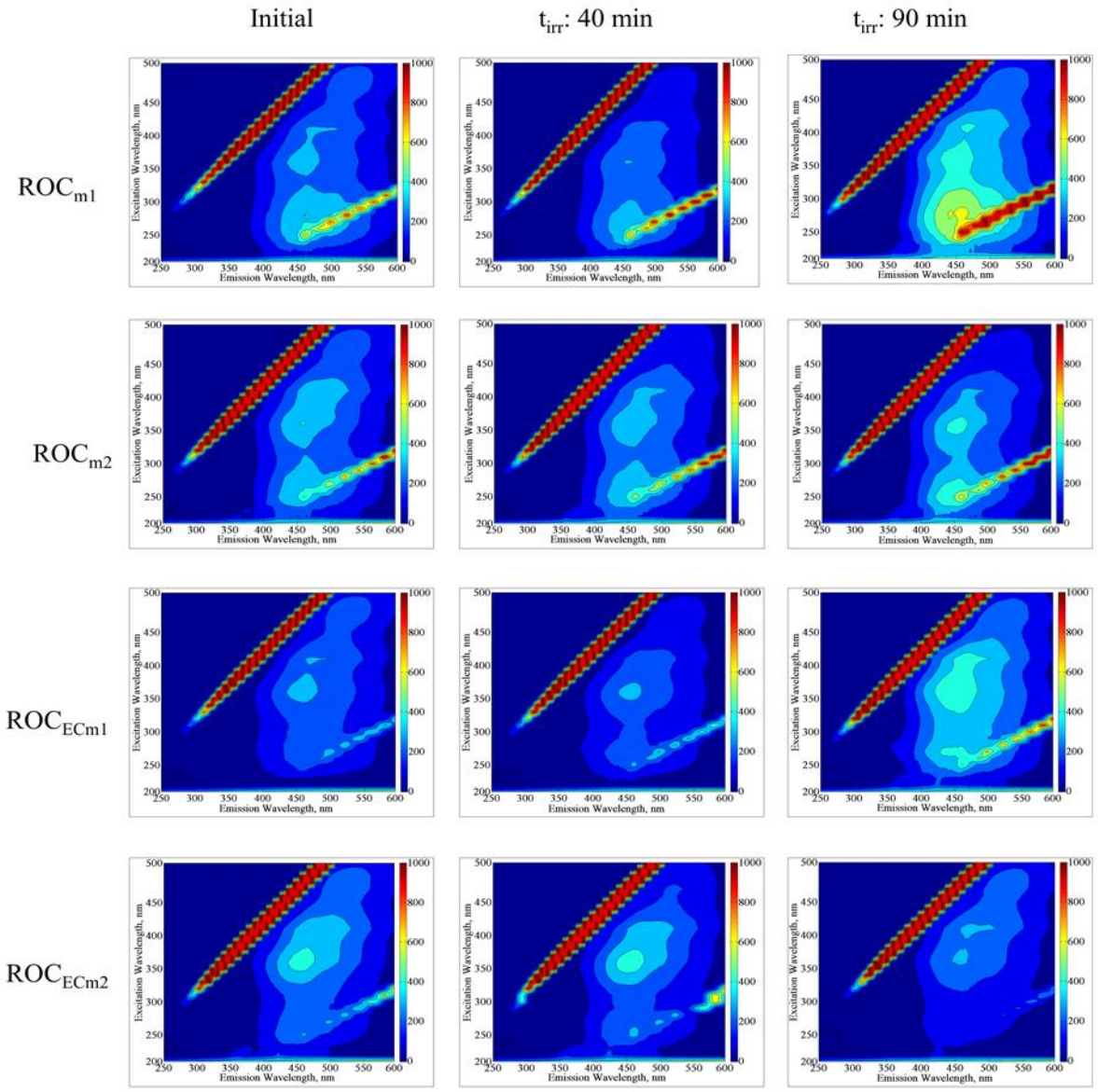

Figure 4.19. EEM fluorescence contour-plots of ROC_m and ROC_{ECm} prior to and following solar photodegradation (I_o: $1.73x10^{16}$ quanta/s, t_{irr}: 40 min and 90 min).

An overall evaluation with respect to irradiation sources were proceeded for comparison purposes. Although NPOC removal efficiencies of ROC_{m1} and ROC_{m2} samples did not express significance, UV_{254} removals displayed noticeable differences under UVC and solar irradiation conditions which could be attributed to susceptibility of UV absorbing centers of HM at λ: 254 nm upon exposure to UVC irradiation. On the other hand, under solar irradiation conditions, mineralization extent was found to me more than UVC photodegradation conditions. The reason could be attributed to consumption of solar light initiated RS by ECs and their phototransformation by-products rather than HM in ROC_{ECm1} and ROC_{ECm2}. It should also be emphasized that solar photodegradation of ECs, ROC_m, and ROC_{ECm} revealed baseline information for solar photocatalytic degradation processes in order make further evaluation under the same experimental conditions.

4.4.2. Solar Photocatalytic Degradation Processes

4.4.2.1. Solar photocatalytic degradation of ECs. Solar photocatalytic degradation of SMX and CMZ using selected photocatalysts were performed and the removal efficiencies of the parent compounds were presented (Figure 4.20). In general, approximately more than 50% removal of ECs were attained upon t_{irr}: 20 min. Moreover, up to 80% removal of both ECs was reached upon t_{irr}: 90 minutes using TiO_2, N-TiO_2, ZnO, and TiO_2/ZnO nanocomposite. From a general perspective, it could be deduced that although earlier stages of solar photocatalysis displayed different trends, negligible differences were observed among the removal efficiencies of the applied photocatalysts for the removal of selected ECs following photocatalytic irradiation period of 90 min.

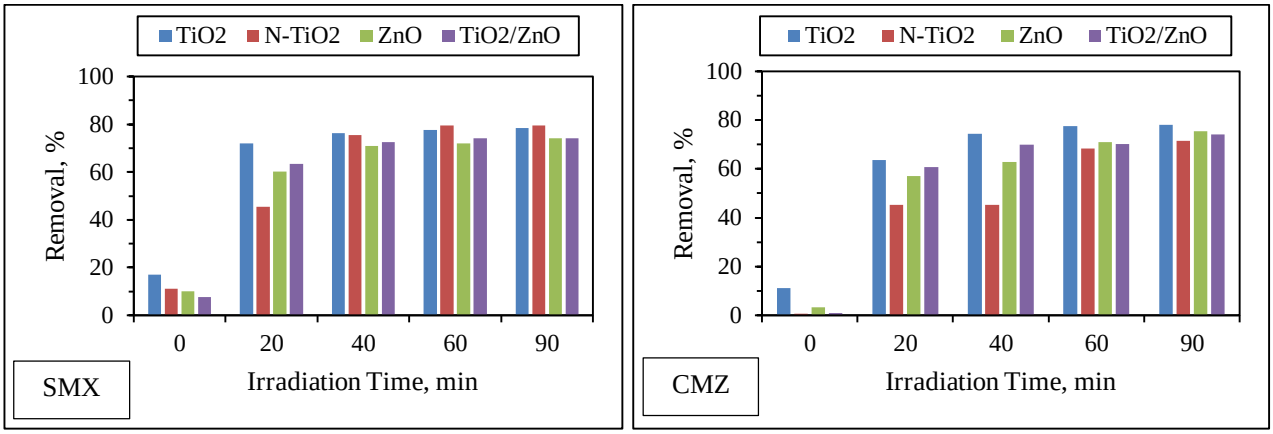

Figure 4.20. Photocatalytic removal efficiencies of SMX and CMZ using selected photocatalyst specimens. 0 indicated initial adsorptive removals under dark conditions (I_o: $1.73x10^{16}$ quanta/s).

With respect to the surface oriented mechanism of photocatalytic degradation process, initial adsorption of substrate onto photocatalyst surface plays a crucial role. It could be deduced from Figure 4.20 that initial adsorption percentage of SMX was found to be 18% for TiO_2, 11% for N-TiO_2, 10% for ZnO, and 8% for TiO_2/ZnO. Surface interactions between the substrate and photocatalysts are strongly dependent on their ionic state in reaction medium. Moreover, ionic state of the target pollutants also has primary importance on its reactivity as well as on its photochemical behavior with respect to pH. SMX has two pK_a values as pK_{a1}: 1.6 and pK_{a2}: 5.7 (Table 4.1) indicating that SMX has cationic form if pH < 1.6, and anionic form if pH > 5.7. Since working solution of SMX has pH value in the range of 5.5-6.0, majority of the SMX is expected to be present in anionic form (Abellán et al., 2007). Since almost all photocatalysts except N-TiO_2 are positively charged under the experimental conditions due to their pH_{zpc} values (Table 4.3), adsorption of negatively charged SMX onto the photocatalysts would be expected. However, despite their protonated state, initial adsorption percentage of ZnO and TiO_2/ZnO was found to be comparatively lower than TiO_2.

The reason could be attributed to specific surface area of ZnO (37 m^2/g) and TiO_2/ZnO (31 m^2/g) which are considerably lower than TiO_2 (55 m^2/g) therefore supplying less area for SMX to be adsorbed on the surface of the photocatalyst even in the presence of fixed photocatalyst concentration of 0.25 mg/mL.

Following solar irradiation period of 90 min, only 22% SMX removal and 6% NPOC removal were achieved via solar photodegradation process, whereas solar photocatalytic degradation process revealed up to 80% removal of the parent compound as well as 36-84% NPOC removal which could be principally related to the generation of ROS, predominantly $HO^{\bullet}$, via solar light driven photocatalysis using TiO_2, N-TiO_2, ZnO, and TiO_2/ZnO. Presence of $HO^{\bullet}$ gives more satisfactory results on the removal of carbon content compared to solar photodegradation process which could be ascribed to the removal of degradation by-products of ECs that are not susceptible to photodegradation (Gonzáles et al., 2009; Nasuhoglu et al., 2011). Removal efficiency of SMX displayed differences within the first 20 min of irradiation period for each photocatalyst, however following irradiation period of 40 min and further periods more than 70% SMX removal was achieved in the presence of all photocatalysts. The reason could be attributed to the accumulation of reaction intermediates during the first 30-40 min of irradiation period, however photocatalytic removal of parent compound as well as these intermediates could be achieved within 60 min of reaction period (Hu et al., 2007). The major transformation pathways of SMX via solar photocatalytic degradation process is based on hydroxylation, isoxazole ring oxidation and hydrolysis processes (Abellán et al., 2007; Hu et al., 2007; Nasuhoglu et al., 2011; Yang et al., 2017). In addition to direct photolysis, $HO^{\bullet}$ attack could end up with the formation of sulfanilic acid, 3-amino-5-methylisoxazole and its hydroxylated analogues (Lam and Mabury, 2005; Hu et al., 2007; Nasuhoglu et al., 2011; Borowska et al., 2019). Moreover, it has been previously reported that breaking of sulfonamide bond via $HO^{\bullet}$ attack also generates various transformation by-products of SMX as a result of photocatalytic degradation process using titanium and silver-doped nanocomposites (Xu et al., 2012).

Pseudo first-order kinetic model was applied to the time dependent SMX solar photocatalytic removal data. Kinetic constants (k, min^{-1}) for SMX were calculated as $2.27x10^{-2}$ min^{-1} for TiO_2, $2.78x10^{-2}$ min^{-1} for N-TiO_2, $2.07x10^{-2}$ min^{-1} for ZnO and $2.17x10^{-2}$ min^{-1} for TiO_2/ZnO. Kinetic constants for solar photocatalytic degradation of SMX were found to be insignificantly different irrespective of the photocatalyst specimen used which could be attributed to the major degradation mechanism of SMX that is based on photolysis. It could be inferred from kinetic data that ZnO and TiO_2/ZnO photocatalysts were found to be slightly more efficient than TiO_2 and N-TiO_2 for the removal of SMX as the parent compound. On the other hand, kinetic rate constants were found to be

for NPOC removal were: $1.95x10^{-2}$ min^{-1} for TiO_2, $1.81x10^{-2}$ min^{-1} for N-TiO_2, $0.51x10^{-2}$ min^{-1} for ZnO, $0.91x10^{-2}$ min^{-1} and TiO_2/ZnO indicating superior mineralization efficiency of TiO_2 and N-TiO_2 in comparison to ZnO and TiO_2/ZnO. Previous literature findings were indicated that photocatalytic degradation of SMX could reach complete removal of the parent compound within 60 min of irradiation period using various metal and non-metal doped TiO_2 specimens, however under the same conditions, overall mineralization efficiency was found to be <50% (Borowska et al., 2019). Under the same experimental conditions, photocatalytic irradiation period of 90 min ended up NPOC removal efficiencies as 84% for TiO_2, 79% for N-TiO_2, 36% for ZnO, and 53% for TiO_2/ZnO. Consequently, it could be concluded that TiO_2 and N-TiO_2 are able to remove both parent compound and its transformation by-products by revealing higher efficiency of overall mineralization. On the other hand, in the presence of ZnO and TiO_2/ZnO nanocomposite, mineralization extent was found to be limited indicating accumulation of transformation by-products in the reaction medium.

In a similar manner attained for photocatalytic degradation of SMX, surface interactions between CMZ and the photocatalysts were evaluated in terms of their ionic states under working natural pH conditions. CMZ has a pK_a value of 13.9 (Table 4.1), therefore it would have cationic form if pH < 13.9, and anionic form if pH > 13.9. Consequently, almost all CMZ is expected to be in protonated form at the pH of working solution (~ 5.5-6.0). Regarding their pH_{ZPC} values, ZnO (8.96) and TiO_2/ZnO nanocomposite (7.69) would present positively charged, N-TiO_2 (6.23) and TiO_2 (6.25) would be negatively charged. Insignificant initial adsorption percentages of CMZ onto ZnO (3%) and TiO_2/ZnO (1%) could be attributed to the charge-charge repulsion mechanism between the substrate and photocatalyst specimens due to their protonated state.

Upon exposure to solar irradiation period of 90 min, only 11% CMZ removal and 16% NPOC removal were achieved via solar photodegradation process, whereas for the same period of reaction, > 70% removal of the parent compound as well as 34-83% NPOC removal were attained by solar photocatalytic degradation process. The reason could be attributed to $HO^{\bullet}$ dependent degradation of CMZ with respect to its chemical and photochemical properties (Kim, 2009; Achilleos et al., 2010; Martínez et al., 2011; Ali et al., 2018). Following solar photocatalysis, CMZ removal efficiency profiles displayed differences within the first 40 min of irradiation period for each photocatalyst, however following irradiation period of 60 min and further periods, up to 70% CMZ removal was achieved in the presence of all photocatalysts. The reason could be attributed to the immediate formation of reaction intermediates of CMZ as a result of $HO^{\bullet}$ attack. Accumulation of these intermediates in the reaction medium might cause a retardant effect on the degradation of parent compound which could be overcome by applying prolonged irradiation periods. Efficient removal of

CMZ in the presence of TiO_2 indicated its higher efficiency for the removal of CMZ as the parent compound as well as its derivatives in comparison to N-TiO_2, ZnO, and TiO_2/ZnO specimens as previously reported by Haroune and colleagues (Haroune et al., 2014).

Pseudo first-order kinetic constants for CMZ removal were calculated as k: $1.53x10^{-2}$ min^{-1} for TiO_2, $1.36x10^{-2}$ min^{-1} for N-TiO_2, $1.41x10^{-2}$ min^{-1} for ZnO and $1.31x10^{-2}$ min^{-1} for TiO_2/ZnO nanocomposite. With respect to its surface oriented mechanism, photocatalytic degradation process could be affected by initial adsorption of the substrate onto the photocatalyst. However, initial adsorption percentages of CMZ onto N-TiO_2, ZnO, and TiO_2/ZnO were found to be negligible (<5%) indicating the major mechanism of the removal of substrate is based on the $HO^{\bullet}$ attack (Achilleos et al., 2010). In addition, kinetic constants of NPOC removal of CMZ were achieved; $2.05x10^{-2}$ min^{-1} for TiO_2, $4.32x10^{-3}$ min^{-1} for N-TiO_2, $1.16x10^{-2}$ min^{-1} for ZnO and $1.31x10^{-2}$ min^{-1} for TiO_2/ZnO. Differences between organic carbon removal kinetics and parent compound kinetics for different photocatalysts could be attributed to the formation of photocatalyst specified transformation by-products. Upon exposure to ROS attack originating from photocatalysis, common transformation by-products of CMZ, such as hydroxycarbamazepine, dihydroxycarbamazepine, acridine-9-carbaldehyde, hydroxyacridine-9-carbaldehyde, acridine and acridone were tentatively detected and reported through the literature (Doll and Frimmel, 2004 and 2005; Aparicio et al., 2019). It's been previously presented that formation of reaction intermediates of CMZ could be photocatalyst type specific and may be differed from each other in the presence of TiO_2 and ZnO. Under the same experimental conditions, photocatalytic degradation of CMZ revealed seven different identified by-products in the presence of TiO_2, whereas only three by-products were detected in the presence of ZnO (Martínez et al., 2011). Therefore, depending on the photocatalyst used, removal profiles of parent compound as well as its by-products may be different. Under the same conditions, photocatalytic irradiation period of 90 min ended up with NPOC removal efficiencies of 83% for TiO_2, 34% for N-TiO_2, 69% for ZnO, and 70% for TiO_2/ZnO indicating by-product formation differences as well as their removal mechanisms. Regarding previous literature findings, TiO_2 was found to be an efficient photocatalyst not only for the removal of CMZ as the parent compound, but also for its derivatives (Haroune et al., 2014) as also observed and reported in this study.

4.4.2.2. Photocatalytic degradation of ROC samples. Photocatalytic degradation of organic matter present in all ROC samples were modeled by pseudo first-order kinetic model (R^2>0.70) as presented in Table 4.5. Since the major organic fraction of ROC samples is composed of humic-like components, specified UV-vis parameters ($Color_{436}$, UV_{365}, UV_{280}, and UV_{254}) were used for the UV-

vis spectral differentiation of humic substances (Uyguner-Demirel and Bekbolet, 2011). UV_{254} is widely used as a surrogate parameter for organic carbon content in water and wastewaters (Uyguner-Demirel and Bekbolet, 2011). In addition to UV_{254}, UV_{280} and UV_{365} also represent aromaticity of organic components and their functional groups whereas $Color_{436}$ indicates the presence of color forming moieties known as chromophoric groups with conjugated double bonds and heteroatoms with lone pair electrons (Uyguner and Bekbolet, 2005; Uyguner-Demirel and Bekbolet, 2011). Changes in these parameters would bring further understanding on the discrimination between photocatalytic degradation profiles of ROC_m (comprising only humic-like matter as the organic matrix) and ROC_{ECm} (having humic-like matter as well as ECs as the organic matrix).

Table 4.5. Pseudo first-order kinetic evaluation of photocatalytic degradation of ROC_m and ROC_{ECm} (Photocatalyst dose: 0.25 mg/mL, I_o: $1.73x10^{16}$ quanta/s).

Photocatalyst /ROC	Rate constant, $kx10^{-2}$, min				
	$Color_{436}$	UV_{365}	UV_{280}	UV_{254}	NPOC
TiO_2					
ROC_{m1}	2.22	2.22	2.39	2.37	1.97
ROC_{m2}	2.32	2.25	2.24	2.14	1.43
ROC_{ECm1}	1.57	1.26	1.33	1.17	0.821
ROC_{ECm2}	1.86	1.56	1.53	1.42	0.701
N-TiO_2					
ROC_{m1}	2.16	1.87	1.64	1.50	1.03
ROC_{m2}	1.26	1.02	0.757	0.671	0.615
ROC_{ECm1}	1.19	0.922	0.574	0.536	0.901
ROC_{ECm2}	0.771	0.592	0.354	0.325	0.361
ZnO					
ROC_{m1}	0.835	0.694	0.576	0.536	0.907
ROC_{m2}	0.673	0.575	0.458	0.413	0.676
ROC_{ECm1}	0.933	0.772	0.478	0.411	0.408
ROC_{ECm2}	0.628	0.491	0.309	0.272	0.318
TiO_2/ZnO					
ROC_{m1}	2.05	1.73	1.36	1.25	0.988
ROC_{m2}	1.38	1.21	1.02	0.968	0.461
ROC_{ECm1}	1.84	1.51	0.894	0.871	0.765
ROC_{ECm2}	0.621	0.524	0.359	0.351	0.281

Kinetic constants calculated for ROC_{ECm1} and ROC_{ECm2} were found to be lower in comparison to ROC_{m1} and ROC_{m2}. Due to its surface oriented mechanism of photocatalysis, initial adsorption of substrate compound onto photocatalysts would play certainly important role during the treatment. Reduction of kinetic constants in the presence of ECs in ROC_{ECm1} and ROC_{ECm2} could be explained by extent of initial adsorption condition. Initial adsorption of NPOC onto TiO_2 was found to be 43% for ROC_{m1}, 20% for ROC_{ECm1}, 37% for ROC_{m2} and 12% for ROC_{ECm2}. In the presence of TiO_2/ZnO, initial adsorption of NPOC was 51% for $ROC_{m1,}$ 39% for ROC_{ECm1}, 5% for ROC_{m2} and 4% for ROC_{ECm2}. TiO_2, N-doped TiO_2, ZnO and TiO_2/ZnO exhibited surface area values of 55 m^2/g, 56 m^2/g, 37 m^2/g, and 31 m^2/g respectively as previously presented in Table 4.3. No direct correlation could

be assessed in between initial adsorption extent of substrates and respective exposed surface area of the photocatalyst specimens. It should be indicated that the role of HM is to predominate over amount of surface coverage extent due to its high molecular weight structure with larger number of functional groups (therefore having more binding opportunities) in comparison to lower molecular weight compounds, resulting in efficient photocatalytic degradation. The compositional and structural differences of HM could be displayed by the presence of oxidized humic sub-fractions constituting the majority of ROC_{m2} and ROC_{ECm2} in comparison to non-degraded and more uniformly distributed fractions of organic matrix in ROC_{m1} and ROC_{ECm1} (Table 4.2). Different adsorption behaviors onto photocatalysts indicated the competition between HM and ECs present in ROC composition (Georgaki et al., 2014). Presence of ECs in solution matrix could resulted in diverse competitive reactions between organics present in ROC composition towards reactive oxygen species (ROS) (Uyguner-Demirel et al., 2017). As an inner effect, matrix of ECs under photocatalytic conditions revealed kinetic constants ($kx10^{-2}$, min^{-1}) for SMX following the order of photocatalyst type as TiO_2>ZnO>TiO_2/ZnO>N-TiO_2 and for CMZ as TiO_2>TiO_2/ZnO>ZnO≥N-TiO_2.

Solar photocatalytic degradation of ROC samples displayed photocatalyst specified differences in mineralization kinetics expressed as NPOC removal. In the presence of TiO_2 and ZnO insignificant differences in k values of NPOC removal was attained for ROC_{m1} and ROC_{m2} that were different from each other in terms of organic carbon content as well as molecular weight. On the other hand, in the presence of similar HM composition, presence of ECs caused noticeable reduction by revealing half of k values attained for ROC_{m1} and ROC_{m2} in comparison to ROC_{ECm1} and ROC_{ECm2}. The reason could be attributed to generation of photocatalytic reaction intermediates of SMX and CMZ hindering overall mineralization efficiency. On the other hand, N-TiO_2 and TiO_2/ZnO revealed k values for ROC_{m2} were found to be two times lower than results attained for ROC_{m1} indicating the influence of organic carbon content as well as molecular size distribution on photocatalyst activity. Higher molecular weight humic components with higher organic carbon content tend to reduce catalytic active sites of the photocatalyst. In addition, surface coverage by HM would enhance light attenuation of photocatalyst specimens therefore hindering photocatalytic activity (Qiao et al., 2002). Consequently, photocatalytic degradation profiles of ROC_m and ROC_{ECm} samples could be regarded photocatalyst type specific for the removal of organic carbon content comprised of both HM, ECs as well as photodegradation/photocatalytic degradation by-products of ECs.

Photocatalysis of several ECs were investigated under various synthetic solution matrices in which commercial NOM analogs were employed (Choi et al., 2014), lake water samples (Doll and Frimmel, 2005), in real wastewater and even groundwater samples (Jelic et al., 2013). The common

conclusion represented that presence of ECs as well as organic carbon content could indicate a retardation effect on the photocatalytic degradation of those compounds via several mechanisms, such as competition between ECs and other organic components for ROS, inner filter effects, light scattering/absorption of NOM, and even surface deactivation of the applied catalysts. Noticeable reduction in kinetic constants of ROC samples in the presence of ECs has proven the effect of above given mechanisms under the specified experimental conditions. ROC_{ECm1} and ROC_{ECm2} displayed differences from each other with regard to humic components as well as organic carbon content (initial NPOC contents were 19.2 mg/L and 28.5 mg/L respectively). NPOC removal kinetic constants were significantly reduced with respect to the increase in organic carbon content of OM, generation of degradation by-products of ECs as well as complexity of the organic matrix (Table 4.2).

Photocatalysis of ROC_{m1} displayed similar pseudo first-order kinetic constants (k, min^{-1}) for $Color_{436}$, UV_{254}, and NPOC following the order of TiO_2>N-TiO_2>TiO_2/ZnO>ZnO. Kinetic constants for ROC_{m2} were found to be in the decreasing order of TiO_2>TiO_2/ZnO>N-TiO_2>ZnO for $Color_{436}$ and UV_{254} whereas the order changed as TiO_2>ZnO>N-TiO_2>TiO_2/ZnO for NPOC. For the photocatalytic degradation kinetics of ROC_{ECm1}, removal of all parameters displayed different orders of k as follows; $Color_{436}$: TiO_2/ZnO>TiO_2>N-TiO_2>ZnO, UV_{254}: TiO_2>TiO_2/ZnO>N-TiO_2>ZnO, and NPOC: N-TiO_2>TiO_2>TiO_2/ZnO>ZnO. ROC_{ECm2} displayed k values for $Color_{436}$ and NPOC in the following order of TiO_2>N-TiO_2>TiO_2/ZnO>ZnO whereas for UV_{254} removal it was found to be in the order of TiO_2>TiO_2/ZnO>N-TiO_2>ZnO. From a general perspective, UV_{365} and UV_{280} displayed slight variations in kinetic constants in between the removals of color forming moieties and UV absorbing centers of organic matrix. Minor effect of ECs (λ_{max}: 265 nm for SMX and 285 nm for CMZ) could also be visualized by insignificant differences in UV_{280} removals.

Considering the NPOC removal kinetics, photocatalyst specimens displayed following order as TiO_2>N-TiO_2>TiO_2/ZnO>ZnO for ROC_{m1} and N-TiO_2>TiO_2>TiO_2/ZnO>ZnO for ROC_{ECm1}. For ROC_{m2} and ROC_{ECm2}, k values gave the order of TiO_2>ZnO>N-TiO_2>TiO_2/ZnO and TiO_2>N-TiO_2>TiO_2/ZnO>ZnO. TiO_2/ZnO expressed lower efficiency in comparison to TiO_2 although an enhancement was expected due to electron transfer occurring from conduction band of ZnO to conduction band of TiO_2 while hole transfer taking place from valence band of TiO_2 to valence band of ZnO ending up with an increase in lifetime of the charge carriers (Janitabaer-Darzi et al., 2009). In addition, the role of humic sub-fractions as the disturbing factor on colloidal stability photocatalyst specimens could be ended up with possibility of aggregation. As a result of heterogeneous reaction medium, effective light harvesting capacity of photocatalysts diminished and therefore lower photocatalytic activity leading to successful removal of the target compounds could be expected.

EEM fluorescence contour-plots of ROC_m and ROC_{ECm} upon exposure to solar photocatalytic degradation process in the presence of selected photocatalysts were displayed in figures 4.21-4.24.

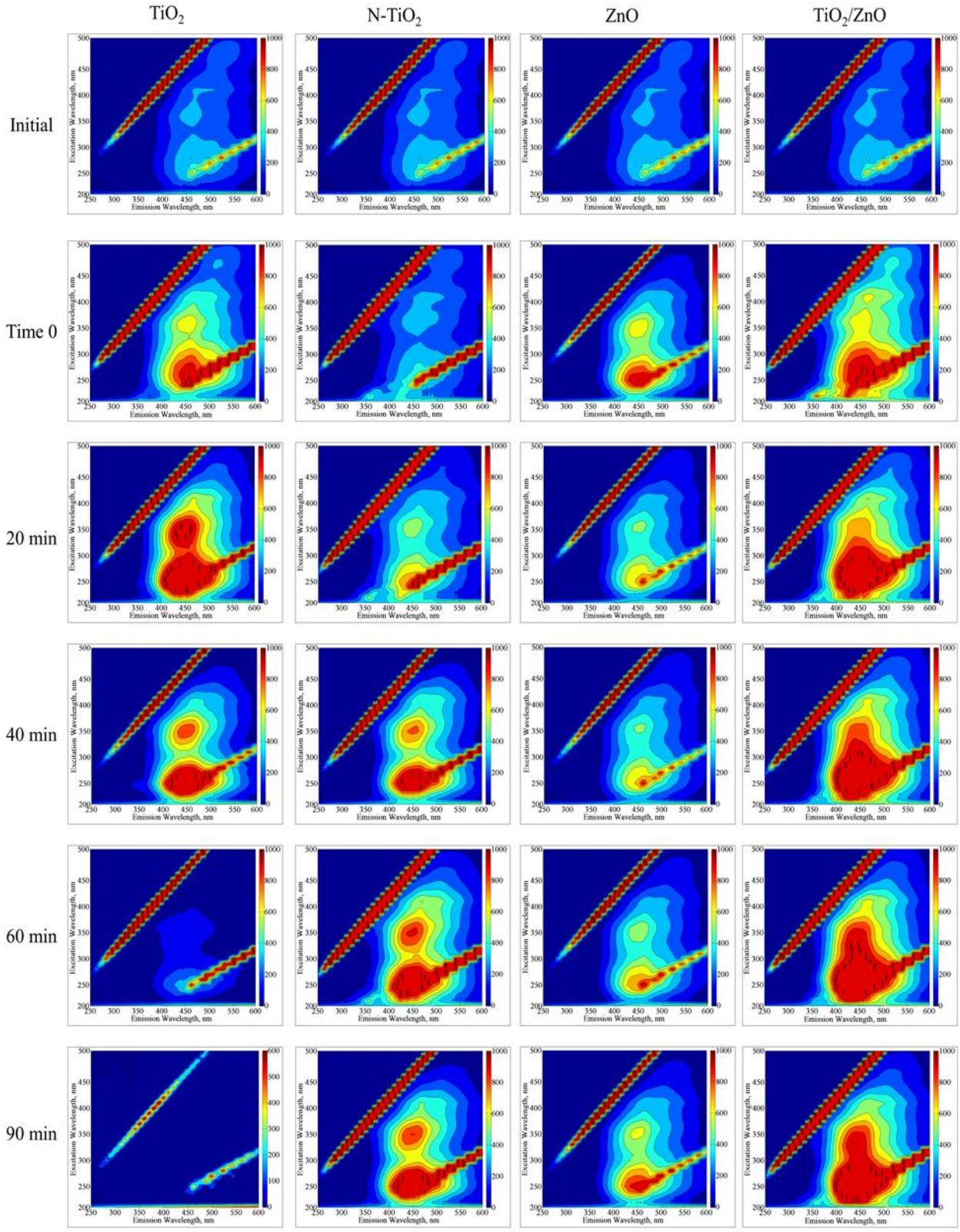

Figure 4.21. Irradiation time dependent EEM fluorescence contour-plots of ROC_{m1} upon exposure to solar photocatalytic degradation (I_o: $1.73x10^{16}$ quanta/s).

Variations in EEM fluorescence contour-plots of ROC_{m1} samples were observed even after instantaneous adsorption on photocatalysts specimens expressed as t0 condition in comparison to initial fluorescence regional speciation (Figure 4.21). Almost insignificant difference was attained in the presence of N-TiO_2, whereas emergence of new humic-like and fulvic-like fluorophores could be noticeably observed for the organic matrix attained upon use of TiO_2, ZnO, and TiO_2/ZnO nanocomposite. Initial adsorption of NPOC onto photocatalyst surfaces were found to be 43% for TiO_2, 11% for N-TiO_2, 24% for ZnO, and 52% for TiO_2/ZnO nanocomposite. The reason could be attributed to the adsorption of high molecular weight humic components onto the photocatalyst eliminating their masking effect on the lower molecular weight humic-like and fulvic-like fluorophores (Miano et al., 1988; Senesi, 1990; Chen et al., 2003; Bekbolet and Sen-Kavurmaci, 2015). Since the lowest adsorption percentage was achieved in the presence of N-TiO_2, eminence of high molecular weight fluorophores caused internal quenching and therefore revealed lower fluorescence intensity.

Following only irradiation period of 20 min, significant changes were attained for humic-like and fulvic-like fluorophores for all samples irrespective of the photocatalyst type. Transformation of humic-like fluorophores into new humic-like and fulvic-like fluorophores were attained in the presence of all photocatalysts. Upon exposure to solar photocatalysis, EEM fluorescence contour-plots of samples displayed distinct profiles with respect to the type of the photocatalyst specimen used, however, irradiation time dependent changes of fluorophores were found to be slightly different from each other for each photocatalyst. Noticeable reduction of humic-like and fulvic-like fluorophores were attained for ROC_{m1} after irradiation period of 60 min. Total disappearance of all fluorophores were attained within 90 min in the presence of TiO_2 whereas all these fluorophoric regions were still evident for the organic matrix in case of other photocatalysts, *i.e.* N-TiO_2, ZnO, and TiO_2/ZnO nanocomposite.

Upon exposure to solar photocatalytic degradation process for t_{irr}: 90 min, remaining NPOC contents of the samples were found to be 2.20 mg/L for TiO_2, 5.20 mg/L for N-TiO_2, 5.76 mg/L for ZnO, and 4.81 mg/L for TiO_2/ZnO nanocomposite. Although treated ROC_{m1} revealed similar NPOC contents using N-TiO_2, ZnO, and TiO_2/ZnO nanocomposite, the shape and intensity of EEM fluorescence contour-plots were distinctly differed from each other. The reason could be attributed to the fluctuations in SFI_{syn} parameter with respect to increasing irradiation periods. In the presence of TiO_2, SFI_{syn} expressed gradual decrease with respect to increasing irradiation period as a result of solar photocatalytic removal of humic fluorophores (Uyguner and Bekbolet, 2005a and c). However, in the presence of N-TiO_2, ZnO, and TiO_2/ZnO nanocomposite, irradiation time dependent decreases

as well as increases of SFI_{syn} (Appendix D, Table D1) was observed which could be attributed to concomitant removal of high molecular weight humic fluorophores and production of new lower molecular weight fluorophores most probably expressing fulvic-like nature via destruction of large humic molecules.

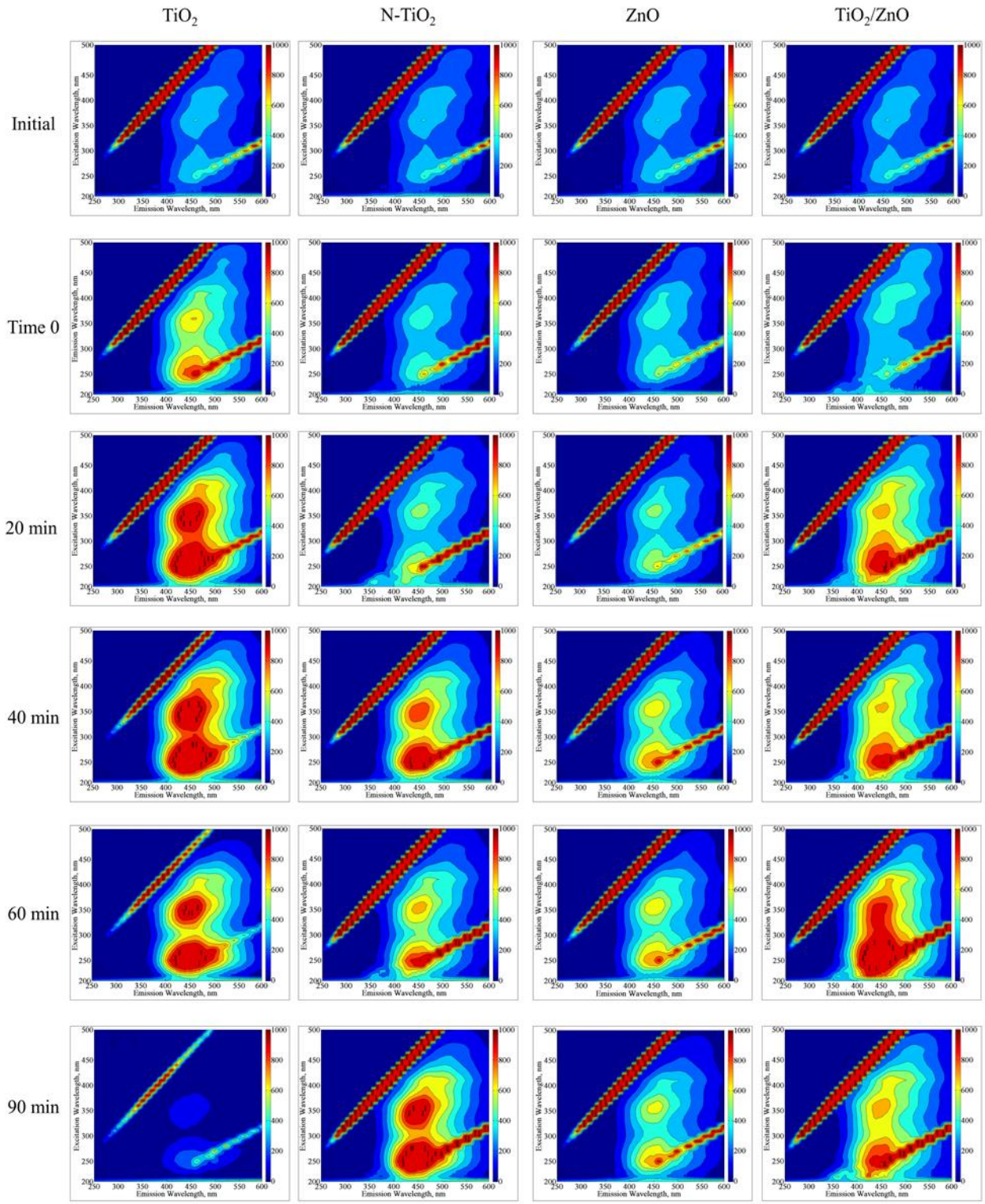

Figure 4.22. Irradiation time dependent EEM fluorescence contour-plots of ROC_{m2} upon exposure to solar photocatalytic degradation (I_o: $1.73x10^{16}$ quanta/s).

Distinct differences in time dependent fluorescence EEM fluorescence contour-plots of ROC_{m2} were attained in the presence of photocatalyst specimens as presented in Figure 4.22. Emergence of new humic-like and fulvic-like fluorophores could be noticeably visualized even after initial adsorption onto TiO_2 whereas minor changes in these fluorophores were attained upon adsorption onto N-TiO_2, ZnO, and TiO_2/ZnO nanocomposite. Following instantaneous attraction onto photocatalyst specimens, NPOC adsorption extent were found to be 37% for TiO_2, 23% for N-TiO_2, 3% for ZnO, and 5% for TiO_2/ZnO which revealed minor changes in the shape and intensity of EEM fluorescence contour-plots in the presence of almost all photocatalysts except TiO_2. Moreover, significant reduction on adsorption percentages of photocatalyst specimens could be related to higher organic carbon content of ROC_{m2} ($NPOC_i$: 23.2 mgOrgC/L, Table 4.2) which was composed of higher concentration humic matter (100 mg/L HA) as well as its photocatalytically degraded molecular size fractions.

Furthermore, solar irradiation time dependent changes in humic-like and fulvic-like fluorophores present in ROC_{m2} were found to be distinctly different from each other upon use of TiO_2, N-TiO_2, ZnO, and TiO_2/ZnO as the photocatalyst specimens. Emergence of new humic-like and fulvic-like fluorophores were observed within 20 min of irradiation in the presence of TiO_2 and TiO_2/ZnO nanocomposite whereas same noticeable change was attained within 40 min of irradiation in the presence of N-TiO_2 and ZnO indicating photocatalyst type specific reactions of ROS with HM present in ROC_{m2}. Irradiation time dependent changes in humic-like and fulvic-like fluorophores remained almost the same for the photocatalytic treatment periods of 20 min, 40 min, and 60 min for TiO_2 however, following extended irradiation period of 90 min, all humic-like and fulvic-like fluorophores were completely disappeared. Humic-like and fulvic-like fluorophores were still eminent in OM following photocatalysis using N-TiO_2, ZnO, and TiO_2/ZnO nanocomposite with varying fluorescence intensities although they expressed similar UV_{254} and NPOC values (Appendix D, Table D2). For this reason, the effectiveness of each photocatalyst specimens could better be visualized by the EEM fluorescence contour-plots (Figure 4.22), *e.g.* t_{irr}: 90 min.

The most irrelevant changes in fluorescence intensities were observed in HM upon use of ZnO which could be attributed to irradiation time dependent insignificant irradiation time dependent changes in UV_{254} and NPOC (< 10% change) for both of the parameters, and SFI_{syn} (almost no change) between t_{irr}: 20 min and 90 min (Appendix D, Table D2). One of the reasons could be expressed as considerably low adsorption capacity of NPOC onto ZnO surface which indicated that majority of the OM with significant NPOC content was present in solution rather than on the surface as expected for surface oriented photocatalytic treatment.

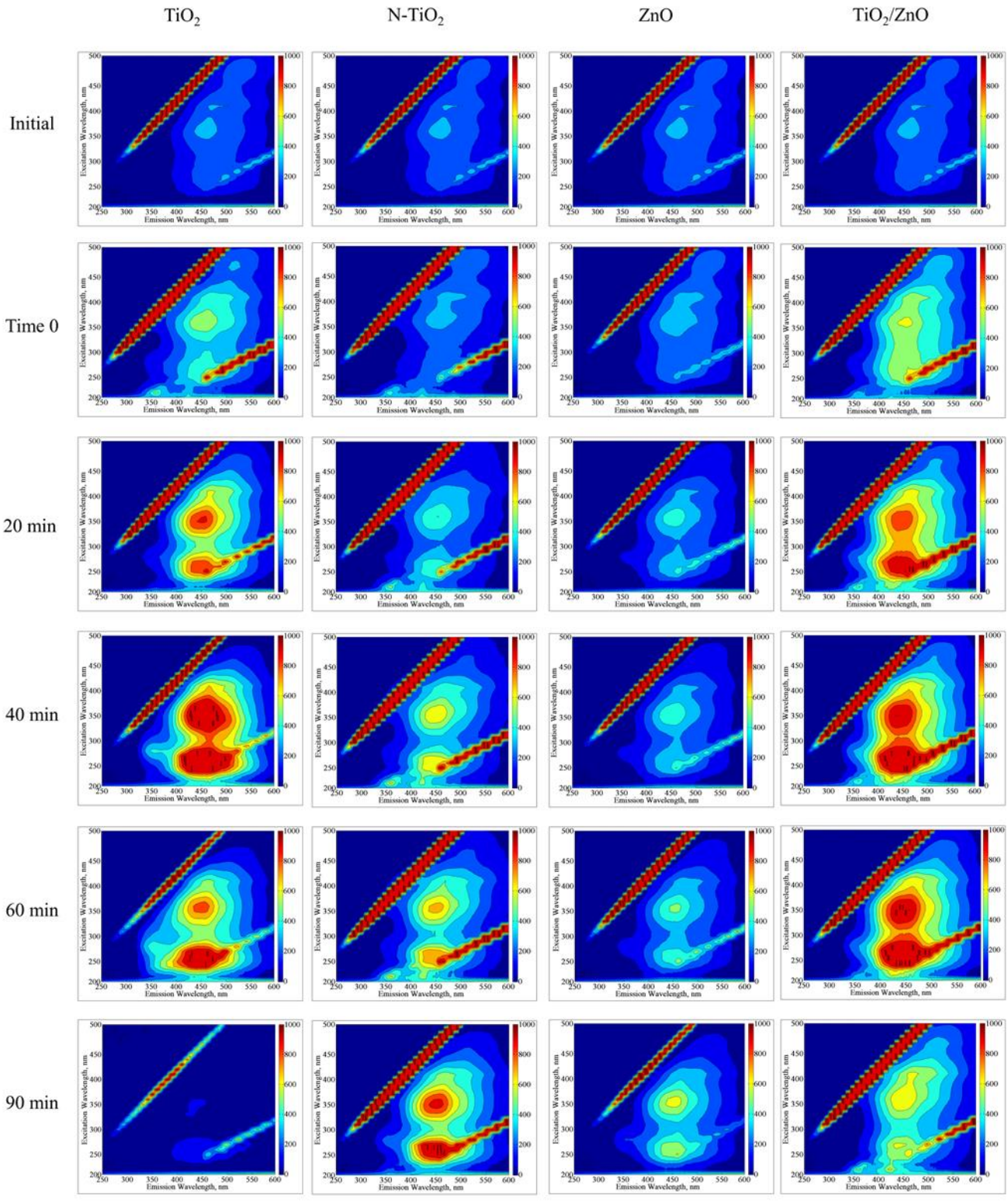

Figure 4.23. Irradiation time dependent EEM fluorescence contour-plots of ROC_{ECm1} upon exposure to solar photocatalytic degradation (I_o: $1.73x10^{16}$ quanta/s).

Irradiation time dependent EEM fluorescence contour-plots of ROC_{ECm1} expressed noticeable differences in comparison to the plots attained for ROC_{m1} (Figures 4.21) as presented in Figure 4.23. Adsorption percentages of NPOC revealed following values as 20% for TiO_2, 7% for N-TiO_2 and ZnO, and 39% for TiO_2/ZnO nanocomposite. Presence of ECs significantly influenced initial

adsorption percentages of NPOC contents of ROC_{ECm1} which were considerably lower than the results attained for ROC_{m1}. The distinct difference could also be visualized by time 0 conditions of EEM fluorescence contour-plots of ROC_{m1} (Figure 4.21) and ROC_{ECm1} (Figure 4.23) in the presence of TiO_2 and TiO_2/ZnO nanocomposite. Initial adsorption percentages were reduced from 43% to 20% for TiO_2 (BET surface area: 57 m^2/g) and from 52% to 39% for TiO_2/ZnO nanocomposite (BET surface area: 37 m^2/g), indicating the prominent role of OM composition dominating over sole surface area effect. Following adsorption onto photocatalyst specimens, remaining NPOC in solutions were found to be two times higher than the values attained for ROC_{m1} samples which could also related to reduction of fluorescence intensity via quenching effect of humic macromolecules (Miano et al., 1988; Senesi, 1990; Chen et al., 2003).

Formation of new humic-like and fulvic-like fluorophores as well as transformation of present fluorophores due to conformational and compositional changes in ROC_{ECm1} could be significantly observed upon use of TiO_2, N-TiO_2, and TiO_2/ZnO nanocomposite. Nitrogen doping of TiO_2 significantly affected the EEM fluorescence contour-plots of ROC_{ECm1} upon exposure to solar photocatalytic degradation up to irradiation period of 90 min. Contrary to the use of sole TiO_2, as a photocatalyst sole ZnO exhibited quite different trend expressing insignificant changes in both fluorescence intensity of humic-like or fulvic-like fluorophores as well as in the spectral shape of the EEM fluorescence contour-plots. As a comparison, it could be indicated that under the same conditions, formation of new humic-like and fulvic-like fluorophores have been detected in earlier reaction periods of the solar photocatalytic degradation of ROC_{m1}. The reason could be attributed to the presence of ECs in ROC_{ECm1} that were in competition with HM towards ROS mainly $HO^{\bullet}$. As a result of these competitive degradation pathway, excessive consumer of these reactive species would cause a reduction on the removal of humic-like and fulvic-like fluorophores. Therefore, insignificant change in humic matter fluorescence profile could be expected until complete removal of these emerging compounds were achieved. Use of TiO_2/ZnO nanocomposite displayed similarities to TiO_2 rather than ZnO in EEM fluorescence contour-plots expressing the dominating role of TiO_2 in TiO_2/ZnO nanocomposite.

Solar photocatalytic irradiation period of 40 min resulted in emergence of SMX related fluorophores which exhibited maxima at Ex/Em: 210-290/350 nm, could be noticeably visualized upon use of TiO_2 and TiO_2/ZnO nanocomposite and slightly observed upon use of ZnO photocatalysis. Since regional fluorescence properties of SMX coincides within the regions related to the aromatic proteins (Ex/Em: 220-250/280-380 nm) (Ben-Abdelmelek et al., 2013; Sgroi et al., 2017) it would also be masked by humic macromolecules due to the same mechanism as previously reported

by Wang and colleagues (Wang et al., 2015). Following t_{irr}: 90 min, SMX related fluorophores were still present upon use of ZnO and it emerged in the presence of N-TiO_2 whereas they were totally disappeared by TiO_2 and TiO_2/ZnO nanocomposite photocatalysis which could be attributed to the complete removal of SMX related fluorophores.

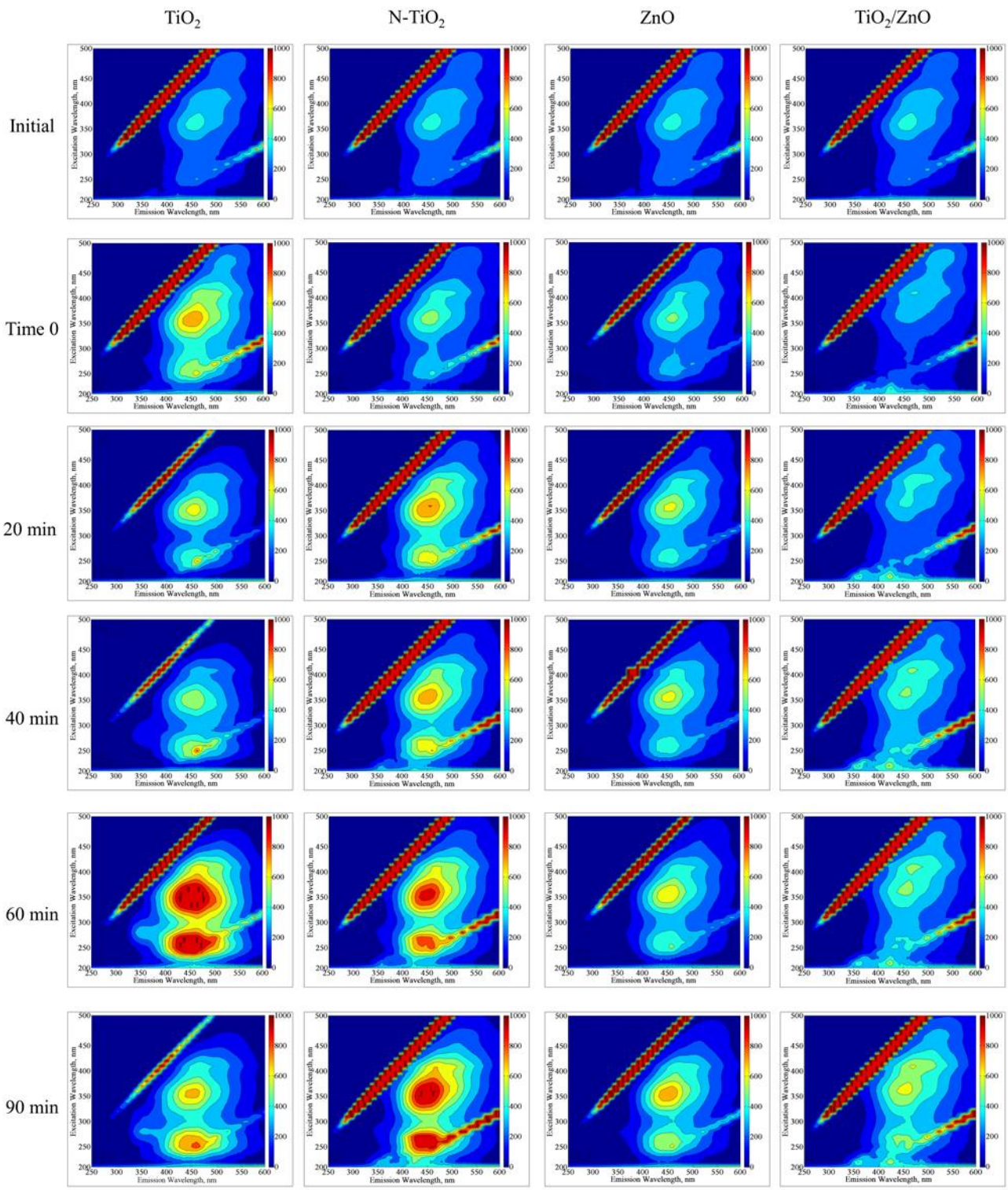

Figure 4.24. Irradiation time dependent EEM fluorescence contour-plots of ROC_{ECm2} upon exposure to solar photocatalytic degradation (I_o: $1.73x10^{16}$ quanta/s).

Upon exposure to solar photocatalytic degradation, fluorescence EEM fluorescence contour-plots of ROC_{ECm2} displayed distinct differences in comparison to ROC_{m1}, ROC_{m2}, and ROC_{ECm1} as visualized in Figure 4.24. Initial adsorption onto photocatalyst specimens' revealed NPOC removals of ROC_{ECm2} samples as follows: 12% for TiO_2 and N-TiO_2, 11% for ZnO, and 4% for TiO_2/ZnO whereas removal efficiencies were found to be 20% for TiO_2, 7% for N-TiO_2 and ZnO, and 39% for TiO_2/ZnO for ROC_{ECm1}. Change in organic matrix influenced primary surface interactions between OM and photocatalyst specimens as could also be visualized via EEM fluorescence contour-plots of ROC_{ECm1} (Figure 4.23) and ROC_{ECm2} (Figure 4.24). Since adsorption percentage of NPOC increased in the presence of N-TiO_2 and ZnO, fluorescence intensities in humic-like region (Ex/Em: 220-470/380-580 nm) were found to be higher than EEM fluorescence contour-plots attained for time 0 condition of ROC_{ECm1}. On the other hand, under the same conditions, EEM fluorescence contour-plots attained for time 0 condition in the presence of TiO_2 and ZnO expressed lower fluorescence intensities which could be attributed to lower adsorption percentages of NPOC causing eminence of high molecular weight humics with their internal quenching effect.

Noticeable changes in humic-like and fulvic-like fluorophores in ROC_{ECm2} could be observed in the presence of all photocatalyst even following irradiation period of 60 min and 90 min, whereas almost featureless changes in these fluorophores were attained up to 40 min. In addition, these fluorophores were still evident after irradiation period of 90 min even in the presence of TiO_2 that was able to remove all humic-like and fulvic-like fluorophores of ROC_{m1}, ROC_{m2}, and ROC_{ECm1} under the same conditions. The reason could be attributed to UV_{254} absorbance and NPOC contents of samples that are three times higher than the results attained for ROC_{m2} after 90 min of irradiation.

Moreover, although presence of SMX could be followed by EEM fluorescence spectra within the regions defined as aromatic proteins (Ex/Em: 220-250/280-380 nm), they were not able to be visualized in ROC_{ECm2} samples even after irradiation period of 90 min. In a similar trend attained for ROC_{ECm1}, visualization of SMX related fluorophores could only be done in the presence of TiO_2 following irradiation period of 40 min, 60 min, and 90 min, whereas these fluorophoric regions were not observed in the presence of N-TiO_2, ZnO, and TiO_2/ZnO in any of the irradiation periods. The reason could be attributed to the presence of high molecular size fractions of humics with higher degree of aromaticity coming from OM matrix of ROC_{ECm2} covering humic matter content composed of oxidized and non-oxidized fractions of humics in comparison to ROC_{ECm1} that contains only non-oxidized fractions of humics with lower organic matter content. Therefore, masking effect of humics present in ROC_{ECm2} would be tremendously higher than the ones within the ROC_{ECm1} composition due to presence of higher molecular weight humic macromolecules (Wang et al., 2015).

EEM fluorescence contour-plots of ROC_m samples displayed photocatalyst type specific profiles upon increasing irradiation periods. During oxidative treatment, both humic-like and fulvic-like fluorophores were non-selectively removed. Transformation of humic-like fluorophores to fulvic-like fluorophores was more evident upon use of N-TiO_2 and TiO_2/ZnO nanocomposite. Removal of all fluorophoric groups upon irradiation period of 60 min could be explained by the resulting NPOC and UV_{254} contents. However, no significant change was observed in fluorophoric regional profiles upon use of ZnO displaying concomitant removal of all humic moieties. Following photocatalytic irradiation period of 90 minutes humic-like and fulvic-like fluorophores were still evident for both ROC_{m1} and ROC_{m2} in the presence of N-TiO_2, ZnO, and TiO_2/ZnO nanocomposite in comparison to TiO_2.

In the presence of ECs, significant difference was observed for ROC_{ECm1} in comparison to ROC_{ECm2} that could be attributed to the organic matrix properties rather than individual effects of CMZ and SMX towards oxidation in the presence of TiO_2/ZnO nanocomposite. Most irrelevant change in EEM fluorescence contour-plots upon increasing irradiation periods were attained in the presence of ZnO for all of the ROC samples.

Advanced evaluation of the individual fluorescent components in ROC_{m1}, ROC_{m2}, ROC_{ECm1}, and ROC_{ECm2} were presented by application of PARAFAC modeling using EEM fluorescence contour-plots.

Further interest was also devoted to in depth characterization of the OM for the assessment of the influence of solar photocatalytic degradation process using TiO_2, N-TiO_2, ZnO, and TiO_2/ZnO nanocomposite. By the application of sequential UF technique, thus obtained molecular size fractions of ROC_{m1}, ROC_{m2}, $ROC_{ECm}1$, and ROC_{ECm2} were subjected to aforementioned advanced analytical procedures.

4.5. Decomposition of EEM Fluorescence Contour-plots of ROC_m and ROC_{ECm} using PARAFAC Modeling Prior to and Following Photodegradation and Photocatalytic Degradation Processes

Conventional characterization techniques, such as TOC and UV-vis absorbance mainly focus on the bulk characteristics of DOM, therefore they would not be sufficient to provide detailed information of sub-fractions present in DOM structure (Uyguner-Demirel and Bekbolet, 2011). Fluorescence spectroscopy, more specifically, three dimensional Excitation Emission Matrix fluorescence spectroscopy could be used as a rapid and sensitive technique for the elucidation of fluorescent components present in DOM fractions (McKnight et al., 2001; Andrade-Eiora et al., 2013a and b; Sen-Kavurmaci and Bekbolet, 2014; Yang et al., 2019). However, major disadvantage of EEM fluorescence spectroscopy is reduction on the selectivity of the technique due to broad spectral overlap or to the presence of other matrix interferences. The most well-known iterative algorithms proposed for three-way data array exhibiting the second-order advantage are alternating trilinear decomposition (ATLD) (Wu et al., 1998; Wang et al., 2011), bilinear least-squares/residual bilinearization (BLLS/RBL) (Bro, 1997; Nikolajesen et al., 2003; Zhu et al., 2009; Wang et al., 2011) generalized rank annihilation method (GRAM) (Sánchez and Kowalski, 1986), multivariate curve resolution-alternating least-squares (MCR-ALS) (Windig and Guilment, 1991; Antunes et al., 2005), the PARAFAC model, and self-weighted alternating trilinear decomposition (SWATLD). Being regarded as an iterative and a least-square type algorithm, PARAFAC decomposes multiple pure spectral profiles multi-way data even in the presence of unknown and uncalibrated data.

PARAFAC belongs to a family of so-called multi-way methods applicable to data that are arranged in three- or higher-order arrays. Fluorescence EEMs (sample-excitation wavelength-emission wavelength), chromatographic data (GC-MS: sample-elution time- m/z structure), sensory data (sample-attribute -judge) and electroencephalography (space-time-frequency) are some of the examples of three-way arrays that could be analyzed by PARAFAC model by which three-way dataset are decomposes the data signal into a set of trilinear terms and a residual array:

$$X_{ijk}=\sum_{f=1}^{F} a_{if} b_{if} c_{kf} + e_{ijk} \quad (4.21)$$

where i=1,..., I; j=1,..., J; k=1,..., K. According to equation … x_{ijk} is the data point corresponding to the i^{th} sample at the j^{th} variable on mode 2 and at the k^{th} variable on mode 3, and e_{ijk} is the residual representing the variability not accounted for by the model. In the case of a fluorescence excitation-emission matrix, the i, j, and k correspond to the sample, emission and excitation modes, respectively

(Figure 4.25). Each f corresponds to a PARAFAC component and each such component has I a-values (scores); one for each sample. Each component also has J b-values; one for each emission wavelength as well as K c-values; one for each excitation wavelength (Murphy et al., 2013).

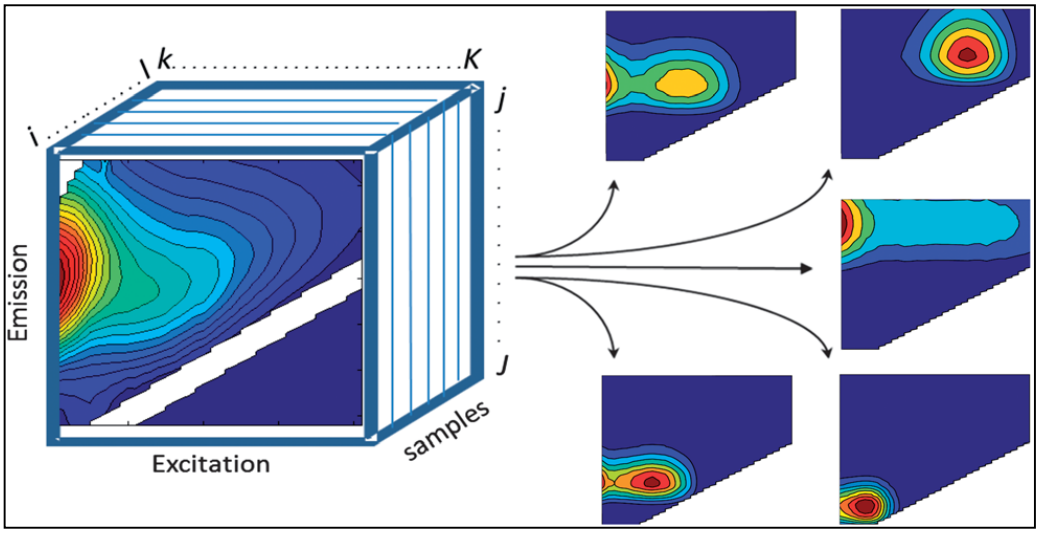

Figure 4.25. EEM dataset arranged in a three-way structure and decomposed into five PARAFAC components (Murphy et al., 2013).

Fluorescent components identified by EEM/PARAFAC have distinct excitation and emission spectrum. On the other hand, identified components may represent a single fluorophore or a group of similar fluorophores. Once identification of the components explaining the greatest variation is proceeded, calculation of the distribution of components could be done for each sample. PARAFAC modeling could make quantitative determination of an analyte possible by adding known amount of this analyte for the determination of its concentration in each sample. Otherwise for an unknown PARAFAC component, it is impossible to convert fluorescence intensities to concentration values. Therefore, the maximum fluorescence intensities (Fmax) of the identified DOM components are used as the representative of the relative proportions of the components. Fmax is derived by multiplying the maximum excitation and maximum emission loading for each component by its score, which produces intensities in the same measurement scale as the original EEMs. On the other hand, quantitative and qualitative information could be attained from changes in the intensity of a given component, or in the ratios of any two components, between samples in the dataset. In addition, the relative abundance of a component (Fmax/ΣFmax) can designate alterations in its overall significance, although this measure is sensitive to changes in the relative abundances of all the components so must be interpreted with care (Murphy et al., 2013).

Validation of the model output comprises one of the most important steps through the process. Therefore, identified PARAFAC components are validated by use of split half analysis, which splits data into halves and then mathematically compares excitation and emission loadings of the models that were run on separate splits of the data using Tuckers Congruence as previously explained by Lorenzo-Seva and Berge (Lorenzo-Seva and Berge, 2006). Following split half analysis, command window indicates whether the model is validated or not. Moreover, following split half analysis, emission and excitation loadings of each split can be plotted and therefore could be compared visually.

Special interest has been devoted to EEM fluorescence spectroscopy in combination with PARAFAC modeling for the characterization of DOM in numerous aquatic environments for more than two decades (Bro, 1997; Stedmon et al., 2003; Coble et al., 2014; Jaffe et al., 2014; Vera et al., 2017). Among all types of aquatic ecosystems, headwater streams, rivers, lakes, wetlands, estuaries, coastal areas and the open ocean are the most commonly environments evaluated by EEM/PARAFAC in order to investigate DOM dynamics (Kowalczuk et al., 2009; Jaffé et al., 2014; Chen et al., 2016). In addition, recent concern has also been dedicated to understand the behavior of DOM in wastewater streams as well (Li et al., 2014).

EEM/PARAFAC comprises a wide range of environmental applications for the assessment of individual fluorescent components arising from DOM under natural as well as engineered systems. Influence of applied treatment systems on the characterization and composition of DOM both in drinking water treatment facilities (Sanchez et al., 2014; Vera et al., 2017; Heibati et al., 2017; Ignatev and Tuhkanen, 2019) and wastewater treatment facilities (Li et al., 2014; Gou et al., 2017) have also been evaluated by employment of EEM/PARAFAC (Yang et al., 2015). THM formation potential in drinking water treatment processes plays a crucial role and can be followed by monitoring fluorescent DOM components via EEM/PARAFAC (Lyon et al., 2014; Yang et al., 2015b). Amphiphilic, multi-ligand and polydisperse characteristics of DOM may express alterations with respect to different molecular size fractions, therefore, investigation of molecular size distribution profiles of DOM either with or without any treatment processes by EEM/PARAFAC brings further understanding to the behavior of DOM components (Romero-Castillo et al., 2014; Lee et al., 2015; Aftab and Hur, 2017; Ateia et al., 2017; Wünsch et al., 2017). Due to its applicability on the assessment of changes in HS as well as the performance of applied system, EEM/PARAFAC has been applied for tracking the variations in DOM structure upon exposure to physicochemical treatment processes, such as adsorption (Lee et al., 2015; Phong and Hur, 2017; Yang et al., 2018), coagulation and flocculation (Sanchez et al., 2014; Aftab and Hur, 2017), and UV/chlorination (Lyon et al., 2014).

With respect to its selective and/or non-selective degradation mechanism, AOPs would alter the chemical composition as well as the fractional distribution of DOM significantly. Therefore, influence of AOPs on degradation profiles of DOM components have been evaluated in a broader spectrum by the application of EEM/PARAFAC modeling (Mazivilla et al., 2019). Recent interest has been devoted to assessment of Fenton, photo-Fenton (García Ballesteros et al., 2017; Caram et al., 2018) and photocatalytic degradation processes for the degradation of DOM, usually represented by commercial substances, in terms of EEM/PARAFAC. Application of PARAFAC modeling in combination with EEM fluorescence contour-plots for the investigation of photocatalytic degradation of terrestrial DOM represented by commercially available humic substances has gained special interest. Since DOM is composed of various components with respect to their own environmental importance and significance, origin related individual degradation profiles of these components rather than overlapping peak intensities would bring further assessment on the understanding of degradation behavior of each component (Chen et al., 2014; Phong and Hur, 2015; Ly et al., 2018; Turong et al., 2019). Moreover, photocatalytic degradation of real water samples, such as stromwater runoff (Zhao et al., 2018), were also evaluated by EEM/PARAFAC to assess changes obtained in DOM.

Comprising multicomponent organic matrices, such as humic-like and fulvic-like matter as well as ECs, EEM fluorescence contour-plots of ROC_m and ROC_{ECm} samples in combination with PARAFAC model prior to and following photolytic and photocatalytic degradation processes would bring further insight into decomposition of overlapping signals of EEM fluorescence features of components. Fluorescence EEM contour plots of all ROC_m and ROC_{ECm} samples upon exposure to UVC and solar photodegradation (36 samples) and solar photocatalytic degradation processes (84 samples) were successfully decomposed by PARAFAC analysis in order to identify the number, type and intensity of individual DOM components. A stepwise analytical procedure was followed as: *i.* importing raw data sets to visualize each EEM contour-plots, *ii.* preprocessing data set includes correcting biases and the removal of Rayleigh and Raman peaks to prevent scattering. *iii.* identification and remove of outliers from the dataset based on instrument errors, artifacts and discrepancy with other samples was processed via an exploratory analysis using non-negatives constraints that constitutes the outlier detection and the visualization of the residuals, *iv.* validation of the model comprising determination of number of components, evaluation of model fit, and sensitivity analyses, finally *v.* the number of components distinguished by the PARAFAC model was validated by split half analysis (S2C2T2; Splits: 2, Combinations: 2, Tests: 2), applying 10 random initializations which was followed by the visualization of the PARAFAC components and obtaining their Fmax values for each sample.

With respect to the excitation and emission maxima values of the identified components (C1, C2, C3, and C4) determined by PARAFAC model was compared with related literature studies in order to classify DOM fluorescence components derived from ROC_m and ROC_{ECm} samples prior to and following photodegradation and photocatalytic degradation processes. Detailed information about PARAFAC models identified for various DOM origins under natural as well as engineered systems are presented in Appendix E.

Identified PARAFAC components could be classified into three categories based on their functionalities, photochemical properties and molecular weight. Ishii and Boyer evaluated reoccurring PARAFAC components by their EEM locations, representative EEMs, and spectral loadings derived from the literature studies dealing with aquatic systems including wastewater, seawater, and agricultural stream. They revealed three most commonly PARAFAC components as follows: *i.* component 1 gives maxima at Ex: < 230-260 nm and Em: 400-500 nm which is classified as UVC humic-like component. Since excitation peak wavelength of this component occurs in UVC region, it is expected to be degraded by UVC irradiation, *ii.* component 2 reveals maxima at Ex: < 240-275 (339-420) and Em: 434-520 nm and defined as UVA+UVC humic-like component which absorbs irradiation in UVA and UVC regions. These type of components are expected to be degraded by UVA irradiation, *iii.* component 3 expresses maxima at Ex: < 240-260 (295-380) nm and Em: 374-450 nm and categorized as UVC humic-like+UVA marine humic-like component that absorbs irradiation in UVC, UVB, and UVA regions and expected to be photodegraded by UVA light, but to a lesser extent than component 2 (Ishii and Boyer, 2012).

Due to surface oriented mechanisms occurring during DOM treatment, identification of PARAFAC component according to functionalities covers prime importance. Yang and colleagues categorized PARAFAC components with respect to majority of their functional groups. C1 gives two maxima at Ex: 250-310 nm, Em: 428 nm that primarily composed of carboxylic-like chromophores. C2 expresses two maxima at Ex: 300-460 nm and Em: 520 nm and C3 also reveals two maxima at Ex: 270-375 nm and Em: 520 nm. Both C2 and C3 are overwhelmingly composed of phenolic-like fluorophores (Yang et al., 2018).

Following photodegradation of ROC_m and ROC_{ECm}, C1 presented a primary maxima at Ex/Em: 250/450 nm and a secondary maxima at Ex/Em: 350/450 nm which could be defined as a humic-like component. C2 exhibited a primary maxima at Ex/Em: 400/525 nm and a secondary maxima at Ex/Em: 450/525 nm as well as a third maxima at Ex/Em: 250/525 nm. C3 displayed a primary maxima at Ex/Em: 275/550 nm and a secondary maxima at Ex/Em: 450/550 nm whereas C4 exhibited one

maxima at Ex/Em: 300/575 nm. Although all identified components were regarded as “humic-like” components as the general classification, they tend to express differences in terms of their chemical and photochemical properties related to the results presented by Ishii and Boyer (Ishii and Boyer, 2012). C1, C2, C3 and C4 could be defined as UVC humic-like and UVA humic-like components that are expected to be degraded by UVA irradiation. Due to their large molecular size and hydrophobic structure they give intensity at longer excitation and emission wavelengths. Depending on their maximum excitation and emission wavelengths, molecular sizes of the components were found to be in the order of C4 > C2 > C3 > C1 that also gives the information about degradation extension of these components upon exposure to photodegradation. Moreover, identified PARAFAC components could be classified according to their functionalities according to results presented by Yang and colleagues (Yang et al., 2018) as follows: C1 is mainly composed of carboxylic-like chromophores, whereas C2, C3, and C4 are overwhelmingly comprises phenolic-like chromophores.

Upon photocatalysis, C1 presented a primary and secondary maxima at 225/425 nm and 265/425 nm, whereas C2 exhibited a primary and secondary maxima at 325/450 nm and 250/450 nm. In addition, C3 displayed a primary and a secondary maxima at 250/550 nm and 380/550 nm. C4 displayed one maxima at 275/575 nm. Based on the origin of the HM present in ROC_m and ROC_{ECm} compositions as well as previous literature findings as presented in Table E.1. in Appendix E, all identified components could be assigned to humic-like components as a general classification (Murphy et al., 2008; Kowalczuk et al., 2009; Ishii and Boyer, 2012; Pifer and Fairey, 2014; Ly et al., 2018; Tang et al., 2019). However, giving different maxima in Ex/Em peaks, these humic-like components vary with respect to the differences in aromaticity and molecular weight properties, functionalities as well as their photochemical properties. Therefore, these components could be further identified depending on their aromaticity, molecular size, functional groups as well as photochemical properties.

C1 is mainly composed of carboxylic-like chromophores whereas C2, C3, and C4 are principally composed of phenolic-like chromophores of HM (Yang et al., 2018). With respect to their Ex/Em maxima, C1 could be defined as UVC humic-like component that absorbs irradiation primarily in UVC region and expected to be comprise of small molecular size components. C2 could be regarded as UVC humic-like and UVA humic-like component absorbing irradiation in both UVC and UVA region. C3 was also regarded as UVC and UVA humic-like component that absorbs light in UVC, UVB, and UVA regions not to a lesser extent than C1 and C2 (Ishii and Boyer, 2012; Ateia et al., 2017; Senga et al., 2018) Among all identified components C4 mostly attributed to typical terrestrial humic-like component with greater degree of structured condensation and large molecular size.

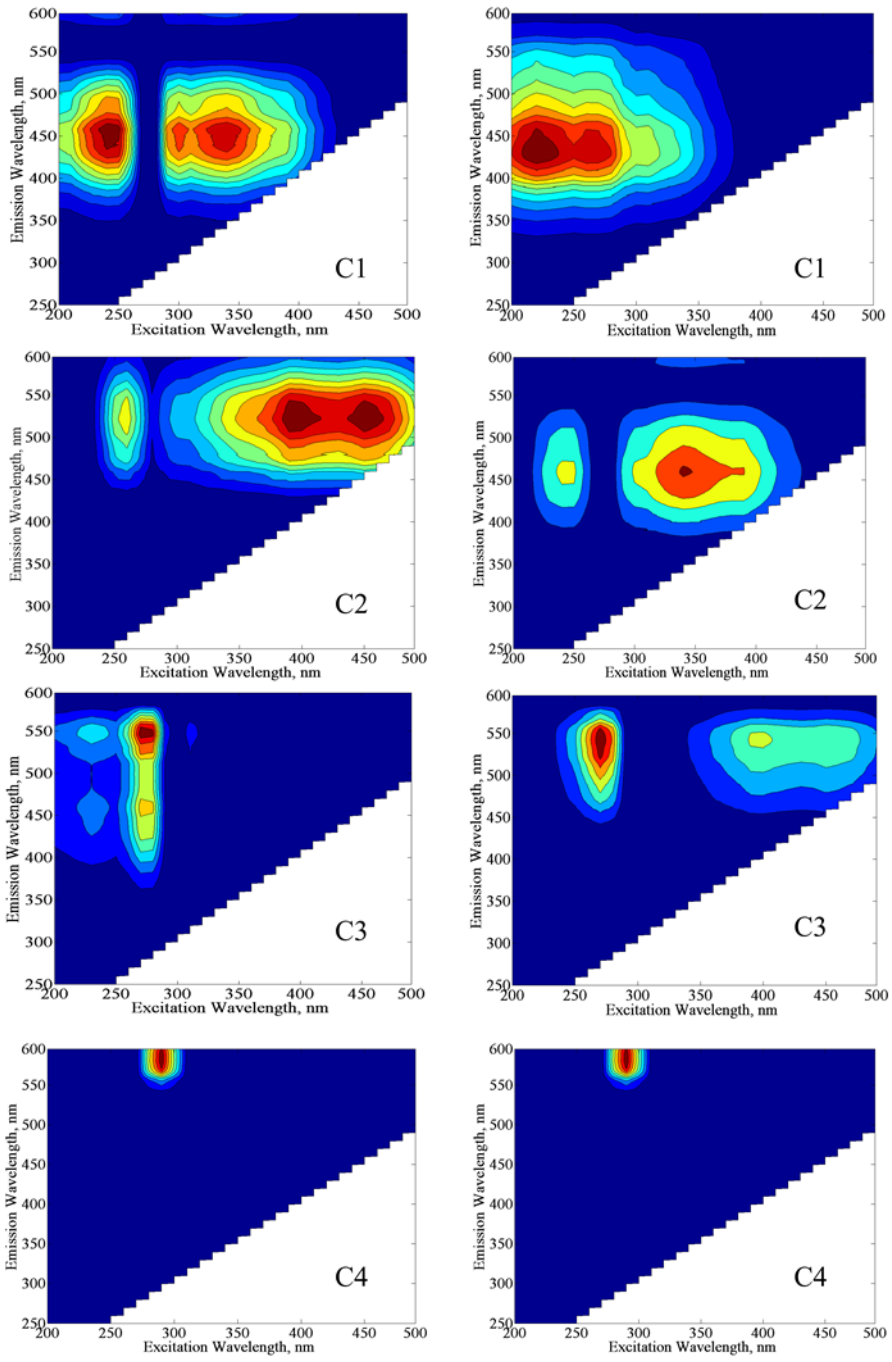

Figure 4.26. EEM contour-plots of four components identified by PARAFAC model for ROC_m and ROC_{ECm} upon exposure to photodegradation (left) and photocatalytic degradation processes (right).

Increase in molecular size and aromatic content of humic substances are associated with fluorescence peaks at longer wavelengths that is regarded as "red-shifting" of the EEM peak (Chen et al., 2003). It was previously reported that larger sized humic fractions with higher degree of aromaticity tend to display noticeable EEM features at longer emission (Em) wavelengths *i.e.* Em> 510 nm (Hur and Kim, 2009; Lee et al., 2015). Therefore, identified fluorescent components could have a higher degree of aromaticity and larger molecular size following the order of C4 > C3 > C2 >

C1 for both photodegradation and photocatalytic degradation. On the other hand, the discriminative differences of Ex/Em peaks of components C1, C2, and C3 could be clearly observed under photodegradation and photocatalysis conditions. Upon exposure to photocatalysis secondary maxima of C1 was disappeared and a gradual shift in Ex/Em of peak into shorter wavelength was observed. The most significant change was observed for C2 whose Ex/Em maxima were noticeably shifted to lower Ex/Em of peaks into shorter wavelengths which is defined as the "blue-shifting" of the peak position. The least significant change in Ex/Em of peak was attained for C3 in comparison to C1 and C2. Either exposed to photodegradation or photocatalytic degradation process, component C4 was present without any shift in Ex/Em maxima of the peak under all experimental conditions indicating presence of humic matter with higher degree of aromaticity and high molecular size fraction even after solar photocatalytic degradation process. Presence of higher degree of aromaticity or larger molecular size could be observed even after oxidative treatment of NOM samples as has been previously reported through the literature (Phong and Hur, 2015 and 2016; Ly et al., 2018). In accordance with results attained for the aromatic character of PARAFAC components, $SUVA_{254}$ values of all samples varied between 4.98 L/mg m and 9.38 L/mg m indicating the existence of hydrophobic aromatic humic moieties even after photocatalytic irradiation period of 90 min as previously explained in Section 4.3.2.1.

Li and colleagues investigated correlation between Fmax values of terrestrial sources and some of the antibiotics, *i.e.* metronidazole, norfloxacin, and sulfamethoxazole by applying Pearson correlation and regression analyses. They concluded that, significant correlations between components C1 and C2 and SMX concentration in reservoir waters were found with correlation coefficients of R^2: 0.91 and 0.68 (Li et al., 2018). Consequently, tracking changes in terrestrial humic-like components would also give information about the fate of the above mentioned antibiotics within the system (Baker and Curry, 2004; Guo et al., 2010). With respect to the literature findings reported and excitation and emission wavelengths derived in this study, as a matter of fact, C1 could be correlated to SMX content of ROC_{ECm} samples.

In order to get a further insight on the assessment of PARAFAC components in terms of their relative abundance, either exposed to photodegradation or photocatalytic degradation processes, irradiation time dependent changes in normalized Fmax values (ratio of Fmax value of the sample to the initial Fmax value of the experimental set) of fluorescent components were determined and subjected to assessment for each system. Results were presented in Figure 4.26 for UVC and solar photodegradation experiments and in figures 4.27-4.30 for photocatalytic degradation experiments performed using all ROC samples.

Upon exposure to UVC photodegradation, the removals of individual components ranged from 26 to 52%, whereas under solar irradiation conditions, 15 to 30% removal efficiencies were attained for the components in ROC_{m1}. Among all fluorescent components, highest removal efficiency was attained for C1 under UVC irradiation in comparison to solar irradiation followed by C2 and C3. The reason could be attributed to the excitation peak wavelength of C1 (Ex: 250 nm) that is close to the irradiation wavelength of UVC lamp (λ: 254 nm) (Del Vecchio and Blough, 2002; Ishii and Boyer, 2012; Phong and Hur, 2016). Lowest removal rate of C4 under UVC and solar irradiation could be attributed to its higher degree of aromaticity as well as molecular weight. Degradation rates of fluorescent components were considerably higher than UV_{254} and DOC removal efficiencies of ROC_m and ROC_{ECm} samples for UVC and solar photodegradation experiments. The reason could be attributed to higher sensitivity of fluorescent components to UVC and solar light than other non-fluorescent components (Sen-Kavurmaci and Bekbolet, 2014; Phong and Hur, 2015 and 2016). Since fluorescence is arised from π-π* and n-π* transitions in organic molecules ending up with rapid extinction under UVC irradiation (Cho and Choi, 2002).

Interestingly, in the presence of ROC_{m2}, normalized Fmax values of the components increased over time. Increase in components upon photodegradation could be attributed to the generation of these fluorophores as a result of photodegradation process. Since ROC_{m2} was composed of higher molecular weight humic components in comparison to ROC_{m1}, conversion of these higher molecular weight components into smaller fragments could be the reason of increase in identified PARAFAC components (Bekbolet and Sen-Kavurmaci, 2015). Following solar photodegradation, Fmax removals of the components were ranged from 7 to 18%, whereas upon exposure to solar photodegradation, 6 to 13% Fmax removals were achieved. Once again lower removal efficiencies of the components could be related to their simultaneous production as well as removal via photodegradation due to humic composition of ROC_{m2}. Consequently, the most insignificant change in all components with respect to increasing irradiation periods were attained for ROC_{m2} either exposed to UVC irradiation or solar irradiation. Time dependent Fmax changes in all fluorescent components were found to be irrelevant for ROC_{ECm1} with respect to solar photodegradation, however upon exposure to UVC photodegradation, 15% removal of C3 and C4 and 10-40% increase in C1 and C2 were attained. The reason could be attributed to photo-transformation of high molecular weight aromatic compounds (C3 and C4) into lower molecular weight ones (C1 and C2) (Phong and Hur, 2015). Consequently, changes attained for normalized Fmax values were found to be insignificant under solar irradiation in comparison to UVC irradiation conditions except for ROC_{ECm2} which revealed time dependent fluctuations for individual fluorescent components ending up to 40% removal efficiencies of Fmax.

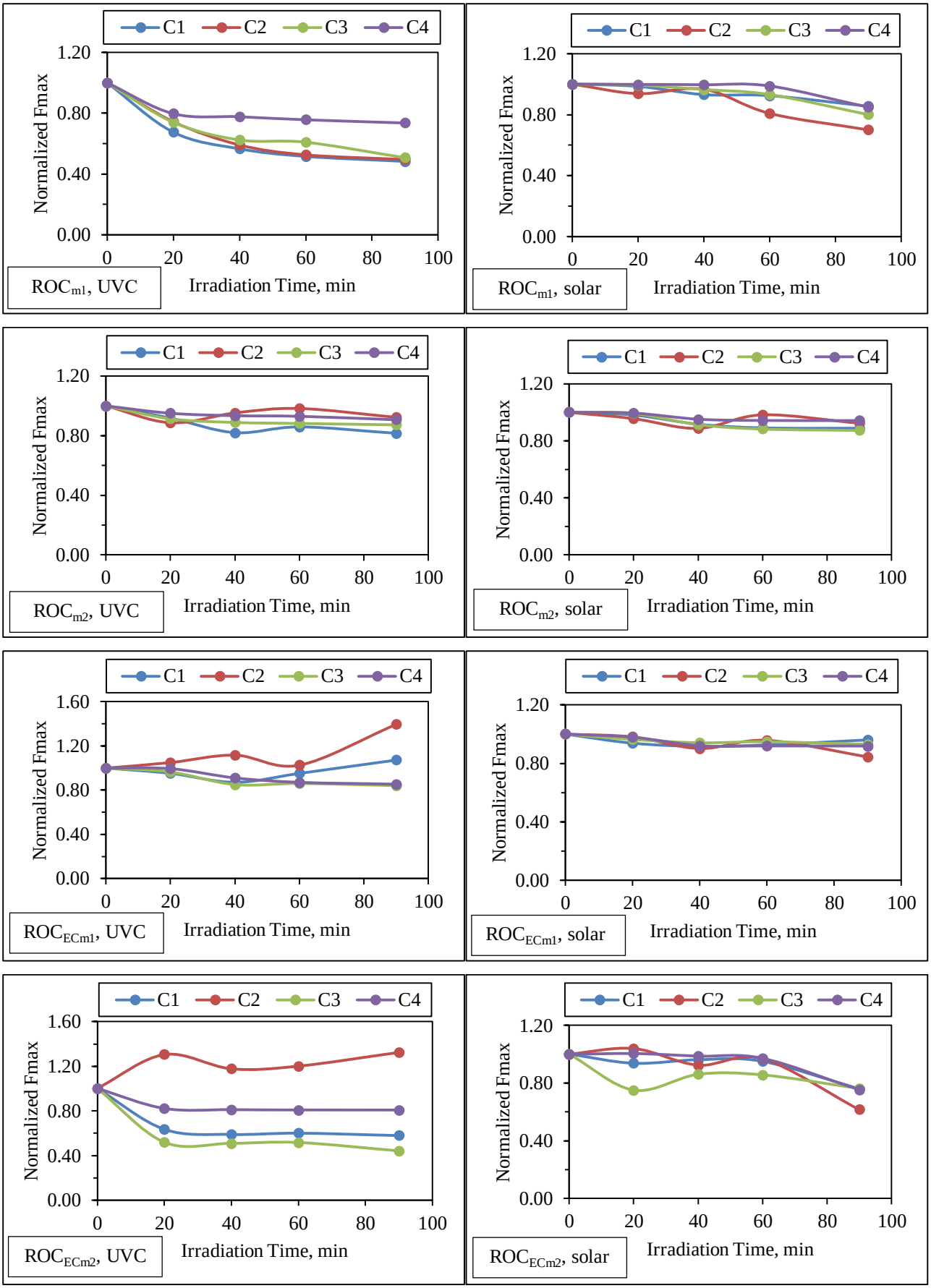

Figure 4.27. Time dependent changes in normalized Fmax values of PARAFAC components identified for ROC_m and ROC_{ECm} upon exposure to UVC and solar photodegradation.

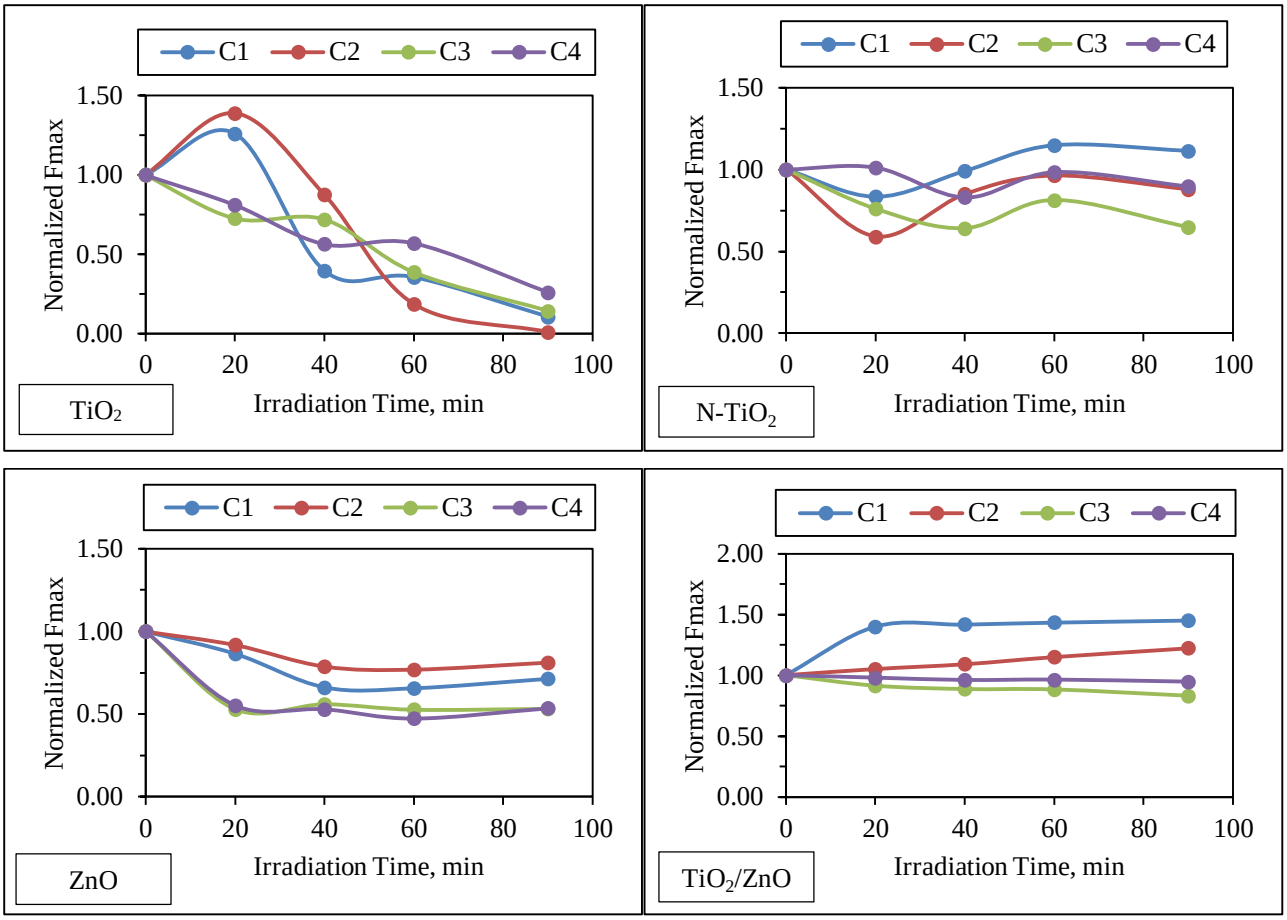

Figure 4.28. Time dependent changes in normalized Fmax values of PARAFAC components identified for ROC_{m1} upon exposure to solar photocatalytic degradation.

Following photocatalytic irradiation period of 20 min, sudden increase of C1 and C2 was attained in the presence of TiO_2 which could be attributed to transformation of higher molecular size components into lower molecular sized ones. More than 90% removal of C1, C2, and C3 were achieved in the presence of TiO_2 following solar irradiation period of 90 min. TiO_2 and ZnO displayed higher removal efficiencies even for the higher molecular size components (C3 and C4), that were followed by N-TiO_2. On the other hand, TiO_2/ZnO was found to be the least efficient (< 10% removal of fluorescent components) photocatalyst indicating difference of reaction mechanisms during photocatalytic degradation of fluorescent components. Depending on the aromatic core structure and hydrophobicity, possible formation of lower molecular weight fluorescent components from higher molecular weight components could be expected as a result of photocatalytic degradation process (Phong and Hur, 2015 and 2016; Turong et al., 2019). When the rate of formation of these components are higher than the removal rates, an increase in Fmax value could be expected. On the other hand, when formation of these lower molecular weight compounds becomes limited due to the reactions between high molecular weight compounds and ROS, then leading mechanism turns into removal of lower molecular weight fluorescent compounds ending up with the reduction of Fmax values.

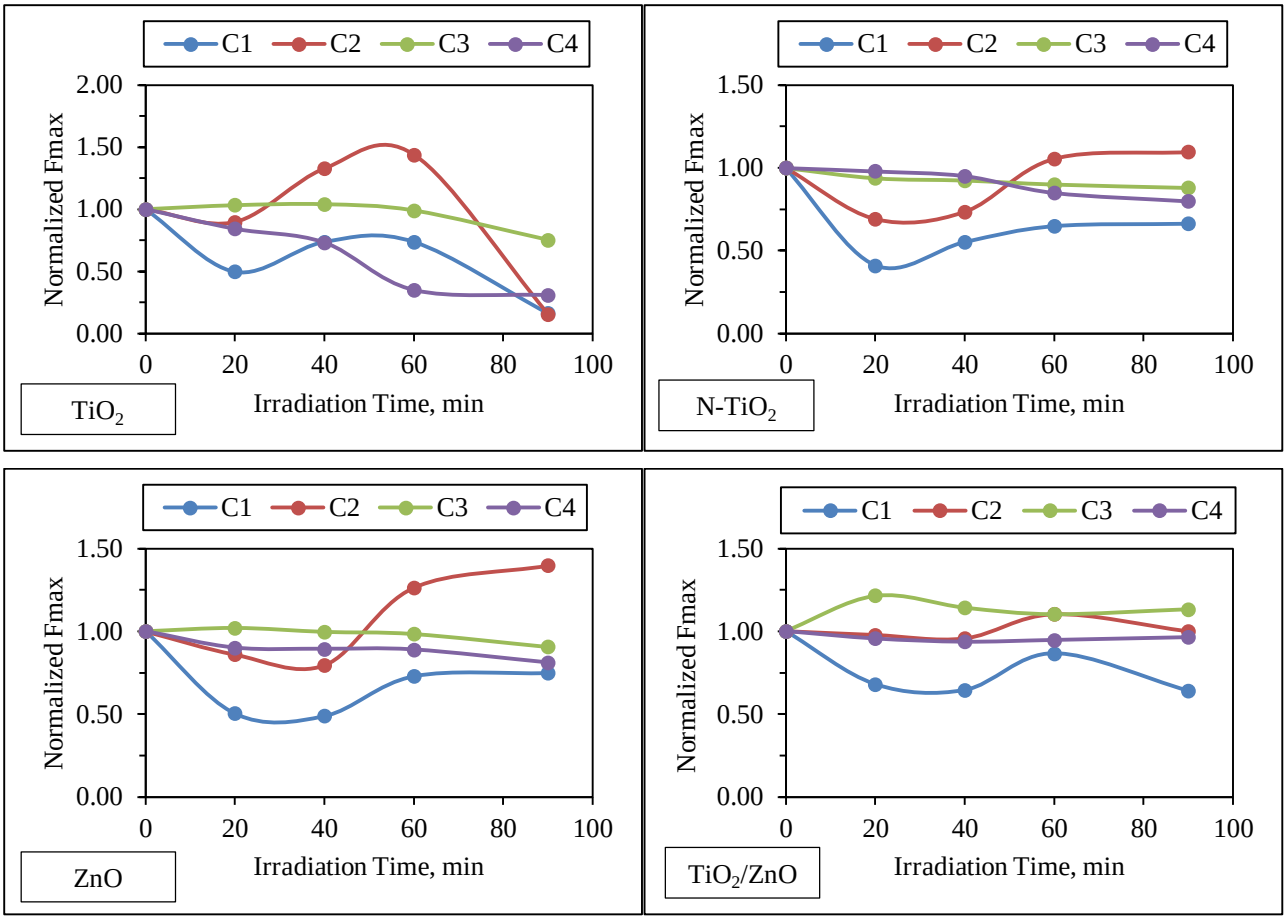

Figure 4.29. Time dependent changes in normalized Fmax values of PARAFAC components identified for ROC_{m2} upon exposure to solar photocatalytic degradation.

Fast removal of C1 and C2 was attained in the first 20 min of the reaction whereas following irradiation periods of 40 min and 60 min, noticeable increase of C1 and C2 was observed in the presence of all photocatalysts. Following solar irradiation period of 90 min, limited removal (< 20%) of C3 and C4 was achieved in the presence of all photocatalyst specimens whereas noticeable formation of C2 was attained in the presence of N-TiO_2, ZnO, and TiO_2/ZnO indicating transformation of high molecular weight components (C3 and C4) into lower molecular weight component (C2) via solar photocatalysis. It has been previously reported that formation of intermediate fluorescent by-products of other PARAFAC components could be released as a result of photo-desorption mechanism occurring in the initial stages of photocatalysis (Wiszniowski et al., 2002; Liu et al., 2008; Nguyen et al., 2013; Ly et al., 2018). Increase in C2 was also observed in the presence of TiO_2 however, upon exposure to solar photocatalysis for 90 min, significant reduction was attained which could be attributed to efficiency of TiO_2 that is able to degrade organic matrix described by various molecular size fractions through a non-selective reaction mechanism. The use of TiO_2 displayed significantly different trend in Fmax of all components in comparison to N-TiO_2, ZnO, and TiO_2/ZnO nanocomposite.

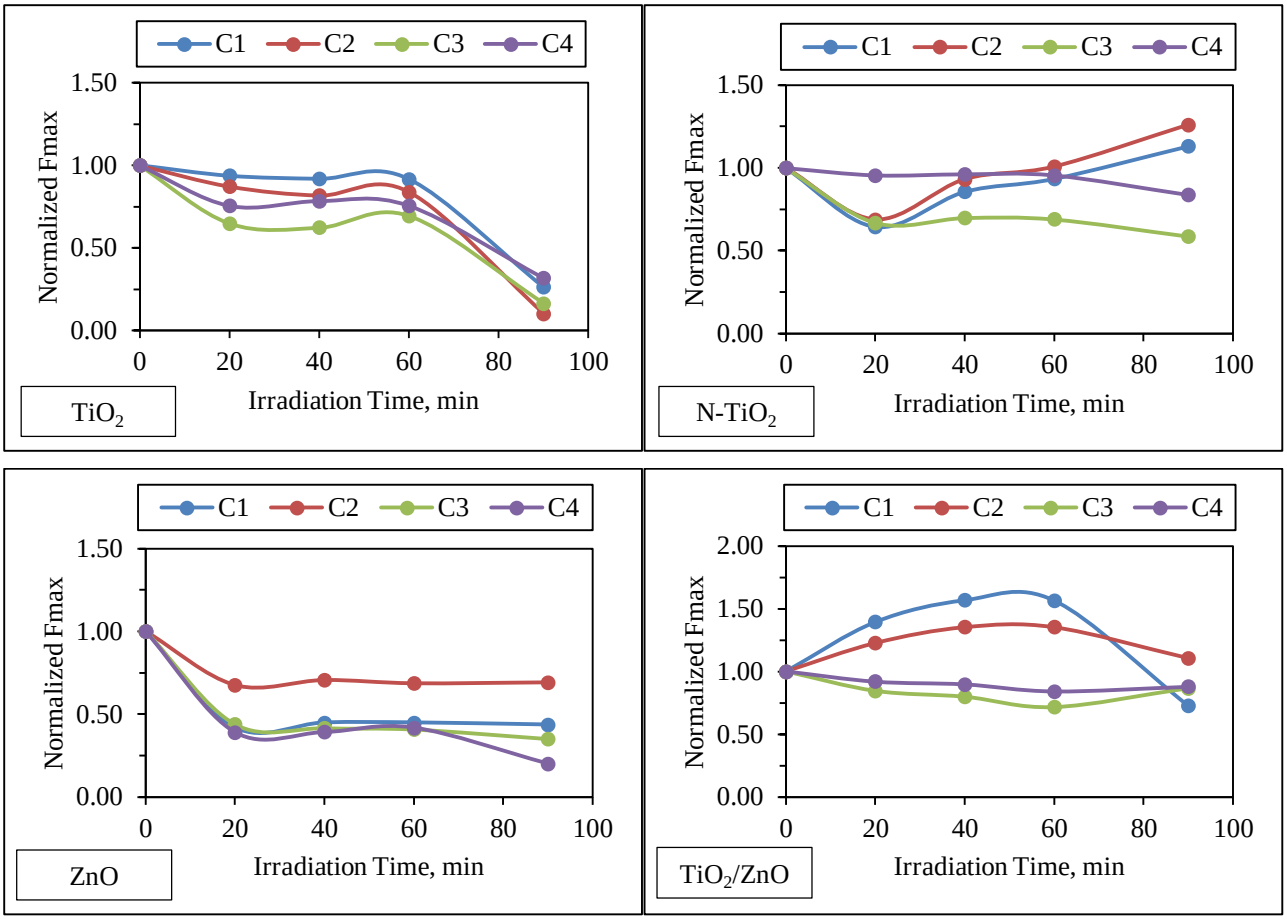

Figure 4.30. Time dependent changes in normalized Fmax values of PARAFAC components identified for ROC_{ECm1} upon exposure to solar photocatalytic degradation.

Rapid removal of all fluorescent components was observed in the early stages of solar photocatalytic reactions in the presence of TiO_2, N-TiO_2, and ZnO, whereas in the presence of TiO_2/ZnO, C1 and C2 tend to increase under the same experimental conditions. Time dependent changes in components were found to be irrelevant in between $t_{irr:}$ 20 min and 60 min for all photocatalysts which could be attributed to the presence of ECs that also react with ROS. Competition between fluorescent components as well as ECs and their reaction intermediates might have caused hindering effect on the removal and/or formation of fluorescent components. Following irradiation period of 90 min, 30-60% removal of all components were attained in the presence of TiO_2 and ZnO as has been reported previously (Zhao et al., 2018). Impulsive changes in fluorophores after 90 min could be addressed to the removal of ECs and their by-products indicating that they were no more present to compete for ROS. On the other hand, N-TiO_2 and TiO_2/ZnO revealed an inverse relationship between high molecular weight compounds and low molecular weight compounds which indicated that during the same irradiation periods, C3 and C4 were decreased while C1 and C2 were increased. The reason could be attributed to break down of large molecular sized aromatic molecules into smaller hydrophilic fragments via photocatalysis (Phong and Hur, 2015; Ly et al., 2018).

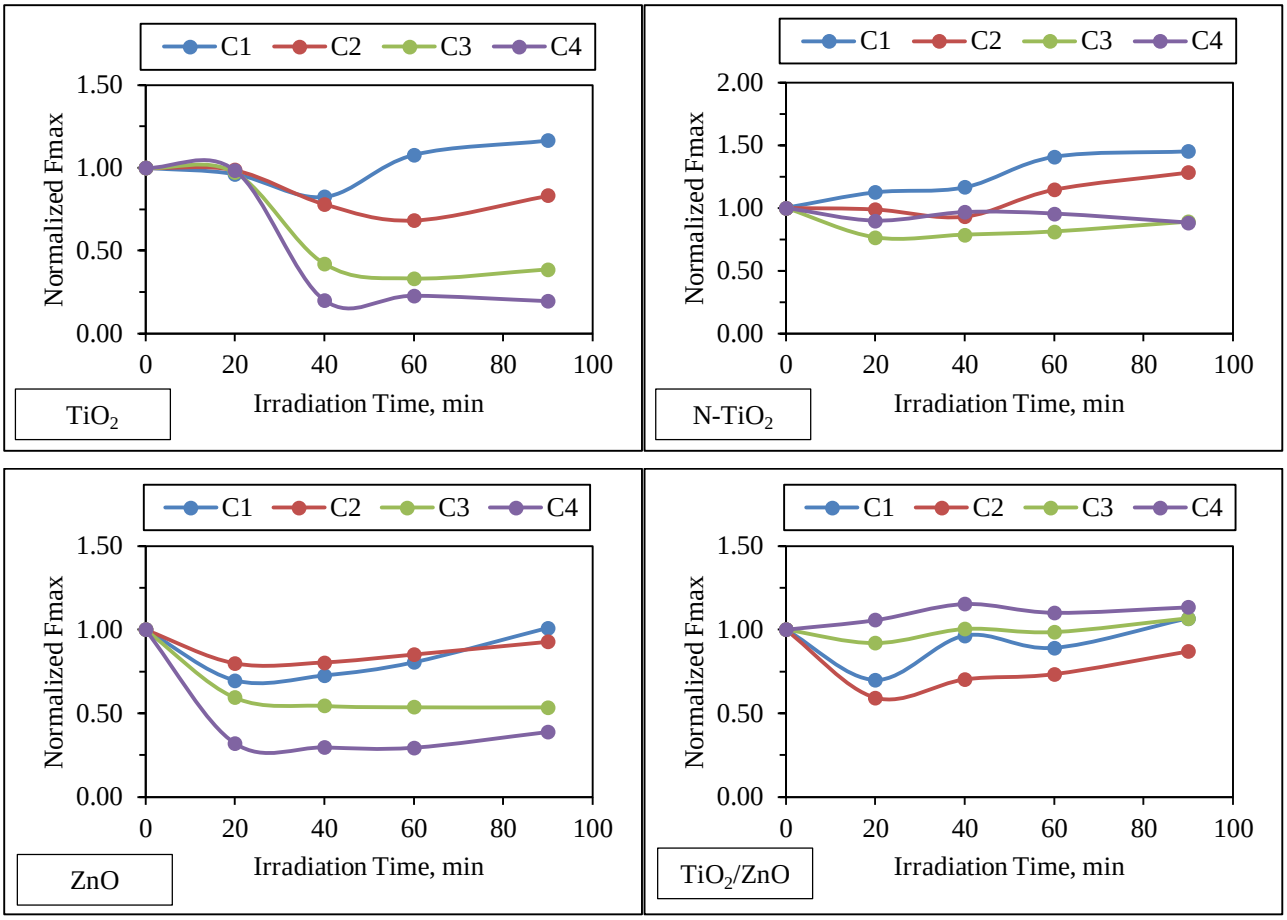

Figure 4.31. Time dependent changes in normalized Fmax values of PARAFAC components identified for ROC_{ECm2} upon exposure to solar photocatalytic degradation.

As a general trend, C1 tend to decrease with respect to increasing irradiation periods in the presence of all photocatalysts for other ROC samples, however, for ROC_{ECm2}, C1 displayed continuous increase upon exposure to solar photocatalysis following irradiation period of 40 min and for further periods even in the presence of TiO_2. In addition, an increase in C3 and C4 was also observed in the presence of N-TiO_2 and TiO_2/ZnO which could be attributed to possible formation of C3 and C4 via photocatalytic degradation of organic matrix present in ROC_{m2} and ROC_{ECm2}. Since ROC_{m2} and ROC_{ECm2} were composed of higher molecular weight HM in comparison to ROC_{m1} and ROC_{ECm1}, solar photocatalytic degradation of HM present in ROC_{m2} and ROC_{ECm2} may cause formation of C3 and C4 could be expected in the early stages (*i.e.* t_{irr}: 20 min) of the reactions (Wiszniowski et al., 2002; Tercero Espinoza et al., 2009; Turong et al., 2019). In addition, changes in C1 and C2 was found to be less noticeable in comparison to ROC_{m1}, ROC_{m2}, and ROC_{ECm2} which could be ascribed to preferential reactions between the photocatalysts and C3 and C4. With respect to concomitant formation and degradation of C3 and C4, there would not be sufficient amount of ROS to react with all fluorescent components especially the ones with more hydrophilic character whose major reaction is based on $HO^{\bullet}$ attack.

4.6. Molecular Size Distribution Profiles of ROC_m and ROC_{ECm} Prior to and Following UVC and Solar Photodegradation and Solar Photocatalytic Degradation Processes

With respect to their self-specific properties, molecular size distribution of organic constituents is a useful analytical tool for the characterization of water and wastewater samples prior to and following treatment processes that express prime importance (Levine et al., 1985). The results enable better interpretation of the following issues: *i.* further understanding of complex interactions between various molecular size fractions of OM and applied treatment processes, *ii.* evaluation, development and selection of finest treatment processes for the removal of target compounds, *iii.* molecular weight cut-off determination of target pollutants that are aimed to be separated by membrane filtration processes (Shon et al., 2006). Fractionation of OM via different methods has gained special interest to obtain information for water and wastewater treatment purposes (Esparza-Soto et al., 2006; Gursoy-Haksevenler and Arslan-Alaton, 2020). Depending on the origin of OM and its chemical structure, several physical and chemical fractionation procedures have been proposed and applied through the literature (Leenher, 1981). Being regarded as the major fraction of OM in water and wastewaters, fractionation of NOM-like components has prime importance (Wershaw and Aiken, 1985; Chon et al., 2017). The most commonly applied physical fractionation techniques comprise ultrafiltration (Alberts and Takács, 1999) and chromatography including HP-SEC (Egeberg et al., 1999) and LC-OCD. In a comparative manner, each technique has its advantages as well as disadvantages (Logan and Jiang, 1990; Egeber et al., 2002).

Among different physical separation techniques, the UF is affordable and thus widely used to separate species by molecular size, shape and charge. This method covers the range of MW distribution from less than 1,000 to more than 100,000 Da. UF involves the selective rejection of solutes by convective flow through a membrane. The targeted MW can be selected in terms of MWCO of membranes. Solutes of larger than the specified MWCO are quantitatively retained, while solutes of smaller MW pass the membrane in the permeate.

Application of physicochemical processes applied either as treatment and/or pretreatment plays a crucial role on the interactions between various molecular size fractions of OM and chemicals used in water and wastewater treatment and even in ROC treatment. Therefore, molecular weight distribution of ROC samples prior to and after coagulation process was evaluated to get a further insight on understanding the role of each molecular size fraction on coagulation process (Zhou et al., 2011; Umar et al., 2014; Umar et al., 2015a; Sun et al., 2016a and b). In addition, influence of MIEX adsorption (Bagastyo et al., 2011), GAC adsorption (Sun et al., 2016a and b; Jamil et al., 2019), and

PAC adsorption (Wang, 2017) on molecular size distribution of ROC has also been evaluated and reported.

Due to their ROS/RS based mechanism, AOPs play a crucial role on the degradation of organics with abundant molecular size distribution profiles (Dong et al., 2010; Awfa et al., 2020). Therefore, assessment of molecular size distribution profiles of water and wastewater samples prior to and following AOPs would bring further understanding on the reactions occurring between RS and fractions of OM, such as: *i.* the dominant fraction or fractions of OM involving reactions with RS, *ii.* resistant fractions that cannot be degraded by applied AOPs, *iii.* improvement of reaction conditions for the degradation of components mentioned in *ii*. Effect of applied AOPs on molecular size distribution profiles of ROC has also been investigated. Influence of various AOPs, such as UVC/H_2O_2 alone or in combination with other processes (Umar et al., 2014 and 2016; Zhang et al., 2018; Pradhan et al., 2020), electrochemical processes (Bagastyo et al., 2011b), and photoelectrochemical processes (Chen et al., 2020), photocatalytic degradation processes (Zhou et al., 2011) on molecular size distribution profiles of ROC was assessed and presented in detail throughout the literature. Further evaluation of the results from this study and through the literature findings will be discussed in following sections.

Specified UV-vis parameters representing the presence of color forming moieties and UV absorbing centers are able to reveal information about the changes occurring in humic characteristics under oxidative and non-oxidative condition (Uyguner-Demirel and Bekbolet, 2011). Further evaluation could be proceeded by spectral differentiation of OM which could be supplied by using absorbance ratios of specified wavelengths. E_{250}/E_{365} or namely E2/E3 ratio regarded as a property for aromaticity and molecular size of the OM (Peuravuori and Pihlaja, 1997; Uyguner and Bekbolet, 200b) whereas E_{254}/E_{436} gives information about ratio of UV absorbing centers to the color forming moieties (Jaffé et al., 2004; Uyguner and Bekbolet, 2005a, b, and c; Rodriguez et al., 2016). In addition, E_{280}/E_{436} reveals additional data of ratio of UV absorbing centers related to aromaticity to color forming moieties and could be assessed comparatively with E_{254}/E_{436} ratio (Uyguner and Bekbolet 2005a and b). E_{465}/E_{665} ratio also known as E_4/E_6 ratio is another parameter as the indicator of condensation degree, aromaticity, particle size and molecular weight of OM (Bloom and Leenheer, 1989; Stevenson, 1982; Chen et al., 1977). However, this parameter should be excluded because it is mostly related to the presence of chromophores absorbing light in the visible region and expresses significance in autochthonous (algal or in situ) sources rather than humic substances. Therefore, with respect to its HA dominated composition and non-existence of color forming moieties as measured absorbances at $\lambda > 500$ nm, E_4/E_6 ratio was not considered for further evaluation of this study.

Based on the above given absorbance ratio information as well as ROC related information, absorbance ratios at 250 nm to 365 nm (E_{250}/E_{365}), 254 nm to 436 nm (E_{254}/E_{436}), 280 nm to 365 nm (E_{280}/E_{365}), and 280 nm to 436 nm (E_{280}/E_{436}) were selected for the assessment of alterations in molecular size fractions of ROC_m and ROC_{ECm} samples prior to and following UVC and solar photodegradation as well as solar photocatalytic degradation processes. Considering the amphiphilic, multi-ligand and polydisperse character of OM that significantly changes with molecular size distribution profiles, the employment of molecular size fractionation of OM present in ROC_m and ROC_{ECm} (Figure 2.2) prior to and following photodegradation and photocatalytic degradation processes were performed. Six nominal molecular weight cut-offs were considered as <0.45 mm ff, <100 kDa fraction, <30 kDa fraction, <10 kDa fraction, <3 kDa fraction and <1 kDa fraction and designated as 0.45 ff, 100 kDa, 30 kDa, 10 kDa, 3 kDa, and 1 kDa respectively.

4.6.1. Specified E Ratios of Molecular Size Fractions of ROC_m and ROC_{ECm} Samples Prior to and Following Photodegradation and Photocatalytic Degradation Processes

In order to achieve baseline information prior to applied processes, changes in specified E ratios of molecular size fractions of ROC_m and ROC_{ECm} samples were presented in Section 4.6.1., Figure 4.32. Then, influence of UVC and solar photodegradation on molecular size distribution profiles of ROC_m and ROC_{ECm} were assessed as presented in Section 4.6.2., figures 4.33-4.36. Since insignificant changes were attained for NPOC removals, fractionation of ROC_m and ROC_{ECm} samples were done following UVC and solar photodegradation period of 90 min. Finally, influence of solar photocatalytic degradation process on molecular size distribution profiles of ROC_m and ROC_{ECm} was assessed using photocatalyst specimens and presented in Section 4.6.3., figures 4.37-4.40. Despite minor changes in NPOC contents of ROC samples upon photodegradation processes, solar photocatalytic degradation causes noticeable alterations due to its ability mineralize carbon content. Therefore, ROC_m and ROC_{ECm} samples were fractioned into nominal molecular weight cut-offs following solar photocatalytic irradiation periods when 50-60% NPOC removal was achieved. Changes in molecular size fractions of ROC_m and ROC_{ECm} samples prior to and following photodegradation and photocatalytic degradation processes were evaluated in terms of specified and specific UV-vis and fluorescence spectroscopic parameters as well as organic carbon contents. Complementary to specified UV-vis parameters, absorbance ratios of these specified UV-vis parameters would bring further insight on the understanding of changes in humic-like matter present in ROC_m and ROC_{ECm}. For this purpose, absorbance ratios as E_{250}/E_{365}, E_{254}/E_{436}, E_{280}/E_{365}, and E_{280}/E_{436} were determined and assessed.

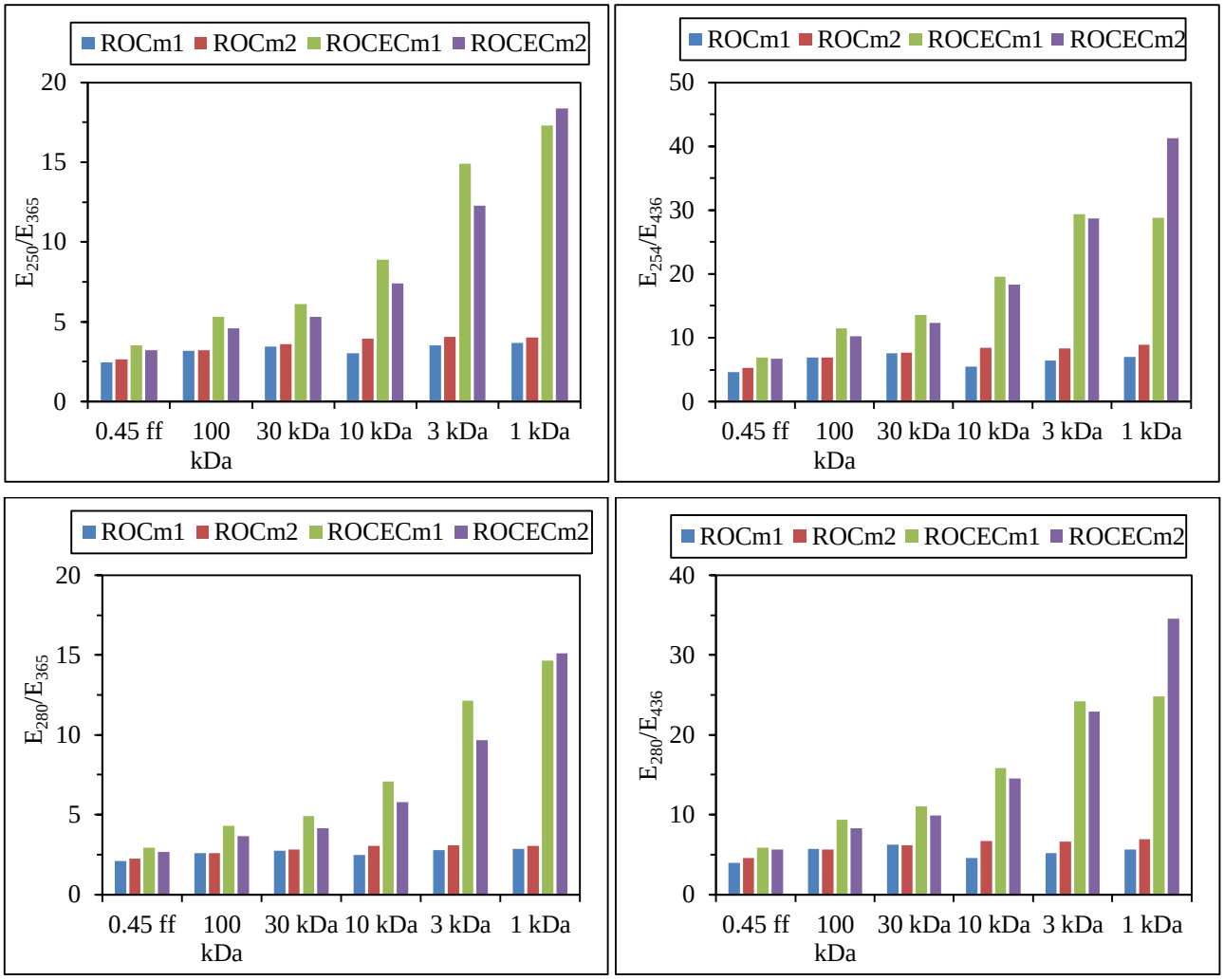

Figure 4.32. Fractional changes in molecular size distribution profiles of ROC_m and ROC_{ECm} expressed as E_{250}/E_{365}, E_{254}/E_{436}, E_{280}/E_{365}, and E_{280}/E_{436} absorbance ratios.

E_{250}/E_{365} ratios were expressed similar values irrespective of the ROC origin between size fractions of 0.45 ff (between 2.47 and 3.21) and 100 kDa (between 3.19 and 4.60), whereas differences were attained for 30 kDa and 10 kDa molecular size fractions of ROC_{ECm1} and ROC_{ECm2} which revealed slight increases in comparison to ROC_{m1} and ROC_{m2}. Moreover, the most significant gap was observed for the lower molecular size fractions of 3 kDa and 1 kDa. With respect to their molecular weight (SMX: 253.28 Da and CMZ: 236.27 Da), presence of ECs even in lower molecular size fractions of ROC_{ECm1} and ROC_{ECm2} is expected. Increase of E ratios for lower molecular size fractions could be attributed to contribution of ECs to the overall aromaticity of ROC_{ECm} samples which was proven by the specified UV-vis parameters as well as NPOC contents as reported previously (Table H1, Appendix H). As a general trend, all specified E ratios displayed irrelevant changes for all ROC samples for the molecular size fractions 0.45 ff, 100 kDa, and 30 kDa, whereas significant differences were attained for the molecular size fractions less than 10 kDa.

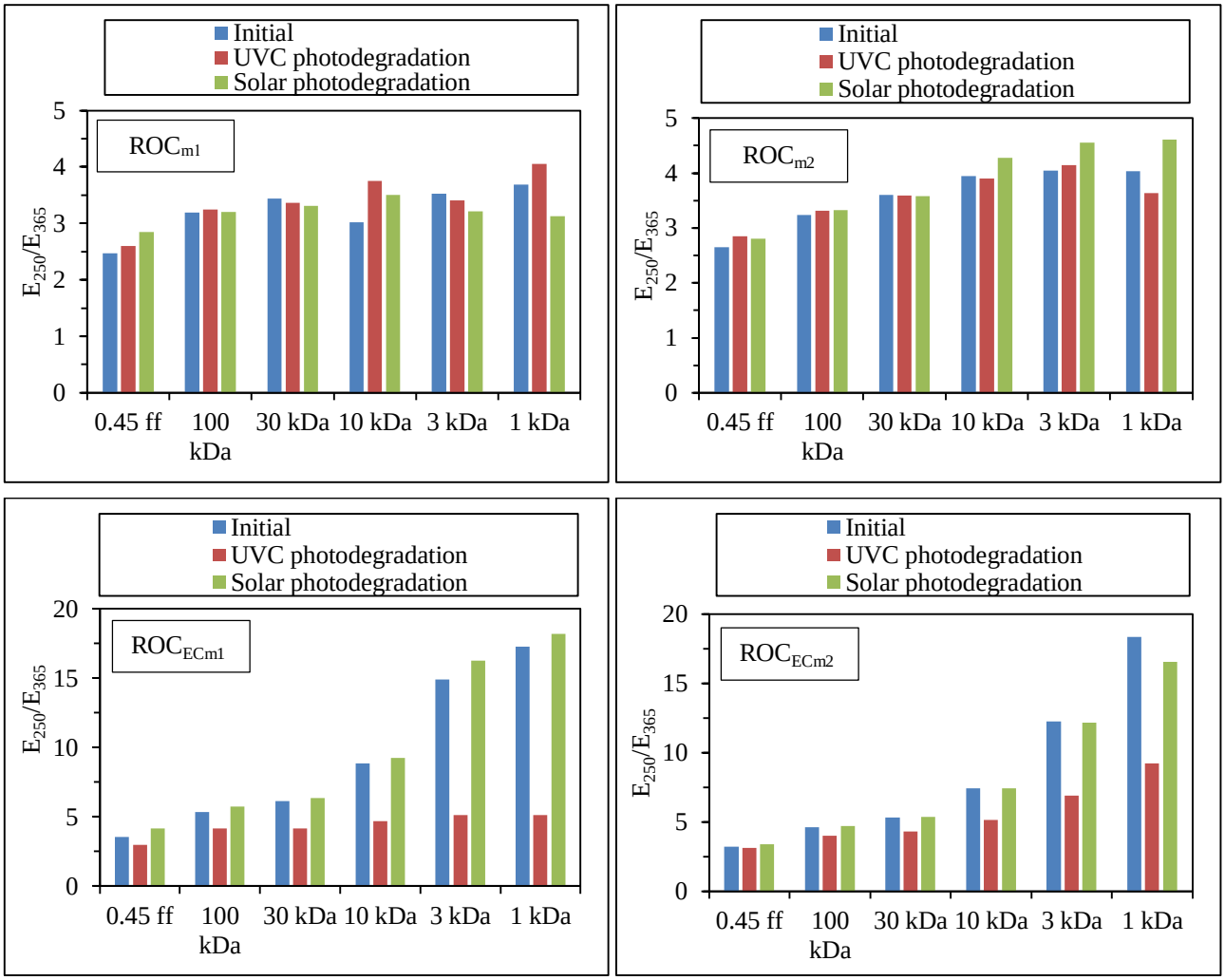

Figure 4.33. E_{250}/E_{365} ratio: Fractional changes in molecular size distribution profiles of ROC_m and ROC_{ECm} prior to and following UVC (λ: 254 nm, I_o: $1.80x10^{17}$ quanta/sec) and solar photodegradation processes (λ: 290-700 nm, I_o: $1.73x10^{16}$ quanta/s).

Upon exposure to UVC and solar photodegradation, slight changes in $E_{250/365}$ ratio were observed for the fractions 10 kDa, 3 kDa, and 1 kDa of ROC_{m1} and ROC_{m2}, whereas in the presence of ROC_{ECm1} and ROC_{ECm2}, distinct differences were attained for the same fractions. In addition, molecular size dependent ratios of ROC_{m1} and ROC_{m2} displayed almost no differences even though their organic matter compositions display distinct spectroscopic features. Upon exposure to solar photodegradation process, slight increase in E_{250}/E_{365} could be attributed to photodegradation and of HM via solar light initiated reactions with the involvement of common anions that also undergo various reactions and forms radicals (reactions 4.13-4.16) as previously reported in Section 4.4.1.2. On the other hand, significant reduction of E_{250}/E_{365} ratio of molecular size fractions of ROC_{ECm1} via UVC photodegradation could be attributed to noticeable reduction of UV_{250} (0.562 cm^{-1} for solar photodegradation and 0.396 cm^{-1} for UVC photodegradation) and insignificant reduction of UV_{365} (0.031 cm^{-1} for solar photodegradation and 0.078 cm^{-1} for UVC photodegradation).

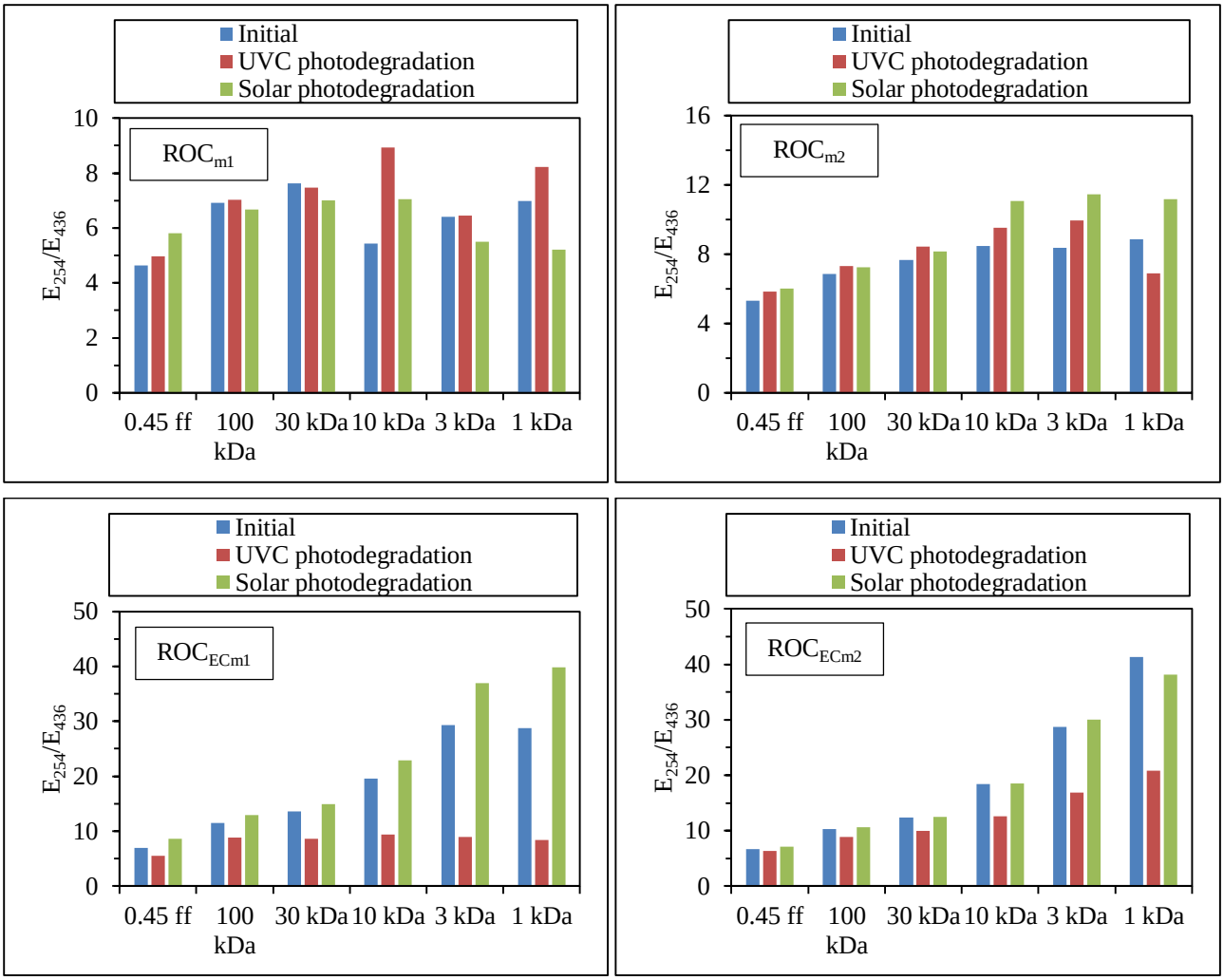

Figure 4.34. E_{254}/E_{436} ratio: Fractional changes in molecular size distribution profiles of ROC_m and ROC_{ECm} prior to and following UVC (λ: 254 nm, I_o: $1.80x10^{17}$ quanta/sec) and solar photodegradation processes (λ: 290-700 nm, I_o: $1.73x10^{16}$ quanta/s).

E_{254}/E_{436} ratio indicates the intensity of UV absorbing functional groups compared to color forming moieties (Uyguner and Bekbolet, 2005b). Almost no discriminative difference was attained for the fractions 0.45 ff, 100 kDa, and 30 kDa of all ROC samples either exposed to UVC or solar photodegradation processes. Photodegradation of HM in ROC composition revealed relatively slower reduction of UV_{254} in comparison to color forming moieties, therefore decrease in $Color_{436}$ and almost no change in UV_{254}, ended up with the increase of E_{254}/E_{436} values. It's been previously reported by Jaffé and colleagues that increase in E_{254}/E_{436} ratio could be attributed to photobleaching of NOM and its analogue compounds via sunlight induced reactions (Jaffé et al., 2004). Although humic matter is the basis of OM in ROC composition, it could also express removal of color forming moieties ($Color_{436}$) similar to photobleaching which explains increase in different molecular size fractions of ROC_m and ROC_{ECm} samples upon solar photodegradation process in comparison to initial conditions.

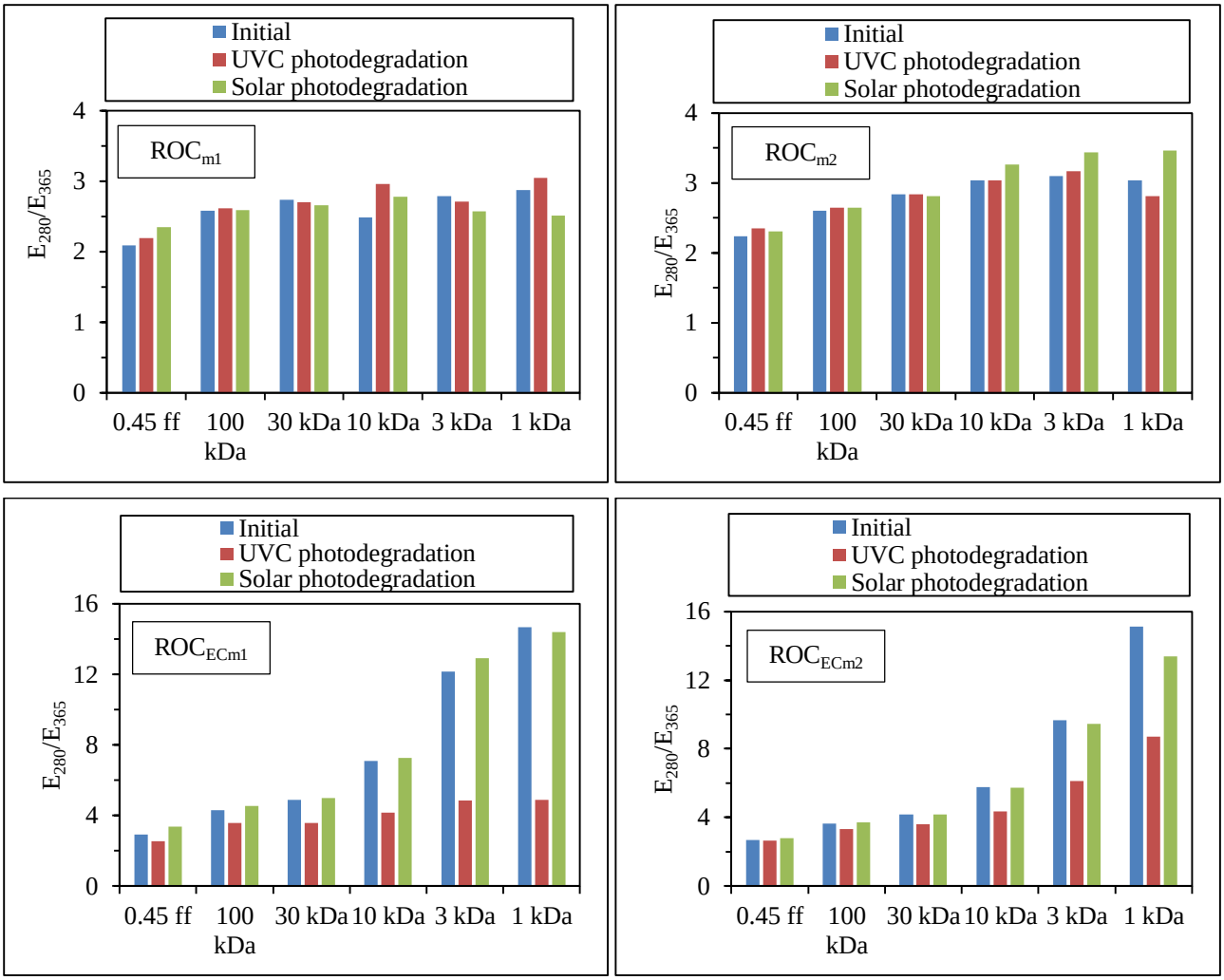

Figure 4.35. E_{280}/E_{365} ratio: Fractional changes in molecular size distribution profiles of ROC_m and ROC_{ECm} prior to and following UVC (λ: 254 nm, I_o: $1.80x10^{17}$ quanta/sec) and solar photodegradation processes (λ: 290-700 nm, I_o: $1.73x10^{16}$ quanta/s).

Similar to E_{250}/E_{365} and E_{254}/E_{436} ratios, insignificant differences were attained for E_{280}/E_{365} ratios of ROC_{m1} and ROC_{m2} for almost all fractions whereas, in the presence of ROC_{ECm1} and ROC_{ECm2}, noticeable difference was observed for the fractions 3 kDa and 1 kDa which could be attributed to the presence of ECs especially CMZ. For 3 kDa fraction of all ROC samples, UV_{280} was found to be in the ranges of 0.124-0.153 cm^{-1} for ROC_{m1}, 0.409-0.466 cm^{-1} for ROC_{ECm1}, 0.153-0.189 cm^{-1} for ROC_{m2}, and 0.448-0.500 cm^{-1} for ROC_{ECm2}, whereas UV_{365} values varied between 0.038 and 0.085 cm^{-1} for all ROC samples (Table H3, H5, H7, and H9, Appendix H). Noticeably higher UV_{280} values for ROC_{ECm1} and ROC_{ECm2} could be related to presence of CMZ giving characteristic absorbance peak at λ: 285 nm and its transformation by-product as 10-hydroxycarbamazepine giving maxima at λ: 270 nm both of which contribute to the absorbance at around 280 nm. In addition, insignificant change between UV_{365} values of ROC_m and ROC_{ECm} samples ended up with higher E_{280}/E_{365} ratios of ROC_{ECm1} and ROC_{ECm2} in comparison to ROC_{m1} and ROC_{m2}.

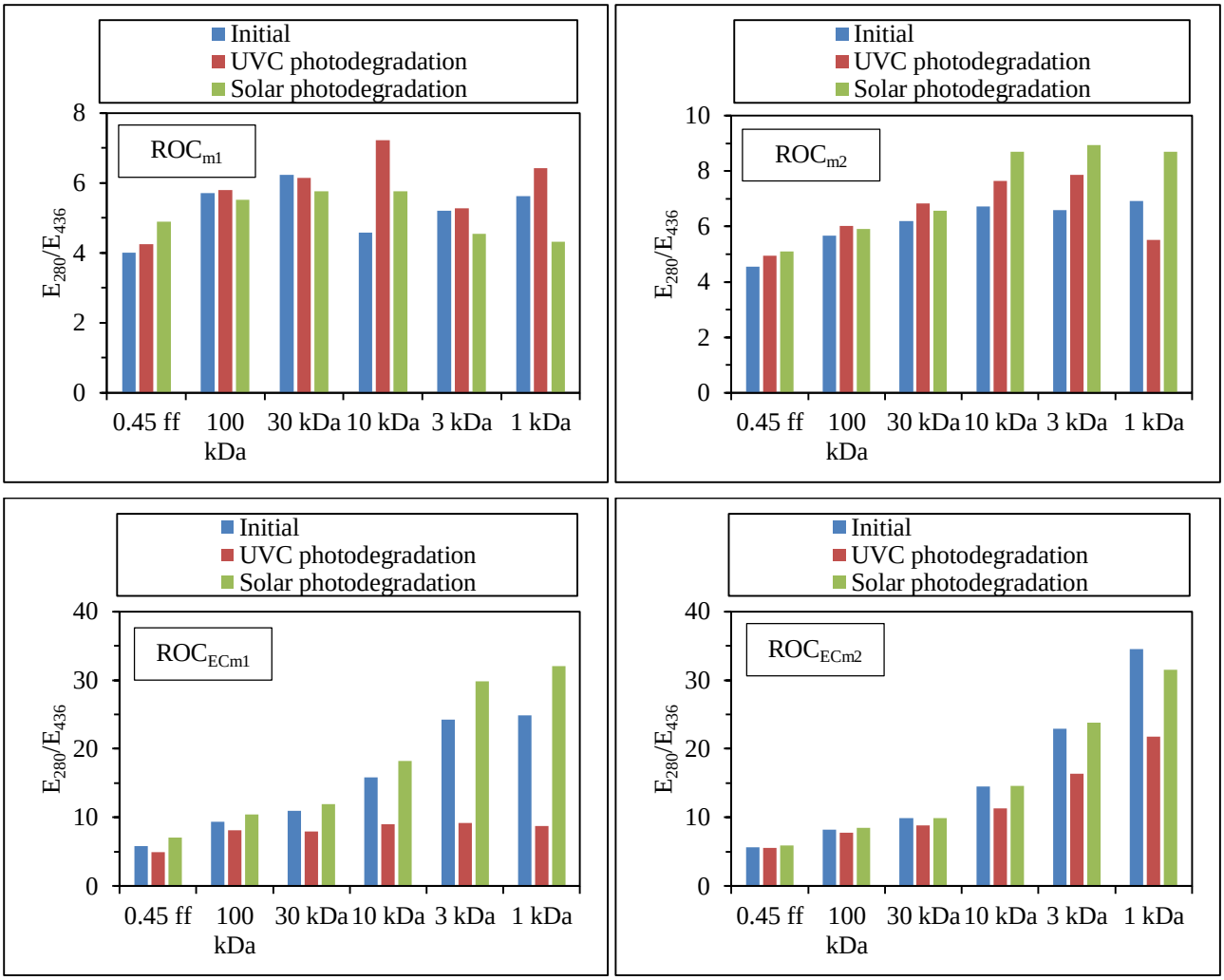

Figure 4.36. E_{280}/E_{436} ratio: Fractional changes in molecular size distribution profiles of ROC_m and ROC_{ECm} prior to and following UVC (λ: 254 nm, I_o: $1.80x10^{17}$ quanta/sec) and solar photodegradation processes (λ: 290-700 nm, I_o: $1.73x10^{16}$ quanta/s).

E_{280}/E_{436} ratios of molecular size fractions of ROC_{m1} and ROC_{m2} revealed slight variations prior to and following UVC and solar photodegradation processes, whereas noticeable differences were attained in the presence of ROC_{ECm1} and ROC_{ECm2}. The reason could be attributed to absorption spectrum of CMZ which gives maxima at λ: 285 nm and therefore absorbs irradiation at this wavelength. In the presence of UVC irradiation, light absorption of SMX and CMZ would be the major degradation mechanism, however, in the presence of solar irradiation, photosensitizing effect of HM as well as solar light initiated reactions of anions (Section 4.4.1.2., reactions 4.13-4.16) would dominate the degradation mechanism which explains distinct profiles of E_{280}/E_{436} ratios of ROC_{ECm1} and ROC_{ECm2}. Although UV_{254} and UV_{280} are interchangeably used to represent the aromaticity of humic matter through the literature, E_{280}/E_{436} and E_{254}/E_{436} were deviated from each other with respect to molecular size fractions by approximately 15-20 % difference indicating the importance of UV_{280} as a discrete parameter especially in the presence of ECs (Uyguner and Bekbolet, 2005b).

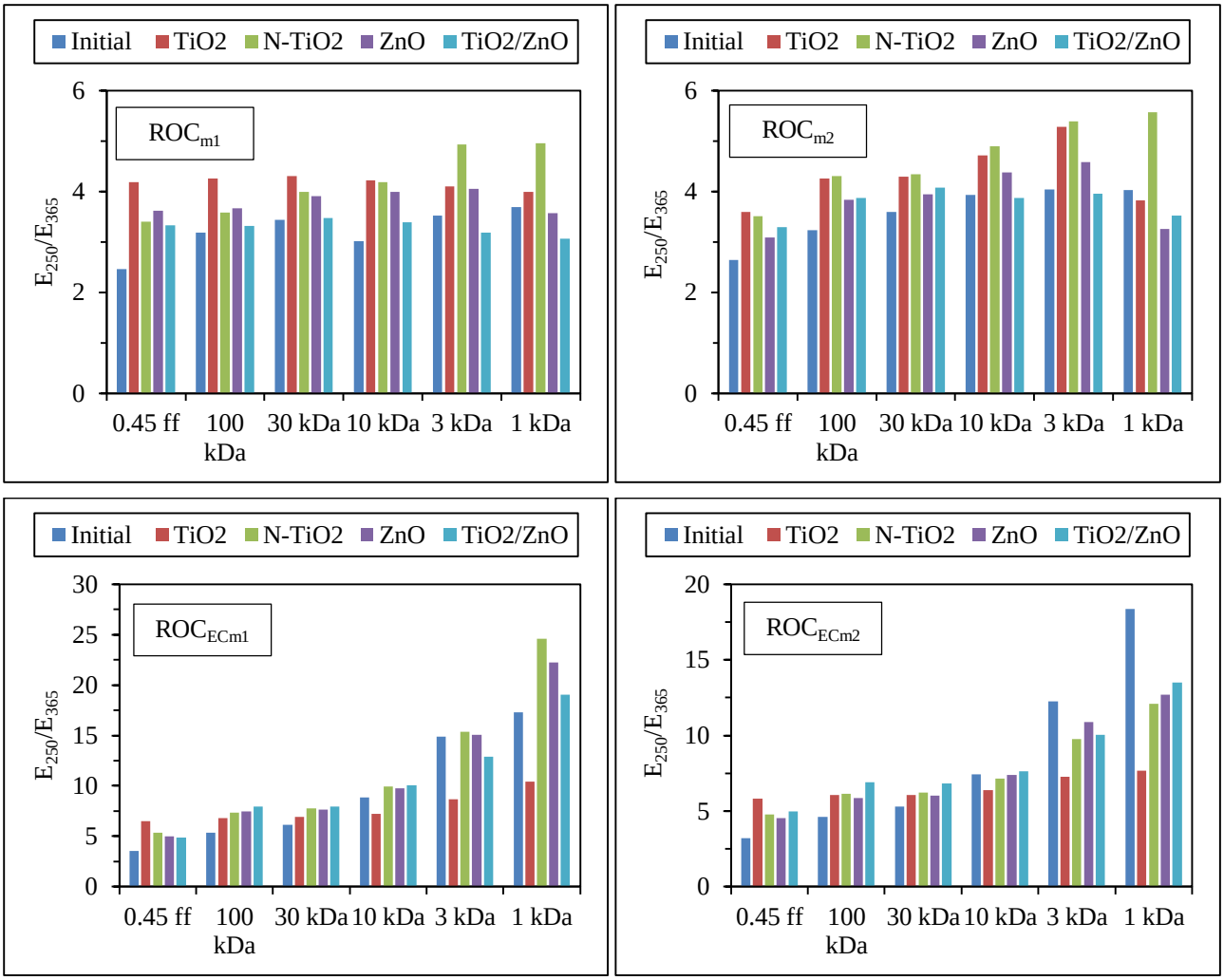

Figure 4.37. E_{250}/E_{365} ratio: Fractional changes in molecular size distribution profiles of ROC_m and ROC_{ECm} prior to and following solar photocatalytic degradation process (I_o: $1.73x10^{16}$ quanta/s).

E_{250}/E_{365} ratios for all ROC samples were expressed similar patterns irrespective of the photocatalyst specimen type between molecular size fractions of 0.45 ff and 30 kDa. Increase in E_{250}/E_{365} ratios for 0.45 ff, 100 kDa, and 30 kDa fractions of all ROC samples following solar photocatalytic degradation process indicated reduction in molecular size in comparison to initial conditions which could be attributed to degradation of high molecular weight humic compounds. However, ROC_{ECm1} and ROC_{ECm2} revealed the most prominent changes in E_{250}/E_{365} ratios for molecular size fractions as 3 kDa and 1 kDa fractions in comparison to ROC_{m1} and ROC_{m2}. The discriminative differences between these samples could be attributed to the presence of ECs whose RS/ROS consumption ended up with lower removal efficiency of aromatic structure of humic matter giving high absorbance values at corresponding wavelengths. Molecular size specific distribution of E_{250}/E_{365} ratio in the absence/presence of ECs could be clearly visualized with respect to the changes attained prior to and following photocatalytic degradation of ROC_m and ROC_{ECm} samples (Uyguner and Bekbolet, 2005b).

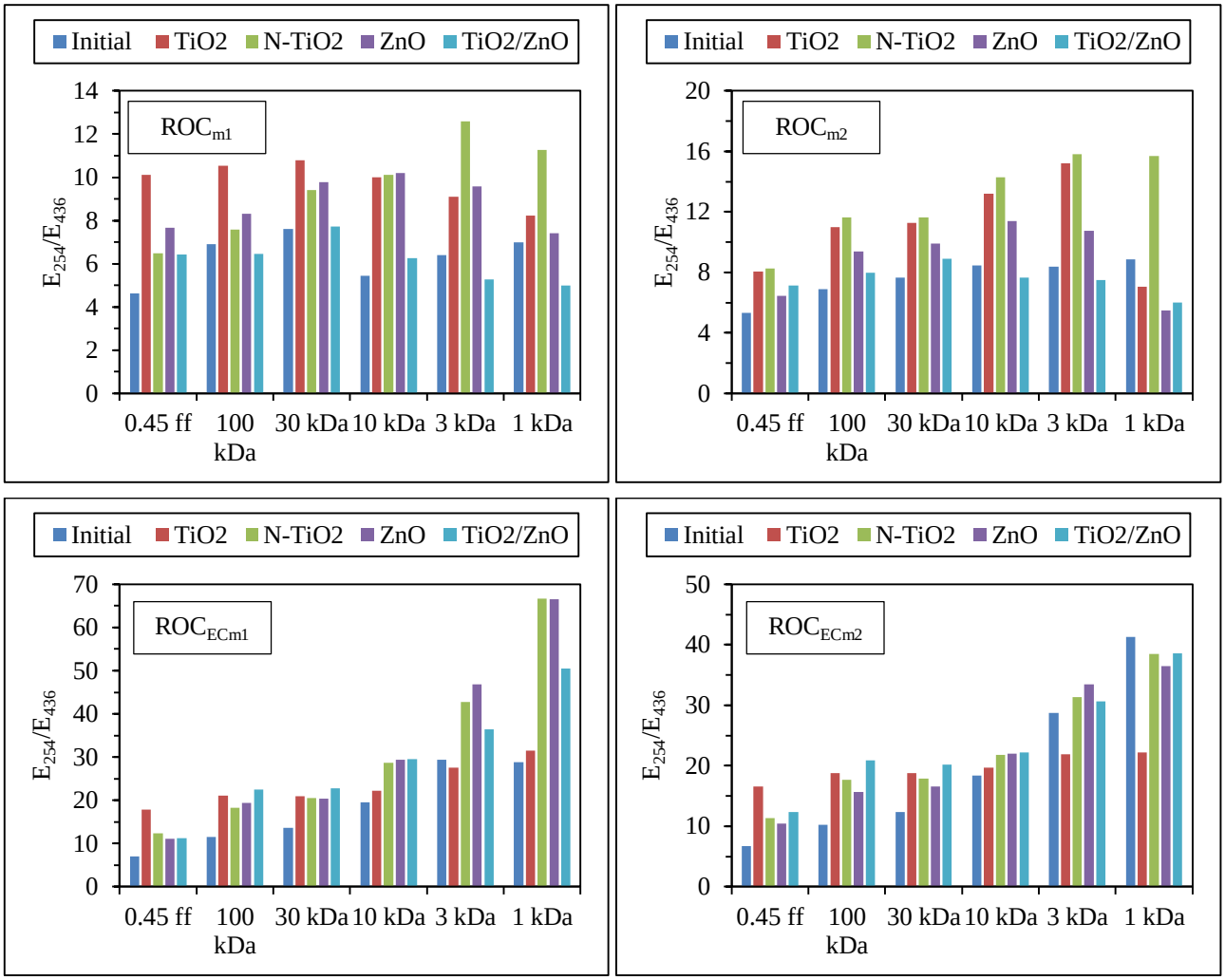

Figure 4.38. E_{254}/E_{436} ratio: Fractional changes in molecular size distribution profiles of ROC_m and ROC_{ECm} prior to and following solar photocatalytic degradation process (I_o: $1.73x10^{16}$ quanta/s).

Noteworthy changes in E_{254}/E_{436} ratios of molecular size distribution of ROC_{ECm} samples were attained even in larger molecular size fractions, *i.e.* 100 kDa in comparison to ROC_m samples which could be attributed to the presence of ECs. Since there is competition between HM and ECs and their transformation products for ROS, removal of the specified UV-vis parameters was hindered as has been previously reported in Section 4.2.2.2. Consequently, the reduction in $Color_{436}$ of ROC_{m1} and ROC_{ECm1} displayed similar results, however, UV_{254} values of size fractions of 3 kDa and 1 kDa of ROC_{ECm1} found to be 2 to 5 times higher than the value attained for ROC_{m1} explaining the drastic increase in $E_{254}/Colo_{436}$ ratio for the fractions 100 kDa, 30 kDa, 10 kDa, and especially for 3 kDa and 1 kDa. The same trend was also observed for ROC_{m2} and ROC_{ECm2} under the same conditions. ROC_{ECm1} revealed almost no difference between the photocatalyst specimens for the fractions 100 kDa, 30 kDa and 10 kDa, whereas photocatalyst specific changes were observed for the fractions 3 kDa and 1 kDa. As a general trend, increase in E_{254}/E_{436} could be attributed to faster removal of color forming moieties in comparison to UV absorbing centers (UV_{254}) as previously reported (Table 4.3).

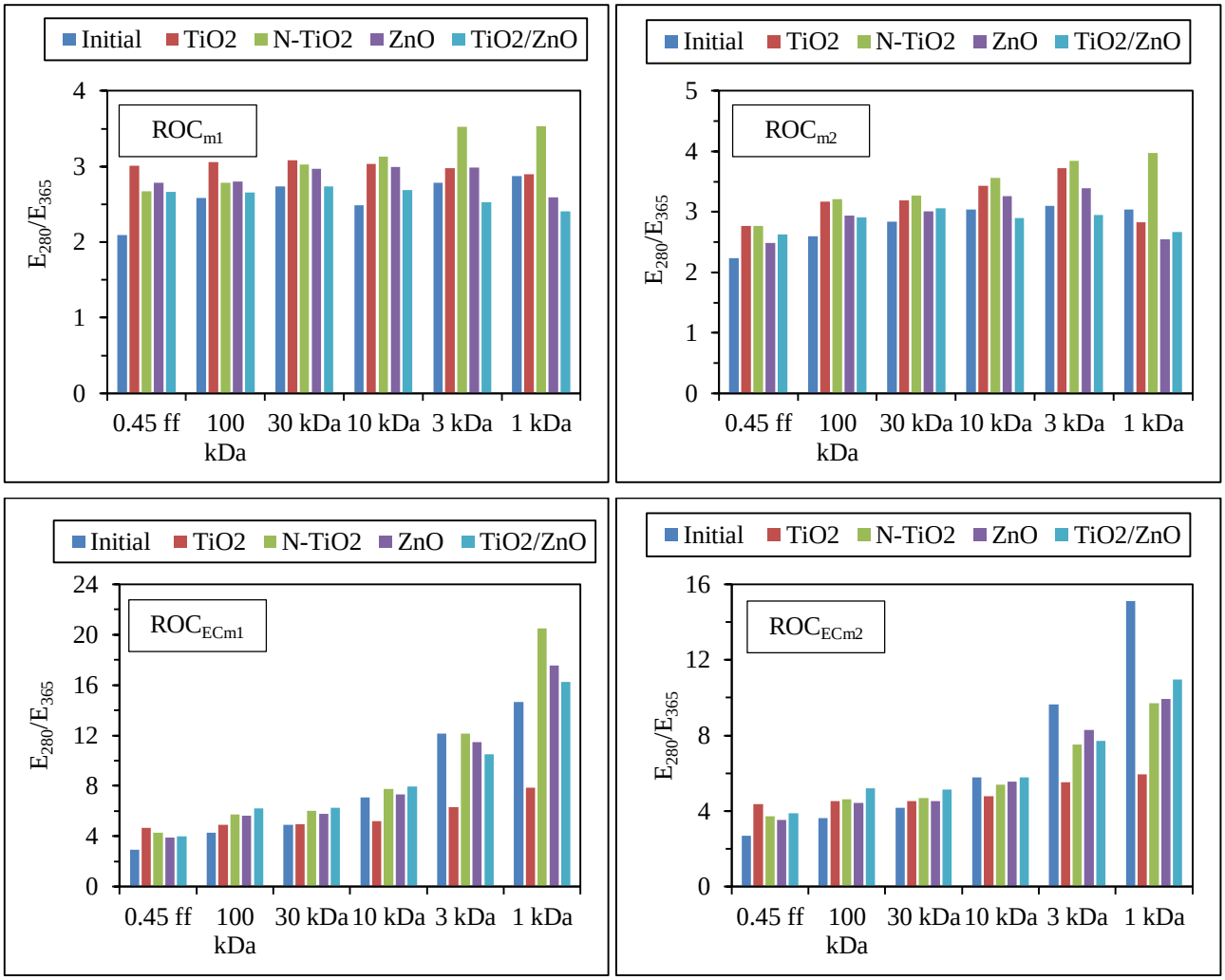

Figure 4.39. E_{280}/E_{365} ratio: Fractional changes in molecular size distribution profiles of ROC_m and ROC_{ECm} prior to and following solar photocatalytic degradation process (I_o: $1.73x10^{16}$ quanta/s).

E_{280}/E_{365} ratios exhibit similar trends with insignificant absorbance ratios for the fractions 0.45 ff, 100 kDa, 30 kDa, and 10 kDa, whereas discriminative differences were observed for 3 kDa and 1 kDa fractions of ROC_{ECm1} and ROC_{ECm2} similarly obtained in previous E ratios. A plausible explanation could be related to the concomitant removal of specified UV-vis parameters via photocatalytic degradation process, however prominence of ECs is still valid for the fractions of 3 kDa and 1 kDa of which UV_{280} values are considerably higher than the values attained for ROC_{m1} and ROC_{m2}. Under the same conditions, concurrent removal of UV_{280} and UV_{365} is expected for ROC_{ECm1} and ROC_{ECm2} as attained for ROC_{m1} and ROC_{m2}, however retardation effect of ECs revealed higher UV_{280} values for ROC_{ECm1} (0.419-0.464 cm^{-1} for 3 kDa fractions and 0.315-0.390 cm^{-1} for 1 kDa fractions) and ROC_{ECm2} (0.490-0.589 cm^{-1} for 3 kDa fractions and 0.374-0.475 cm^{-1} for 1 kDa fractions) compared to ROC_{m1} (0.124-0.246 cm^{-1} for 3 kDa fractions and 0.075-0.157 cm^{-1} for 1 kDa fractions) and ROC_{m2} (0.153-0.245 cm^{-1} for 3 kDa fractions and 0.081-0.216 cm^{-1} for 1 kDa fractions) therefore ended up with higher E_{280}/E_{365} ratios.

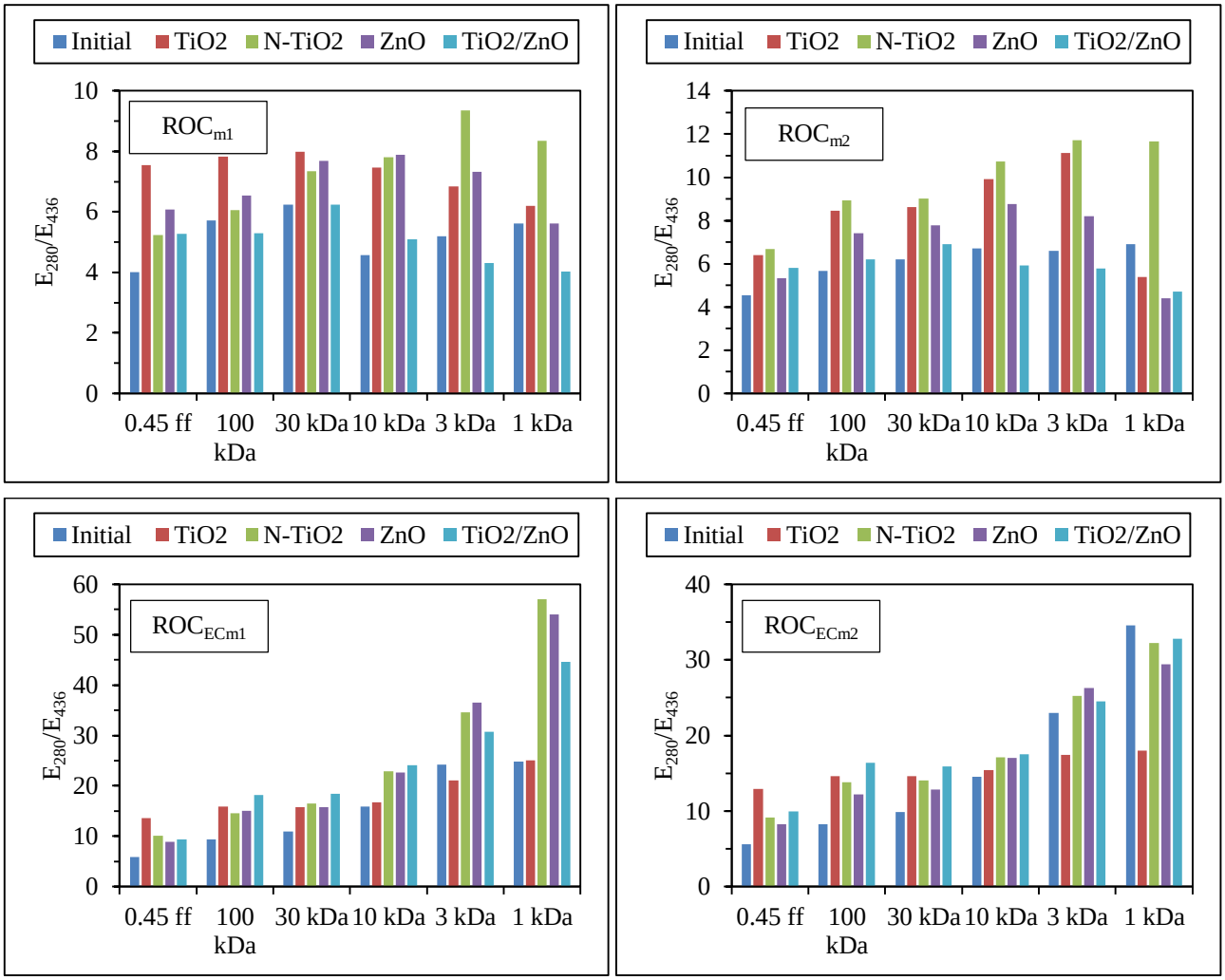

Figure 4.40. E_{280}/E_{436} ratio: Fractional changes in molecular size distribution profiles of ROC_m and ROC_{ECm} prior to and following solar photocatalytic degradation process (I_o: $1.73x10^{16}$ quanta/s).

E_{250}/E_{365}, E_{254}/E_{436}, and E_{280}/E_{365} ratios of ROC samples tend to display noticeable differences preferably for lower molecular size fractions, such as 3 kDa and 1 kDa fractions of ROC_{ECm1} and ROC_{ECm2} samples, whereas distinct E_{280}/E_{436} ratios were attained even for ROC_{m1} and ROC_{m2} samples and for all of their molecular size fractions. Although similar $Colo_{436}$ values were attained for the same molecular size fractions of ROC_{m1} (in the ranges of 0.006 cm^{-1} and 0.094 cm^{-1}) and ROC_{ECm1} (in the range of 0.007 cm^{-1} and 0.108 cm^{-1}) as well as for ROC_{m2} (in the ranges of 0.010 cm^{-1} and 0.137 cm^{-1}) and ROC_{ECm2} (in the ranges of 0.011 cm^{-1} and 0.141 cm^{-1}), UV_{280} values of ROC_{m1} (in the ranges of 0.075 cm^{-1} and 0.499 cm^{-1}), ROC_{m2} (in the ranges of 0.113 cm^{-1} and 1.173 cm^{-1}), ROC_{ECm1} (in the ranges of 0.343 cm^{-1} and 0.954 cm^{-1}), and ROC_{ECm2} (in the ranges of 0.374 cm^{-1} and 1.267 cm^{-1}) samples were tremendously differed from each other due to presence of ECs as well as their transformation by-products explained in detail previously. Consequently, prominence of UV absorbing centers addressed to ECs in lower molecular size fractions caused noticeable differences in E_{280}/E_{436} ratios of ROC_{ECm1} and ROC_{ECm2} in comparison to ROC_{m1} and ROC_{m2}.

4.6.2. Proportional NPOC Distribution Profiles of Molecular Size Fractions of ROC_m and ROC_{ECm} Prior to and Following UVC and Solar Photodegradation as well as Solar Photocatalytic Degradation Processes

Molecular size distribution profiles provide information on *i.* degradation of each molecular size fraction via oxidation, *ii.* in-situ fragmentation of higher molecular size fractions to lower molecular size fractions. Owing to its insignificant change in NPOC removal efficiencies with respect to increasing irradiation periods, molecular size fractionation of ROC samples was carried out by using samples exposed to photodegradation for t_{irr}: 60 min. On the other hand, for photocatalytic degradation experiments, upon 50-60% NPOC removal was achieved, samples were subjected to molecular size fractionation using selected photocatalyst specimens. Prior to and following photolysis and photocatalysis processes, ROC_{m1}, ROC_{m2}, ROC_{ECm1} and ROC_{ECm2} were fractioned into 6 nominal molecular weight cut-offs and each fraction (F) was defined as follows: 0.45 μm ff >F1>100 kDa, 100 kDa>F2>30 kDa, 30kDa>F3>10 kDa, 10kDa>F4>3kDa, 3kDa>F5>1kDa, and F6<1kDa. Transformations observed on the fractional distribution percentages of each ROC_m and ROC_{ECm} samples were expressed in terms of NPOC, and results were presented in Figure 4.41.

Molecular size fractionation of ROC samples before treatment processes has been investigated and each fraction was expressed in terms of NPOC: 80% NPOC corresponded to MW <10 kDa, 10% corresponded to 10-100 kDa, and 10% corresponded to >100 kDa indicating the majority of organics lower molecular size (Lee et al., 2009). Another study categorized molecular size fractions of ROC in terms of NPOC percentages as 47% for <1 kDa, 37% for 1-10 kDa, 11% for 10-100 kDa and 5% for < 1kDa (Zhou et al., 2011). In our study, under initial conditions, % NPOC distribution of fractions were found to be higher for higher molecular size fractions of F1, F2, and F3 whose molecular weight cut-off corresponding to the fractions > 30 kDa. The differences between these studies and our results could mainly be attributed to the differences in ROC origin at hereby to organic matter composition. Obtaining ROC samples from real wastewater reclamation plants could end up in diverse organic components. On the other hand, molecular size distribution process for ROC samples originated from municipal wastewater reclamation expressed majority of NPOC percentage assigned to humics (50%) and biopolymers (8%) with molecular weight cut-offs of 1-20 kDa and > 20 kDa indicating possible existence and superiority of higher molecular weight complex organics in ROC consortia (Umar et al., 2014). Although only difference between ROC_m samples and ROC_{ECm} samples was the presence of ECs in solution matrix, its impact on the molecular size distribution profiles of initial conditions could be easily observed. The reason could be attributed to the potential host-guest interactions between humic fractions and ECs (Uyguner-Demirel et al., 2017).

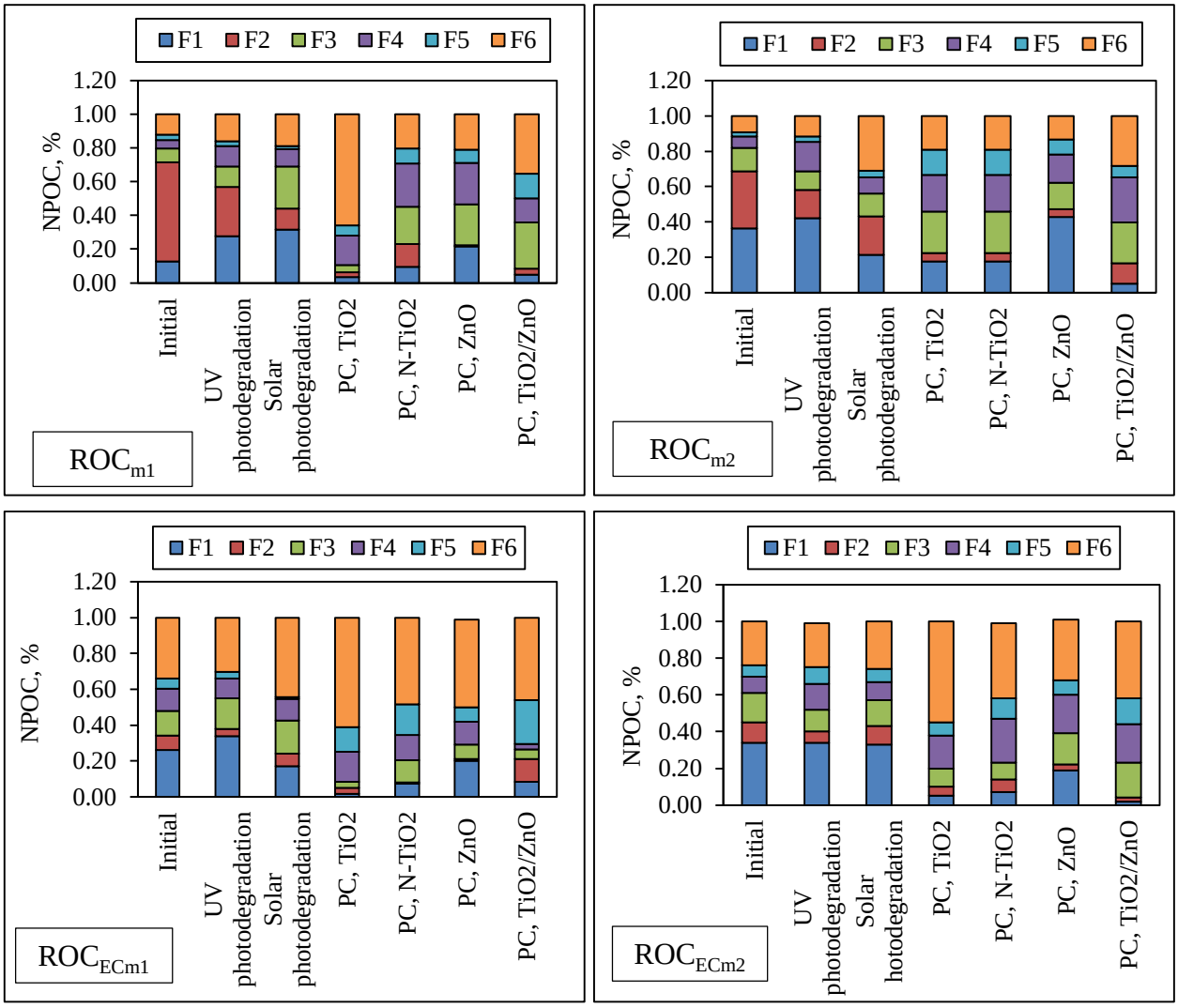

Figure 4.41. Changes in molecular size distribution profiles of ROC_m and ROC_{ECm} prior to and following photodegradation and photocatalytic degradation processes expressed in terms of NPOC (PC denotes photocatalytic degradation).

Shift from higher molecular size fractions to lower molecular size fractions in ROC_{m1} was observed even after UV and solar photodegradation degradation processes. On the other hand, the most significant shift from higher fractions to lower fractions was observed for the photocatalytic degradation of ROC_{m1} in the presence of TiO_2, by which percentage of fraction F6 increased from 11% to 66%. The main contributors to the formation of organics in F6 were fractions F1 and F2 whose percentages reduced from 55% to 3% and from 19% to 3%. Following photocatalytic degradation process, fraction F2 was almost removed in the presence of all photocatalysts. On the other hand, fraction F3 was still prominent in the presence of N-TiO_2, ZnO, and TiO_2/ZnO nanocomposite in comparison to TiO_2 by which percentage of F3 was reduced to < 5%. Results were found to be in accordance with the previous studies in which potential effect of ozonation on the molecular size distribution profiles of ROC investigated in terms of three nominal molecular weight

cut-offs of 100 kDa, 10 kDa, and 1 kDa and percent distribution of these fractions were expressed in terms of TOC. Reduction in organics with MW in the ranges of 10-100 kDa was noticeably observed with respect to increasing ozone dose as well as contact time signifying that main target of ozone was the organic molecules within this region. While 36% to 72% reduction of organics with MW 10-100 kDa was observed, fraction of organic compounds with MW < 1 kDa was increased from 37% to 65% concurrently indicating the degradation of organics with MW 10-100 kDa into these smaller fractions. On the other hand, higher molecular weight organics MW> 100 kDa tend to remain without any significant reduction (Lee et al., 2009). Effect of UV/H_2O_2 process on the molecular size distribution profile of municipal ROC samples were studied and resulted transformation of higher molecular weight fractions with sizes > 20 kDa and 1-20 kDa and into lower molecular size fractions with the sizes of 300-500 Da which was found to be in agreement within the results reported in this study (Umar et al., 2014).

Instead of having majority of the lowest molecular size fraction of F6, transformation from higher molecular size fraction F1 to F4 and F5 was noticeably observed for ROC_{m2} following photocatalytic degradation process in the presence of TiO_2, N-TiO_2 and TiO_2/ZnO nanocomposite whereas fraction F1 was still prominent in the presence of ZnO. The reason could be attributed the presence of partially degraded fractions of NOM in ROC_{m2}.

Considering the fractional NPOC distribution profiles of ROC_{ECm1}, F1 and F2 were found to be the major contributors of the transformation from higher molecular size fractions to lower molecular size fractions with respect to photocatalytic degradation processes. Insignificant change in fraction F4 (<2% change with respect to photodegradation and photocatalytic degradation processes) was clearly observed under both photodegradation and photocatalytic degradation conditions in comparison to the initial conditions.

Fractional NPOC distribution profiles of ROC_{ECm2} almost did not change following either UV or solar photodegradation degradation processes in comparison to initial conditions (< 5% reduction in fraction F1). However, following solar photocatalytic degradation process, shift to lower molecular size fractions from higher molecular size fraction of F1 was noticeably perceived. Increase in NPOC percentages of F4 and F6 indicated transformation of F1 into these smaller molecular size fractions. Almost no change was observed for the fraction F5 under photocatalytic degradation processes irrespective of the photocatalyst used. Among all ROC_m and ROC_{ECm} samples, the most prominent shift from higher molecular size fractions to lower ones were obtained via photocatalytic degradation using TiO_2 as the photocatalyst followed by N-TiO_2, TiO_2/ZnO nanocomposite and ZnO respectively.

Regional speciation of EEM fluorescence spectral features of molecular size fractions of all samples prior to and following photodegradation and photocatalytic degradation were presented in figures 4.42-4.49.

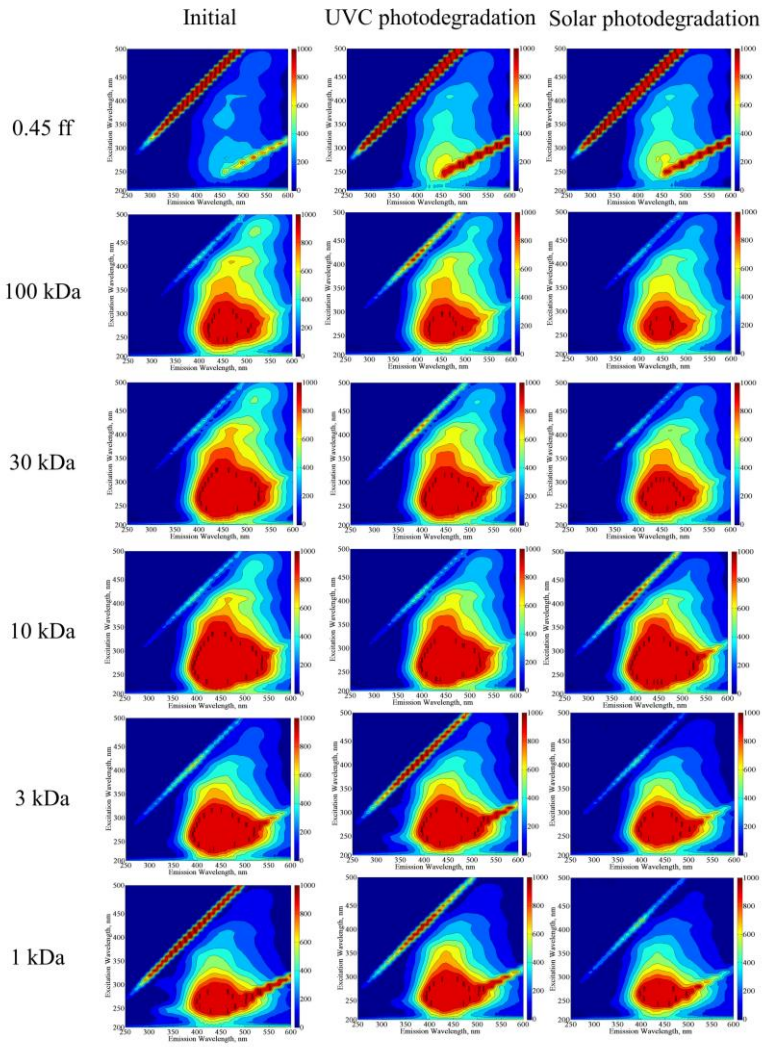

Figure 4.42. EEM fluorescence contour-plots of molecular size distribution profiles of ROC_{m1} prior to and following UVC and solar photodegradation processes.

Humic-like and fulvic-like fluorophores were observed for 0.45 ff of ROC_{m1} in comparison to initial conditions. Despite its higher organic carbon content and aromaticity, fluorescence intensity of ROC_{m1} was considerably lower than fluorescence intensity attained after UVC photodegradation and solar photodegradation processes. The reason could be attributed to self-quenching mechanism of humic macro-molecules (Miano et al., 1988; Senesi, 1990). In addition, greater proximity of aromatic chromophores and the consequent greater probability of deactivation of excited states by internal quenching in high molecular weight organic molecules could also be the another reason for current situation. Almost no discriminative difference was observed for 3 kDa and 1 kDa fractions of

ROC_{m1} prior to and following UVC and solar photodegradation process which could be related to similar NPOC contents as well as UV_{254} values of these fractions indicating irrelevant changes in aromaticity with respect to molecular size fractions.

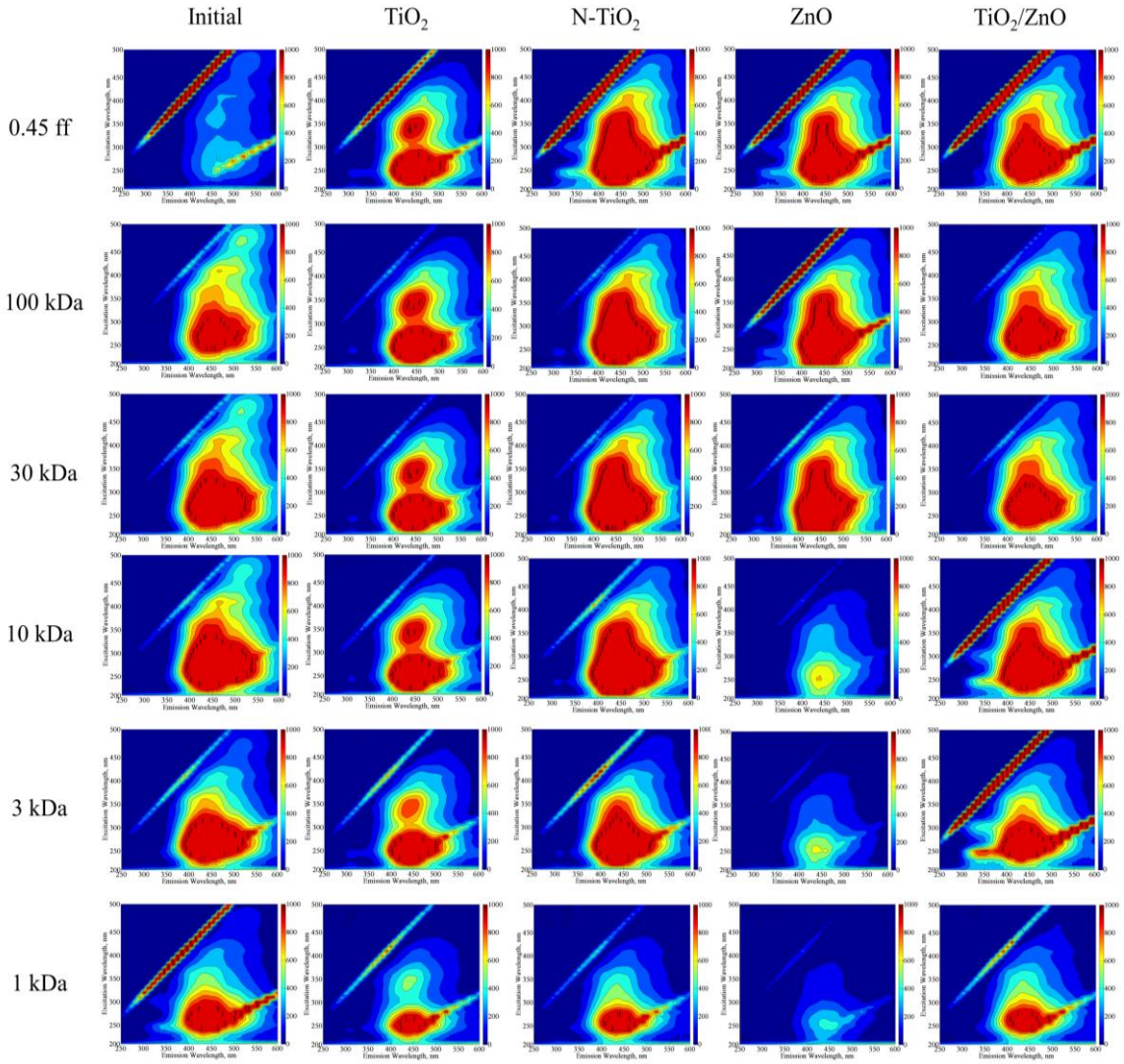

Figure 4.43. EEM fluorescence contour-plots of molecular size distribution profiles of ROC_{m1} prior to and following photocatalytic degradation processes.

Photocatalytic degradation process alters HM by transforming them from high molecular weight aggregated components into lower molecular weight more fluorescent components, which could be noticeably observed via EEM fluorescence contour-plots of molecular size fractions of ROC_{m1} following solar photocatalytic degradation exhibiting new fluorescent components in humic-like and fulvic-like regions with higher intensities in the presence of all photocatalyst specimens as also previously reported by Bekbolet and Sen-Kavurmaci (Bekbolet and Sen-Kavurmaci, 2015). Fraction dependent changes for the same set of experiments were found to be irrelevant for 100 kDa, 30 kDa, and 10 kDa in the presence of same photocatalyst specimens except ZnO, whereas slightly

discriminative differences were attained for 3 kDa and 1 kDa fractions of all samples. In the presence of N-TiO_2, and TiO_2/ZnO, humic-like and fulvic-like fluorophores exhibited similar shape and intensities, whereas they expressed NPOC contents of 1.41 mg/L, 2.75 mg/L indicating photocatalyst specific degradation mechanism of fluorophores.

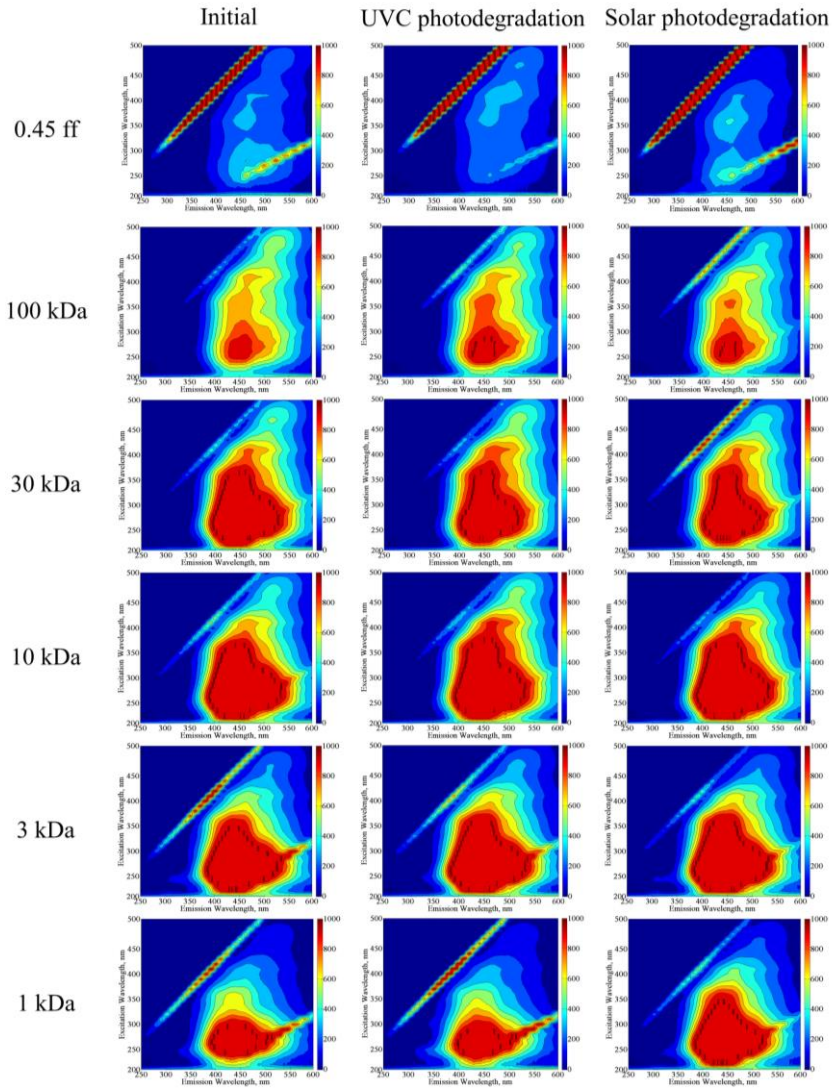

Figure 4.44. EEM fluorescence contour-plots of molecular size distribution profiles of ROC_{m2} prior to and following UVC and solar photodegradation processes.

Although 0.45 ff of ROC_{m1} displayed differences between initial and photodegradation conditions, ROC_{m2} did not express any significant difference in shape and intensity of EEM fluorescence contour-plots for the same fractions indicating prominence of high molecular weight humic components in ROC_{m2} composition that are able to quench other lower molecular weight humics. The most distinct differences in shape and size of the contour-plots were observed for the fractions of 100 kDa and 30 kDa. Almost no difference was observed for the fractions 10 kDa and 3 kDa indicating no influence of photodegradation processes on the alterations of fluorophores in these

fractions. The most noticeable difference was attained for 1 kDa fraction following solar photodegradation which could be attributed to significant amount of NPOC (4.78 mg/L) in comparison to initial (2.15 mg/L) and UVC photodegradation (1.57 mg/L) conditions. Higher NPOC contents in 1 kDa fraction of ROC_{m2} could be related to transformation of high molecular weight humics into lower ones.

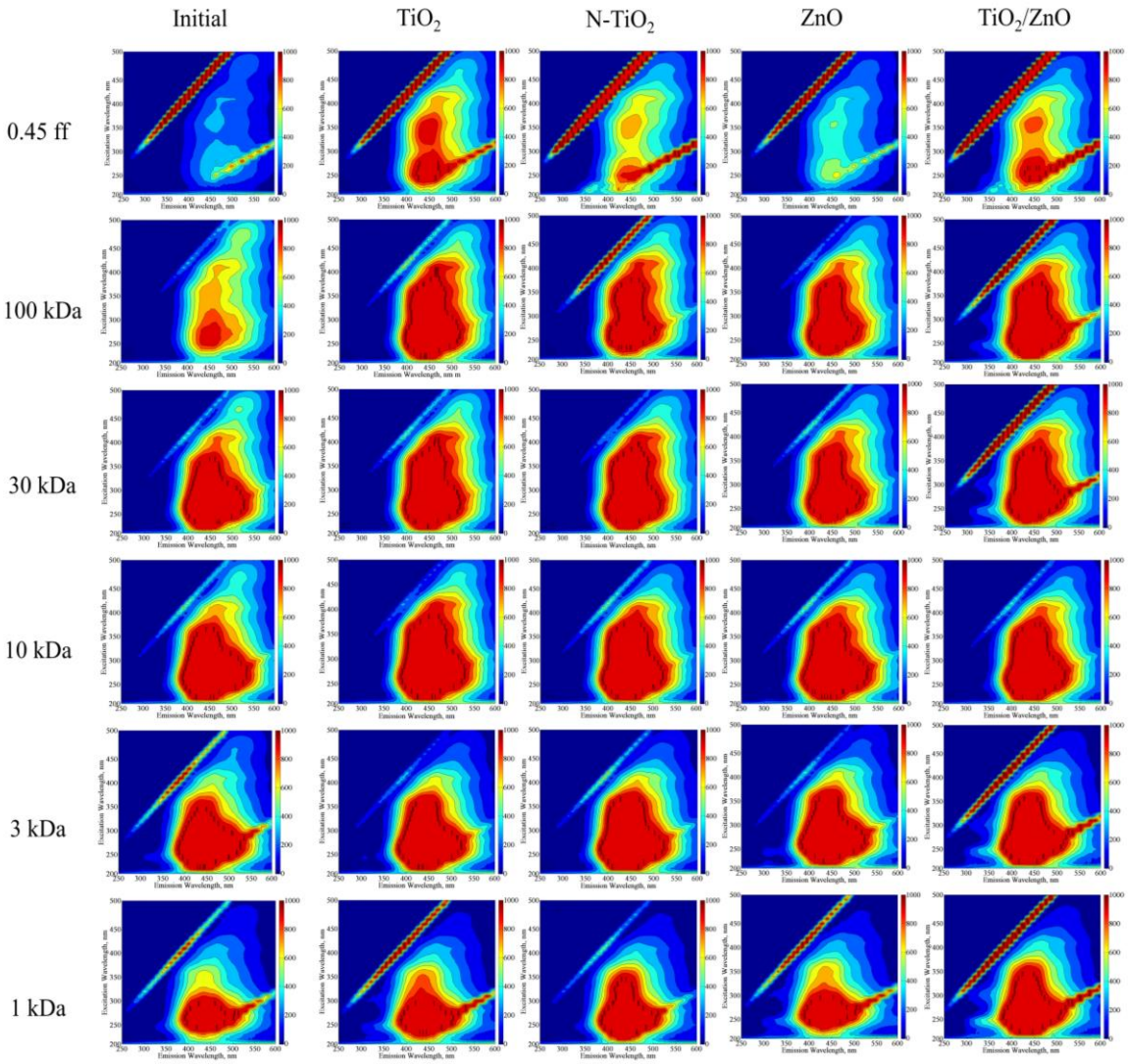

Figure 4.45. EEM fluorescence contour-plots of molecular size distribution profiles of ROC_{m2} prior to and following photocatalytic degradation processes.

Under all conditions, no significant change of humic-like and fulvic-like fluorophores were attained for 30 kDa, 10 kDa and 3 kDa fractions of the samples whereas significant change in humic-like and fulvic-like fluorophores could be observed for 0.45 μm ff and 100 kDa fraction exposing to photocatalytic degradation process. The reason could be attributed to the attack of ROS to the high and medium molecular weight components (0.45 μm ff and 100 kDa fractions) and transferring them into medium and lower molecular weight organics (<30 kDa fraction). Another reason could be the

molecular size distribution profile of organic matrix used in ROC_{m2} composition comprising partially oxidized fractions of humic-like matter that could present humic-like and fulvic-like fluorophores with much higher intensity in EEM fluorescence contour-plots.

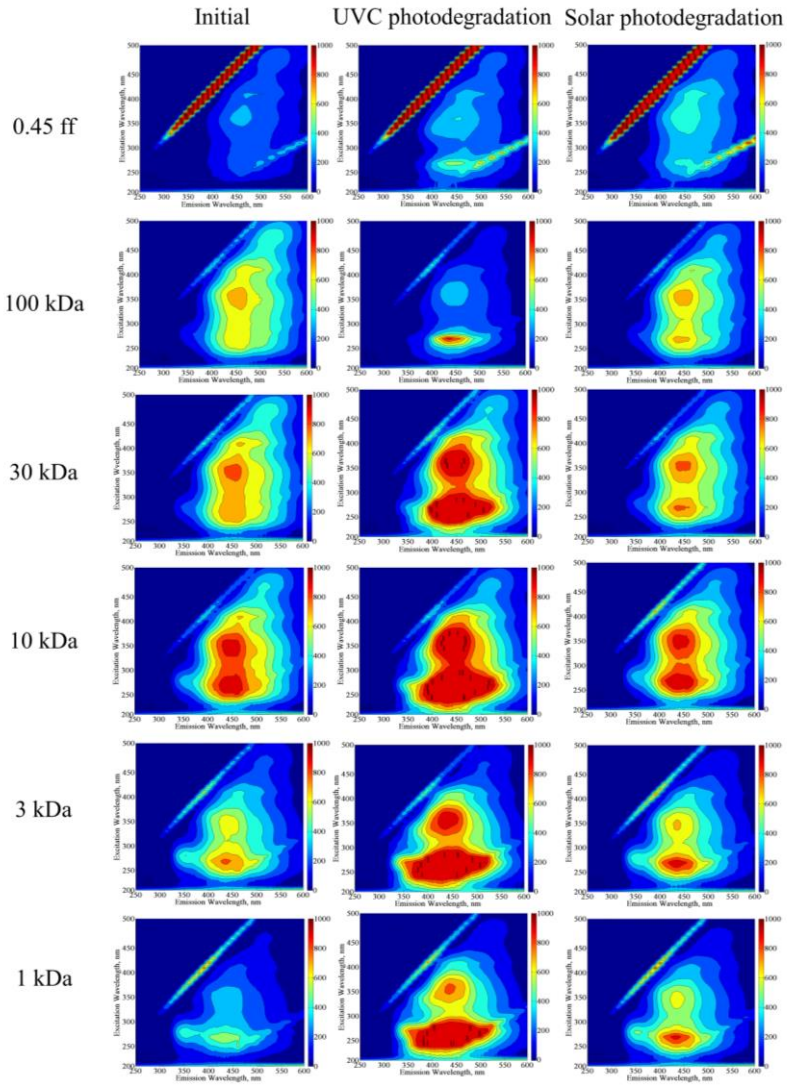

Figure 4.46. EEM fluorescence contour-plots of molecular size distribution profiles of ROC_{ECm1} prior to and following UVC and solar photodegradation processes.

Discriminative differences depending on the applied processes were observed for almost all fractions of ROC_{ECm1} prior to and following photodegradation processes. Presence of SMX in ROC_{ECm1} could be visualized noticeably for the fractions 3 kDa and 1 kDa fractions due to its fluorescence maxima at Ex/Em: 210-290/350 nm for initial and solar photodegradation conditions, whereas it is almost disappeared or expressed lower intensity following UVC photodegradation which could be attributed to susceptibility of SMX to UVC photodegradation. Under the same conditions, 80% and 22% removal of SMX could be achieved via UVC photodegradation and solar photodegradation processes (Section 4.3.1.1 and 4.4.1.1). For 1 kDa fraction of all conditions, NPOC

contents were found to be as 6.16 mg/L for initial, 5.21 mg/L for UVC photodegradation, and 7.39 mg/L for solar photodegradation indicating eminence of SMX and/or its phototransformation by-products even after exposed to solar photodegradation process.

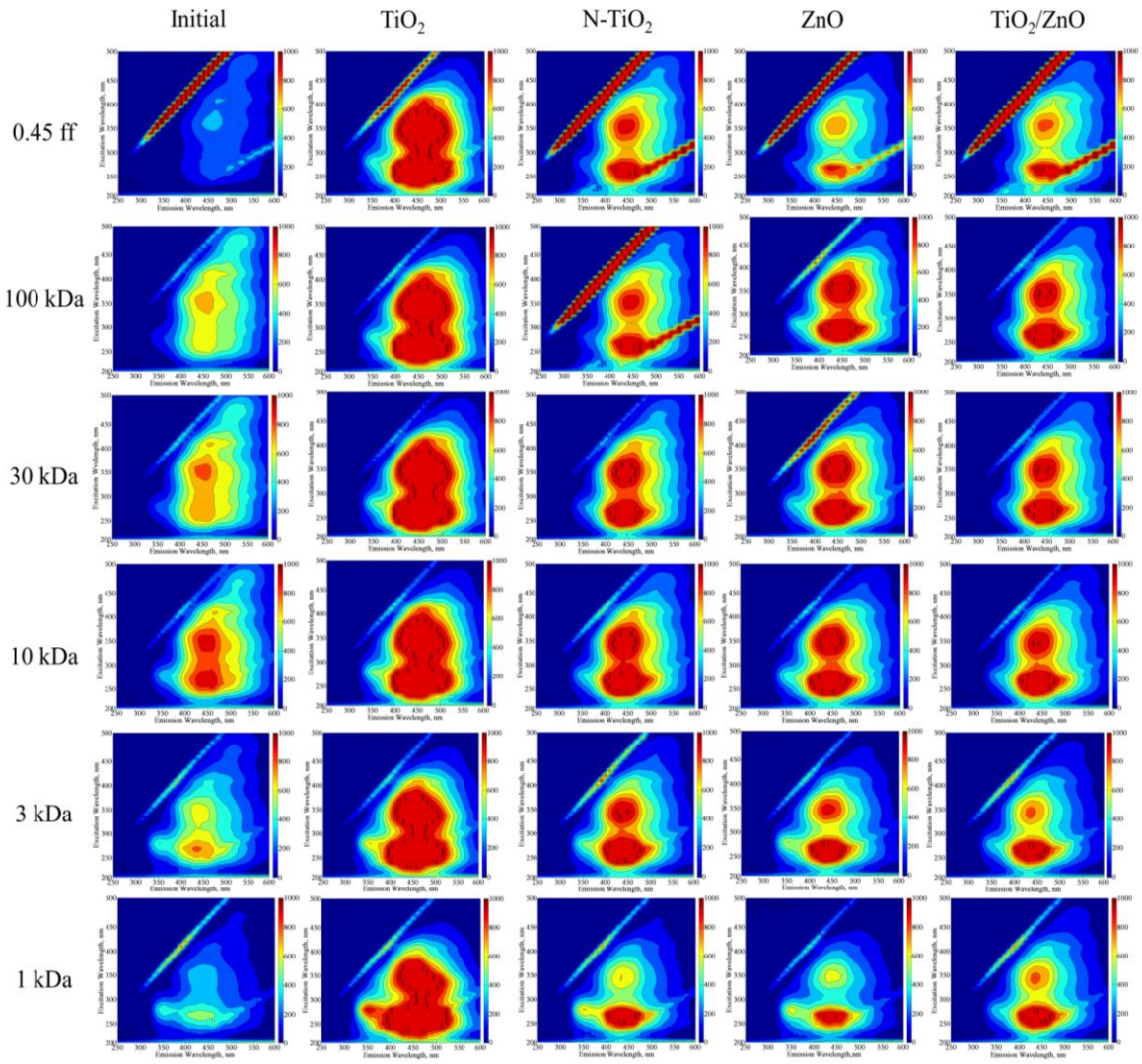

Figure 4.47. EEM fluorescence contour-plots of molecular size distribution profiles of ROC_{ECm1} prior to and following photocatalytic degradation processes.

Distinct differences of humic-like and fulvic-like fluorophores could be observed for each molecular size fractions of ROC_{ECm1} samples prior to and following photodegradation and photocatalytic degradation processes. Emergence of protein-like fluorophores could be visualized for ROC_{ECm1} samples following photolytic and photocatalytic degradation processes in comparison to ROC_{m1} and ROC_{m2}. The reason could be attributed to the presence of ECs that are fluorescent and gives intensity at protein-like fluorophore regions. Since protein-like fluorophores could be quenched by higher molecular size fractions of humic-like and fulvic-like fluorophores, observation of these protein-like structures could be accessed only in presence of lower molecular size fractions of humic-

like and fulvic-like fluorophores as attained in EEM fluorescence contour-plots of 3 kDa and 1 kDa fractions of ROC_{ECm1} prior to and following photodegradation and photocatalytic degradation processes.

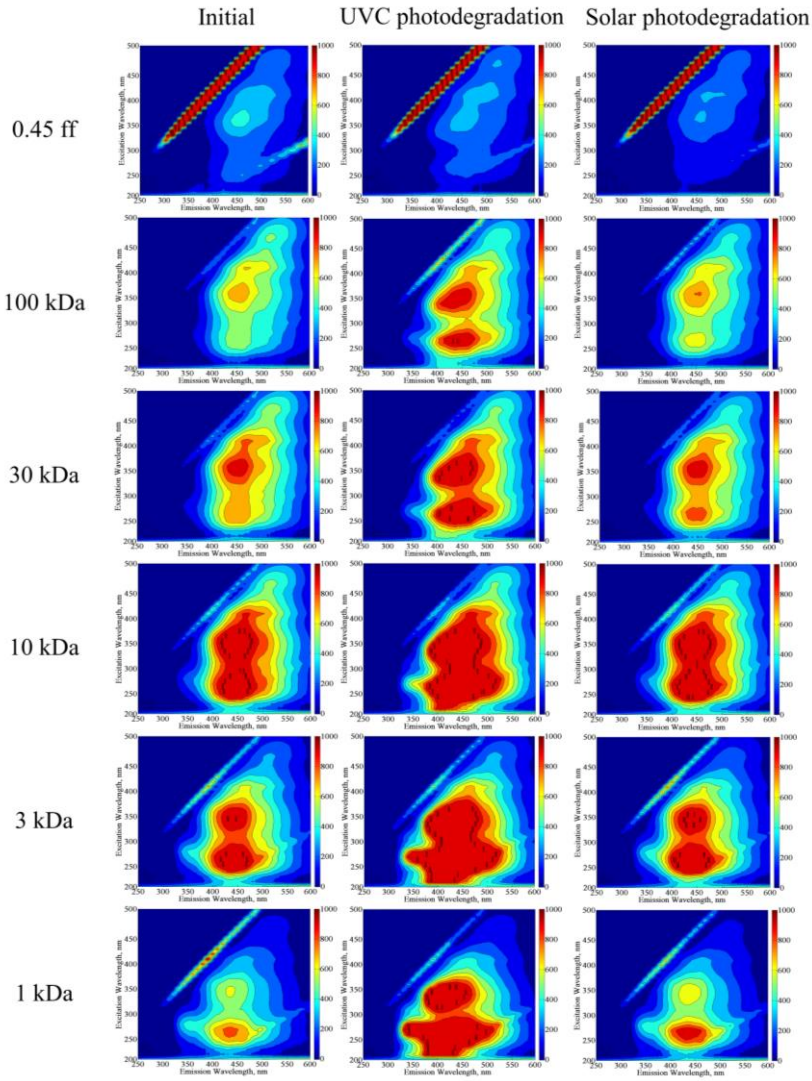

Figure 4.48. EEM fluorescence contour-plots of molecular size distribution profiles of ROC_{ECm2} prior to and following UVC and solar photodegradation processes.

With respect to emergence of humic-like and fulvic-like fluorophores under all conditions, discriminative differences in fluorescence intensity and shape of EEM fluorescence contour-plots were observed for almost all fractions of ROC_{ECm2} except 0.45 ff which still has humic macromolecules with their self-quenching fluorescence effect as explained previously. As a result of presence of SMX in ROC_{ECm2} composition, SMX related fluorophores could be visualized noticeably for the fractions 3 kDa and 1 kDa fractions due to its fluorescence maxima at Ex/Em: 210-290/350 nm under all conditions whereas intensity of SMX related fluorophores were more evident with higher fluorescence intensity in ROC_{ECm2} in comparison to ROC_{ECm1}. The reason could be attributed to lower removal efficiency of SMX in the presence of higher HM content causing light attenuation.

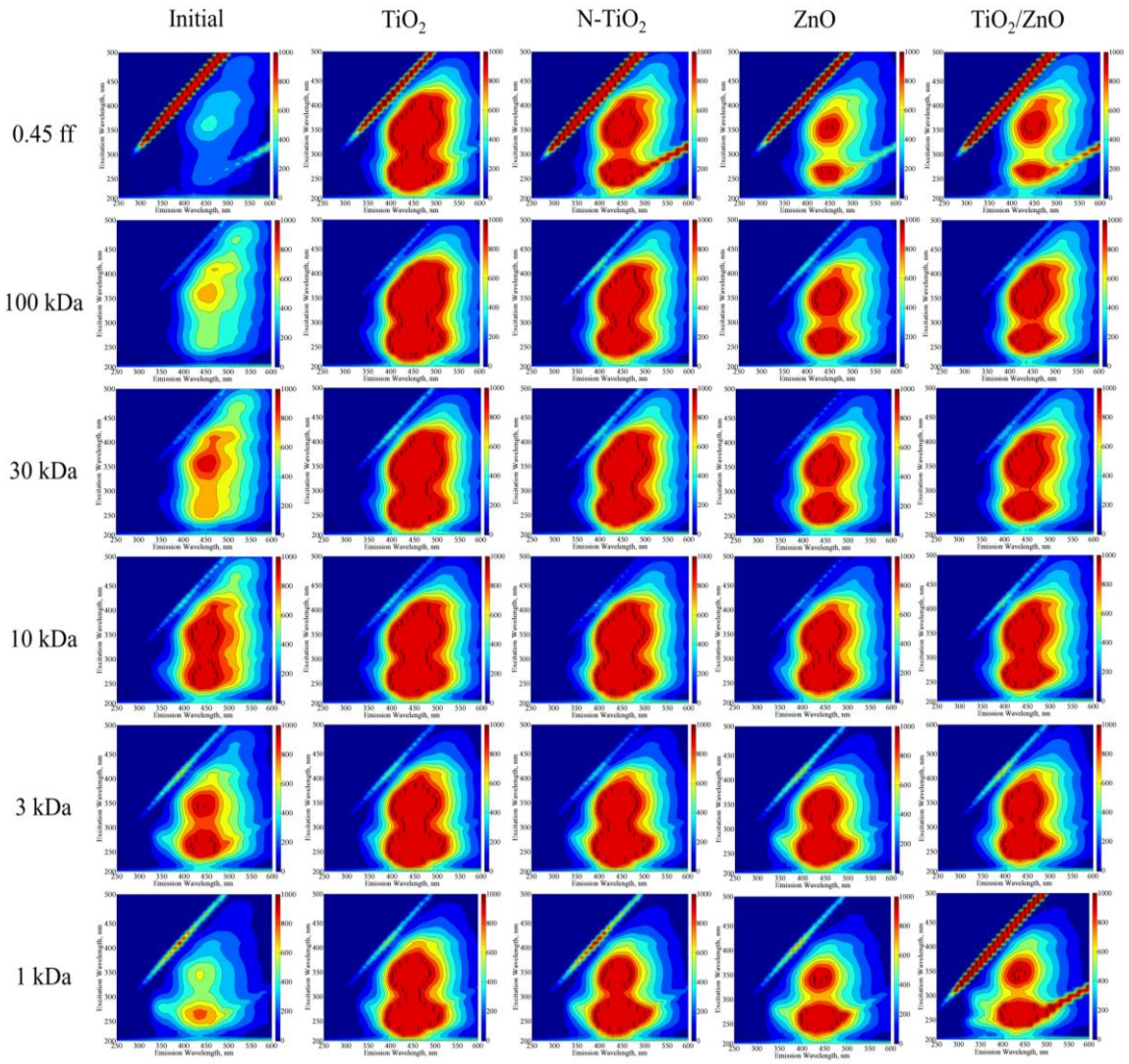

Figure 4.49. EEM fluorescence contour-plots of molecular size distribution profiles of ROC_{ECm2} prior to and following photocatalytic degradation processes.

In contrast to the EEM fluorescence contour-plots attained for ROC_{m1} and ROC_{ECm1}, presence of humic-like and fulvic-like fluorophores could be significantly visualized for all molecular size fractions of ROC_{ECm2} even under non-oxidative conditions as well as photodegradation conditions as observed in ROC_{m2}. EEM fluorescence contour-plots of higher molecular size fractions of ROC_{ECm2} prior to and following photodegradation were distinctly different from photocatalytic degradation conditions. The reason could be attributed to the conversion of fluorophores present in medium (100 kDa) and high (0.45 ff) molecular size fractions of humic matter into lower molecular size fractions of fluorophores expressing higher intensities at lower molecular size fractions (<30 kDa). Insignificant change in humic-like and fulvic-like fluorophores were attained in all molecular size fractions of ROC_{ECm2} samples irrespective of the photocatalyst used. In a similar trend attained for ROC_{ECm1}, emergence of protein-like fluorophores originating from ECs could only be observed for 1 kDa fraction of all ROC_{ECm2} samples.

Fluorescence EEMs of molecular size fractions of all ROC samples prior to and following photodegradation and photocatalytic degradation processes were successfully decomposed by PARAFAC analysis into a four-component (C1, C2, C3, and C4) model as displayed in Figure 4.50.

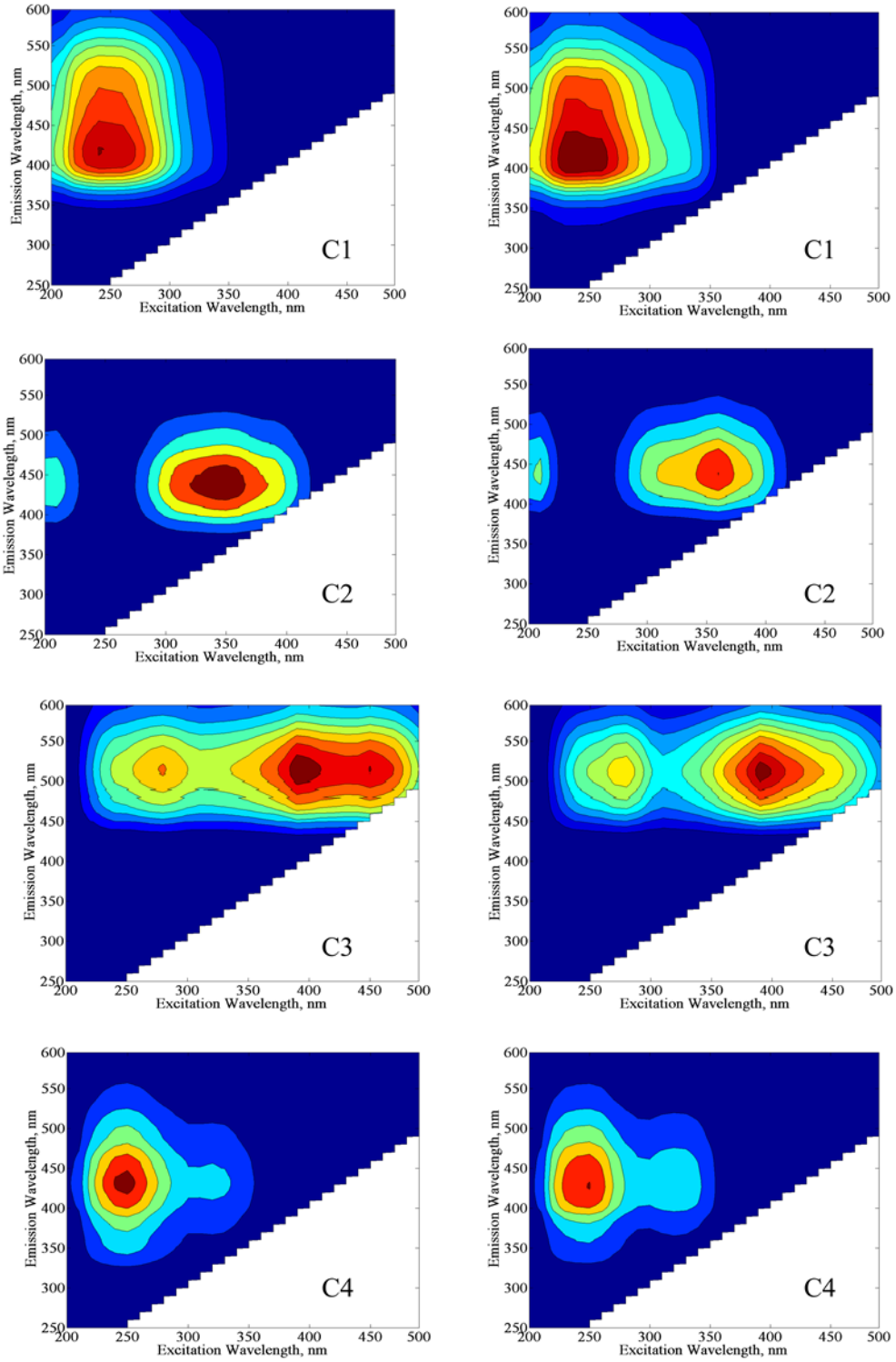

Figure 4.50. EEM contour-plots of four components (C1, C2, C3, and C4) identified by PARAFAC model for molecular size fractions of ROC_m and ROC_{ECm} prior to and following photolytic and photocatalytic degradation processes.

Following photodegradation, C1 and C2 presented maxima (Ex/Em) at 250/410 nm and 350/450 nm. C3 displayed a primary and a secondary maxima at 275/550 nm and 275/450 nm whereas C4 exhibited one maxima at 250/440 nm. Upon photocatalysis, C1 and C2 presented one maxima at 250/410 nm and 350/450 nm. In addition, C3 displayed one primary and one secondary maxima at 400/510 nm and 275/510 nm. C4 displayed one maxima at 225/425 nm that could be regarded as humic-like component. Based on the origin of the HM present in ROC_m and ROC_{ECm} compositions as well as previous literature findings, all identified components could be assigned to humic-like components as a general classification (Murphy et al., 2008; Kowalczuk et al., 2009; Pifer and Fairey, 2014; Ly et al., 2018; Tang et al., 2019).

Discriminative difference between the peak positions of C4 could be clearly observed for photodegradation and photocatalytic degradation processes ending up with the shift from longer wavelengths to the shorter wavelength both in Ex and Em. Moreover, although shift for the peak positions of C1, C2, and C3 was not observed, reduction in the intensities of these components were noticed. Either shift from longer Ex/Em wavelengths to shorter ones or reduction in the intensities could be attributed to solar photocatalytic degradation of HM. In a similar manner attained for PARAFAC modeling on photodegradation and photocatalytic degradation of ROC samples, noticeable EEM features at longer emission (Em) wavelengths *i.e.* Em> 510 nm (Hur and Kim, 2009; Lee et al., 2015) indicates larger sized humic fractions with higher degree of condensation. Therefore, identified fluorescent components could have a higher structural condensation and/or larger molecular size following the order of C3>C2>C4>C1 for both photodegradation and photocatalytic degradation processes.

Difference of fluorescent components in terms of peak positions of Ex/Em as well as their intensities could be noticeably observed between photodegradation and photocatalytic degradation processes and molecular size fractions following photodegradation and photocatalytic degradation processes. Components of sole photodegradation/photocatalytic degradation processes displayed humic-like components with higher molecular size and aromaticity expressing maxima at longer emission wavelengths whereas molecular size fractions following photodegradation/photocatalytic degradation revealed fluorescent components with lower molecular weight. The reason could be attributed to the molecular size fractionation process giving fluorescence EEMs of samples for six different fractions (to <1 kDa), whereas components of sole photodegradation/photocatalytic degradation processes comprise only one gross fraction of <0.45 ff.

4.7. Toxicity Assessment

Toxicity evaluation of wastewater samples upon photocatalytic detoxification processes were performed by application of several tests, such as *Vibrio fischeri* bioluminescence's assay, *Daphnia magna* immobilization test, *Pseudokirchneriella subcapitata, Anabaena flos-aquae, Brachionus calyciflorus,* estrogenic test (HELN ERa cell line), genotoxicity assessment (LS 174T cell line) and phytotoxicity test (Rueda Marquez et al., 2020). Preference of *Vibrio fischeri* as the toxicity test could be related to its various advantageous properties, such as shorter test duration, sensitivity, cost-effectiveness, reproducibility, and ease of the operation. Moreover, its' equal applicability to almost all types of matrices make *Vibrio fischeri* bioluminescence test more favorable in comparison to other conventional bioassays based on plants, algae, daphnids, fish and crusteceans (Parvez et al., 2006; Villa et al., 2012; Ma et al., 2014; Abbas et al., 2018).

Vibrio fischeri (earlier referred as *Photobacterium phosphoreum*) is a marine Gram negative bacterium whose specific strain has been widely used for acute toxicity testing as well as in commercial test kits based on this strain (Farre and Barceló, 2003). Toxicity testing with *Vibrio fischeri* was commercialized in 1978 as Microtox test (Bulich and Isenberg, 1981) which involves mixing of 1.5 mL bacterial suspension with the same amount of test chemical previously dissolved in 2% NaCl solution. Quantification of emitted fluorescence could be followed by using fluorescence spectrometer or luminometer. Since light production is directly proportional to the metabolic activity of the bacterial population, potential inhibition of enzymatic activity would end up with reduction in bioluminescence. The amount of toxic compound causing 50% reduction in luminescence after the specified time is denoted as EC_{50} value.

Upon reaction with the reduced form of nicotinamide adenine dinucleotide phosphate (NAD(P)H), Flavin mononucleotide (FMN) is reduced to Flavin mononucleotide ($FMNH_2$) in the presence of Flavin reductase enzyme (Reaction 4.22).

$$NAD(P)H + H + FMN \xrightarrow{\text{Flavin reductase}} NADP + FMNH_2 \quad (4.22)$$

$$FMNH_2 + O_2 + R\text{-}CHO \xrightarrow{\text{Luciferase}} FMN + H_2O + R\text{-}COOH + h\nu\ (\lambda: 490\ nm) \quad (4.23)$$

In the presence of aldehyde and luciferase enzymes, reduced $FMNH_2$ is oxidized into FMN and H_2O upon reaction with molecular oxygen and by this reaction blue-green light of wavelength at λ: 490 nm is emitted (Raection 4.23) (Inouye, 1994). Since bioluminescence is directly linked to

respiration, over the electron transport chain, it reveals the cellular metabolic status and therefore regarded as a key element of xenobiotic-mediated toxicity (Abbas et al., 2018).

4.7.1. *Vibrio fischeri* Bioluminescence Inhibition Test of ECs, ROC_m and $ROEC_m$ Prior to and Following Photodegradation and Photocatalytic Degradation Processes

Potential toxicity of ECs, ROC_m and ROC_{ECm} samples were expressed as percent relative inhibition of the luminescence of photobacteria with respect to the light emitted under test conditions (Figure 4.51). In order to gain baseline information about the toxicity potential of ECs, ROC_m and ROC_{ECm} samples, toxicity analyses were also performed for ECs, ROC_m and ROC_{ECm} samples prior to photodegradation and photocatalytic degradation processes. Toxicity assessment of SMX and CMZ were performed for the samples upon exposure to UVC and solar photodegradation for t_{irr}: 90 min, whereas for solar photocatalytic degradation experiments, samples by which 70-80% removal of the parent compound was achieved were taken into consideration for toxicity assessment. On the other hand, for ROC_m and ROC_{ECm}, toxicity tests were conducted for the samples following t_{irr}: 90 min under the same experimental conditions in order to make a comparative evaluation of ROC_m and ROC_{ECm} samples for the most prolonged irradiation period. Evaluation of the inhibition percentages could be considered as follows: If inhibition percentage is less than 25%, it is defined as non-toxic, if inhibition percentage is less than 50% and more than 25%, then it is defined as low toxic, if inhibition percentage is less than 75% and more than 50%, then it is defined as toxic, if inhibition percentage is higher than 75%, then it is defined as highly toxic (Ricco et al., 2004).

SMX presented moderate toxicity prior to any applied processes whereas following photodegradation and photocatalytic degradation processes, fluctuations in inhibition percentages were attained in the order of TiO_2/ZnO, PC>UV photodegradation> ZnO, PC>solar photodegradation>N-TiO_2, PC>TiO_2, PC>initial. Inhibition percentage of SMX under UVC irradiation was found to be noticeably higher than the value attained for solar photodegradation process. The reason could be attributed to susceptibility of SMX to UVC photodegradation (almost 80% SMX removal was attained) rather than solar photodegradation (only 22% removal of SMX was achieved). Although photodegradation and photocatalytic degradation processes were able to remove SMX as the parent compound to some extent, concomitant formation of phototransformation by-products of SMX is also expected. Since UVC phototransformation by-products of SMX are not prone to photodegradation and tend to accumulate in the reaction medium, they could be regarded as the main source of potential toxicity (Nasuhoglu et al., 2011; Gmurek et al., 2015). Being as one of

the phototransformation by-products of SMX, sulfanilic acid, which is regarded as “toxic”, is not susceptible to photodegradation and therefore tend to accumulate in the reaction medium upon photodegradation ending up with contribution to toxicity (El-Ghenymy et al., 2012).

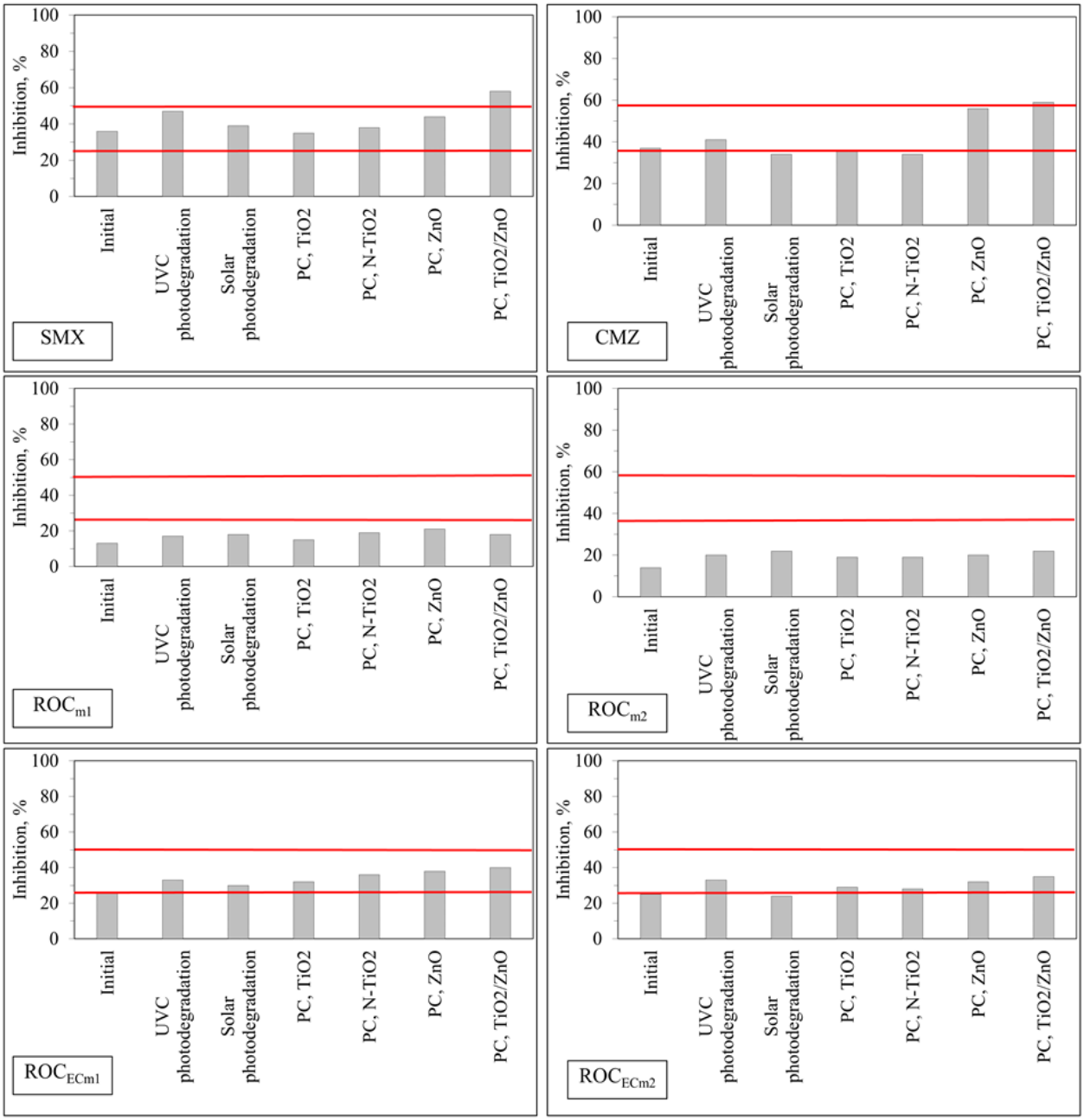

Figure 4.51. Toxicity assessment of ECs, ROC_m and ROC_{ECm} upon exposure to photodegradation and photocatalytic degradation processes (PC denotes photocatalytic degradation).

Upon solar photocatalytic degradation, slight reduction in inhibition percentage of SMX was observed compared to initial conditions, whereas significant reduction of inhibition percentage was attained in comparison to UVC and solar photodegradation processes except for ZnO and TiO_2/ZnO. The reason could be attributed to photocatalyst originated ROS attack to the parent compound as well

as its transformation by-products that enable their rapid removal under the specified experimental conditions (Niu et al., 2013; Mirzaei et al., 2018). No discriminative difference on the toxicity reduction was observed among all photocatalyst specimens except for ZnO and TiO_2/ZnO that changed toxicity level from “low toxic” to “toxic”. The reason could be attributed to inefficient removal of transformation by-products accumulates in the reaction medium. Although ZnO and TiO_2/ZnO revealed up to 80% removal of parent compound, lower NPOC removal efficiencies (< 50%) indicated prominence of reaction intermediates which still indicates toxicity potential. In the presence of TiO_2 and N-TiO_2, close inhibition percentages could be attributed to similar SMX removal as well as NPOC removal efficiencies (80% for TiO_2 and 73% for N-TiO_2) indicating effective mineralization of both parent compound as well as transformation by-products.

However, in the presence of ZnO there was a noticeable gap between the removal efficiencies of the parent compound and NPOC contents indicating the accumulation of transformation by-products in the reaction medium causing toxicity. Moreover, another reason could be related to photo-corrosion of ZnO under acidic conditions due to attack of photogenerated holes to Zn-O bond ending up with the release of Zn^{2+} into the solution (Kudo and Miseki, 2009). Although initial pH of the SMX solution lays in the range of 6-7, upon exposure to photodegradation or photocatalytic degradation process, one of SMX’s transformation by-products namely sulfanilic acid would release into the reaction medium which is able to drop pH (Niu et al., 2013). Therefore, significant increase in inhibition percentage of SMX using ZnO and TiO_2/ZnO could be related to photodissociation of ZnO as has been previously reported by Vela and colleagues (Vela et al., 2018b).

Following UVC and solar photodegradation processes, changes in inhibition % was attained for CMZ was found to be in the order of TiO_2/ZnO, PC>ZnO, PC>UVC photodegradation> solar photodegradation>TiO_2, PC>initial>N-TiO_2, PC respectively. Upon exposure to UVC and/or solar irradiation, toxicity of CMZ could increase with respect to formation and predominance of acridine and acridone that are known to be considerably more toxic than the parent compound (Chiron et al., 2006; Alharbi et al., 2017). The differences between inhibition percentages of UVC photodegradation and solar photodegradation processes could be attributed to removal efficiencies of CMZ as the parent compound of which 37% and 11% removals were attained following UVC photodegradation and solar photodegradation processes. Higher removal efficiency via UVC photodegradation process promoted formation and accumulation of toxic by-products in the reaction medium, therefore expressed higher toxicity potential. On the other hand, presence of ROS can reduce potential toxicity below detection limit by removing parent compound as well as toxic reaction intermediates (Rizzo et al., 2009; Oroposa et al., 2018; Mestre and Carvalho, 2019).

In comparison to the initial conditions, reduction of inhibition % was attained in the presence of TiO_2 and N-TiO_2 whereas 59% and 51% increases in inhibition percentages were attained in the presence of ZnO and TiO_2/ZnO specimens which also changed status of the samples from "low toxic" to "toxic". The reason could be attributed to photocatalyst specific removal mechanisms of CMZ that could involve concomitant production and removal of various toxic products during solar photocatalytic degradation process (Jelic et al., 2013). CMZ removal efficiencies were found to be considerably lower for N-TiO_2, ZnO, and TiO_2/ZnO for the early stages of solar photocatalytic degradation process (Section 4.4.2.1., Figure 4.20) which could be related to the immediate formation of transformation by-products right after ROS attack to the parent compound. In addition, inefficient removal of toxic products that accumulates in the reaction medium could be another reason of significant increase even after photocatalytic degradation. Under the same experimental conditions, photocatalytic degradation of CMZ could express no potential toxicity by using TiO_2, whereas significant toxicity could be attained in the presence of ZnO. Bohdziawicz and colleagues investigated background effect of sole TiO_2 and ZnO photocatalysis in the absence of target pharmaceuticals. It was concluded that TiO_2 itself exhibited no toxicity (inhibition percentage was found to be less than 25%) whereas upon exposure to irradiation for 30 min, water solution containing ZnO exhibited toxicity as inhibition percentage of 40% which was increased to 70% following t_{irr}: 60 min. The reason was attributed to production of toxic by-product as a result of photocatalyst decomposition (Bohdziewicz et al., 2014).

The only OM present in ROC_{m1} and ROC_{m2} composition is HM which would expose to photodegradation as well as photocatalytic degradation processes under the specified experimental conditions. Toxicity potential of HS has been reported throughout the literature in order to understand its potential impact on toxicity of other components', such as heavy metals, nanoparticles, pharmaceuticals, ionic liquids, *etc.* (Abbas et al., 2018; Rueda Marquez et al., 2020). According to previously reported literature findings, HM was not regarded as "toxic", however, it may have an impact on the enzymatic activities of bioluminescent bacteria that is used for toxicity analysis. Therefore, HM has the potential to interfere with the enzymatic activity to which bacteria would respond as a reduction in luminescence. It's been reported that HM may inhibit bioluminescence with concentration value greater than 100 mg/L in case of bacterial assay (Tarasova et al., 2012). Reduction of bioluminescence in the presence of HS could be attributed to two reasons: *i.* high concentrations of HM would contain higher amount of color forming moieties which suppress bioluminescent intensity due to the effect of optical filter, *ii.* diffusion of humic macromolecules causing interferences with coupling of enzymes, binding of the substrates, cellular membrane's protective functionality, *etc.* (Tarasova et al., 2011 and 2012; Kudryasheva and Tarasova, 2015).

Since ROC_{m1} and ROC_{m2} samples did not contain significant amount of color forming moieties and/or significant reduction of these color forming moieties could be achieved via solar photocatalytic degradation process, increase in inhibition percentages upon solar photocatalytic degradation process could be attributed to interference of humic sub-fractions with enzymatic reactions of *Vibrio fischeri*. In order to understand estrogenic effect as well as increase in levels of detoxification enzymes, possible interactions of various HS with estrogen receptor (ER) and aryl hydrocarbon receptor (AhR) were evaluated. With respect to its large molecular weight, HS could not bind to ligand-binding region of AhR, however since HS are consisted of low molecular weight aggregated fractions, these lower molecular weight fractions would have affinity to AhR (Bittner et al., 2006; Janošek et al., 2007). Therefore, AhR-mediated activity of HA would play a crucial role on the assessment of bioluminescence of *Vibrio fischeri*.

Baseline inhibition percentages for ROC_{m1} and ROC_{m2} were found to be 13% and 14% which could be regarded as "non-toxic", however upon exposure to photodegradation and solar photocatalytic degradation processes, noticeable increases in inhibition percentages (15-60% increase for ROC_{m1} and 36-57% increase for ROC_{m2}) were attained in comparison to initial condition. The increase in inhibition percentages of ROC_{m1} and ROC_{m2} samples upon exposure to solar photocatalytic degradation could be attributed to aforementioned HM diffusion mechanism interfering bacterial enzymatic mechanisms explained previously. Since photocatalytic degradation process would end up with transformation of hydrophilic lower molecular weight humic-like and fulvic-like components, their tendency of diffusion into the cell or binding onto ligand-binding region of AhR could be expected to be more probable than the high molecular weight humic components.

It was concluded that although organic matrix content of ROC_{m1} and ROC_{m2} are distinctly different from each other in terms of organic carbon content as well as molecular size distribution, their toxicity potentials expressed insignificant differences neither exposed to UVC and solar photodegradation nor solar photocatalytic degradation processes. The reason could be attributed to non-toxic content of initial samples that is only composed of HM as the organic matrix. On the other hand, response of different conditions expressed as inhibition percentage was found to be distinctly different as follows: for ROC_{m1} inhibition percentages were found to be in the order of ZnO, PC>N-TiO_2, PC>TiO_2/ZnO, PC= solar photodegradation>UVC photodegradation>initial, whereas ROC_{m2} revealed inhibition percentages in the order of TiO_2/ZnO, PC=solar photodegradation>ZnO, PC=UVC photodegradation>TiO_2, PC=N-TiO_2, PC>initial respectively.

Initial inhibition percentages of ROC_{ECm1} and ROC_{ECm2} were found to be 26% and 25% which are two times higher than the values attained for ROC_{m1} as 13% and for ROC_{m2} as 14%. The reason could be attributed to contribution of SMX and CMZ to the inhibition percentage of ROC_{ECm1} and ROC_{ECm2}. Inhibition percentages for the selected conditions were found to be in the order of TiO_2/ZnO, PC>ZnO, PC>N-TiO_2, PC>UVC photodegradation>TiO_2, PC>solar photodegradation> initial, whereas it was in the following order of TiO_2/ZnO, PC>UVC photodegradation>ZnO>TiO_2, PC>N-TiO_2, PC>solar photodegradation>initial for ROC_{ECm2}. It was concluded that all applied processes, except solar photodegradation process, triggered increase in inhibition percentages of ROC_{ECm1} and ROC_{ECm2} in comparison to initial conditions. Although ROC_{ECm2} is composed of HM both with high and low molecular weight components either photocatalytically degraded or not, inhibition percentages following photodegradation and photocatalytic degradation processes were found to be lower than the results attained for ROC_{ECm1}. ECs could entrap into humic structure of ROC_{ECm2} due to its higher degree of aromaticity and molecular weight rather than ROC_{ECm1} whose humic composition comprises non-oxidized and more uniformly distributed structure. Consequently, the lower inhibition percentage of ROC_{ECm2} could be related to its ability to entrap ECs into its humic structure rather than efficient photocatalytic removal mechanism.

Following UV and solar photodegradation, inhibition % of ROC_{ECm1} and ROC_{ECm2} was found to be noticeably higher than the values obtained for ROC_{m1} and ROC_{m2}. The reason could be attributed to the formation of toxic by-products originating from the photodegradation of ECs present in ROC_{ECm1} and ROC_{ECm2} (Trovó et al., 2009; Donner et al., 2013). In comparison to photodegradation conditions, reduction on inhibition percentages could be observed via solar photocatalytic degradation process, indicating the removal of toxic by-products in ROC_{ECm1} and ROC_{ECm2} via the attack of ROS were found to be irrespective of the photocatalyst specimens. Since SMX and CMZ exhibited moderate toxicity even after solar photocatalytic degradation process, eminence of toxicity in ROC_{ECm1} and ROC_{ECm2} under the same conditions could be attributed to moderate toxicity of SMX and CMZ remaining even after solar photocatalytic degradation process. Noticeable inhibition % attained for SMX and CMZ was not observed for ROC_{ECm1} and ROC_{ECm2} in the presence of ZnO and TiO_2/ZnO. The reason could be related to host-guest relationship occurring between humic macromolecules and ECs due to their molecular sizes (1-5 kDa), ECs could be entrapped by humic-like and fulvic-like components (13-150 kDa) (Liu et al., 2007). Upon exposure to photocatalyst surface, HM with encapsulated EC could be adsorbed on the surface and can be eliminated from the reaction medium via adsorption process instead of any degradation mechanism (Uyguner-Demirel et al., 2017). Another reason could be attributed to efficient removal of ECs in ROC_{ECm1} and ROC_{ECm2} composition with respect to photosensitizing effect of HM which enhances

removal efficiency of ECs, therefore reduces toxicity.

It's been previously reported that, as a general trend, upon exposure to photocatalysis, decrease in potential toxicity of wastewaters containing ECs could be expected due to the removal of parent compound as well as its' reaction intermediates that might be more toxic than the parent compound (He et al., 2016; Rueda Marquez et al., 2020). In addition, comparative findings presented by Zhou and colleagues concluded that application of UVA/TiO_2 and UVC/TiO_2 processes ended up with slight reduction on the initial inhibition percentage of real ROC_m samples (Zhou et al., 2011). Another study performed by Justo and colleagues investigated potential toxicity of a municipal ROC sample upon application of UVC/H_2O_2 and ozonation processes which concluded no apparent toxicity of ROC sample prior to and following UVC/H_2O_2 process which could be attributed to complete removal of almost all ECs present in ROC composition (Justo et al., 2013).Another reason could be attributed to concentration of ECs in real ROC samples which are found to be in the range of 0.018 µg/L to 50 µg/L (Section 2.1.2), therefore parent compounds as well as their reaction intermediates may not pose significant risk in terms of their toxicity potential. In case of this study, initial concentration values of ECs (C_i: 5 mg/L) were selected significantly higher than the values attained for real ROC samples which could be attributed to assuring certain amount of substrate in the reaction medium even after treatment processes in order to detect ECs by spectroscopic methods as well as organic carbon contents properly.

5. CONCLUSIVE REMARKS

The main findings of this study are as follows:

This study aimed to investigate applicability of homogeneous and heterogeneous AOPs for the removal of organics present in synthetically prepared municipal ROC sources comprising constituents of real ROC composition, such as humic-like components, common anions and cations as well as ECs. With respect to the organic matrix effect, two different ROC samples were prepared in terms of their organic carbon content and molecular size distribution within the expected composition range. ROC_{m1} was comprised of non-oxidized fractions of HM with lower organic carbon content, whereas ROC_{m2} was combination of both non-oxidized and oxidized fractions of HM with considerably higher organic carbon content. Being regarded as two of the most commonly detected ECs in ROC compositions, SMX and CMZ were selected as the target ECs and added to ROC_{m1} and ROC_{m2} to make ROC_{ECm1} and ROC_{ECm2}. Comparative evaluation of ROC_m and ROC_{ECm} samples would reveal further assessment of influence of ECs on the removal of organics in ROC matrix upon applied processes.

UVC/H_2O_2, Fenton and photo-Fenton systems were nominated as homogeneous AOPs. In order achieve baseline information, UVC photodegradation of ECs, ROC_m and ROC_{ECm} samples were also accomplished for further evaluation of selected AOPs. Solar photocatalytic degradation process using TiO_2, N-TiO_2, ZnO, and TiO_2/ZnO as the photocatalyst specimens was selected as the heterogeneous AOP within the scope of this study. All commercially available and synthesized photocatalyst specimens were characterized in terms of their physicochemical and photochemical properties. In a similar manner attained in the assessment of homogenous AOPs, solar photodegradation of ECs, ROC_m and ROC_{ECm} samples were also accomplished for further evaluation of solar photocatalytic degradation process.

Characterization of organic matter present in ROC_m and ROC_{ECm} were followed by using UV-vis and fluorescence spectroscopic techniques as well as organic carbon contents as the general parameters. Further evaluation was followed by using specified and specific UV-vis and fluorescence parameters. In addition to two dimensional fluorescence spectroscopy in synchronous scan mode, EEM fluorescence spectroscopy was performed for the discrimination of fluorophore-specific components. Toxicity potential of ECs, ROC_m and ROC_{ECm} were assessed prior to and following UVC and solar photodegradation as well as solar photocatalytic degradation processes were assessed.

Irrelevant changes in organic matrix were attained for all ROC samples either exposed to UVC or solar photodegradation processes revealing insignificant changes in specified and specific UV-vis and fluorescence parameters as well as NPOC contents, whereas noticeable differences were attained for ROC_{ECm1} and ROC_{ECm2} compared to ROC_{m1} and ROC_{m2}. Distinct differences between NPOC removal efficiencies of ROC_m and ROC_{ECm} samples could be attributed to susceptibility of ECs to UVC photodegradation in ROC_{ECm} composition and therefore formation of reaction intermediates hindering overall mineralization extent. In addition, either exposed to UVC or solar photodegradation processes, $SUVA_{254}$ values changed insignificantly compared to the initial values indicating the prominence of aromatic structure as well as high molecular weight components of ROC samples even after irradiation period of 90 min. In comparison to UVC photodegradation, UVC/H_2O_2 process accelerated removal efficiencies of specified UV-vis parameters, however still expressed limited mineralization. On the other hand, application of Fenton and photo-Fenton revealed the highest removals for the specified UV-vis parameters and even NPOC contents.

In a comparative manner of view, process efficiency of selected homogeneous AOPs were found to be in the order of photo-Fenton>Fenton>>UVC/H_2O_2>>UVC photodegradation on the removal of specified UV-vis parameters as well as NPOC contents. The superior efficiency of photo-Fenton processes could be attributed to following pathways: *i.* enhancement of $HO^{\bullet}$ generation via UVC photolysis of H_2O_2, and *ii.* catalyzing effect of Fe cycle between its +2 and +3 oxidation states accelerating $HO^{\bullet}$ formation. On the other hand, presence of ECs significantly affected the overall mineralization extent of ROC_{ECm} samples in comparison to ROC_m samples irrespective of the AOPs applied. The reason could be attributed to competition reactions occurring between the removal of HM, ECs, and reaction intermediates of ECs all of which are able to consume $HO^{\bullet}$ present in the reaction medium.

Based on the kinetic data, performance of TiO_2 was found to be superior in comparison to N-doped TiO_2, ZnO and TiO_2/ZnO nanocomposite specimens under solar irradiation simulated reaction conditions. Regarding photocatalytic performance of all photocatalysts, an order of TiO_2>N-TiO_2>TiO_2/ZnO>ZnO could be indicated for successful demineralization (up to 85% NPOC removal in 60 min) of ROC_m and ROC_{ECm} samples. Among all photocatalysts, ZnO was found to be the least effective photocatalyst under simulated solar light in terms of removal of UV absorbing centers as well as mineralization extent. Although ZnO displayed ineffective photocatalytic activity on its own, enhanced photoactivity of TiO_2/ZnO was observed in comparison to ZnO, the reason could be attributed to the presence of TiO_2. In comparison to UVC/H_2O_2 process, photocatalysis was found to be more efficient on the removal of organics present in ROC_m and ROC_{ECm} for the removal of

specified UV-vis parameters as well as NPOC.

Among all homogeneous and heterogeneous AOPs applied for ROC_m and ROC_{ECm} treatment, photo-Fenton process was found to be the most efficient one for the removal of all organics by revealing almost complete removal of the selected parameters within irradiation period of 60 min. However, this process should be carefully interpreted in terms of different aspects, such as cost efficiencies in terms of use of chemicals both in the process and in removing excess H_2O_2 and pH adjustment which could be overcome by applying photocatalysis that needs only photocatalyst as the chemical and could be removed from the reaction medium only by filtration.

Discrimination of various fluorophores with respect to their different characteristics were assessed by using EEM fluorescence spectroscopy as the sophisticated technique. EEM fluorescence contour-plots of ROC_m samples displayed photocatalyst type specific profiles with respect to increasing irradiation periods. During oxidative treatment, both humic-like and fulvic-like fluorophores were non-selectively removed. Emergence of new humic-like and fulvic-like fluorophores upon degradation of high molecular weight humic-like components were also attained. Influence of ECs, especially SMX was clearly observed via EEM fluorescence features of ROC_{ECm1} and ROC_{ECm2} expressed SMX related fluorophores giving fluorescence within the same region of Aromatic Proteins I and II as previously reported in the literature. Moreover, differences in composition of HM also affected EEM fluorescence contour-plots of ROC_{ECm1} and ROC_{ECm2} indicating differences in reaction pathways between ECs, HM and photocatalysts specimens with respect to changes in humic structure and content.

Further evaluation of EEM fluorescence contour-plots were accomplished by the employment of PARAFAC model as the state of the art of multi-way analysis. A four component PARAFAC model was successfully applied for the decomposition of fluorescence EEM fluorescence contour-plots of all samples with respect to photodegradation and photocatalytic degradation processes. Moreover, time dependent normalized Fmax values of identified components revealed further understanding on the changes attained during photodegradation and photocatalytic degradation processes. Photocatalyst specific removal profiles of Fmax with respect to irradiation periods indicated that consideration of gross parameters, such as UV-vis spectroscopy and NPOC contents would supply a general information, whereas EEM in combination with multiway analysis, such as PARAFAC model would give detailed information about behavior of individual fluorescent components present in ROC_m and ROC_{ECm} composition. Despite successive removal of UV_{254} and NPOC contents, four humic-like fluorescent component were still evident and two of them with λ_{max}

at longer emission wavelengths, *i.e.* Em_{max}>510 nm indicating presence of aromatic humic-like centers in accordance with the respective $SUVA_{254}$ results.

Organic composition of ROC may express differences in terms of its amphiphilic, multi-ligand,, and polydisperse character with respect to molecular size distribution profiles, therefore molecular size fractionation of ROC_m and ROC_{ECm} samples were performed prior to and following photodegradation and photocatalytic degradation processes. Self-specific properties of each fraction would reveal better interpretation of interactions between the fractions and reactants upon applied processes. Differentiation of specified E ratios of molecular size fractions of ROC_m and ROC_{ECm} prior to and following photodegradation and photocatalytic degradation processes revealed further assessment of alterations in UV absorbing centers, color forming moieties, and molecular weight with respect to applied processes. In addition, fractional changes in normalized NPOC values were also contributed to consideration of transformation EEM fluorescence features facilitated for understanding changes in fluorophores with respect to molecular size fractions under oxidative and non-oxidative conditions. Characterization of molecular size fractions in terms of selected methods has broadened assessment of experimental outcomes in terms of ROC specific conditions, irradiation source specific conditions for photodegradation processes, and photocatalyst specific conditions for solar photocatalytic degradation process.

Toxicity potential of ROC_m and ROC_{ECm} samples exhibited moderate inhibition under both photodegradation and photocatalytic degradation conditions in accordance with the previous literature studies, however ZnO and TiO_2/ZnO transformed toxicity levels from “low toxic” to “toxic” upon solar photocatalytic degradation which could be attributed to instability and photodissociation of ZnO. Although HM itself has not been reported as “toxic” throughout the literature, its potential impact on the enzymatic reactions of bioluminescent bacteria may interfere with toxicity assessment. Therefore, decision of toxicity assessment should be cautiously interpreted for target matrices in order to eliminate all interferences within the applied system. Under the same experimental conditions, ECs displayed higher toxicity potential in comparison to ROC_{ECm} samples, therefore detrimental impact of HM on the toxicity potential of ECs were clearly demonstrated.

Since all emerging contaminants and specific examples (SMX and CMZ) could always be present along with HM, studies on their individual removals in natural as well as engineered systems could only provide limited information. Although ECs were used as a mixture in ROC related experiments, individual behavior of each EC was also indicated their response to UVC and solar light initiated reactions as well as reactions with ROS. Moreover, photodegradation and photocatalytic

degradation profiles of ECs could be considered as one of the key points in consideration of removal of ECs in waters and wastewater matrices by excluding host-guest relationships with NOM components. Denoting HM as “radical scavenger” in these systems would not be sufficient to understand whole mechanism. However, information presented in this study brings a broader view to the understanding changes in ECs and HM in ROC composition upon applied processes. In addition, behavior of HM in the presence of ECs should also been interpreted cautiously to understand possible interactions between ECs and HM under oxidative and non-oxidative conditions.

RECOMMENDATIONS

Being regarded as the major organic ingredients of water and wastewater composition as well as ROC samples originated from these sources, influence of NOM-like fractions should be cautiously interpreted in the absence/presence of other organic and inorganic components to visualize possible interactions between these elements as well as their response to proposed treatment processes. Detailed information about the interactions between ECs and NOM-like fractions of ROC would reveal broader perspective for the assessment of current limitations and future research needs.

In addition to SMX and CMZ, ROC composition may contain various classifications of ECs with distinct characteristics, therefore further research interest could be devoted to applicability of proposed treatment processes for the removal of other types of ECs present in real ROC samples. On the other hand, detection of ECs precisely in the presence of organic and inorganic matrices could be one of the major challenges of the overall study. Identification of ECs in the presence of organic macromolecules, especially NOM-like components could not be appropriate due to host-guest relationships between these structures enabling accurate and precise measurement of EC quantitatively.

Proposed treatment alternatives could also be applied for the treatment of other origins of ROC, such as ROC_l, ROC_d, and ROC_x. However, for example, in the case of ROC_l, application of solar photocatalytic degradation process alone would not be sufficient to remove target pollutants due to extremely high concentration values of organic and inorganic constituents coming from leachate even following treatment processes. Therefore, application of physicochemical processes as pre-treatment step, such as coagulation and adsorption prior to AOPs would enhance overall removal efficiency of the target pollutants.

Application of solar photocatalytic degradation process on the removal of organics present in ROC could be assessed in a wider perspective by proposing alternatives of this study. Synthesis, characterization and application of various novel photocatalyst specimens, which are active under solar irradiation, could be recommended for future research needs. On the other hand, disadvantages related to the reaction conditions due to use of slurry type reactors could be eliminated by the assessment of photocatalytic degradation systems involving immobilized form of the photocatalyst specimens. Energy efficiency as well as stability of the immobilized systems should also be interpreted cautiously.

Consequently, cost-benefit analysis of these processes should be cautiously investigated for every single unit of the system to reveal detailed information. Utilization of solar light with respect to the modification of photocatalyst specimens could reduce overall energy consumption, however other variables of the system, such as energy consumption for pumping, mixing, etc. as well as chemical consumption should also be interpreted. Prior to application of this system in large scales, a pilot plant would give further information about the efficiency as well as applicability of this system to real scales.

REFERENCES

Abellán, M.N., Bayarri, B., Gimenéz, J., Costa, J., 2007. Photocatalytic degradation of sulfamethoxazole in aqueous suspension of TiO_2. Applied Catalysis B: Environmental, 74, 233-241.

Achilleos, A., Hapeshi, E., Xekoukoulotakis, N.P., Mantzavinos, D., Fatta-Kassinos, D., 2010. UV-A and solar photodegradation of ibuprofen and carbamazepine catalyzed by TiO_2. Separation Science and Technology, 45 (11), 1564-1570.

Adham, S., Burbano, A., Chiu, K., Kumar, M., 2005. Development of a NF/RO Knowledgebase, California Energy Commission, Public Interest Energy Research Program Report.

Aftab, B., Hur, J., 2017. Fast tracking the molecular weight changes of humic substances in coagulation/flocculation processes via fluorescence EEM-PARAFAC. Chemosphere, 178, 317-324.

Alberts J.J., Takács, M., 1999. Characterization of natural organic matter from eight Norwegian surface waters: the effect of ash on molecular size distribution and CHN content. Environment International, 25, 237-244.

Alexander, L., Klug, H.P., 1930. Determination of crystallite size with the X-Ray spectrometer. Journal of Applied Physics, 21, 137-142.

Alfonso-Olivares, C., Fernández-Rodríguez, C., Ojeda-González, R.J., Sosa-Ferrera, Z., Santana-Rodríguez, J.J., Doña Rodríguez, J.M., 2016. Estimation of kinetic parameters and UV doses necessary to remove twenty-three pharmaceuticals from pre-treated urban wastewater by UV/H_2O_2. Journal of Photochemistry and Photobiology A: Chemistry, 329, 130-138.

Alharbi, S.K., Kang, J., Nghiem, N.D., van de Merwe, J.P., Leusch, F.D.L., Price, W.E., 2017. Photolysis and UV/H_2O_2 of diclofenac, sulfamethoxazole, carbamazepine, and trimethoprim: Identification of their major degradation products by ESI-LC-MS and assessment of the toxicity of reaction mixtures. Process Safety and Environmental Protection, 112, 222-234.

Ali, F., Khan, J.A., Shah, N.S., Sayed, M., Khan, H.M., 2018. Carbamazepine degradation by UV and UV-assisted AOPs: Kinetics, mechanism and toxicity investigations. Process Safety and Environmental Protection, 117, 307-314.

Andrade-Eiroa, Á., Canle, M., Cerdá, V., 2013a. Environmental applications of excitation-emission spectrofluorimetry: An in-depth review I., Applied Spectroscopy Reviews, 48, 1-49.

Andrade-Eiroa, Á., Canle, M., Cerdá, V., 2013b. Environmental applications of excitation-emission spectrofluorimetry: An in-depth review II. Applied Spectroscopy Reviews, 48, 77-141.

Andreozzi, R., Raffaele, M., Nicklas, P., 2003. Pharmaceuticals in STP effluents and their solar photodegradation in aquatic environment. Chemosphere, 50, 1319-1330.

Ang, W.S., Elimelech, M., 2007. Protein (BSA) fouling of reverse osmosis membranes: Implications for wastewater reclamation. Journal of Membrane Science, 296, 83-92.

Antunes, M.C.G., Esteves da Silva, J.C.G., 2005. Multivariate curve resolution analysis excitation-emission matrices of fluorescence of humic substances. Anaytica Chimica Acta, 546, 52-59.

Aparicio, F., Escalada, J.P., De Gerónimo, E., Aparicio, V.C., García Einschlag, F.S., Magnacca, G., Carlos, L., Mártire, D.O., 2019. Carbamazepine degradation mediated by light in the presence of humic substances-coated magnetite nanoparticles. Nanomaterials, 9, 1379.

Arola, K., Kallioinen, M., Reinikainen, S.-P., Hatakka, H., Mänttäri, M., 2018. Advanced treatment of membrane concentrate with pulsed corona discharge. Separation and Purification Technology, 198, 121-127.

Arola, K., Van der Bruggen, B., Mänttäri, M., Kallioinen, M., 2019. Treatment options for nanofiltration and reverse osmosis concentrates from municipal wastewater treatment: A review. Critical Reviews in Environmental Science and Technology, 49, 22, 2049-2116.

Ateia, M., Ran, J., Fujii, M., Yoshimura, C., 2017. The relationship between molecular composition and fluorescence properties of humic substances. International Journal of Environmental Science and Technology, 14, 867-880.

Awfa, D., Ateia, M., Fujii, M., Yoshimura, C., 2020. Photocatalytic degradation of organic micropollutants: Inhibition mechanisms by different fractions of natural organic matter. Water Research, 174, 115643.

Azaïs, A., Mendret, J., Cazals, G., Petit, E., Brosillon, S., 2017. Ozonation as a pretreatment process for nanofiltration brines: Monitoring of transformation products and toxicity evaluation. Journal of Hazardous Materials, 338, 381-393.

Backlund, P., 1992. Degradation of aquatic humic material by ultraviolet light. Chemosphere, 25, 1869-1878.

Badia-Fabregat, M., Lucas, D., Gros, M., Rodríguez-Mozaz, S., Barceló, D., Caminal, G., Vicent, T., 2015. Identification of some factors affecting pharmaceutical active compounds (PhACs) removal in real wastewater. Case study of fungal treatment of reverse osmosis concentrate. Journal of Hazardous Materials, 283, 663-671.

Badruzzaman, M., Oppenheimer, J., Adham, S., Kumar, M., 2009. Innovative beneficial reuse of reverse osmosis concentrate using bipolar membrane electrodialysis and electrochlorination processes. Journal of Membrane Science, 326, 392-399.

Baeza, C., Knappe, D.R.U., 2011. Transformation kinetics of biochemically active compounds in low-pressure UV Photolysis and UV/H_2O_2 advanced oxidation processes. Water Research, 45, 4531-4543.

Bagastyo, A.Y., Keller, J., Poussade, Y., Batstone, D.J., 2011a. Characterization and removal of recalcitrants in reverse osmosis concentrates from water reclamation plants. Water Research, 45, 2415-2427.

Bagastyo, A.Y., Radjenovic, J., Mu, Y., Rozendal, R.A., Batstone, D.J., Rabaey K., 2011b. Electrochemical oxidation of reverse osmosis concentrate on mixed metal oxide (MMO) titanium coated electrodes. Water Research, 45, 4951-4959.

Bagastyo, A.Y., Batstone, D.J., Rabaey, K., Radjenovic, J., 2013. Electrochemical oxidation of electrodialysed reverse osmosis concentrate on Ti/Pt-IrO_2, Ti/SnO_2-Sb and boron-doped diamond electrodes. Water Research, 47, 242-250.

Bekbolet, M., Sen-Kavurmaci, S., 2015. The effect of photocatalytic oxidation on molecular size distribution profiles of humic acid. Photochemical and Photobiological Sciences, 14, 576-582.

Ben Abdelmelek, S., Greaves, J., Ishida, K.P., Cooper, W.J., Song, W., 2011. Removal of pharmaceutical and personal care products from reverse osmosis retentate using advanced oxidation processes. Environmental Science and Technology, 45, 3665-3671.

Benito, Y., Ruiz, M.L., 2002. Reverse osmosis applied to metal finishing wastewater, Desalination, 142, 229-234.

Benner, J., Salhi, E., Ternes, T., von Gunten, U., 2008. Ozonation of reverse osmosis concentrate: Kinetics and efficiency of beta blocker oxidation. Water Research, 42, 3003-3012.

Birben, N.C., Uyguner-Demirel, C.S., Sen-Kavurmaci, S., Gurkan, Y.Y., Turkten, N., Cinar, Z., Bekbolet, M., 2015. Comparative evaluation of anion doped photocatalysts on the mineralization and decolorization of natural organic matter. Catalysis Today, 240, 125-131.

Birben, N.C., Uyguner-Demirel, C.S., Sen-Kavurmacı, S., Gürkan, Y.Y., Türkten, N., Kılıç, M., Çınar, Z., Bekbolet, M., 2016. Photocatalytic performance of anion doped TiO_2 on the degradation of complex organic matrix. Journal of Advanced Oxidation Technologies, 19, 2, 199-207.

Birben, N.C., Uyguner-Demirel, C.S., Bekbolet, M., 2017. Organics in reverse osmosis concentrate: Composition and treatment alternatives. Current Organic Chemistry, 21, 1-14.

Birben, N.C., Bekbolet, M., 2019. Role of emerging contaminants on solar photocatalytic treatment of organic matter in reverse osmosis concentrate. Catalysis Today, 326, 101-107.

Blough, N.V., Zepp, R.G., 1995. Reactive Oxygen Species in Natural Waters. In: Foote, C.S., Valentine, J.S. (Eds.), Active Oxygen in Chemistry, 280-333, Chapman and Hall, New York.

Bohdziewicz, J., Kudlek, E., Dudziak, M., 2016. Influence of the catalyst type (TiO_2 and ZnO) on the photocatalytic oxidation of pharmaceuticals in the aquatic environment. Desalination and Water Treatment, 57, 3, 1552-1563.

Borowska, E., Gomes, J.F., Martins, R.C., Quinta-Ferreira, R.M., Horn, H., Gmurek, M., 2019. Solar photocatalytic degradation of sulfamethoxazole by TiO_2 modified with noble metals. Catalysts, 9, 500.

Bro, R., 1997. PARAFAC. Tutorial and applications. Chemometrics and intelligent laboratory systems, 38, 149-171.

Cai, Q.Q., Wu, M.Y., Li, R., Deng, S.H., Lee, B.C.Y., Ong, S.L., Hu, J.Y., 2020. Potential of combined advanced oxidation-biological process for cost-effective organic matters removal in reverse osmosis concentrate produced from industrial wastewater reclamation: Screening of AOP pre-treatment technologies. Chemical Engineering Journal, 389, 123419.

Calisto, V., Domingues, M.R.M., Erny, G.L., Esteves, V.I., 2011. Direct photodegradation of carbamazepine followed by micellar electrokinetic chromatography and mass spectrometry. Water Research, 45, 1094-1104.

Calvert, J.G., Pitts, J.N. (Eds), 1966. Photochemistry, John Wiley and Sons Inc., USA.

Canonica, S., Meunier, L., von Gunten, U., 2008. Phototransformation of selected pharmaceuticals during UV treatment of drinking water. Water Research 42, 1-2, 121-128.

Caram, B., García-Ballesteros, S., Santos-Juanes, L., Arques, A., García-Einschlag, F.S., 2018. Humic like substances for the treatment of scarcely soluble pollutants by mild photo-Fenton process. Chemosphere, 198, 139-146.

Carlson, J.C., Stefan, M.I., Parnis, J.M., Metcalfe, C.D., 2015. Direct UV photolysis of selected pharmaceuticals, personal care products and endocrine disruptors in aqueous solution. Water Research, 84, 350-361.

Chaplin, B.P., Scharder, G., Farrel, J., 2010. Electrochemical destruction of N-nitrosodimethylamine in reverse osmosis concentrate using boron-doped diamond film electrodes. Environmental Science and Technology, 44, 11, 4264-4269.

Chelme-Ayala, P., Smith, D.W., El-Din, M.G., 2009. Membrane concentrate management options: a comprehensive critical review. Canadian Journal of Civil Engineering, 36, 1107-1119.

Chen, J., LeBoeuf, E.J., Dai, S., Gu, B., 2003. Fluorescence spectroscopic studies of natural organic matter fractions. Chemosphere, 50, 5, 639-647.

Chen, W., Qian, C., Liu, X.-Y., Yu, H.-Q., 2014. Two-dimensional correlation spectroscopic analysis on the interaction between humic acids and TiO_2 nanoparticles. Environmental Science and Technology, 48, 11119-11126.

Chen, H., Lei, K., Wang, X., 2016. Terrestrial humic substances in Daliao River and its estuary: optical signatures and photoreactivity to UVA light. Environmental Science and Pollution Research, 23, 6459-6471.

Chen, Y., Baygents, C.J., Farrell, J., 2017. Evaluating electrocoagulation and chemical coagulation for removing dissolved silica from high efficiency reverse osmosis (HERO) concentrate solutions. Journal of Water Process Engineering, 16, 50-55.

Chen, Y., Li, S., Hu, J., 2020. Photoelectrocatalytic degradation of organics and formation of disinfection byproducts in reverse osmosis concentrate. Water Research, 168, 115105.

Chiron, S., Minero, C., Vione, D., 2006. Photodegradation processes of the antiepileptic drug carbamazepine, relevant to estuarine waters. Environmental Science and Technology, 40, 5977-5983.

Cho, Y., Choi, W., 2002. Visible light-induced reactions of humic acids on TiO_2. Journal of Photochemistry and Photobiology A: Chemistry, 48, 129-135.

Choi, J., Lee, H., Choi, Y., Kim, S., Lee, S., Lee, S., Choi, W., Lee, J., 2014. Heterogeneous photocatalytic treatment of pharmaceutical micropollutants: Effects of wastewater effluent matrix and catalyst modifications. Applied Catalysis B: Environmental, 147, 8-16.

Chon, K., Chon, Ky., Cho, J., 2017. Characterization of size fractionated dissolved organic matter from river water and wastewater effluent using preparative high performance size exclusion chromatography. Organic Geochemistry, 103, 105-112.

Coble, P.G., 1996. Characterization of marine and terrestrial DOM in seawater using excitation-emission matrix spectroscopy. Marine Chemistry, 51, 325-346.

Coble, P.G., Lead, J., Baker, A., Reynolds, D.M., Spencer, R.G.M., 2014. Aquatic Organic Matter Fluorescence in Aquatic Organic Matter Fluorescence. Cambridge University Press, UK.

Cooper, W.J., Zika, R.G., Petasne, R.G., Fischer, A.M., 1989. Sunlight-Induced Photochemistry of Humic Substances in Natural Waters: Major Reactive Species. In Aquatic Humic Substances: Influence on Fate and Treatment of Pollutants. Suffet, I.H., MacCarthy, P., (Eds.), American Chemical Society: Washington, DC, Advances in Chemistry Series 219.

De la Cruz, N., Esquius, L., Grandjean, D., Magnet, A., Tungler, A., de Alencastro, L.F., Pulgarín, C., 2013. Degradation of emergent contaminants by UV, UV/H_2O_2 and neutral photo-Fenton at pilot scale in a domestic wastewater treatment plant. Water Research, 47, 5836-5845.

Del Vecchio, R., Blough, N.V., 2002. Photobleaching of chromophoric dissolved organic matter in natural waters: kinetics and modeling. Marine Chemistry, 78, 231-253.

Deng, J., Shao, Y., Gao, N., Xia, S., Tan, C., Zhou, S., Hu, X., 2013. Degradation of the antiepileptic drug carbamazepine upon different UV-based advanced oxidation processes in water. Chemical Engineering Journal, 222, 150-158.

Deng, H., 2020. Ozonation mechanism of carbamazepine and ketoprofen in RO concentrate from municipal wastewater treatment: Kinetic regimes, removal efficiency and matrix effect. Science of the Total Environment, 717, 137150.

Dialynas, E., Mantzavinos, D., Diamadopoulos, E., 2008. Advanced treatment of the reverse osmosis concentrate produced during reclamation of municipal wastewater. Water Research, 42, 4603-4608.

Dignac, M.F., Ginestet, P., Rybacki, D., Bruchet, A., Urbain, V., Scribe, P., 2000. Fate of wastewater organic pollution during activated sludge treatment: nature of residual organic matter. Water Research, 34**,** 4185-4194.

Dionysiou, D.D., Li Puma, G., Ye, J., Schneider, J., Bahnemann, D., 2016. Photocatalysis Applications, Royal Society of Chemistry, Cambridge, U.K.

Doll, T.E., Frimmel, F.H., 2004. Kinetic study of photocatalytic degradation of carbamazepine, clofibric acid, iomeprol and iopromide assisted by different TiO_2 materials-determination of intermediates and reaction pathways. Water Research, 38, 955-964.

Doll, T.E., Frimmel, F.H., 2005. Photocatalytic degradation of carbamazepine, clofibric acid and iomeprol with P25 and Hombikat UV100 in the presence of natural organic matter (NOM) and other organic water constituents. Water Research, 39, 2-3, 403-411.

Dong, M.M., Mezyk, S.P., Rosario-Ortiz, F.L., 2010. Reactivity of effluent organic matter (EfOM) with hydroxyl radical as a function of molecular weight. Environmental Science and Technology, 44, 15, 5714-5720.

Dong, M.M., Trenholm, R., Rosario-Ortiz, F.L., 2015. Photochemical degradation of atenolol, carbamazepine, meprobamate, phenytoin and primidone in wastewater effluents. Journal of Hazardous Materials, 282, 216-223.

Donner, E., Kosjek, T., Qualmann, S., Kusk, K.O., Heath, E., Revitt, D.M., Ledin, A., Andersen, H.R., 2013. Ecotoxicity of carbamazepine and its UV photooxidation transformation products. Science of the Total Environment, 443, 870-876.

Edzwald, J.K., Becker, W.C., Wattier, K.L., 1985. Surrogate parameters for monitoring organic matter and THM precursors. Journal of American Water and Wastewater Association, 77, 122-132.

Egeberg, P.K., Eikenes, M., Gjessing, E.T., 1999. Organic nitrogen distribution in NOM size classes. Environment International, 25, 225-236.

Egeberg, P.K., Christy, A.A., Eikenes, M., 2002. The molecular size of natural organic matter (NOM) determined by diffusivimetry and seven other methods. Water Research, 36, 925-932.

Esparza-Soto, M., Fox, P., Westerhoff, P., 2006. Transformation of molecular weight distributions of dissolved organic carbon and UV-absorbing compounds at full-scale wastewater-treatment plants. Water Environment Research, 78, 3, 253-262.

Farías, T., Ruiz-Salvador, A.R., Rivera, A., 2003. Interaction studies between drugs and a purified natural clinoptilolite. Microporous and Mesoporous Materials, 61, 117-125.

Faust, B.C., Hoigné, J., 1990. Photolysis of Fe (III)-hydroxy complexes as sources of OH radicals in clouds, fog and rain. Atmospheric Environment Part A General, 24, 1, 79-89.

Fenton, H.J.H., 1894. LXXIII.-Oxidation of tartaric acid in presence of iron. Journal of the Chemical Society, Transactions, 65, 899-910.

Fujioka, T., Khan, S.J., Poussade, Y., Drewes, J.E., Nghiem, L.D., 2012. N-Nitrosamine removal by reverse osmosis for indirect potable water reuse e a critical review based on observations from laboratory-, pilot- and full-scale studies. Separation and Purification Technologies, 98, 503-515.

Fujishima, A., Rao, T.N., Tryk, D.A., 2000. Titanium dioxide photocatalysis. Journal of Photochemistry and Photobiology C: Photochemistry Reviews, 1, 1-21.

Gabelich, C.J., Rahardianto, A., Northrup, C.R., Yun, T.I., Cohen, Y., 2011. Process evaluation of intermediate chemical demineralization for water recovery enhancement in production-scale brackish water desalting. Desalination, 272, 36-45.

García Ballesteros, S., Costante, M., Vicente, R., Mora, M., Amat, A.M., Arques, A., Carlos, L., García Einschlag, F.S., 2017. Humic-like substances from urban waste as auxiliaries for photo-Fenton treatment: a fluorescence EEM-PARAFAC study. Photochemical and Photobiological Sciences, 16, 38-45.

Georgaki, I., Vasilaki, E., Katsarakis, N., 2014. A study on the degradation of carbamazepine and ibuprofen by TiO_2 and ZnO photocatalysis upon UV/visible-light irradiation. American Journal of Analytical Chemistry, 5, 518-534.

Ghafour, E.E.A., 2002. Enhancing RO system performance utilizing antiscalants. Desalination, 153, 149-153.

Glaze, W.H., Kang, J.W., Chapin, D.H., 1987. The chemistry of water treatment processes involving ozone, hydrogen peroxide and ultraviolet radiation. Ozone Science and Engineering, 9, 4, 335-352.

Gmurek, M., Horn, H., Majewsky, M., 2015. Phototransformation of sulfamethoxazole under simulated sunlight: Transformation products and their antibacterial activity toward *Vibrio fischeri*. Science of the Total Environment, 538, 58-63.

Goldstone, J.V., Ullin, M.J., Bertilsson, P.S., Voelker, B.M., 2002. Reactions of hydroxyl radical with humic substances: Bleaching, mineralization, and production of bioavailable carbon substrates. Environmental Science and Technology, 36, 364-372.

González, O., Sans, C., Esplugas, S., Malato, S., 2009. Application of solar advanced oxidation processes to the degradation of the antibiotic sulfamethoxazole. Photochemical and Photobiological Sciences, 8, 1032-1039.

Gopalan, S., Savage, P.E.J., 1994. Reaction mechanism for phenol oxidation in supercritical water. Journal of Physical Chemistry, 98, 12646-12652.

Gou, X., Zhang, P., Song, Y., Qian, F., Yu, H., Zen, G., 2017. Novel insights into the coagulation process for pharmaceutical wastewater treatment with fluorescence EEMs-PARAFAC. Water Science and Technology, 76, 11-12, 3246-3257.

Gray, S.R., Ritchie, C.B., Tran, T., Bolto, B.A., 2007. Effect of NOM characteristics and membrane type on microfiltration performance. Water Research, 41, 3833-3841.

Greenlee, L.F., Lawler, D.F., Freeman, B.D., Marrot, B., Moulin P., 2009. Reverse osmosis desalination: Water sources, technology, and today's challenges. Water Research, 43, 2317-2348.

Gurkan, Y.Y., Turkten, N., Hatipoglu, A., Cinar, Z., 2012. Photocatalytic degradation of cefazolin over N-doped TiO_2 under UV and sunlight irradiation: Prediction of the reaction paths via conceptual DFT. Chemical Engineering Journal, 184, 113-124.

Gursoy-Haksevenler, B.H., Arslan-Alaton, I., 2020. Effects of treatment on the characterization of organic matter in wastewater: a review on size distribution and structural fractionation. Water Science and Technology, 82, 5, 799-828.

Haag, W.R., Hoigné, J., 1986. Singlet oxygen in surface waters: 3. Photochemical formation and steady-state concentrations in various types of waters. Environmental Science and Technology, 20, 341-348.

Haroune, L., Salaun, M., Ménard, A., Legault, C.Y., Bellenger, J.-P., 2014. Photocatalytic degradation of carbamazepine and three derivatives using TiO_2 and ZnO: Effect of pH, ionic strength, and natural organic matter. Science of the Total Environment, 475, 16-22.

Hatchard, C.G., Parker, C.A., 1953. A new sensitive actinometer. I. Some trials with potassium ferrioxalate. Proceedings of the Royal Society A, 220, 104-116.

Hatchard, C.G., Parker, C.A., 1956. A new sensitive chemical actinometer-II. Potassium ferrioxalate as a standard chemical actinometer. Proceedings of the Royal Society A, 235, 518-536.

He, Y., Sutton, N.B., Rijnaarts, H.H.H., Langenhoff, A.A.M., 2016. Degradation of pharmaceuticals in wastewater using immobilized TiO_2 photocatalysis under simulated solar irradiation. Applied Catalysis B: Environmental, 182, 132-141.

Heibati, M., Stedmon, C.A., Stenroth, K., Rauch, S., Toljander, J., Säve-Söderbergh, M., Murphy, K. R., 2017. Assessment of drinking water quality at the tap using fluorescence spectroscopy. Water Research, 125, 1-10.

Helms, J.R., Stubbins, A., Ritchie, J.D., Minor, E.C., Kieber, D.J., Mopper, K., 2008. Absorption spectral slopes and slope ratios as indicators of molecular weight, source, and photobleaching of chromophoric dissolved organic matter. Limnology and Oceanography, 53, 955-969.

Helms, J.R., Mao, J., Stubbins, A., Schmidt-Rohr, K., Spencer, R.G.M., Hernes, P.J., Mopper, K., 2014. Loss of optical and molecular indicators of terrigenous dissolved organic matter during long-term photobleaching. Aquatic Science, 76, 353-373.

Hermosilla, D., Cortijo, M., Huang, C.P., 2009. The role of iron on the degradation and mineralization of organic compounds using conventional Fenton and photo-Fenton processes. Chemical Engineering Journal, 155, 3, 637-646.

Hermosilla, D., Merayo, N., Ordóñez, R., Blanco, A., 2012. Optimization of conventional Fenton and ultraviolet-assisted oxidation processes for the treatment of reverse osmosis retentate from a paper mill. Waste Management, 32, 1236-1243.

Hu, L., Flanders, P.M., Miller, P.L., Strathmann, T.J., 2007. Oxidation of sulfamethoxazole and related antimicrobial agents by TiO_2 photocatalysis. Water Research, 41, 2612-2626.

Hudson, N., Baker, A., Reynolds, D., 2007. Fluorescence analysis of dissolved organic matter in natural, waste and polluted waters-a review. River Research and Applications, 23, 631-649.

Hur, J., Kim, G., 2009. Comparison of the heterogeneity within bulk sediment humic substances from a stream and reservoir via selected operational descriptors. Chemosphere, 75, 4, 483-490.

Hurwitz, G., Hoek, E.M.V., Liu, K., Fan, L., Roddick, F.A., 2014. Photo-assisted electrochemical treatment of municipal wastewater reverse osmosis concentrate. Chemical Engineering Journal, 249, 180-188.

Ignatev, A., Tuhkanen, T., 2019. Monitoring WWTP performance using size-exclusion chromatography with simultaneous UV and fluorescence detection to track recalcitrant wastewater fractions. Chemosphere, 214, 587-597.

Ikehata, K., El-Din, M.G., 2004. Degradation of recalcitrant surfactants in wastewater by ozonation and advanced oxidation processes: A review. Ozone: Science & Engineering, 26, 327-343.

Isaias, N.P., 2001. Experience in reverse osmosis pretreatment. Desalination, 139, 57-64.

Ishii, S.K.L., Boyer, T.H., 2012. Behavior of reoccurring PARAFAC components in fluorescent dissolved organic matter in natural and engineered systems: A critical review. Environmental Science and Technology, 46, 2006-2017.

ISO 11348-3:2007, Water quality-Determination of the inhibitory effect of water samples on the light emission of *Vibrio fischeri*.

Jaffé, R., Boyer, J.N., Lu, X., Maie, N., Yang, C., Scully, N.M., Mock, S., 2004. Source characterization of dissolved organic matter in a subtropical mangrovedominated estuary by fluorescence analysis. Marine Chemistry, 84, 195-210.

Jaffé, R., Cawley, K.M., Yamashita, Y., 2014. Applications of excitation emission matrix fluorescence with parallel factor analysis (EEM-PARAFAC) in assessing environmental dynamics

of natural dissolved organic matter (DOM) in aquatic environments: A Review in Advances in the Physicochemical Characterization of Dissolved Organic Matter: Impact on Natural and Engineered Systems. ACS Symposium Series, Volume 1160.

Jamil, S., Jeong, S., Vigneswaran, S., 2016. Application of pressure assisted forward osmosis for water purification and reuse of reverse osmosis concentrate from a water reclamation plant. Separation and Purification Technology, 171, 182-190.

Jamil, S., Loganathan, P., Kandasamy, J., Listowski, A., Khourshed, C., Naidu, R., Vigneswaran, S., 2019. Removal of dissolved organic matter fractions from reverse osmosis concentrate: Comparing granular activated carbon and ion exchange resin adsorbents. Journal of Environmental Chemical Engineering, 7, 103126.

Janitabar-Darzi, S., Mahjoub, A.R., 2009. Investigation of phase transformations and photocatalytic properties of sol-gel prepared nanostructured ZnO/TiO_2 composites. Journal of Alloys and Compounds, 486, 805-808.

Jelic, A., Michael, I., Achilleos, A., Hapeshi, E., Lambropoulou, D., Peréz, S., Petrovic M., Fatta-Kassinos, D., Barceló, D., 2013. Transformation products and reaction pathways of carbamazepine during photocatalytic and sonophotocatalytic treatment. Journal of Hazardous Materials, 263, 1, 177-186.

Joo, S.H., 2014. Combined adsorbents and reactive oxygen species (ROS) generators in soil for treating reverse osmosis concentrates. Powder Technology, 264, 9-21.

Joo, S.H., Tansel, B., 2015. Novel technologies for reverse osmosis concentrate treatment: A review. Journal of Environmental Management, 150, 322-335.

Justo, A., González, O., Aceña, J., Pérez, S., Barceló, D., Sans, C., Esplugas, S., 2013. Pharmaceuticals and organic pollution mitigation in reclamation osmosis brines by UV/H_2O_2 and ozone. Journal of Hazardous Materials, 263, 268-274.

Kang, Y.W., Hwang, K., 2000. Effects of reaction conditions on the oxidation efficiency in the Fenton process. Water Research, 34, 2786-2790.

Karunakaran, C., Rajeswari, V., Gomathisankar, P., 2011. Enhanced photocatalytic and antibacterial activities of sol–gel synthesized ZnO and Ag-ZnO. Materials Science in Semiconductor Processing, 14, 133-138.

Kim, H.Y., Kim, T.-H., Yu, S., 2015. Photolytic degradation of sulfamethoxazole and trimethoprim using UV-A, UV-C and vacuum-UV (VUV). Journal of Environmental Science and Health, Part A, 50, 292-300.

Kim, I., Tanaka, H., 2009. Photodegradation characteristics of PPCPs in water with UV treatment. Environment International, 35, 793-802.

Kim, I., Yamashita, N., Tanaka, H., 2009. Photodegradation of pharmaceuticals and personal care products during UV and UV/H_2O_2 treatments. Chemosphere, 77, 518-525.

King, J.F., Szczuka, A., Zhang, Z., Mitch, W.A., 2020. Efficacy of ozone for removal of pesticides, metals and indicator virus from reverse osmosis concentrates generated during potable reuse of municipal wastewaters. Water Research, 176, 115744.

Kisch, H., 2015. Semiconductor Photocatalysis: Principles and Applications. Wiley-VCH Weinheim.

Kosjeck, T., Andersen, H.R., Kompare, B., Ledin, A., Heath, E., 2009. Fate of carbamazepine during water treatment. Environmental Science and Technology, 43, 6256-6261.

Kowalczuk, P., Durako, M.J., Young, H., Kahn, A.E., Cooper, W.J., Gonsior, M., 2009. Characterization of dissolved organic matter fluorescence in the South Atlantic Bight with use of PARAFAC model: Interannual variability. Marine Chemistry, 113, 182-196.

Kubelka, P., Munk, F., 1931. Ein Beitrag Zur Optik der Farbanstriche. Zeitschrift für Technische Physik, 12, 593-601.

Kumar, M., Badruzzman, M., Adham, S., Oppenheimer, J., 2007. Beneficial phosphate recovery from reverse osmosis concentrate of an integrated membrane system using polymeric ligand exchanger (PLE). Water Research, 41, 2211-2219.

Lam, M.W., Mabury, S.A., 2005. Photodegradation of the pharmaceuticals atorvastatin, carbamazepine, levofloxacin, and sulfamethoxazole in natural waters. Aquatic Sciences, 67, 177-188.

Lanzalunga, O., Bietti, M., 2000. Photo-and radiation chemical induced degradation of lignin model compounds. Journal of Photochemistry and Photobiology B: Biology, 56, 85-108.

Lay, Y.S., 1989. Oxidation of 1,2-Dibromo-3-chloropropane in Ground Water Using Advanced Oxidation Processes, PhD Thesis, University of California at Los Angeles, USA.

Lazarova, V., Asano, T., Bahri, A., Anderson, J. (Eds.), 2013. Milestones in Water Reuse: The Best Success Stories, 1st Ed., IWA Publishing, London.

Le, N.L., Nunes, S.P., 2016. Materials and membrane technologies for water and energy sustainability. Sustainable Materials and Technologies, 7, 1-28.

Lee, B.-M., Seo, Y.-S., Hur, J., 2015. Investigation of adsorptive fractionation of humic acid on graphene oxide using fluorescence EEM-PARAFAC. Water Research, 73, 242-251.

Lee, L.Y., Ng, H.Y., Ong, S.L., Tao, G., Kekre, K., Viswanath, B., Lay, W., Seah, H., 2009. Integrated pretreatment with capacitive deionization for reverse osmosis reject recovery from water reclamation plant. Water Research, 43, 4769-4777.

Lee, M.-Y., Wang, W.-L., Du, Y., Wu, Q.-Y., Huang, N., Xu, Z.-B., Hu, H.-Y., 2020. Comparison of UV/H_2O_2 and UV/PS processes for the treatment of reverse osmosis concentrate from municipal wastewater reclamation. Chemical Engineering Journal, 388, 124260.

Leenher, J.A., 1981. Comprehensive approach to preparative isolation and fractionation of dissolved organic carbon from natural waters and wastewaters. Environmental Science and Technology, 15, 578-587.

Lekkerkerker-Teunissen, K., Benotti, M.J., Snyder, S.A., van Dijk, H.J., 2012. Transformation of atrazine, carbamazepine, diclofenac and sulfamethoxazole by low and medium pressure UV and UV/H_2O_2 treatment. Separation and Purification Technology, 96, 33-43.

Levine, A., Tchobanoglous, G., Asano, T., 1985. Characterization of the size distribution of contaminants in wastewater: treatment and reuse implications. Water Pollution Control Federation, 57, 7, 805-816.

Li, Q., Xu, Z., Pinnau, I., 2007. Fouling of reverse osmosis membranes by biopolymers in wastewater secondary effluent: Role of membrane surface properties and initial permeate flux. Journal of Membrane Science, 290, 173-181.

Li, W.-T., Chen, S.-Y., Xu, Z.-X., Li, Y., Shuang, C.-D., Li, A.-M., 2014. Characterization of dissolved organic matter in municipal wastewater using fluorescence PARAFAC analysis and chromatography multi-excitation/emission scan: a comparative study. Environmental Science and Technology, 48, 2603-2609.

Li, S., Ju, H., Ji, M., Zhang, J., Song, K., Chen, P., Mu, G., 2018. Terrestrial humic-like fluorescence peak of chromophoric dissolved organic matter as a new potential indicator tracing the antibiotics in typical polluted watershed. Journal of Environmental Management, 228, 65-76.

Li, N., Wang, X., Zhang, H., Zhang, Z., Ding, J., Lu, J., 2019. Comparing the performance of various nanofiltration membranes in advanced oxidation-nanofiltration treatment of reverse osmosis concentrates. Environmental Science and Pollution Research, 26, 17472-17481.

Lin, L., Xu, X., Papelis, C., Cath, T.Y., Xu, P., 2014. Sorption of metals and metalloids from reverse osmosis concentrate on drinking water treatment solids. Separation and Purification Technology, 134, 37-45.

Lin, X.H., Li, S.F.Y., 2014a. Determination of organic pollutants in municipal reverse osmosis concentrate by electrospray ionization-quadrupole time-of-flight tandem mass spectrometry and photocatalytic degradation methods. Desalination, 344, 206-211.

Lin, X.H., Sriramulu, D., Li, S.F.Y., 2014b. Selective removal of photocatalytic non-degradable fluorosurfactants from reverse osmosis concentrate. Water Research, 68, 831-838.

Lin, X.H., Li, S.F.Y., 2015. Impact of the spatial distribution of sulfate species on the activities of SO_4^{2-}/TiO_2 photocatalysts for the degradation of organic pollutants in reverse osmosis concentrate. Applied Catalysis B: Environmental, 170-171, 263-272.

Lin, L., Wang, H., Luo, H., Xu, P., 2016. Photocatalytic treatment of desalination concentrate using optical fibers coated with nanostructured thin films: Impact of water chemistry and seasonal climate variations. Photochemistry and Photobiology, 92, 379-387.

Lin, L., Jiang, W., Xu, P., 2017. Comparative study on pharmaceuticals adsorption in reclaimed water desalination concentrate using biochar: Impact of salts and organic matter. Science of the Total Environment, 601-602, 857-864.

Linsebigler, A.L., Lu, G., Yates, Jr., J.T., 1995. Photocatalysis on TiO_2 surfaces: principles, mechanisms and selected results. Chemical Reviews, 95, 735-758.

Liu, K., Roddick, F.A., Fan, L.H., 2012. Impact of salinity and pH on the UVC/H_2O_2 treatment of reverse osmosis concentrate produced from municipal wastewater reclamation. Water Research, 46, 3229-3239.

Liu, S., Lim, M., Fabris, R., Chow, C., Chiang, K., Drikas, M., Amal, R., 2008. Removal of humic acid using TiO_2 photocatalytic process-fractionation and molecular weight characterization studies. Chemosphere, 72, 2, 263-271.

Logan, B.E., Jiang, Q., 1990. Molecular Size Distributions of Dissolved Organic Matter. Journal of Environmental Engineering, 116, 6, 1046-1062.

Lu, J., Fan, L., Roddick, F.A., 2013. Potential of BAC combined with UVC/H_2O_2 for reducing organic matter from highly saline reverse osmosis concentrate produced from municipal wastewater reclamation. Chemosphere, 93, 683-688.

Luo, S., Wei, Z., Spinney, R., Zhang, Z., Dionysiou, D.D., Gao, L., Chai, L., Wang, D., Xiao, D., 2018. UV direct photolysis of sulfamethoxazole and ibuprofen: An experimental and modelling study. Journal of Hazardous Materials, 343, 132-139.

Lütke Eversloh, C., Henning, N., Schulz M., Ternes, T.A., 2014. Electrochemical treatment of iopromide under conditions of reverse osmosis concentrates-elucidation of the degradation pathway. Water Research, 48, 237-246.

Ly, Q. V., Kim, H.-C., Hur, J., 2018. Tracking fluorescent dissolved organic matter in hybrid ultrafiltration systems with TiO_2/UV oxidation via EEM-PARAFAC. Journal of Membrane Science, 549, 275-282.

Lyon, B.A., Cory, R.M., Weinberg, H.S., 2014. Changes in dissolved organic matter fluorescence and disinfection byproduct formation from UV and subsequent chlorination/chloramination. Journal of Hazardous Materials, 264, 411-419.

Mack, J., Bolton, J.R., 1999. Photochemistry of nitrite and nitrate in aqueous solution: A review. Journal of Photochemistry and Photobiology A: Chemistry, 128, 1-13.

Malamis, S., Katsou, E., Takopoulos, K., Demetriou, P., Loizidou, M., 2012. Assessment of metal removal, biomass activity and RO concentrate treatment in an MBR-RO system. Journal of Hazardous Materials, 209-210, 1-8.

Martínez-Costa, J.I., Rivera-Utrilla, J., Leyva-Ramos, R., Sánchez-Polo, M., Velo-Gala, I., Mota, A.J., 2018. Individual and simultaneous degradation of the antibiotics sulfamethoxazole and trimethoprim in aqueous solutions by Fenton, Fenton-like and photo-Fenton processes using solar and UV radiations. Journal of Photochemistry and Photobiology A: Chemistry, 360, 95-108.

Matamoros, V., Duhec, A., Albaigés, J., Bayona, J.M., 2009. Photodegradation of carbamazepine, ibuprofen, ketoprofen and 17α-ethinylestradiol in fresh and seawater. Water Air Soil Pollution, 196, 161-168.

Mestre, A.S., Carvalho, A.P., 2019. Photocatalytic degradation of pharmaceuticals carbamazepine, diclofenac, and sulfamethoxazole by semiconductor and carbon materials: A review. Molecules, 24, 3702.

Tchobanoglous, G., Burton, F.L., 1991. Wastewater Engineering, Treatment, Disposal, and Reuse, McGraw-Hill, Inc., New York.

McKnight, D.M., Boyer, E.W., Westerhoff, P.K., Doran, P.T., Kulbe, T., Andersen, D.T., 2001. Spectrofluorometric characterization of dissolved organic matter for indication of precursor organic material and aromaticity. Limnology and Oceanography, 46, 38-48.

Miano, T.M., Sposito, G., Martin, J.P., 1988. Fluorescence spectroscopy of humic substances. Soil Science Society of American Journal, 52, 1016-1019.

Mirales-Cuevas, S., Oller, I., Agüera, A., Sánchez Pérez, J.A., Malato, S., 2017. Strategies for reducing cost by using solar photo-Fenton treatment combined with nanofiltration to remove microcontaminants in real municipal effluents: Toxicity and economic assessment. Chemical Engineering Journal, 318, 161-170.

Mirzaei, A., Yerushalmi, L., Chen, Z., Haghighat, F., Guo, J., 2018. Enhanced photocatalytic degradation of sulfamethoxazole by zinc oxide photocatalyst in the presence of fluoride ions: Optimization of parameters and toxicological evaluation. Water Research, 132, 241-251.

Mo, H., Tay, K. G., Ng, H.Y., 2008. Fouling of reverse osmosis membrane by protein (BSA): Effects of pH, calcium, magnesium, ionic strength and temperature. Journal of Membrane Science, 315, 28-35.

Monsalvo, V.M., Lopez, J., Munoz, M., de Pedro, Z.M., Casas, J.A., Mohedano, A.F., Rodriguez, J.J., 2015. Application of Fenton-like oxidation as pre-treatment for carbamazepine biodegradation. Chemical Engineering Journal, 264, 856-862.

Mostafa, S., Rosario-Ortiz, F.L., 2013. Singlet oxygen formation from wastewater organic matter. Environmental Science and Technology, 47, 8179-8186.

Murphy, K.R., Stedmon, C.A., Waite, T.D., Ruiz, G.M. 2008. Distinguishing between terrestrial and autochthonous organic matter sources in marine environments using fluorescence spectroscopy. Marine Chemistry, 108, 1-2, 40-58.

Murphy, K.R., Stedmon, C.A., Graeber, D., Bro, R., 2013. Fluorescence spectroscopy and multi-way techniques. PARAFAC. Analytical Methods, 5, 6557-6566.

Nasuhoglu, D., Yargeau, V., Berk, D., 2011. Photo-removal of sulfamethoxazole (SMX) by photolytic and photocatalytic processes in a batch reactor under UV-C radiation (λ_{max}= 254 nm). Journal of Hazardous Materials, 186, 67-75.

Neta, P., Huie, R.E., Ross, A.B., 1988. Rate constants for reactions of inorganic radicals in aqueous solution. Journal of Physical and Chemical Reference Data, 17, 1027-1284.

Neyens, E., Baeyens, J., 2003. A review of classic Fenton's peroxidation as an advanced oxidation technique. Journal of Hazardous Materials B, 98, 33-50.

Ng, H.Y., Lee, L.Y., Ong, S.L., Tao, G., Viswanath, B., Kekre, K., Lay, W., Seah, H., 2008. Treatment of RO brine-towards sustainable water reclamation practice. Water Science and Technology, 58, 931-936.

Nguyen, H.V.-M., Lee, M.-H., Hur, J., Schlautman, M.A., 2013. Variations in spectroscopic characteristics and disinfection byproduct formation potentials of dissolved organic matter for two contrasting storm events. Journal of Hydrology, 481, 132-142.

Nikolajsen, R.P.H., Booksh, K.S., Hansen, A.M., Bro, R, 2003. Quantifying catecholamines using multi-way kinetic modelling. Analytica Chimica Acta, 475, 137-150.

Niu, J., Zhang, L., Li, Y., Zhao, J., Lv, S., Xiao, K., 2013. Effects of environmental factors on sulfamethoxazole photodegradation under simulated sunlight irradiation: Kinetics and mechanism. Journal of Environmental Sciences, 25, 6, 1098-1106.

Ollis, D.F., 1985. Contaminant degradation in water. Environmental Science and Technology, 19, 480-484.

Oropesa, A.L., Beltrán, F.J., Floro, A.M., Sagasti, J.J.P., Palma, P., 2018. Ecotoxicological efficiency of advanced ozonation processes with TiO_2 and black light used in the degradation of carbamazepine. Environmental Science and Pollution Research, 25, 1670-1682.

Parsons, S. (Eds.), 2004. Advanced Oxidation Processes for Water and Wastewater Treatment, IWA Publishing, London.

Pereira, V.J., Linden, K.G., Weinberg, H.S., 2007. Evaluation of UV irradiation for photolytic and oxidative degradation of pharmaceutical compounds in water. Water Research, 41, 4413-4423.

Peuravuori, J., Koivikko, R., Pihlaja, K., 2002. Characterization, differentiation and classification of aquatic humic matter separated with different sorbents: synchronous scanning fluorescence spectroscopy. Water Research, 36, 4552-4562.

Pérez, G., Fernández-Alba, A.R., Urtiaga, A.M., Ortiz, I., 2010. Electro-oxidation of reverse osmosis concentrates generated in tertiary water treatment. Water Research, 44, 2763-2772.

Pérez-González, A., Urtiaga, A.M., Ibánez, R., Ortiz, I., 2012. State of the art and review on the treatment technologies of water reverse osmosis concentrates. Water Research, 46, 267-283.

Petrovic, M., Barceló, D., 2007. LC-MS for identifying photodegradation products of pharmaceuticals in the environment. Trends in Analytical Chemistry, 26, 6, 486-493.

Peuravuori, J., Pihlaja, K., 1997. Molecular size distribution and spectroscopic properties of aquatic humic substances. Analytica Chimica Acta, 337, 133-149.

Phong, D.D., Hur, J., 2015. Insight into photocatalytic degradation of dissolved organic matter in UVA/TiO_2 systems revealed by fluorescence EEM-PARAFAC. Water Research, 87, 119-126.

Phong, D.D., Hur, J., 2018. Using two-dimensional correlation size exclusion chromatography (2D-CoSEC) and EEM-PARAFAC to explore the heterogeneous adsorption behavior of humic substances on nanoparticles with respect to molecular sizes. Environmental Science and Technology, 52, 2, 427-435.

Pichat, P., 2013. Photocatalysis and Water Purification: From Fundamentals to Recent Applications, Wiley-VCH Verlag GmbH & Co. KGaA.

Pifer, A.D., Fairey, J.L., 2014. Suitability of organic matter surrogates to predict trihalomethane formation in drinking water sources. Environmental Engineering Science, 31, 117-126.

Pignatello, J.J., 1992. Dark and photoassisted Fe^{3+}-catalyzed degradation of chlorophenoxy herbicides by hydrogen peroxide. Environmental Science and Technology, 26, 5, 944-951.

Pignatello, J.J., Oliveros, E., MacKay, A., 2006. Advanced oxidation processes for organic contaminant destruction based on the Fenton reaction and related chemistry. Critical Reviews in Environmental Science and Technology, 36, 1-84.

Porcal, P., Dillon, P.J., Molot, L.A., 2014. Interaction of extrinsic chemical factors affecting photodegradation of dissolved organic matter in aquatic ecosystems. Photochemical and Photobiological Sciences, 13, 799-812.

Pradhan, S., Fan, L., Roddick, F.A., Shahsavari, E., Ball, A.S., Zhang, X., 2020. A comparative study of biological activated carbon based treatments on two different types of municipal reverse osmosis concentrates. Chemosphere, 240, 124925.

Qiao, S., Sun, D.D., Tay, J.H., Easton, C., 2002. Photocatalytic oxidation technology for humic acid removal using a nano-structured TiO_2/Fe_2O_3 catalyst. Water Science and Technology, 47, 1, 211-217.

Radjenovic, J., Petrovic, M., Ventura, F., Barceló, D., 2008. Rejection of pharmaceuticals in nanofiltration and reverse osmosis membrane drinking water treatment. Water Research, 42, 3601-3610.

Radjenovic, J., Bagastyo, A., Rozendal, R.A., Mu, Y., Keller, J., Rabaey, K., 2011. Electrochemical oxidation of trace organic contaminants in reverse osmosis concentrate using RuO_2/IrO_2-coated titanium anodes. Water Research, 45, 1579-1586.

Rajeshwar, K., 1995. Photoelectrochemistry and environment. Journal of Applied Electrochemistry, 25, 1067-1082.

Ren, Y., Yuan, Y., Lai, B., Zhou, Y., Wang, J., 2016. Treatment of reverse osmosis (RO) concentrate by the combined Fe/Cu/air and Fenton process (1stFe/Cu/air-Fenton-2ndFe/Cu/air). Journal of Hazardous Materials, 302, 36-44.

Rittmann, B.E., Bae, W., Namkung, E., Lu, C.J., 1987. A critical evaluation of microbial product formation in biological processes. Water Science and Technology, 19, 517-28.

Rittman, B., McCarty, P. (Eds.), 2001. Environmental Biotechnology: Principles and Applications, London, McGraw-Hill.

Rizzo, L., Meric, S., Guida, M., Kassinos, D., Belgiorno, V., 2009 Heterogenous photocatalytic degradation kinetics and detoxification of an urban wastewater treatment plant effluent contaminated with pharmaceuticals. Water Research, 43, 4070-4078.

Roberts, D.A., Johnston, E.L., Knott, N.A., 2010. Impacts of desalination plant discharges on the marine environment: A critical review of published studies. Water Research, 44, 5117-5128.

Rodríguez, F.J., Schlenger, P., García-Valverde, M., 2016. Monitoring changes in the structure and properties of humic substances following ozonation using UV-Vis, FTIR and 1H NMR techniques. Science of the Total Environment, 541, 623-637.

Romera-Castillo, C., Chen, M., Yamashita, Y., Jaffé, R., 2014. Fluorescence characteristics of size-fractionated dissolved organic matter: Implications for a molecular assembly based structure? Water Research, 55, 40-51.

Rosario-Ortiz, F.L., Wert, E.C., Snyder, S.A., 2010. Evaluation of UV/H_2O_2 treatment for the oxidation of pharmaceuticals in wastewater. Water Research, 44, 1440-1448.

Rueda-Marquez, J.J., Levchuk, I., Fernández Ibañez, P., Sillanpää, M., 2020. A critical review on application of photocatalysis for toxicity reduction of real wastewaters. Journal of Cleaner Production, 258, 120694.

Sanchez, N.P., Skeriotis, A.T., Miller, C.M., 2014. A PARAFAC-based long-term assessment of DOM in a multi-coagulant drinking water treatment scheme. Environmental Science and Technology, 48, 1582-1591.

Sánchez, E., Kowalski, B.R., 1986. Generalized rank annihilation factor analysis. Analytical Chemistry, 58, 496-499.

Saran, M., Beck-Speier, I., Fellerhoff, B., Bauer, G., 1999. Phagocytic killing of microorganisms by radical processes: Consequences of the reaction of hydroxyl radicals with chloride yielding chlorine atoms. Free Radical Biology and Medicine, 26, 482-490.

Scherrer, P., 1918. Estimation of the size and internal structure of colloidal particles by means of röntgen. Nachrichten von der Gesellschaft der Wissenschafen zu Göttingen, 2, 96-100.

Sen-Kavurmaci, S., Bekbolet, M., 2014. Tracing TiO_2 photocatalytic degradation of humic acid in the presence of clay particles by excitation-emission matrix (EEM) fluorescence spectra. Journal of Photochemistry and Photobiology A: Chemistry, 82, 53-61.

Senesi, N., 1990. Molecular and quantitative aspects of the chemistry of fulvic acid and its interactions with metal ions Part II. The fluorescence spectroscopy approach. Analaytica Chimica Acta, 232, 77-106.

Senga, Y., Naruoka, C., Moriai, S., Nohara, S., 2018. Characterizing the transformation of aquatic humic substances exposed to ultraviolet radiation using excitation-emission matrix fluorescence spectroscopy and PARAFAC. Inland Waters, 8, 4, 505-511.

Sgroi, M., Roccaro, P., Korshin, G.V., Greco, V., Sciuto, S., Anumol, T., Synder, S.A., Vagliasindi, F.G.A., 2017. Use of fluorescence EEM to monitor the removal of emerging contaminants in full scale wastewater treatment plants. Journal of Hazardous Materials, 323A, 367-376.

Sharpless, C.M., Aeschbacher, M., Page, S.E., Wenk, J., Sander, M., McNeill, K., 2014. Photooxidation-induced changes in optical, electrochemical, and photochemical properties of humic substances. Environmental Science and Technology, 48, 2688-2696.

Shon, H.-K., Kim, S.-H., Erdei, L., Vigneswaran, S., Analytical methods of size distribution for organic matter in water and wastewater. Korean Journal of Chemical Engineering, 23, 4, 581-591.

Shon, H., Vigneswaran, S., Snyder, S., 2006. Effluent organic matter (EfOM) in wastewater: constituents, effects, and treatment. Critical Reviews in Environmental Science and Technology, 36, 4, 327-374.

Sioutopoulos, D.C., Karabelas, A.J., Yiantsios, S.G., 2010a. Organic fouling of RO membranes: Investigating the correlation of RO and UF fouling resistances for predictive purposes. Desalination, 261, 272-283.

Sioutopoulos, D.C., Yiantsios, S.G., Karabelas, A.J., 2010b. Relation between fouling characteristics of RO and UF membranes in experiments with colloidal organic and inorganic species. Journal of Membrane Science, 350, 62-82.

Smith, E.J., Davison, W., Hamilton-Taylor, J., 2002. Methods for preparing synthetic freshwaters. Water Research, 36, 1286-1296.

Solley, D., Gronow, C., Tait, S., Bates, J., Buchanan, A., 2010. Managing the reverse osmosis concentrate from the Western Corridor recycled water scheme. Water Practice and Technology, 5, 1-8.

Standard Methods for the Examination of Water and Wastewater, 2012. APHA, AWWA, WPCF, 22nd Edition, American Water Works Association, Washington D.C., USA.

Stedmon, C.A., Markager, S., Bro, R., 2003. Tracing dissolved organic matter in aquatic environments using a new approach to fluorescence spectroscopy. Marine Chemistry, 82, 239-254.

Stedmon, C.A., Bro, R., 2008. Characterizing dissolved organic matter fluorescence with parallel factor analysis: a tutorial. Limnology and Oceanography Methods, 6, 572-579.

Sun, Y.-X., Gao, Y., Hu, H.-Y., Tang, F., Yang, Z., 2014. Characterization and biotoxicity assessment of dissolved organic matter in RO concentrate from a municipal wastewater reclamation reverse osmosis system. Chemosphere, 117, 545-551.

Sun, X.-Y., Hu, H.-Y., Shi, C.-Z., Yang, Z., Tang, F., 2016a. Changes in the components and biotoxicity of dissolved organic matter in a municipal wastewater reclamation reverse osmosis system. Environmental Technology, 37, 17, 2149-2156.

Sun, Y.-X., Yang, Z., Ye, T., Shi, N., Tian, Y., 2016b. Evaluation of the treatment of reverse osmosis concentrates from municipal wastewater reclamation by coagulation and granular activated carbon adsorption. Environmental Science and Pollution Research, 23, 13543-13553.

Świetlik, J., Sikorska, E., 2004. Application of fluorescence spectroscopy in the studies of natural organic matter fractions reactivity with chlorine dioxide and ozone. Water Research, 38, 3791-3799.

Tang, J., Li, X., Cao, C., Lin, M., Qiu, Q., Xu, Y., Ren, Y., 2019. Compositional variety of dissolved organic matter and its correlation with water quality in peri-urban and urban river watersheds. Ecological Indicators, 104, 459-469.

Tang, W., Zhang, Y., Bai, J., Li, J., Wang, J., Li, L., Zhou, T., Chen, S., Rahim, M., Zhou, B., 2020. Efficient denitrification and removal of natural organic matter, emerging pollutants simultaneously for RO concentrate based on photoelectrocatalytic radical reaction. Separation and Purification Technology, 234, 116032.

Tarasova, A.S., Kislan, S.L., Fedorova, E.S., Kuznetsov, A.M., Mogilnaya, O.A., Stom, D.I., Kudryasheva, N.S., 2012. Bioluminescence as a tool for studying detoxification processes in metal salt solutions involving humic substances. Journal of Photochemistry and Photobiology B: Biology, 117, 164-170.

Ternes, T.A., Joss, A., 2007. Human Pharmaceuticals, Hormones and Fragrances: The Challenge of Micropollutants in Urban Water Management, International Water Association, New York.

Trovó, A.G., Nogueira, R.F.P., Agüera, A., Sirtori, C., Fernández-Alba, A.R., 2009. Photodegradation of sulfamethoxazole in various aqueous media: Persistence, toxicity and photoproducts assessment. Chemosphere, 77, 1292-1298.

Truong, H.B., Huy, B.T., Ly, Q.V., Lee, Y.-I., Hur, J., 2019. Visible light-activated degradation of natural organic matter (NOM) using zinc-bismuth oxides-graphitic carbon nitride (ZBO-CN) photocatalyst: Mechanistic insights from EEM-PARAFAC. Chemosphere, 224, 597-606.

Turkten, N., Bekbolet, M., 2020. Photocatalytic performance of titanium dioxide and zinc oxide binary system on degradation of humic matter. Journal of Photochemistry and Photobiology A. Chemistry, 401, 112748.

Umar, M., Roddick, F., Fan, L., 2014. Effect of coagulation on treatment of municipal wastewater reverse osmosis concentrate by UVC/H_2O_2. Journal of Hazardous Materials, 266, 10-18.

Umar, M., Roddick, F.A., Fan, L., Autin, O., Jefferson, B., 2015. Treatment of municipal wastewater reverse osmosis concentrate using UVC-LED/H_2O_2 with and without coagulation pre-treatment. Chemical Engineering Journal, 260, 649-656.

Urtiaga, A.M., Pérez, G., Ibañez, R., Ortiz, I., 2013. Removal of pharmaceuticals from a WWTP secondary effluent by ultrafiltration/reverse osmosis followed by electrochemical oxidation of the RO concentrate. Desalination, 331, 26-34.

Uyguner, C.S., Bekbolet, M., 2005a. Evaluation of humic acid photocatalytic degradation by UV-vis and fluorescence spectroscopy. Catalysis Today, 101, 3-4, 267-274.

Uyguner, C.S., Bekbolet, M., 2005b. Implementation of spectroscopic parameters for practical monitoring of natural organic matter. Desalination, 176, 47-55.

Uyguner-Demirel C.S., Bekbolet M., 2011. Significance of analytical parameters for the understanding of natural organic matter in relation to photocatalytic oxidation. Chemosphere, 84, 1009-1031.

Uyguner-Demirel, C.S., Birben, N.C., Bekbolet, M., 2017. Elucidation of background organic matter matrix effect on photocatalytic treatment of contaminants using TiO_2: A review. Catalysis Today, 284, 202-214.

Van der Bruggen, B., Lejon, L., Vandecasteele, C., 2003. Reuse, treatment, and discharge of the concentrate of pressure-driven membrane processes. Environmental Science and Technology, 37, 3733-3738.

Van Hege, K., Verhaege, M., Vrestraete, W., 2004. Electro-oxidative abatement of low-salinity reverse osmosis membrane concentrates. Water Research, 38, 1550-1558.

Vaughan, P.P., Blough, N.V., 1998. Photochemical formation of hydroxyl radical by constituents of natural waters. Environmental Science and Technology, 32, 2947-2953.

Vela, N., Calín, M., Yáñez-Gascón, M.J., Garrido, I., Pérez-Lucas, G., Fenoll, J., Navarro, S., 2018a. Photocatalytic oxidation of six pesticides listed as endocrine disruptor chemicals from wastewater using two different TiO_2 samples at pilot plant scale under sunlight irradiation. Journal of Photochemistry and Photobiology A: Chemistry, 353, 271-278.

Vela, N., Calín, M., Yáñez-Gascón, M.J., Garrido, I., Pérez-Lucas, G., Fenoll, J., Navarro, S., 2018b. Photocatalytic oxidation of six endocrine disruptor chemicals in wastewater using ZnO at pilot plant scale under natural sunlight. Environmental Science and Pollution Research, 25, 34995-35007.

Vendramel, S.M.R., Justo, A., González, O., Sans, C., Esplugas, S., 2013. Reverse osmosis concentrate treatment by chemical oxidation and moving bed biofilm processes. Water Science and Technology, 68, 11, 2421-2426.

Vera, M., Cruz, S., Boleda, M.R., Mesa, J., Martín-Alonso, J., Casas, S., Gibert, O., Cortina, J.L., 2017. Fluorescence spectroscopy and parallel factor analysis as a dissolved organic monitoring tool to assess treatment performance in drinking water trains. Science of the Total Environment, 584-585, 1212-1220.

Vogna, D., Marotta, R., Andreozzi, R., Napolitano, A., d'Ischia, M., 2004. Kinetic and chemical assessment of the UV/H_2O_2 treatment of antiepileptic drug carbamazepine. Chemosphere, 54, 497-505.

von Wandruszka, R., 2000. Humic acids: Their detergent qualities and potential uses in pollution remediation. Geochemistry Transactions, 1, 10-15.

Wang, G.-S., Hsieh, S.-T., Hong, C.-S., 2000. Destruction of humic acid in water by UV light-catalyzed oxidation with hydrogen peroxide. Water Research, 34, 15, 3882-3887.

Wang, H.B., Zhang, Y.J., Xiao, X., Yu, S.H., Liu, W. Q., 2011. Application of excitation emission matrix fluorescence combined with second-order calibration algorithm for the determination of five polycyclic aromatic hydrocarbons simultaneously in drinking waters. Analytical Methods, 3, 688-695.

Wang, J., Jiang, Z., Zhang, L., Kang, P., Xie, Y., Lv, Y., Xu, R., Zhang, X., 2009. Sonocatalytic degradation of some dyestuffs and comparison of catalytic activities of nano-sized ZnO and TiO_2/ZnO powders under ultrasonic irradiation. Ultrasonics Sonochemistry, 16, 225-231.

Wang, Y.-N., Tang, C. Y., 2011. Protein fouling of nanofiltration, reverse osmosis, and ultrafiltration membranes-The role of hydrodynamic conditions, solution chemistry, and membrane properties. Journal of Membrane Science, 376, 275-281.

Wang, Z., Cao, J., Meng, F., 2015. Interactions between protein-like and humic-like components in dissolved organic matter revealed by fluorescence quenching. Water Research, 68, 404-413.

Wang, L., Liu, A., Zhang, Z., Zhao, B., Xia, Y., Tan, Y., 2017. Catalytic ozonation of thymol in reverse osmosis concentrate with core/shell Fe_3O_4@SiO_2@Yb_2O_3 catalyst: Parameter optimization and degradation pathway. Chinese Journal of Chemical Engineering, 25, 665-670.

Watkinson, A.J., Murby, E.J., Costanzo, S.D., 2007. Removal of antibiotics in conventional and advanced wastewater treatment: Implications for environmental discharge and wastewater recycling. Water Research, 41, 4164-4176.

Wei, X., Gu, P., Zhang, G., Huang, J., 2015. Occurrence of emerging and priority pollutants in municipal reverse osmosis concentrates. Environmental Science Processes and Impacts, 17, 2, 488-494.

Weng, J., Jia, H., Wu, B., Pan, B., 2018. Is ozonation environmentally benign for reverse osmosis concentrate treatment? Four-level analysis on toxicity reduction based on organic matter fractionation. Chemosphere, 191, 971-978.

Wershaw, R.L., Aiken, G.R., 1985. Molecular size and weight measurements of humic substances. In: Aiken G.R., McKnight, D.M., Wershaw, R.L., MacCarthy P. (Eds.), Humic substances in soil sediment and water. New York: Wiley.

Westerhoff, P., Chen, W., Esparza, M., 2001. Organic compounds in the environment. Fluorescence analysis of a standard fulvic acid and tertiary treated wastewater. Journal of Environmental Quality, 30, 2037-2046.

Westerhoff, P., Moon, H., Minakata, D., Crittenden, J., 2009. Oxidation of organics in retentates from reverse osmosis wastewater reuse facilities. Water Research, 43, 3992-3998.

Willach, S., Lutze, H.V., Eckey, K., Löppenberg, K., Lüling, M., Wolbert, J.-B., Kujawinski, D.M., Jochmann, M.A., Karst, U., Schmidt, T.C., 2018. Direct photolysis of sulfamethoxazole using various irradiation sources and wavelength ranges-insights from degradation product analysis and compound-specific stable isotope analysis. Environmental Science and Technology, 52, 1225-1233.

Windig, W., Guilment, J., 1991. Interactive self-modeling mixture analysis. Analytical Chemistry, 63, 1425-1432.

Wiszniowski, J., Robert, D., Surmacz-Gorska, J., Miksch K., Weber, J.V., 2002. Photocatalytic decomposition of humic acids on TiO_2 Part I: Discussion of adsorption and mechanism. Journal of Photochemistry Photobiology A: Chemistry, 152, 267-273.

Wu, H.L., Shibukawa, M., Oguma, K., 1998. An alternating trilinear decomposition algorithm with application to calibration of HPLC-DAD for simultaneous determination of overlapped chlorinated aromatic hydrocarbons. Journal of Chemometrics, 12, 1-26.

Wünsch, U.J., Murphy, K.R., Stedmon, C.A., 2017. The one-sample PARAFAC approach reveals molecular size distributions of fluorescent components in dissolved organic matter. Environmental Science and Technology, 51, 20, 11900-11908.

Xiang, Q., Fukahori, S., Yamashita, N., Tanaka, H., Fujiwara, T., 2017. Removal of crotamiton from reverse osmosis concentrate by a TiO_2/zeolite composite sheet. Applied Sciences, 7, 778-794.

Xiang, Q., Nomura, Y., Fukahori, S., Mizuno, T., Tanaka, H., Fujiwara, T., 2019. Innovative treatment of organic contaminants in reverse osmosis concentrate from water reuse: A mini review. Current Pollution Reports, 5, 294-307.

Xu, L., Wang, G., Ma, F., Zhao, Y., Lu, N., Guo, Y., Yang, X., 2012. Photocatalytic degradation of an aqueous sulfamethoxazole over the metallic silver and Keggin unit codoped titania nanocomposites. Applied Surface Science, 258, 7039-7046.

Xu, X., Xi, Z., Li, L., Huang, Q., He, C., Wang, J., 2020. Catalytic ozonation of organics in reverse osmosis concentrate with catalysts based on activated carbon. Molecules, 24, 4365.

Yang, C., Liu, Y., Cen, Q., Zhu, Y., Zhang, Y., 2018. Insight into the heterogeneous adsorption of humic acid fluorescent components on multi-walled carbon nanotubes by excitation-emission matrix and parallel factor analysis. Ecotoxicology and Environmental Safety, 148, 194-200.

Yang, L., Hur, J., Zhuang, W., 2015a. Occurrence and behaviors of fluorescence EEM-PARAFAC components in drinking water and wastewater treatment systems and their applications: a review. Environmental Science and Pollution Research, 22, 6500-6510.

Yang, L., Kim, D., Uzun, H., Karanfil, T., Hur, J., 2015b. Assessing trihalomethanes (THMs) and N-nitrosodimethylamine (NDMA) formation potentials in drinking water treatment plants using fluorescence spectroscopy and parallel factor analysis. Chemosphere, 121, 84-91.

Yang, Y., Pignatello, J.J., Ma, J., Mitch, W.A., 2016. Effect of matrix components on UV/H_2O_2 and UV/$S_2O_8^{2-}$ advanced oxidation processes for trace organic degradation in reverse osmosis brines from municipal wastewater reuse facilities. Water Research, 89, 192-200.

Yang, Q., Liu, Y., Li, Y., 2010. Control of protein (BSA) fouling in RO system by antiscalants. Journal of Membrane Science, 364, 372-379.

Yang, Y., Lu, X., Jiang, J., Ma, J., Liu, G., Cao, Y., Liu, W., Li, J., Pang, S., Kong, X., Luo, C., 2017. Degradation of sulfamethoxazole by UV, UV/H_2O_2 and UV/persulfate (PDS): Formation of oxidation products and effect of bicarbonate. Water Research, 118, 196-207.

Yang, Y.Z., Peleato, N.M., Legge, R.L., Andrews, R.C., 2019. Towards real-time detection of wastewater in surface waters using fluorescence spectroscopy. Journal of Environmental Sciences, 86, 195-202.

Ye, X., Sun, H., Gao, S., Qiao, L., 2018. Kinetic Model of organics degradation of reverse osmosis concentrate by UV/H_2O_2 processing. IOP Conference Series: Earth and Environmental Science, 170, 052044.

Yigit, Z., Inan, H., 2009. A study of the photocatalytic oxidation of humic acid on anatase and mixed-phase anatase-rutile TiO_2 nanoparticles. Water, Air, Soil Pollution: Focus, 9, 237-243.

Zafiriou, O.C., True, B., 1979. Nitrate photolysis in seawater by sunlight. Marine Chemistry, 8, 9-32.
Zafiriou, O.C., 1983. Chemical Oceanography, Vol. 8, Academic Press, London.

Zafiriou, O.C., Joussot-Dubien, J., Zepp, R.G., Zika, R., 1984. Photochemistry of natural waters. Environmental Science and Technology, 18, 358A-371A.

Zepp, R.G., Hoigné, J., Bader, H., 1987. Nitrate-induced photooxidation of trace organic chemicals in water. Environmental Science and Technology, 21, 443-450.

Zepp, R.G., Schlotzhauer, P.F., 1981. Comparison of photochemical behavior of various humic substances in water: III. Spectroscopic properties of humic substances. Chemosphere 10, 5, 479-486.

Zepp, R.G., Schlotzhauer, P.F., Sink, R.M., 1985. Photosensitized transformations involving electronic energy transfer in natural waters: Role of humic substances. Environmental Science and Technology, 19, 1, 74-81.

Zhang, X., Lin, J., Ye, W., Zhou, W., Jia, X., Zhao, S., Ye, C., 2018. Potential of coagulation/GAC adsorption combined with UV/H_2O_2 and ozonation for removing dissolved organic matter from secondary RO concentrate. Journal of Chemical Technology and Biotechnology, 94, 1091-1099.

Zhang, L., Ran, J., Qiao, S.-Z., Jaroniec, M., 2019. Characterization of semiconductor photocatalysts. Chemical Society Reviews, 48, 5184-5206.

Zhang, X., Yang, C.-W., Li, J., Yuan, L., Sheng, G.-P., 2019. Spectroscopic insights into photochemical transformation of effluent organic matter from biological wastewater treatment plants. Science of the Total Environment, 649, 1260-1268.

Zhao, C., Wang, Z., Wang, C., Li, X., Wang, C.-C., 2018. Photocatalytic degradation of DOM in urban stormwater runoff with TiO_2 nanoparticles under UV light irradiation: EEM-PARAFAC analysis and influence of co-existing inorganic ions. Environmental Pollution, 243, 177-188.

Zhou, T., Lim, T.-T., Chin, S.-S., Fane, A. G., 2011. Treatment of organics in reverse osmosis concentrate from a municipal wastewater reclamation plant: Feasibility test of advanced oxidation processes with/without pretreatment. Chemical Engineering Journal, 166, 932-939.

Zhou, W., Moore, D.E., 1994. Photochemical decomposition of sulfamethoxazole. International Journal of Pharmaceutics, 110, 1, 55-63.

Zhu, S.H., Wu, H.L., Xia, A.L., Nie, J.F., Bian, Y.C., Cai, C.B., Yu, R.Q., 2009. Excitation emission-kinetic fluorescence coupled with third-order calibration for quantifying carbaryl and investigating the hydrolysis in effluent water. Talanta, 77, 1640-1646.

APPENDIX A: ACTINOMETRY MEASUREMENTS

Liquid-phase chemical actinometry

Due to its sensitivity to wide range of wavelengths (from 250 to 577 nm) and simple application, incident photon flux of UVC reactor and solar simulator was determined by means of liquid-phase chemical actinometry developed by Parker and Hatchard (Parker and Hatchard, 1953 and 1956). The method was based on the irradiation of sulfuric acid solutions of potassium ferrioxalate ($K_3Fe(C_2O_4)_3$) in the range of 250 to 577 nm, by which simultaneous reduction of iron to the ferrous state and oxidation of oxalate ion occurred. A standard calibration graph for analysis of Fe^{2+} was prepared. Upon exposure to 1,10 phenanthroline in the presence of buffer solution (NaO_2CCH_3), ferrous ion form red colored 1,10-phenanthroline-Fe^{2+} complex which gives maxima at 510 nm. Concentration dependent UV-vis absorption spectra of 1,10-phenanthroline-Fe^{2+} complex is displayed in Figure A.1.

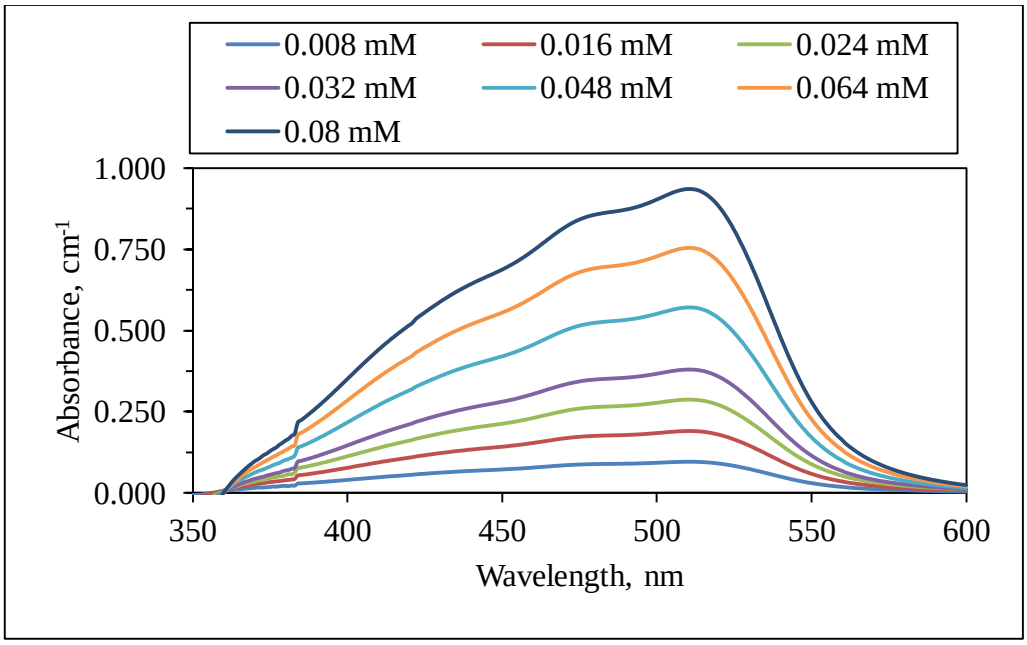

Figure A.1. Concentration dependent UV-vis absorption spectra of 1,10-phenanthroline-Fe^{2+} complex.

A linear plot of $\log I_o/I$ derived from Figure A.1 versus molar concentration of Fe^{2+} (0.008 mM, 0.016 mM, 0.024 mM, 0.032 mM, 0.048 mM, 0.064 mM, 0.08 mM) were plotted to calculate the apparent molar extinction coefficient which is used for the determination of incident photon flux as presented in Figure A.2.

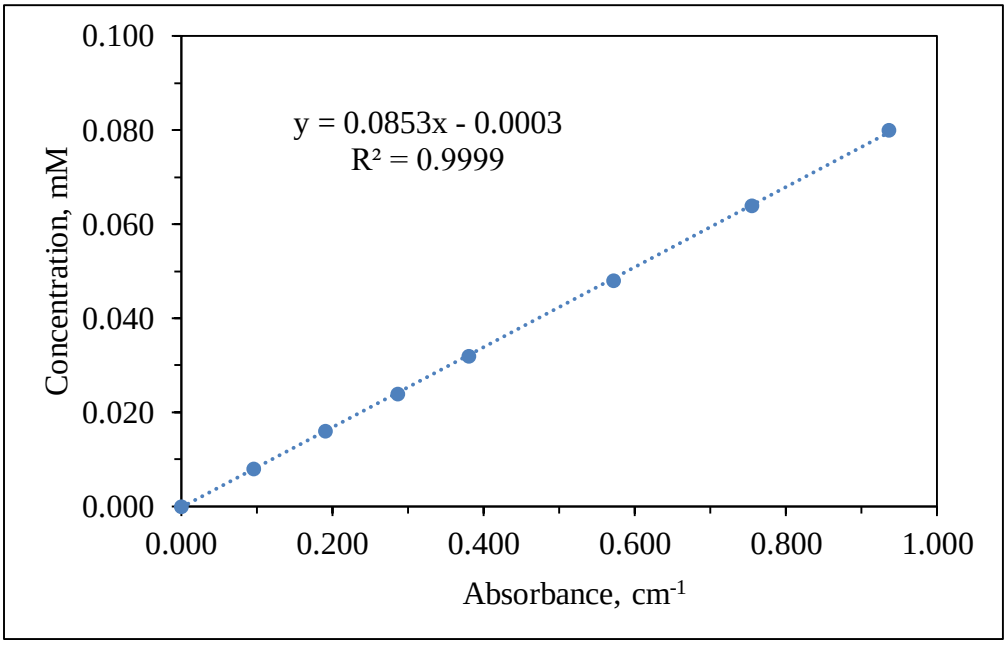

Figure A2. Absorbance vs concentration graph for Fe^{2+}.

Appropriate concentration of ferrioxalate solution (0.006 M for wavelength region of 253.7 nm and 366 nm, and 0.15 M for wavelength region of 366 nm and 577 nm) was added to the photochemical reaction cell and irradiated. Following irradiation period of t, an aliquot of sample (V2) was taken from well mixed solution into a small volumetric flask of volume (V3). After adding 2 ml of phenanthroline solution and buffer solution (equals to one half of the volume of photolyte taken), volume completed to V3 with water and allow to stand for 1 hour. An identical solution without exposure to irradiation was also prepared as the blank solution in the reference beam. Absorbance values of time dependent irradiated and prepared samples was recorded at 510 nm using blank solution in the reference beam using 1 cm standard path length. From these data the number of Fe^{2+} ions formed during photolysis (n_{Fe}^{2+}) is calculated by following equation:

$$n_{Fe}^{2+} = \frac{6.023x10^{20} * V1 * V3 * Log10(\frac{I}{Io})}{V2 * l * \varepsilon} \quad (1.1)$$

where V1: the volume of actinometer solution irradiated, mL

V2: the volume of aliquot taken for analysis, mL

V3: the final volume to which aliquot V2 is diluted, mL

$Log_{10}(I_o/I)$: the measured optical density of the solution at 510 nm

l: the path length of the spectrometer cell used, cm

ε: the experimental value of molar extinction coefficient of Fe^{2+} complex as determined from the slope of calibration plot (Figure A.2).

By using n_{Fe}^{2+} calculated from this equation and the value of Φ_{Fe}^{2+} selected from reference table with respect to appropriate wavelength (Calvert and Pitts, 1966), the time of exposure and the fraction of the light absorbed by the length of actinometer solution used, the incident photon flux of photoreactor can be calculated by following equation:

$$Io^{i} = \frac{n_{Fe^{2+}}}{\Phi_{Fe^{2+}} * t * (1 - 10^{-\varepsilon[A]l})} \; quanta/sec \qquad (1.2)$$

From Eq 1.2, time dependent incident photon flux of UVC photoreactor and solar photoreactor was calculated for t_{irr}: 0-30 min and results were presented in Table A1. Since solar simulator comprises both UVA and visible light regions due to its polychromatic light source, two different incident photon flux values of solar simulator was determined for UVA and visible light regions.

Table A.1. Time dependent incident fluxes calculated for UVC and solar photoreactors.

I_o, quanta/sec	UV reactor 254 nm	Solar reactor	
		302-313 nm	509 nm
5 min	2.47E+17	2.25E+16	2.77E+16
10 min	7.74E+16	1.13E+16	1.68E+16
15 min	5.72E+16	-	-
30 min	3.71E+16	3.74E+15	6.28E+15
Average	1.08E+17	1.51E+16	1.94E+16

APPENDIX B: UV-VIS ABSORPTION SPECTRA OF ROC SAMPLES UPON SOLAR PHOTOCATALYTIC DEGRADATION

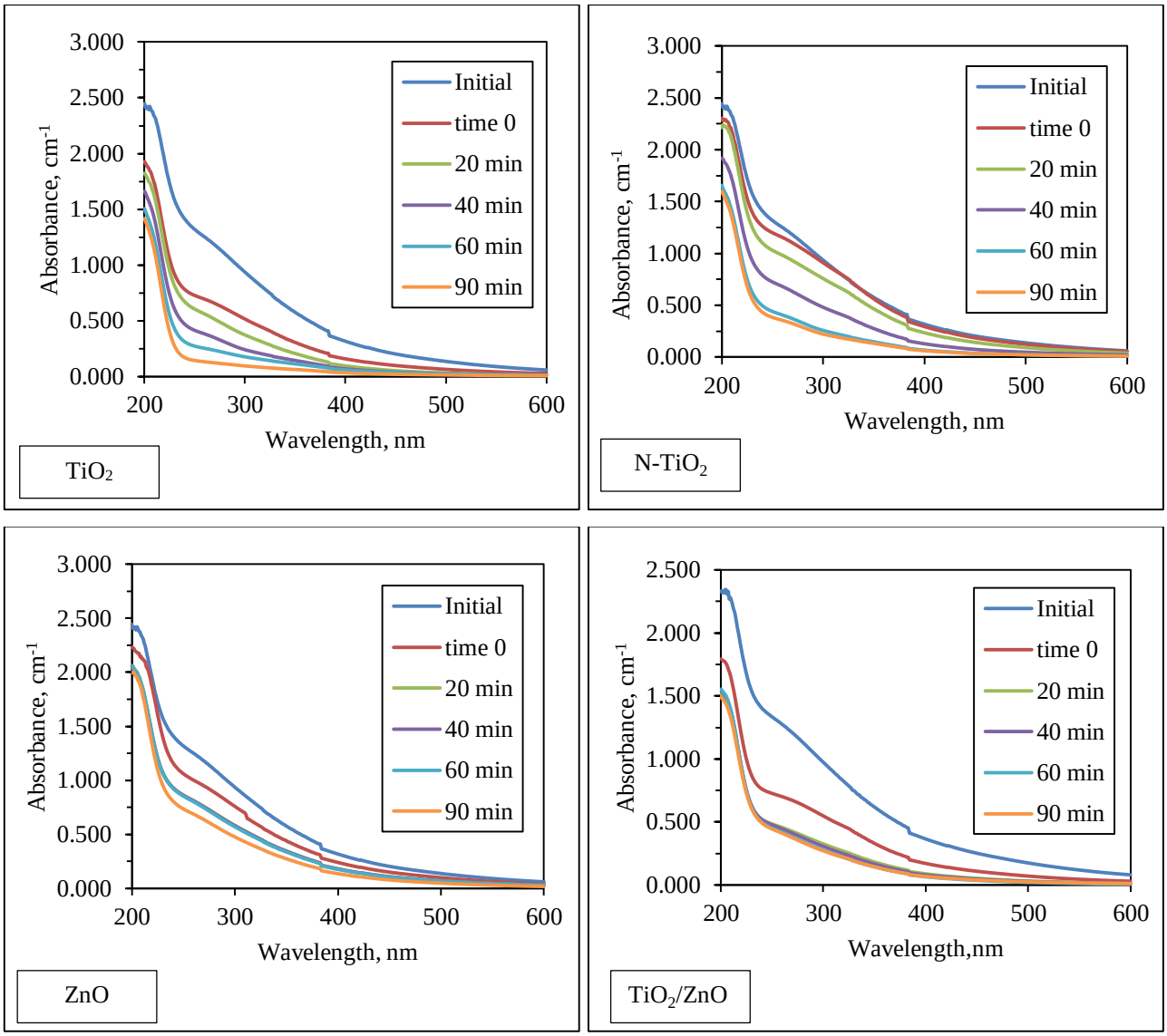

Figure B.1. UV-vis absorption spectra of ROC_{m1} upon solar photocatalytic degradation using TiO_2, N-TiO_2, ZnO, and TiO_2/ZnO nanocomposite.

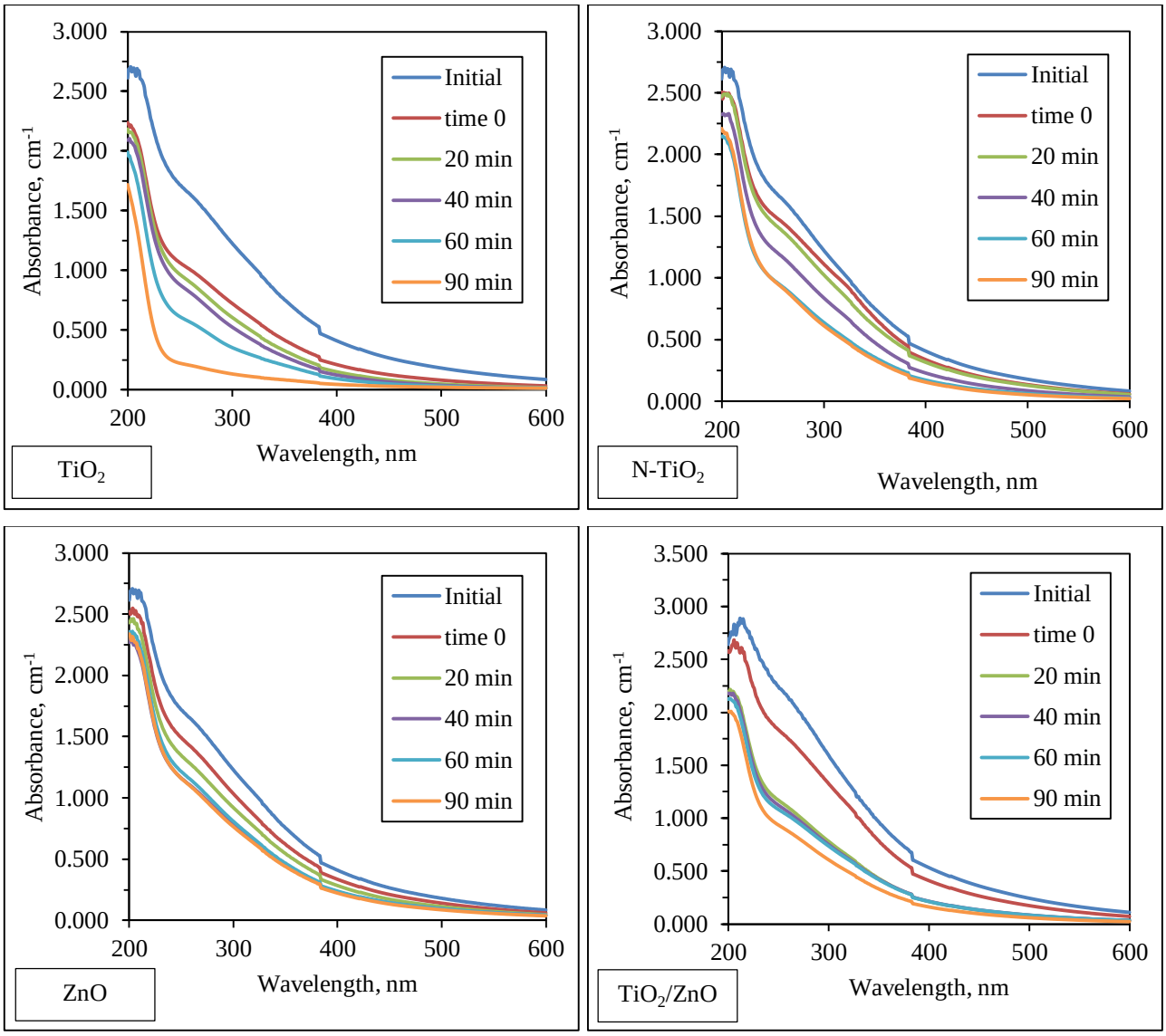

Figure B.2. UV-vis absorption spectra of ROC_{m2} upon solar photocatalytic degradation using TiO_2, N-TiO_2, ZnO, and TiO_2/ZnO nanocomposite.

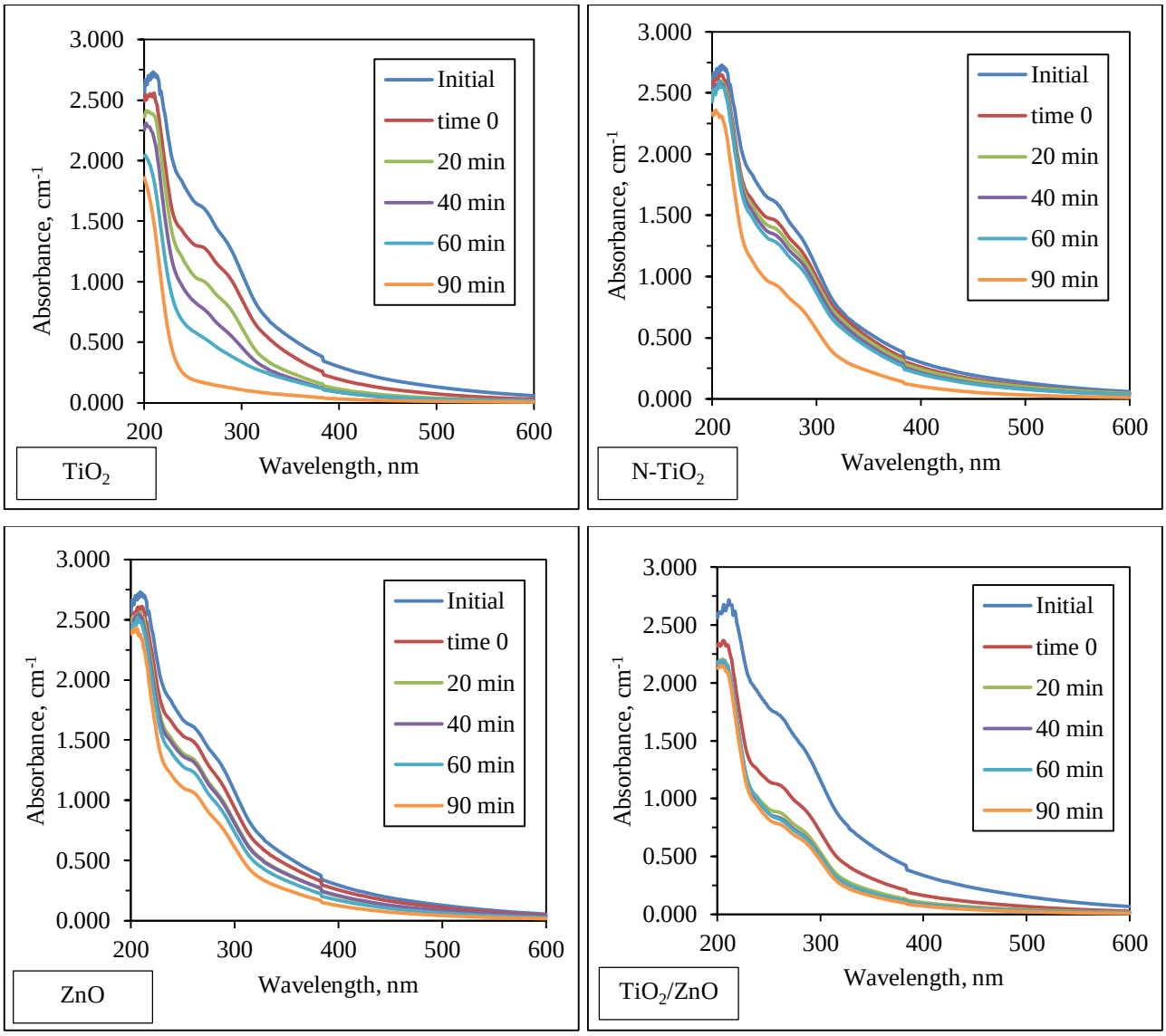

Figure B.3. UV-vis absorption spectra of ROC_{ECm1} upon solar photocatalytic degradation using TiO_2, N-TiO_2, ZnO, and TiO_2/ZnO nanocomposite.

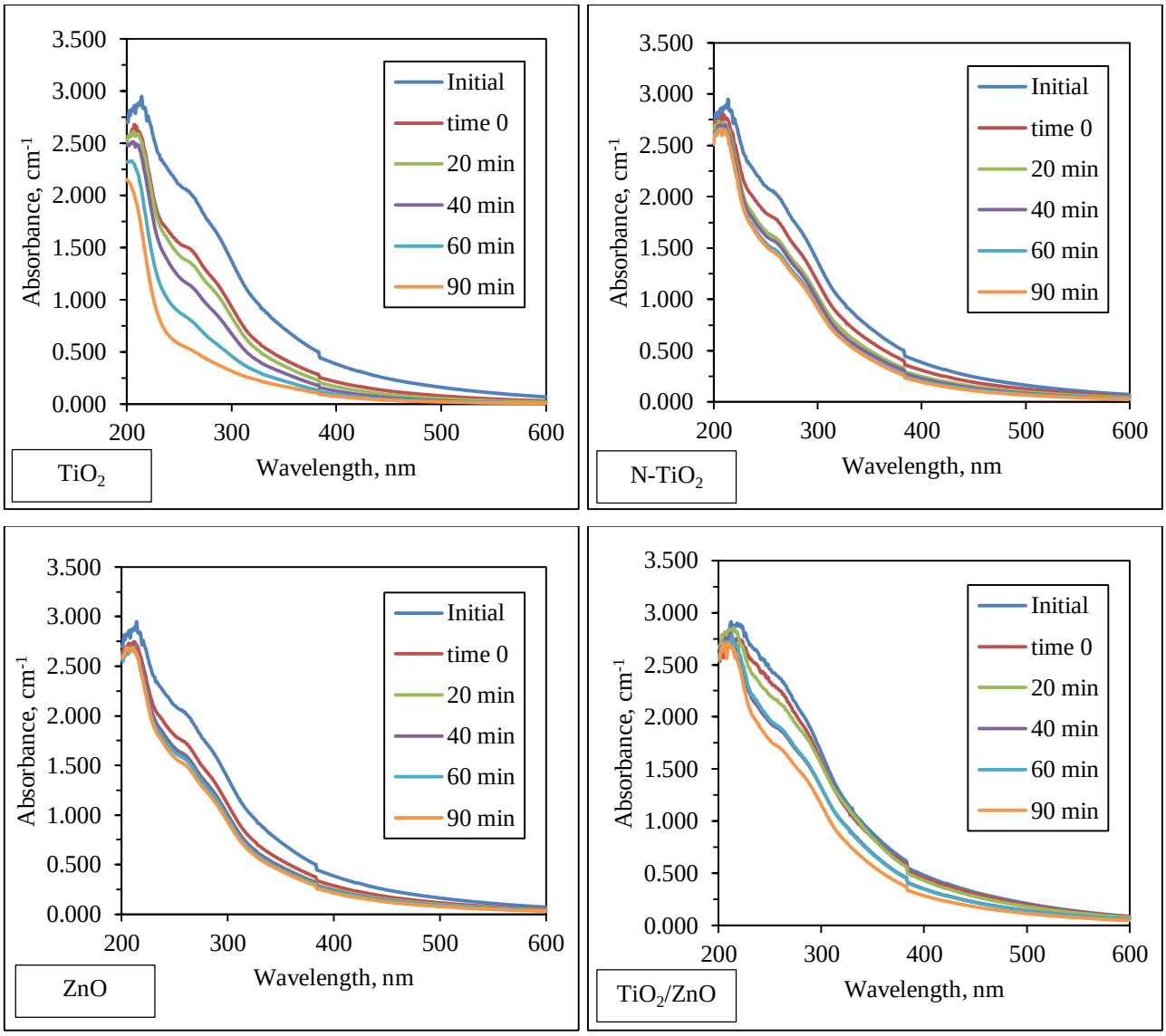

Figure B.4. UV-vis absorption spectra of ROC_{ECm2} upon solar photocatalytic degradation using TiO_2, N-TiO_2, ZnO, and TiO_2/ZnO nanocomposite.

APPENDIX C: SYNCHRONOUS SCAN FLUORESCENCE SPECTRA OF ROC SAMPLES UPON SOLAR PHOTOCATALYTIC DEGRADATION

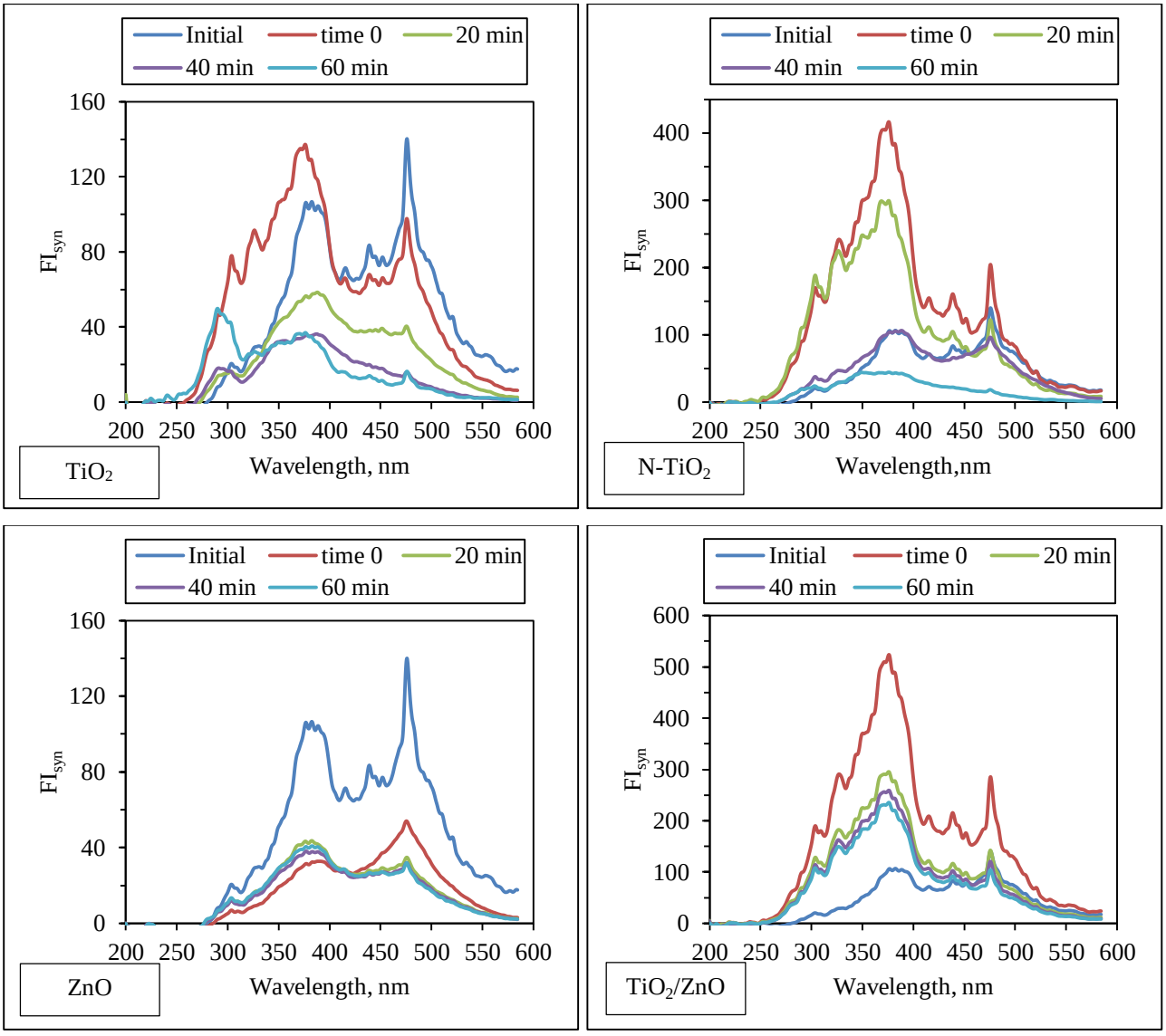

Figure C.1. Synchronous scan fluorescence spectra of ROC_{m1} upon solar photocatalytic degradation using TiO_2, N-TiO_2, ZnO, and TiO_2/ZnO nanocomposite.

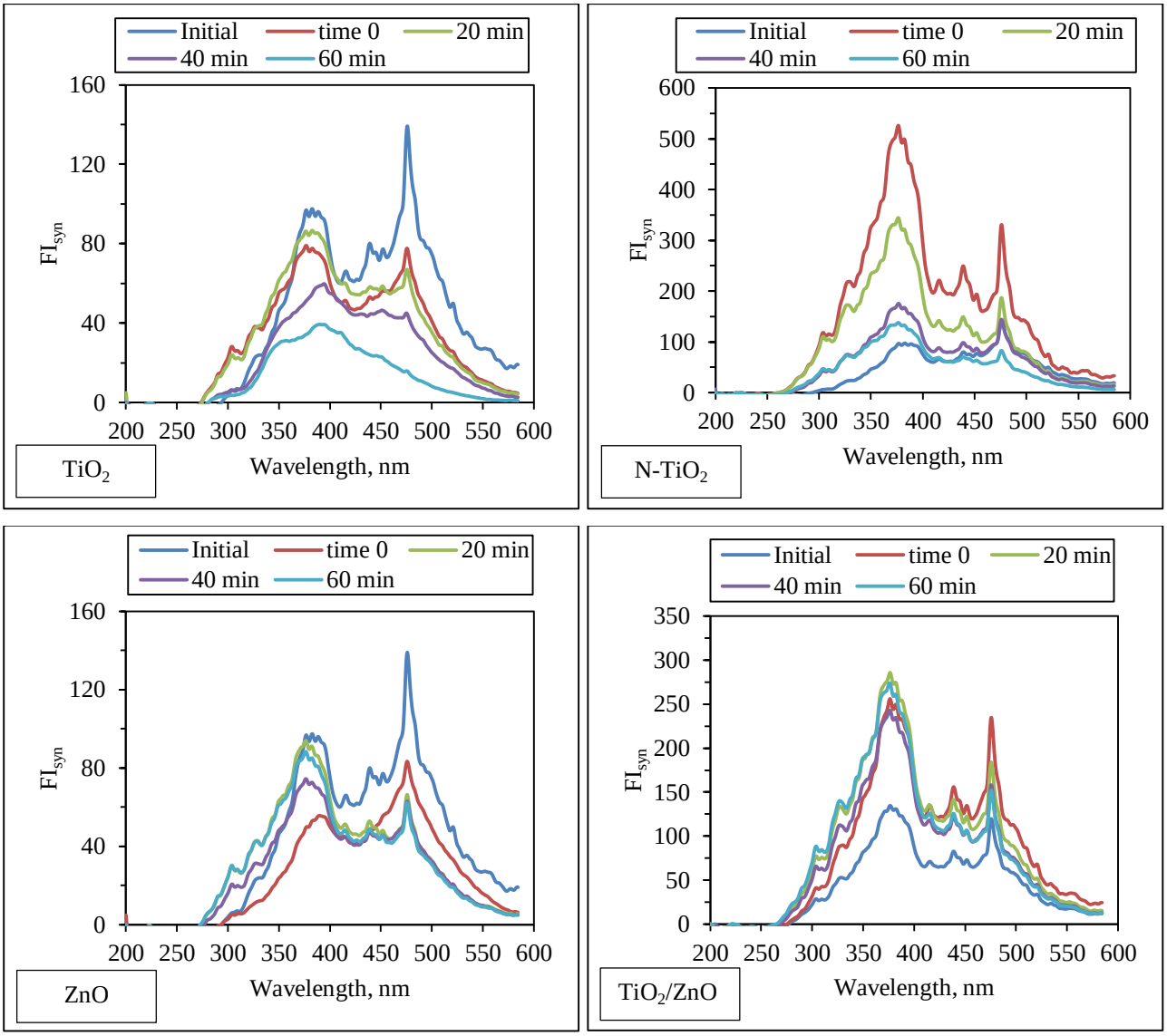

Figure C.2. Synchronous scan fluorescence spectra of ROC_{m2} upon solar photocatalytic degradation using TiO_2, N-TiO_2, ZnO, and TiO_2/ZnO nanocomposite.

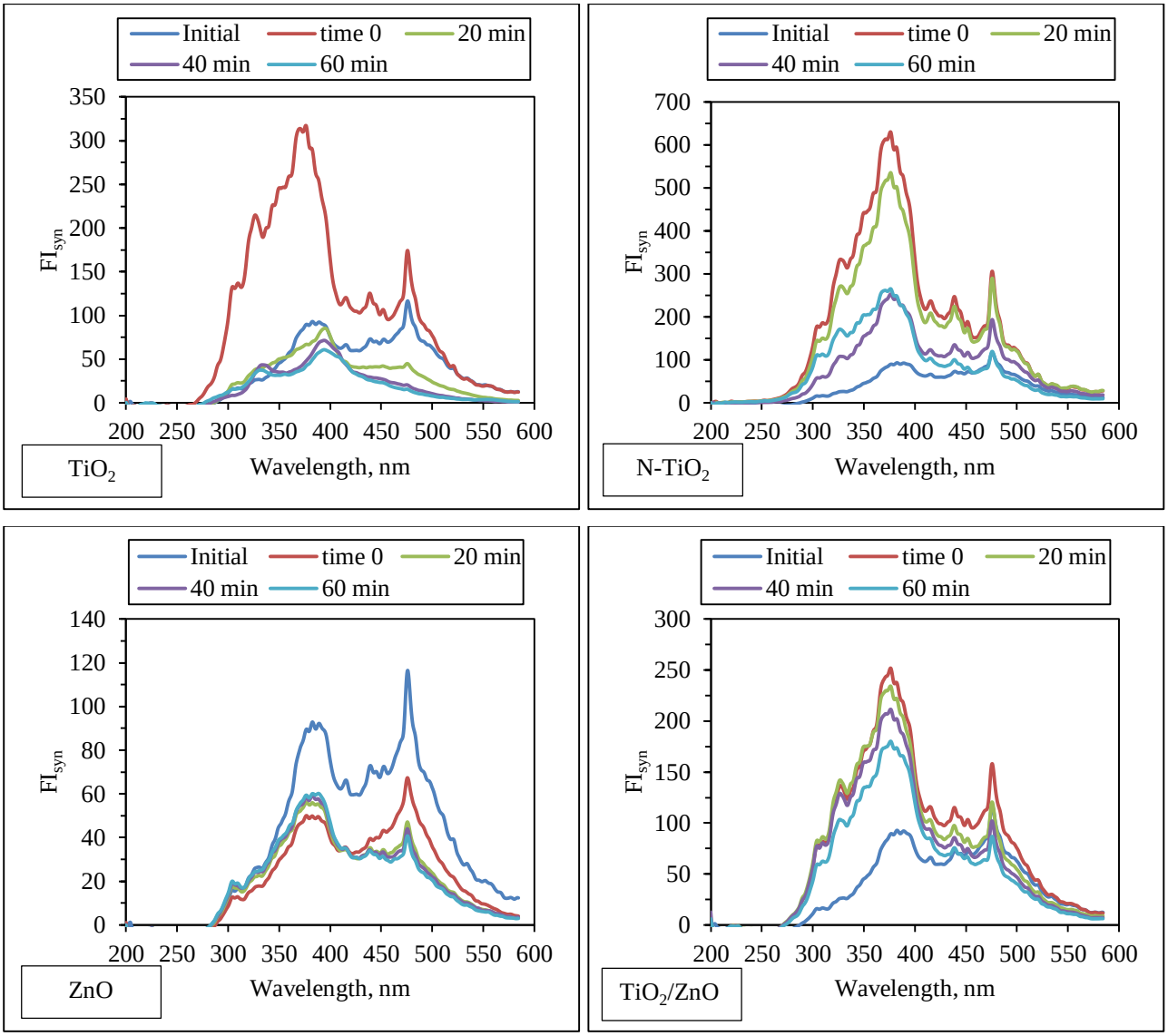

Figure C.3. Synchronous scan fluorescence spectra of ROC_{ECm1} upon solar photocatalytic degradation using TiO_2, N-TiO_2, ZnO, and TiO_2/ZnO nanocomposite.

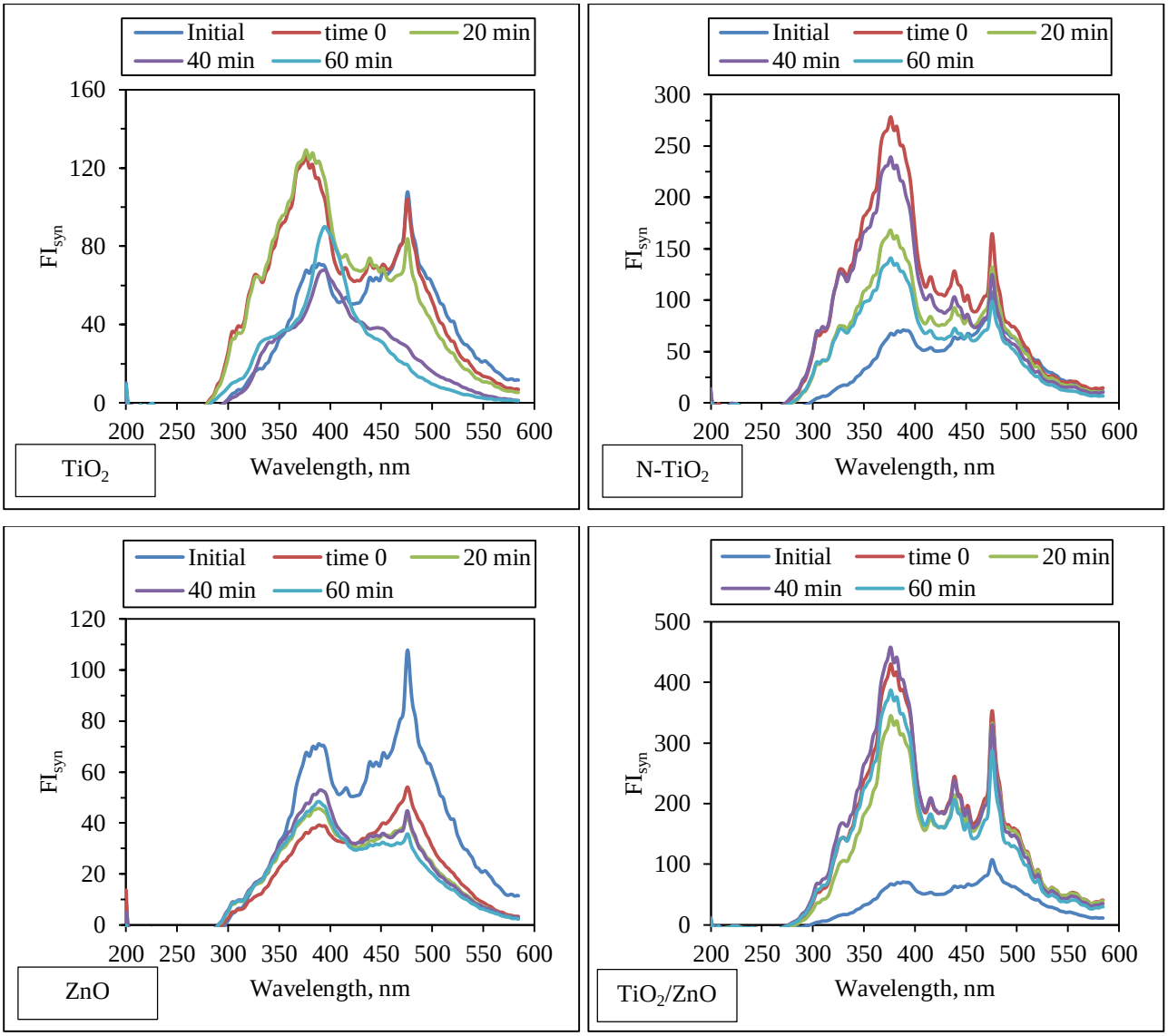

Figure C.4. Synchronous scan fluorescence spectra of ROC_{ECm2} upon solar photocatalytic degradation using TiO_2, N-TiO_2, ZnO, and TiO_2/ZnO nanocomposite.

APPENDIX D: SPECIFIED AND SPECIFIC UV-VIS AND FLUORESCENCE PARAMETERS OF ROC SAMPLES UPON SOLAR PHOTOCATALYTIC DEGRADATION

Table D.1. Specified and specific UV-vis and fluorescence parameters of ROC_{m1} following solar photocatalytic degradation.

	$Color_{436}$	UV_{365}	UV_{280}	UV_{254}	NPOC	$SUVA_{254}$	FI_{syn}	SFI_{syn}
TiO_2								
Initial	0.230	0.494	1.100	1.290	14.3	9.03	94.3	6.60
time 0	0.115	0.257	0.613	0.715	8.14	8.79	76.2	9.37
20 min	0.063	0.169	0.465	0.588	6.62	8.88	36.5	5.52
40 min	0.046	0.120	0.309	0.400	5.29	7.56	13.9	2.64
60 min	0.040	0.096	0.214	0.263	3.50	7.52	10.1	2.90
90 min	0.024	0.055	0.1148	0.139	2.20	6.35	9.35	4.24
N-TiO_2								
Initial	0.230	0.494	1.100	1.290	14.29	9.03	94.3	6.60
time 0	0.210	0.470	1.041	1.181	12.74	9.31	124	9.81
20 min	0.165	0.388	0.874	1.011	8.18	12.4	78.6	9.61
40 min	0.086	0.221	0.578	0.706	6.84	10.3	83.4	12.2
60 min	0.042	0.120	0.328	0.424	5.94	7.14	15.6	2.62
90 min	0.040	0.109	0.287	0.371	5.21	7.12	14.8	2.84
ZnO								
Initial	0.230	0.494	1.100	1.290	14.29	9.03	94.3	6.60
time 0	0.172	0.377	0.891	1.037	10.85	9.55	47.8	4.41
20 min	0.124	0.290	0.697	0.841	8.26	10.2	30.8	3.73
40 min	0.124	0.291	0.695	0.839	7.83	10.7	28.3	3.62
60 min	0.119	0.283	0.683	0.831	6.59	12.6	27.4	4.15
90 min	0.0925	0.2303	0.5824	0.7167	5.76	12.4	25.9	4.51
TiO_2/ZnO nanocomposite								
Initial	0.2794	0.5358	1.1310	1.3106	14.3	9.17	94.3	6.60
time 0	0.1211	0.2694	0.6329	0.7149	6.82	10.5	184	27.0
20 min	0.0611	0.1491	0.3918	0.4730	6.59	7.17	97.5	14.8
40 min	0.0524	0.1328	0.3733	0.4620	6.55	7.05	84.5	12.9
60 min	0.0442	0.1161	0.3455	0.4381	6.38	6.86	72.4	11.3
90 min	0.0454	0.1149	0.3362	0.4294	4.81	8.93	68.1	14.2

Table D.2. Specified and specific UV-vis and fluorescence parameters of ROC_{m2} following solar photocatalytic degradation.

	$Color_{436}$	UV_{365}	UV_{280}	UV_{254}	NPOC	$SUVA_{254}$	FI_{syn}	SFI_{syn}
TiO_2								
Initial	0.298	0.640	1.438	1.685	19.8	8.53	95.7	4.85
time 0	0.144	0.345	0.866	1.040	12.4	8.39	65.6	5.29
20 min	0.097	0.266	0.750	0.940	12.2	7.68	57.9	4.73
40 min	0.078	0.223	0.665	0.854	10.7	7.98	42.6	3.98
60 min	0.058	0.167	0.455	0.592	9.20	6.43	16.3	1.77
90 min	0.031	0.069	0.162	0.212	4.81	4.40	15.1	3.15
N-TiO_2								
Initial	0.298	0.640	1.438	1.685	19.76	8.52	95.7	4.85
time 0	0.239	0.559	1.286	1.487	15.19	9.79	195	12.9
20 min	0.224	0.511	1.206	1.419	14.98	9.47	117	7.79
40 min	0.160	0.390	1.005	1.211	13.23	9.15	96.1	7.26
60 min	0.114	0.290	0.781	0.963	12.46	7.73	61.5	4.94
90 min	0.101	0.271	0.761	0.958	10.89	8.80	56.6	5.20
ZnO								
Initial	0.298	0.640	1.438	1.685	19.8	8.53	95.7	4.85
time 0	0.239	0.526	1.227	1.459	19.2	7.61	70.5	3.68
20 min	0.199	0.460	1.095	1.313	14.4	9.15	49.4	3.44
40 min	0.165	0.386	0.972	1.182	13.5	8.75	49.2	3.64
60 min	0.163	0.376	0.934	1.132	12.9	8.81	46.8	3.64
90 min	0.153	0.367	0.921	1.129	12.7	8.90	43.5	3.43
TiO_2/ZnO nanocomposite								
Initial	0.401	0.820	1.883	2.205	19.76	11.16	78.7	3.98
time 0	0.299	0.652	1.550	1.802	18.85	9.56	151	8.01
20 min	0.149	0.350	0.942	1.142	16.24	7.03	126	7.74
40 min	0.152	0.351	0.907	1.097	13.76	7.98	109	7.89
60 min	0.150	0.346	0.884	1.060	13.63	7.77	106	7.75
90 min	0.113	0.271	0.743	0.913	12.81	7.13	94.1	7.34

Table D.3. Specified and specific UV-vis and fluorescence parameters of ROC_{ECm1} following solar photocatalytic degradation.

	$Color_{436}$	UV_{365}	UV_{280}	UV_{254}	NPOC	$SUVA_{254}$	FI_{syn}	SFI_{syn}
TiO_2								
Initial	0.217	0.457	1.377	1.639	20.7	7.93	84.9	4.11
time 0	0.134	0.325	1.105	1.298	16.6	7.84	118	7.10
20 min	0.074	0.202	0.848	1.028	15.0	6.85	40.7	2.71
40 min	0.056	0.167	0.619	0.817	12.2	6.70	20.9	1.71
60 min	0.056	0.153	0.428	0.571	11.0	5.19	15.7	1.43
90 min	0.022	0.055	0.136	0.182	9.60	1.89	14.8	1.54
N-TiO_2								
Initial	0.217	0.457	1.377	1.639	20.7	7.93	84.9	4.11
time 0	0.187	0.420	1.262	1.480	19.2	7.72	180	9.37
20 min	0.170	0.392	1.206	1.413	17.7	8.00	171	9.69
40 min	0.145	0.360	1.160	1.362	15.7	8.70	127	8.08
60 min	0.141	0.342	1.110	1.309	14.0	9.38	79.6	5.70
90 min	0.067	0.184	0.778	0.959	12.1	7.93	74.1	6.12
ZnO								
Initial	0.217	0.457	1.377	1.639	20.66	7.93	84.9	4.11
time 0	0.185	0.400	1.230	1.517	19.23	7.89	53.9	2.80
20 min	0.141	0.333	1.094	1.370	17.17	7.98	36.9	2.15
40 min	0.147	0.329	1.076	1.348	16.65	8.10	33.9	2.04
60 min	0.118	0.280	0.998	1.260	15.95	7.90	31.6	1.98
90 min	0.085	0.214	0.851	1.088	13.69	7.95	30.1	2.19
TiO_2/ZnO nanocomposite								
Initial	0.252	0.505	1.474	1.752	21.10	8.31	84.9	4.11
time 0	0.116	0.255	0.943	1.131	12.78	8.85	113	8.83
20 min	0.069	0.165	0.741	0.891	12.17	7.32	86.3	7.09
40 min	0.057	0.146	0.701	0.848	10.86	7.81	73.8	6.80
60 min	0.056	0.147	0.692	0.843	10.75	7.84	63.6	5.92
90 min	0.048	0.128	0.657	0.797	10.60	7.52	57.9	5.46

Table D.4. Specified and specific UV-vis and fluorescence parameters of ROC_{ECm2} following solar photocatalytic degradation.

	$Color_{436}$	UV_{365}	UV_{280}	UV_{254}	NPOC	$SUVA_{254}$	FI_{syn}	SFI_{syn}
TiO_2								
Initial	0.278	0.613	1.725	2.071	26.9	7.69	122	4.53
time 0	0.147	0.357	1.228	1.517	23.7	6.40	80.8	3.41
20 min	0.107	0.296	1.118	1.393	20.4	6.83	66.2	3.25
40 min	0.079	0.242	0.920	1.182	19.1	6.20	30.4	1.59
60 min	0.058	0.181	0.622	0.854	17.1	4.98	20.7	1.21
90 min	0.046	0.141	0.413	0.557	13.6	4.10	18.2	1.34
N-TiO_2								
Initial	0.278	0.613	1.725	2.071	26.9	7.69	122	4.53
time 0	0.218	0.497	1.495	1.815	23.7	7.65	104	4.38
20 min	0.173	0.414	1.342	1.635	22.7	7.20	91.1	4.01
40 min	0.158	0.390	1.298	1.590	20.3	7.82	82.9	4.08
60 min	0.139	0.350	1.227	1.514	19.7	7.69	70.9	3.60
90 min	0.129	0.339	1.205	1.486	19.2	7.74	65.2	3.39
ZnO								
Initial	0.278	0.613	1.725	2.071	26.9	7.69	122	4.53
time 0	0.202	0.462	1.437	1.770	24.0	7.38	48.1	2.01
20 min	0.174	0.405	1.324	1.646	21.9	7.52	37.9	1.73
40 min	0.162	0.397	1.315	1.632	21.6	7.56	36.8	1.71
60 min	0.159	0.380	1.281	1.598	20.6	7.76	32.1	1.56
90 min	0.143	0.362	1.234	1.543	19.4	7.94	30.2	1.56
TiO_2/ZnO nanocomposite								
Initial	0.354	0.746	2.044	2.424	29.6	8.18	122	4.53
time 0	0.337	0.709	1.942	2.302	28.5	8.08	210	7.38
20 min	0.314	0.695	1.874	2.175	26.3	8.26	199	7.59
40 min	0.255	0.572	1.634	1.915	25.7	7.46	198	7.72
60 min	0.249	0.561	1.642	1.939	24.5	7.91	174	7.11
90 min	0.201	0.466	1.466	1.738	22.5	7.73	164	7.28

APPENDIX E: PARAFAC COMPONENT TABLE DERIVED FROM LITERATURE REVIEW

System variables	Comp	Ex	Em	Identification of the components	Reference
Six water recycling treatment plants in four Australian states were sampled over a 10-12 week period between March 2008 and June 2009, typically on a weekly schedule	C1	< 250, 370	464	Terrestrial humic-like fluorescence in high nutrient and wastewater impacted environment	Murphy et al., 2011
	C2	< 250, 320	400	Microbial humic-like fluorescence	
	C3	350	428	Wastewater, nutrient enrichment	
	C4	250	304	Tyrosine-like protein fluorescence	
	C5	< 250	348	Tryptophan-like protein fluorescence	
	C6	290	352	Protein, tryptophan-like	
	C7	270	300	Protein, tyrosine-like	
Reoccurring PARAFAC components derived from literature studies between 2000 and 2012	C1	< 230-260	400-500	UVC humic-like, absorbs primarily in UVC region, expected to consist small molecular size components	Ishii and Boyer, 2012
	C2	< 240-275 < 339-420	434-520	UVC humic-like and UVA humic-like, absorbs light in UVC and UVA region, expected to be degraded by UVA, consist of large molecular size components	

	C3	< 240-260	434-450	UVC humic-like and UVA marine humic-like, absorbs light in UVC, UVB, and UVA region, expected to be degraded UVA light but not to a lesser extent than C2, consists of compounds with molecular sizes fall between C1 and C2	
Nineteen water samples were collected from different points along the process trains of five municipal wastewater treatment plants	C1	230	310	Tyrosine-like component	Li et al., 2014
	C2	235/290	340	Tryptophan-like component	
	C3	250/350	440	Humic-like component	
	C4	225/280	300/330	Tryptophan-like component	
settled water from the Orange Water and Sewer Authority drinking water treatment plant (Carrboro, NC, USA) was concentrated by a factor of 15 (by volume) using a custom-built portable RO system UV and subsequent chlorination Concentrated hypochlorite or pre-formed mono-chloramine solution Chlorine dose: 1.0 ± 0.4 mg Cl_2/L after 24 h of contact time	C1	< 250/320	414	Microbial humic-like component	Lyon et al., 2014
	C2	< 250/360	434	Humic-like component	
	C3	< 250/360	489	Terrestrial humic-like component	
	C4	< 250/280	350	Protein, tryptophan-like component	
Two of the surface water samples were collected at peat-based environments, representing a	C1	< 260/345	462	Humic-like component	Romero-Castillo et al., 2014
	C2	< 260	454	Terrestrial humic-like component	
	C3	< 260/305	416	Terrestrial humic-like, fulvic acid type component	

freshwater marsh site at Shark River Slough and an oligohaline mangrove estuarine site. The other two were from two agricultural drainage canals Molecular size fractionation with SEC	C4	< 260/305	376	Microbial humic-like	
	C5	275/405	> 500	Terrestrial humic-like, humic acid type component	
	C6	325	406	Ubiquitous humic-like, product of microbial activity, and agricultural land use derived	
	C7	275	326	Protein-like component	
	C8	300	342	Protein-like component	
Raw and clarified water samples after coagulation treatment (treated-alum and treated-ACH water) were obtained one to three times a week from the Akron DWTP	C1	234/319	400	Humic-like component	Sanchez et al., 2014
	C2	< 224/354	468/470	Humic-like fluorophore with terrestrial/allochthonous origin	
	C3	224/284	342	Protein-like component similar to tryptophan	
Effluent, limnic, and riverine waters were collected three times from a water reclamation center in Seoul, Lake Uiam in Gangwon province, and Han River in Seoul, Korea Resin fractionation by two different methods	C1	250-280 325-360	370-480	UVC humic-like component	He and Hur, 2015
	C2	260-300 350-400	420-520	Humic-like component	
	C3	275-350	350-450	Marine humic-like substance	
	C4	250-300	320-400	Tryptophan-like component	
Elliott soil humic acid (ESHA) and Suwannee River fulvic acid (SRFA) DOC_i: 15 mgC/L Graphene oxide adsorption Adsorbent dose: 300 mg/L and 500 mg/L pH: 4 and 6	C1	270	510	Humic-like component, condensed structure with larger molecular size	Lee et al., 2015
	C2	250 265	440 440	Humic-like component, having lower molecular size than C1, associated with fulvic acids	
	C3	250 290	365 365	Aromatic amino acid component or tryptophan-like component	

PLFA, ESHA Leaf litter-derived organic matter (LLOM) UVA/TiO_2 photocatalysis P-25 TiO_2 UVA lamp, λ: 352 nm, I_o: 6450 mW/cm^2	C1	280	358	Tryptophan-like or protein-like component	Phong and Hur, 2015
	C2	250/335	418	Microbially derived fulvic acid, or humic-like component of DOM released from degradation of phytoplankton	
	C3	310	428	Terrestrially derived organic matter, could also be microbial transformation products of terrestrially derived organic matter	
	C4	265/370	490	Larger molecular size of a terrestrial humic acid	
Drinking water and wastewater treatments	C1	220-230 270-290	340-360 340-360	Tryptophan-like component	Yang et al., 2015
	C2	220-230 270-280	300-320 300-320	Tyrosine-like component	
	C3	n. p.	< 430	Microbial humic-like or fulvic acid like components	
	C4	n.p.	>440	Terrestrial humic-like or humic acid-like components	
Samples from Daliao River and its estuary UVA photodegradation 8W UVA lamp λ: 320-400 nm I_o: 17 W/m^2	C1	279/310	425	Humic-like FDOM	Chen et al., 2016
	C2	303	340	Tryptophan-like FDOM	
	C3	310/380	530	Humic-like FDOM	
	C4	325	424	Humic-like FDOM	
	C5	380	485	Humic-like FDOM	
Commercial HA, Sigma Aldrich alum and $ZrCl_4$ coagulation Coagulant dose: 0.1 -1.5 mg/L for alum and 0.05-0.4 mg/L for $ZrCl_4$	C1	260	455	Humic-like component	Aftab and Hur, 2017
	C2	220/235	435	Humic-like component	
	C3	225/270	390	Humic-like component	
Seventeen chemically well-defined humic substances	C1	275/350	306/460	Amino acids free or bound to proteins UVA humic-like fraction (terrestrial)	Ateia et al., 2017

purchased from the IHSS and JHSS 5 mg/L of each humic substance	C2	240/300	444	UVC humic-like fraction (terrestrial) Marine humic-like	
	C3	270/440	492	UVC humic-like Undefined but found in terrestrial humic acid	
Elliott soil humic acid (ESHA) and Suwannee River humic acid (SRHA) Adsorption with commercially available TiO_2 and ZnO Adsorbent dose: 0-1 g/L pH: 7	C1	270	502	Terrestrial humic-like component derived from soil humic acid	Phong and Hur, 2017
	C2	220	406	Humic-like component derived from aquatic humic acid	
	C3	255	459	Aquatic humic-like component	
Four allochthonous samples (Lake Lillsjon, Sweden; Rio Negro, Brazil; Svartan River, Sweden; Rio 98 Tapajos, Brazil) and two autochthonous samples (Pacific Ocean & Pony Lake) Molecular size fractionation with HPSEC	C1	250	350	Humic-like component	Wünsch et al., 2017
	C2	350	405	Humic-like component	
	C3	300	430	Humic-like component	
	C4	350	450	Humic-like component	
	C5	250	510	Humic-like component	
SRHA and ESHA were purchased from the IHSS. Litter leaf organic matter (LLOM) was prepared according to methodology presented in the paper UVA/TiO_2 photocatalysis	C1	270	500	Terrestrial humic-like component	Ly et al., 2018
	C2	220/320	440	Terrestrial humic-like component	

P-25 TiO_2 Dose: 0.4-0.6 g/L 8W UVA lamp λ: 352 nm, I_o: 6540 mW/cm^2	C3	270	400	Microbial humic-like or algal organic matter or microbial transformation product of terrestrial DOM	
	C4	220/289	330	Protein/polyphenol-like substances such as gallic acid which acts as a crucial constituent of hydrolysable and condensed tannins	
Surface water samples. Photodegradation with a UVA lamp λ_{max}: ~360 nm, I_o: 3.1 W/m^2 or a UV-B lamp λ_{max}: ~310 nm, I_o: 3.5 W/m^2	C1	252/336	446	UVA, major degradation, flocculation UVB, degradation	Senga et al., 2018
	C2	264/372	495	UVA, slight degradation UVA, humification with LMW and degradation with LMW	
	C3	288	413	UVA, slight degradation UVB, major degradation, flocculation	
Commercial HA, Aldrich DOC_i: 20 mg/L Adsorption with multi-walled carbon nanotubes (MWCNT) Adsorbent dose: 100 mg/L	C1	250/310	428	Carboxylic-like chromophores	Yang et al., 2018
	C2	300/460	552	Phenolic-like chromophores	
	C3	270/375	520	Phenolic-like chromophores	
The runoff water samples. 50 mL quartz bottles were placed in the photochemical reaction system equipped with nine identical LED lamps λ: 385 nm, I_o: 300mW/cm^2. P-25 TiO_2 TiO_2 doses:10, 20, 30, 40 mg	C1	250	350	Protein-like or tryptophan-like constituent, terrestrial fluorescent materials	Zhao et al., 2018
	C2	250/300	440	Humic-like fluorescence or fulvic-like constituent with aromatic terrestrial structures and macromolecular weight	
	C3	275	313	Tyrosine-like fluorophore	
Unchlorinated Lake Ontario water was	C1	220	404	Humic-like or terrestrial humic-like	Yang et al., 2019

collected over three weeks from the intakes of two conventional water treatment plants. Chlorinated wastewater final effluent samples were collected during the same period from the outfall of a wastewater treatment plant which discharges into the same lake	C2	345/240	426	Wastewater tracer/ microbial humic-like	
	C3	220/280	324	Protein-like	
	C4	250/360	476	Terrestrial humic-like	
	C5	230/285	354	Protein-like	
Full-scale antibiotic wastewater treatment plant	C1	225/270	300		Tang et al., 2019
	C2	340/245	410	Fulvic acid-like component	
	C3	360	450/460	Humic acid-like component	
		270-275	450	Humic acid-like component	
	C4	345/250	435	Humic-like component	
	C5	230/270/ 320	420	Humic-like component	
Elliott soil humic acid (ESHA), Suwannee River humic acid (SRHA), and Suwannee River natural organic matter (SRNOM) DOC_i: 5±0.3 mgC/L Photocatalytic degradation using zinc-bismuth oxides-graphitic carbon nitride (ZBO-CN)	C1	280/370	500	Terrestrial humic-like component with greater degree of structural condensation and a large molecular size humic-like	Turong et al., 2019
	C2	260/325	445	Typical humic-like component	
	C3	290	410	Microbial degradation product of terrestrial humic-like organic matter	

8W UVA lamps λ: 310-400 nm and 8W-UVC lamps λ: 100-280 nm Catalyst dose: 0.25-1.50 mg/L	C4	270	340	Tryptophan-like fluorescence component	
Soil was taken from the botanical garden located within the campus of Chung-Ang University, Seoul, Republic of Korea TiO_2 nanoparticles were used as amendments	C1	225 (260,360)	435	Microbial humic-like component	Zahra et al., 2019
	C2	315	408	Fulvic-like component	
	C3	275	472	Terrestrial humic-like component	
Two lake samples Photodegradation using mercury lamp with I_o at 4 wavelengths λ: 254 nm, I_o: 361 mW/cm^2 λ: 297 nm, I_o: 354 mW/cm^2 λ: 365 nm, I_o: 7120 mW/cm^2 λ: 420 nm, I_o: 395 mW/cm^2	C1	340/275	478	Humic-like components with carboxylic-like groups	Zhang et al., 2020
	C2	315/245	412	Fulvic-like components with carboxylic-like and phenolic-like groups	
	C3	275	475/340	Protein-like components bound to humic acid	
	C4	< 220	500	Cannot be categorized due to uncertainty of the location of the peak	

APPENDIX F: UV-VIS ABSORPTION SPECTRA OF MOLECULAR SIZE FRACTIONS OF ROC_m and ROC_{ECm} FOLLOWING PHOTODEGRADATION AND PHOTOCATALYTIC DEGRADATION

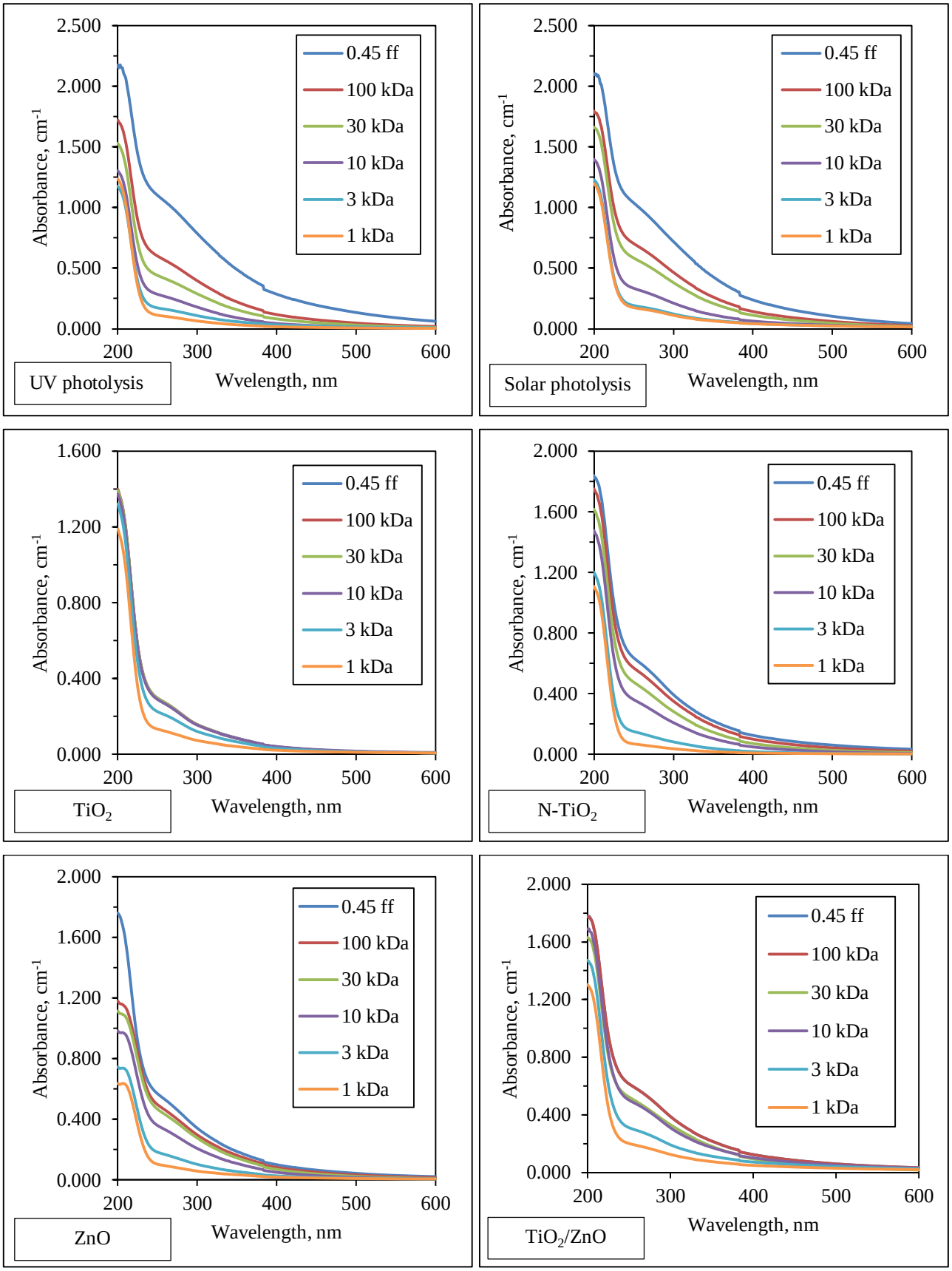

Figure F.1. UV-vis absorption spectra of molecular size fractions of ROC_{m1} following photodegradation and photocatalytic degradation processes.

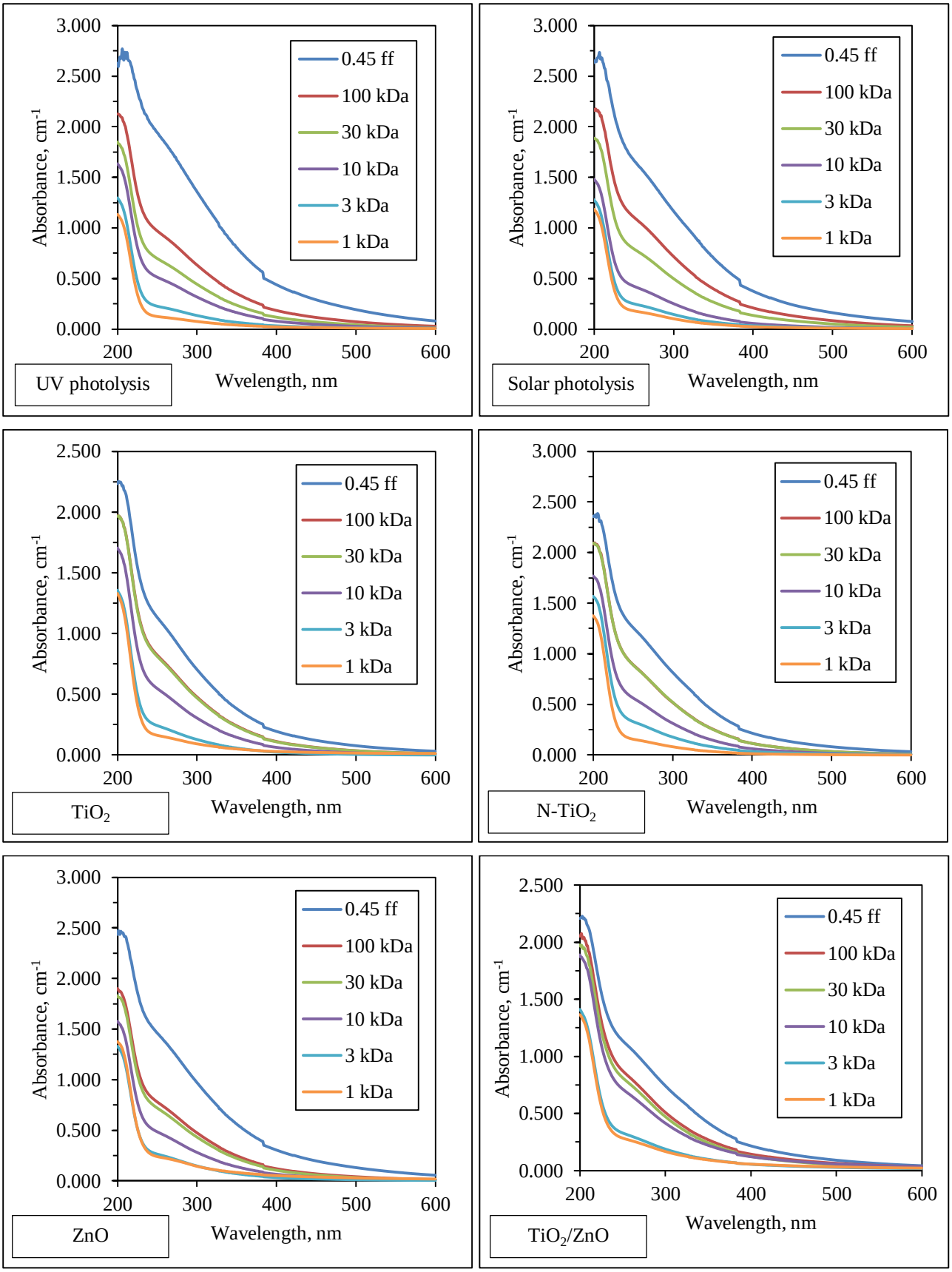

Figure F.2. UV-vis absorption spectra of molecular size fractions of ROC_{m2} following photodegradation and photocatalytic degradation processes.

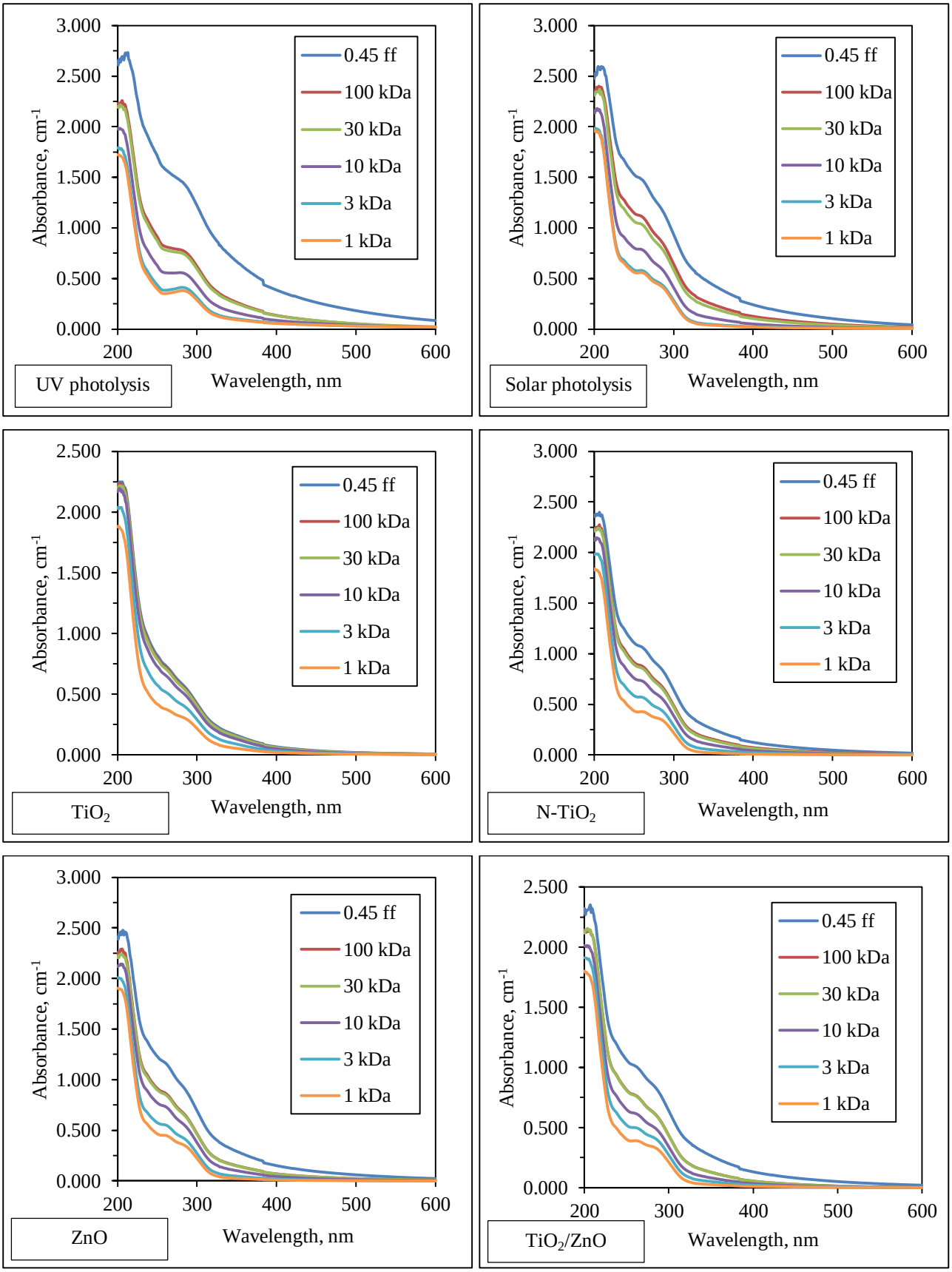

Figure F.3. UV-vis absorption spectra of molecular size fractions of ROC_{ECm1} following photodegradation and photocatalytic degradation processes.

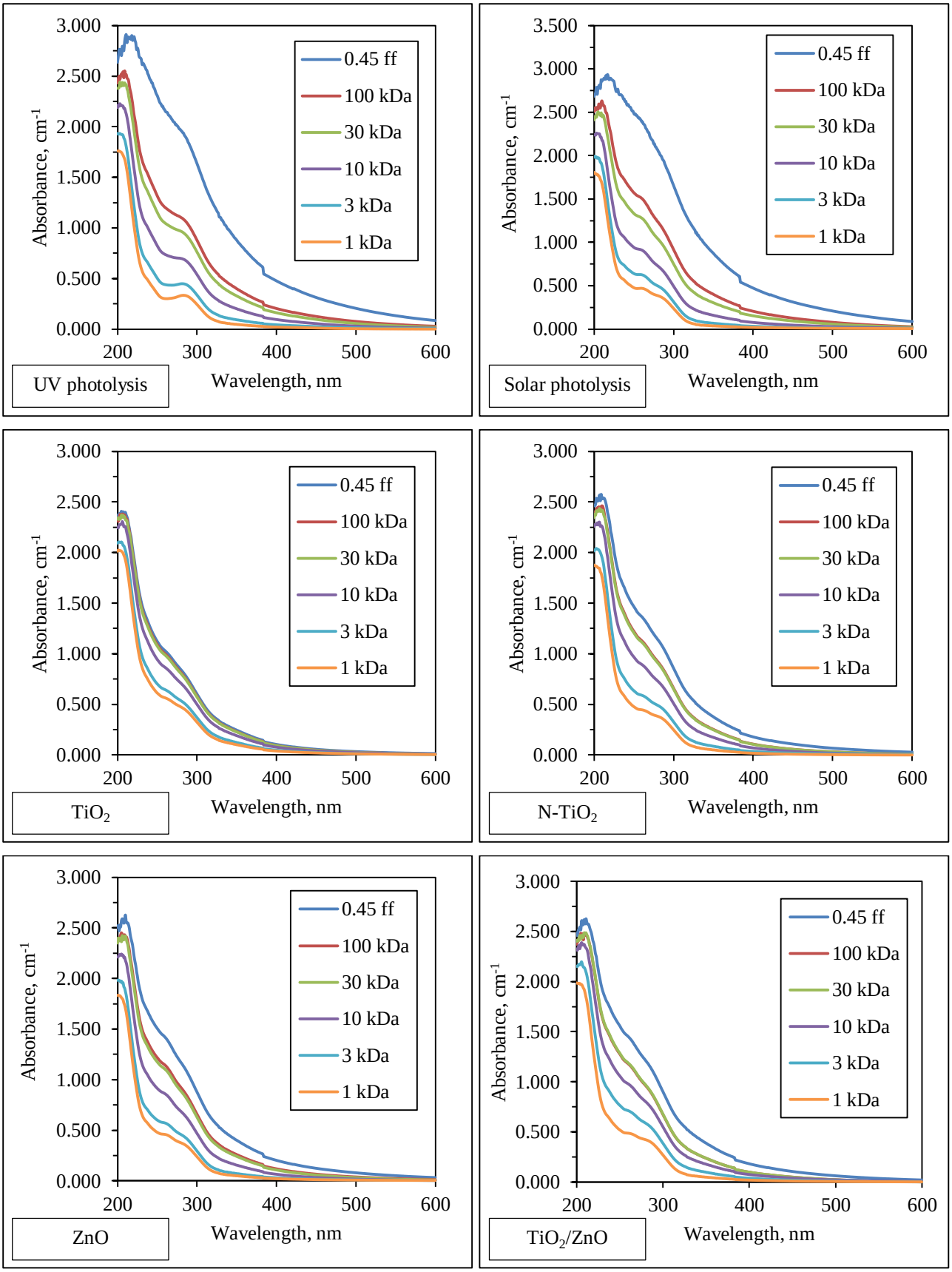

Figure F.4. UV-vis absorption spectra of molecular size fractions of ROC_{ECm2} following photodegradation and photocatalytic degradation processes.

APPENDIX G: SYNCHRONOUS SCAN FLUORESCENCE SPECTRA OF MOLECULAR SIZE FRACTIONS OF ROC_m and ROC_{ECm} FOLLOWING PHOTODEGRADATION AND PHOTOCATALYTIC DEGRADATION PROCESSES

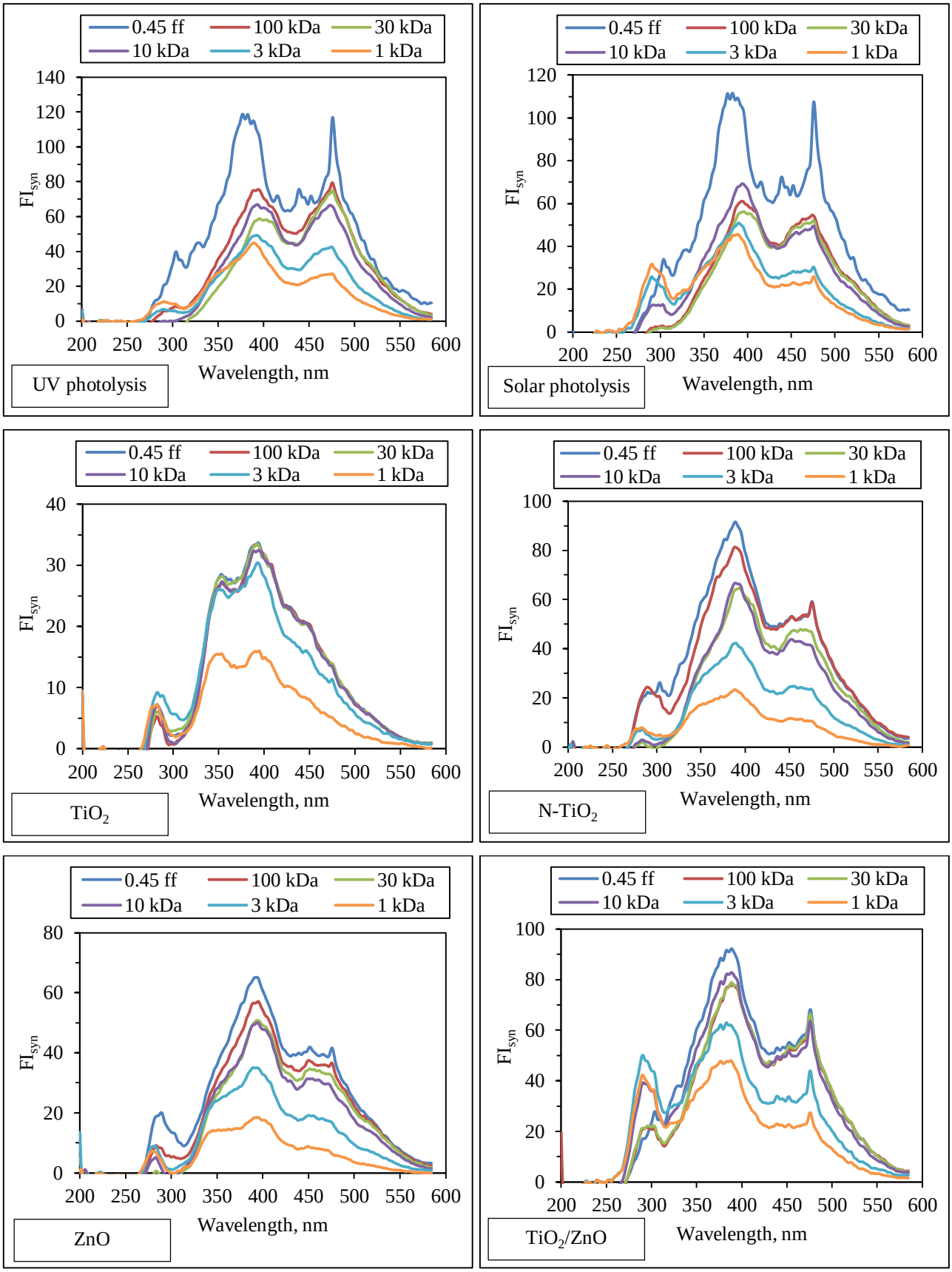

Figure G.1. Synchronous scan fluorescence spectra of molecular size fractions of ROC_{m1} following photodegradation and photocatalytic degradation processes.

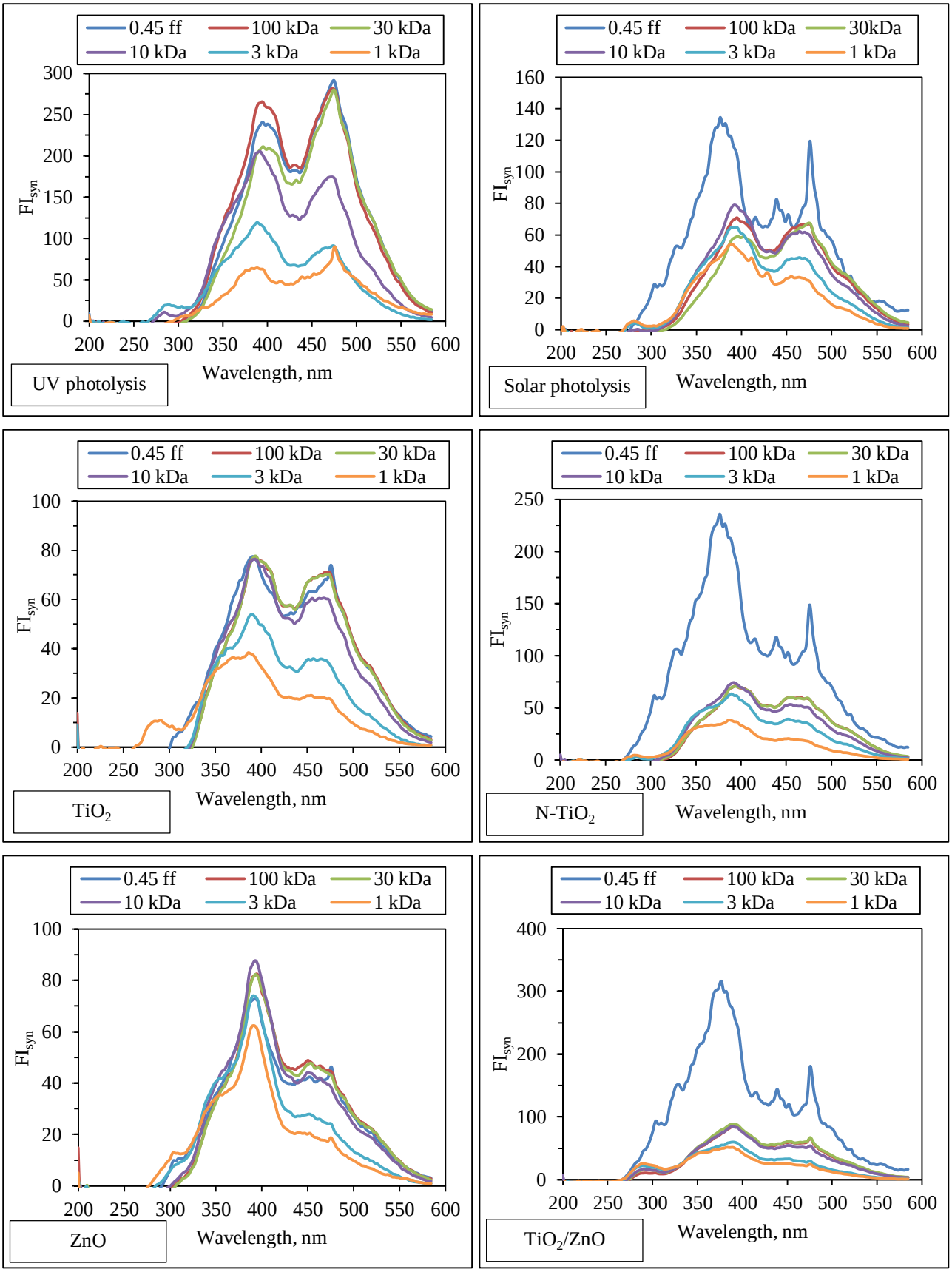

Figure G.2. Synchronous scan fluorescence spectra of molecular size fractions of ROC_{m2} following photodegradation and photocatalytic degradation processes.

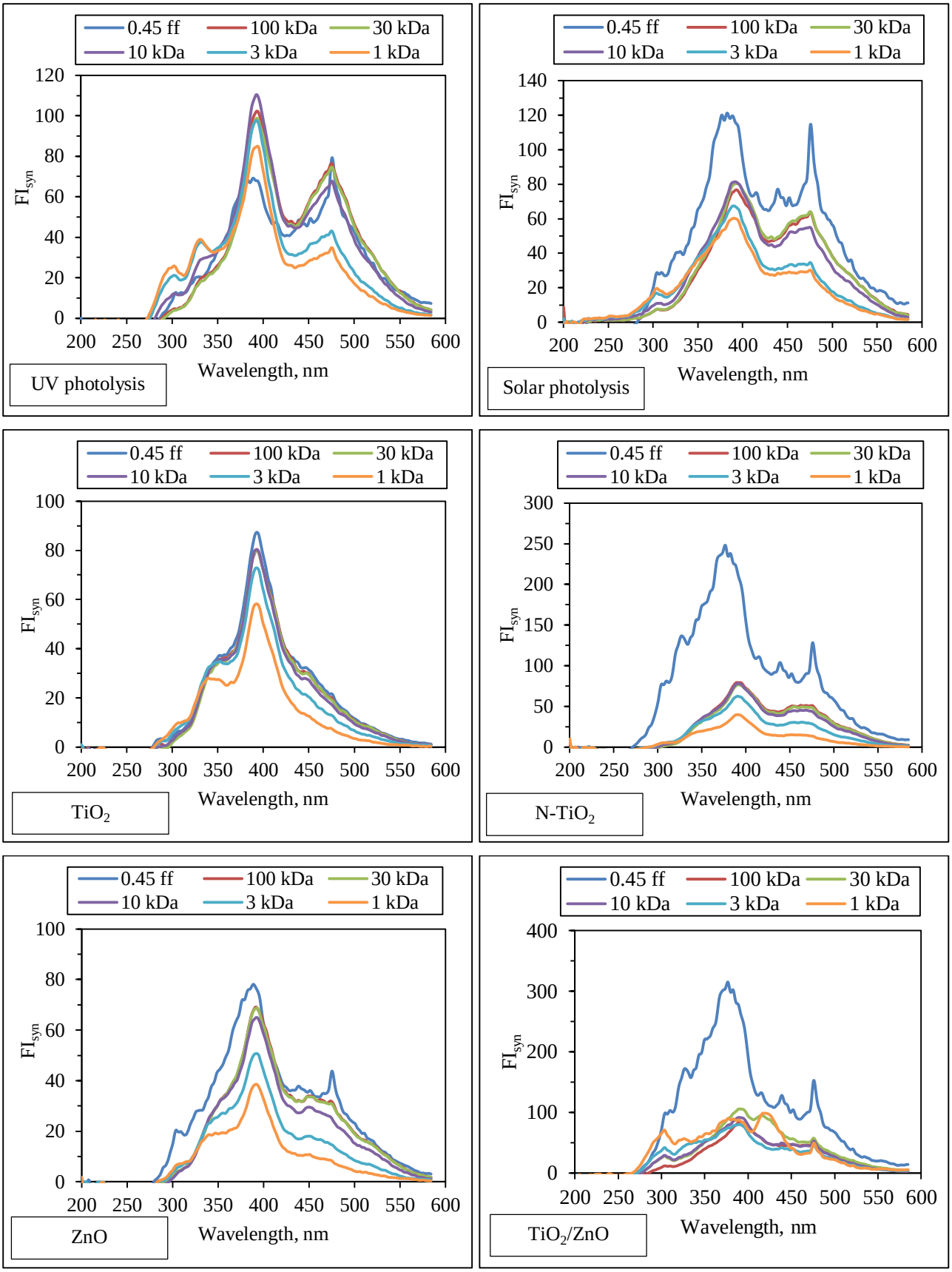

Figure G.3. Synchronous scan fluorescence spectra of molecular size fractions of ROC_{ECm1} following photodegradation and photocatalytic degradation processes.

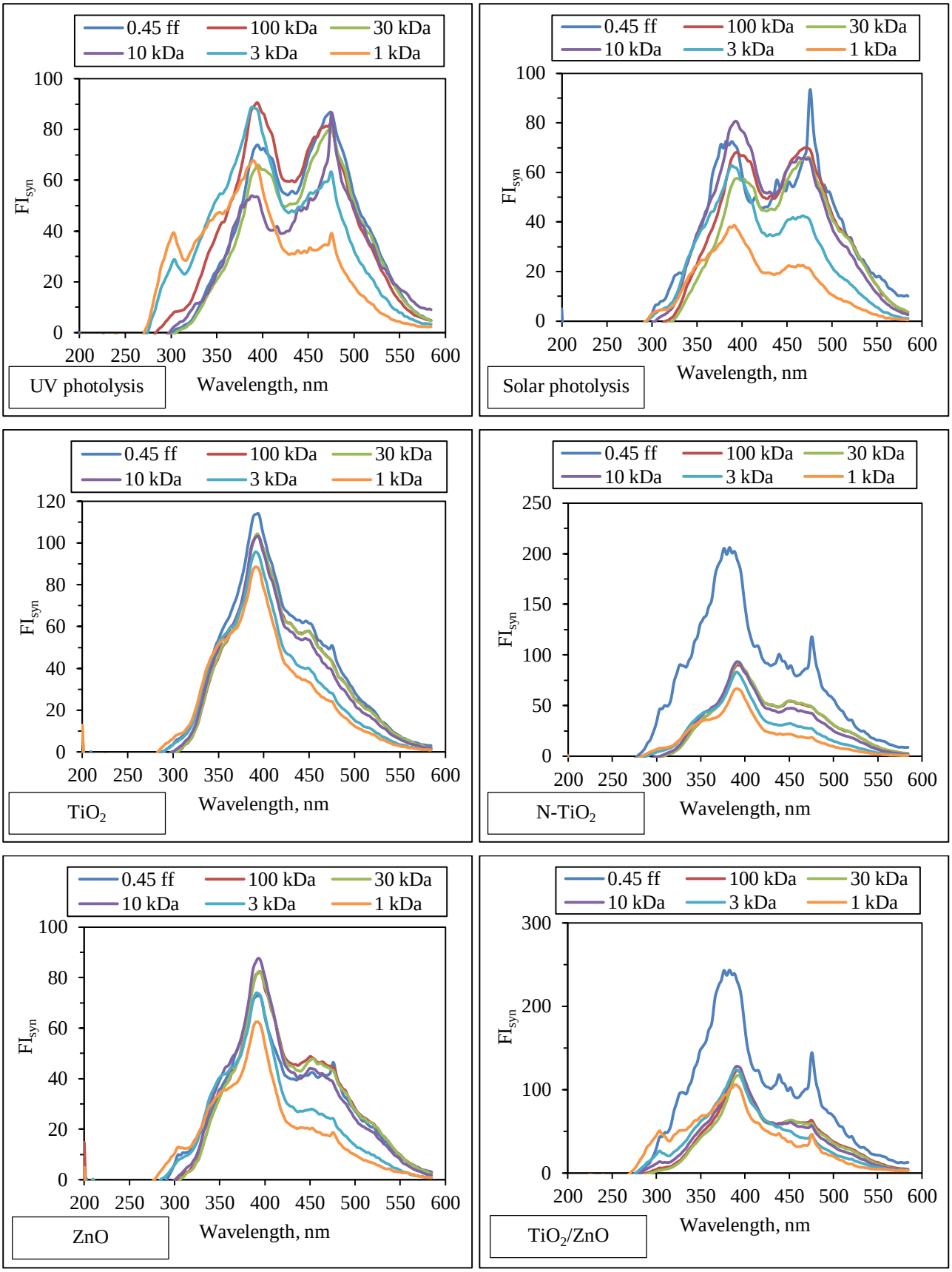

Figure G.4. Synchronous scan fluorescence spectra of molecular size fractions of ROC_{ECm2} following photodegradation and photocatalytic degradation processes.

APPENDIX H: SPECIFIED AND SPECIFIC UV-VIS AND FLUORESCENCE PARAMETERS OF MOLECULAR SIZE FRACTIONS OF ROC_m and ROC_{ECm} FOLLOWING PHOTODEGRADATION AND PHOTOCATALYTIC DEGRADATION PROCESSES

Table H.1. Specified UV-vis parameters of MSD of ROC samples.

	$Color_{436}$	UV_{365}	UV_{280}	UV_{254}	UV_{250}	NPOC	FI_{syn}
ROC_{m1}							
0.45 ff	0.311	0.595	1.245	1.442	1.468	13.3	94.2
100 kDa	0.095	0.210	0.543	0.656	0.672	11.6	79.3
30 kDa	0.058	0.131	0.358	0.438	0.450	3.79	80.1
10 kDa	0.080	0.147	0.364	0.433	0.443	2.69	72.5
3 kDa	0.024	0.045	0.124	0.152	0.157	2.03	38.3
1 kDa	0.014	0.027	0.077	0.096	0.099	1.61	29.2
ROC_{m2}							
0.45 ff	0.442	0.899	2.009	2.344	2.381	23.2	95.7
100 kDa	0.197	0.430	1.117	1.356	1.390	14.7	90.3
30 kDa	0.065	0.141	0.401	0.496	0.509	7.28	90.4
10 kDa	0.043	0.096	0.291	0.367	0.378	4.21	77.8
3 kDa	0.023	0.049	0.153	0.194	0.200	2.72	48.6
1 kDa	0.012	0.027	0.081	0.104	0.107	2.15	31.1
ROC_{ECm1}							
0.45 ff	0.252	0.505	1.474	1.752	1.782	18.1	84.9
100 kDa	0.098	0.216	0.925	1.133	1.150	13.4	78.5
30 kDa	0.074	0.165	0.811	0.999	1.014	11.9	76.4
10 kDa	0.039	0.086	0.610	0.753	0.763	9.42	69.6
3 kDa	0.019	0.038	0.458	0.555	0.562	7.16	39.6
1 kDa	0.016	0.027	0.390	0.452	0.460	6.16	20.8
ROC_{ECm2}							
0.45 ff	0.385	0.809	2.169	2.567	2.594	28.1	81.3
100 kDa	0.153	0.348	1.267	1.571	1.598	18.6	91.1
30 kDa	0.105	0.249	1.039	1.299	1.321	15.5	87.1
10 kDa	0.050	0.126	0.726	0.918	0.933	11.0	84.4
3 kDa	0.022	0.052	0.500	0.626	0.635	8.50	52.4
1 kDa	0.011	0.026	0.387	0.463	0.470	6.72	26.4

Table H.2. Specific UV-vis and fluorescence parameters of MSD of ROC samples.

	$SUVA_{254}$	$SUVA_{280}$	$SUVA_{365}$	$SCoA_{436}$	SFI_{syn}
ROC_{m1}					
0.45 ff	10.8	9.34	4.47	2.34	7.08
100 kDa	5.64	4.67	1.81	0.82	6.82
30 kDa	11.6	9.46	3.45	1.52	21.1
10 kDa	16.1	13.5	5.45	2.96	27.0
3 kDa	7.51	6.10	2.19	1.17	18.9
1 kDa	5.94	4.78	1.66	0.85	18.1
ROC_{m2}					
0.45 ff	10.1	8.66	3.87	1.90	4.13
100 kDa	9.20	7.58	2.92	1.34	6.13
30 kDa	6.81	5.50	1.94	0.89	12.4
10 kDa	8.71	6.91	2.28	1.03	18.5
3 kDa	7.13	5.62	1.82	0.85	17.9
1 kDa	4.82	3.76	1.24	0.54	14.5
ROC_{ECm1}					
0.45 ff	9.72	8.14	2.79	1.39	4.69
100 kDa	8.48	6.92	1.61	0.74	5.87
30 kDa	8.40	6.82	1.39	0.62	6.42
10 kDa	8.00	6.47	0.91	0.41	7.39
3 kDa	7.75	6.39	0.53	0.26	5.54
1 kDa	7.33	6.33	0.43	0.25	3.37
ROC_{ECm2}					
0.45 ff	9.14	7.72	2.88	1.37	2.89
100 kDa	8.43	6.80	1.87	0.82	4.89
30 kDa	8.39	6.71	1.61	0.68	5.63
10 kDa	8.38	6.63	1.15	0.46	7.70
3 kDa	7.36	5.89	0.61	0.26	6.17
1 kDa	6.88	5.75	0.38	0.17	3.92

Table H.3. Specified UV-vis and fluorescence parameters of MSD of ROC_{m1} prior to and following photodegradation.

	$Color_{436}$	UV_{365}	UV_{280}	UV_{254}	UV_{250}	NPOC	FI_{syn}
ROC_{m1}, initial							
0.45 ff	0.311	0.595	1.245	1.442	1.468	13.3	94.2
100 kDa	0.095	0.210	0.543	0.656	0.672	11.6	79.3
30 kDa	0.058	0.131	0.358	0.438	0.450	3.79	80.1
10 kDa	0.080	0.147	0.364	0.433	0.443	2.69	72.5
3 kDa	0.024	0.045	0.124	0.152	0.157	2.03	38.3
1 kDa	0.014	0.027	0.077	0.096	0.099	1.61	29.2
ROC_{m1}, UVC photodegradation λ: 254 nm, I_o: $1.80x10^{17}$ quanta/sec, t_{irr}: 90 min							
0.45 ff	0.218	0.422	0.925	1.079	1.100	9.77	83.6
100 kDa	0.083	0.185	0.482	0.584	0.599	7.07	73.9
30 kDa	0.057	0.131	0.353	0.428	0.440	4.22	72.0
10 kDa	0.031	0.076	0.225	0.278	0.286	3.04	65.1
3 kDa	0.026	0.051	0.138	0.169	0.174	1.84	41.9
1 kDa	0.013	0.028	0.085	0.108	0.113	1.57	26.7
ROC_{m1}, solar photodegradation λ: 290-700 nm, I_o: $1.60x10^{16}$ quanta/sec, t_{irr}: 90 min							
0.45 ff	0.175	0.364	0.854	1.016	1.038	11.1	76.5
100 kDa	0.103	0.220	0.569	0.686	0.703	7.60	53.4
30 kDa	0.081	0.177	0.470	0.570	0.584	6.19	50.8
10 kDa	0.046	0.095	0.265	0.324	0.334	3.45	47.8
3 kDa	0.034	0.060	0.153	0.185	0.191	2.29	28.2
1 kDa	0.032	0.056	0.140	0.168	0.174	2.11	22.9

Table H.4. Specific UV-vis and fluorescence parameters of MSD of ROC_{m1} prior to and following photodegradation.

	$SUVA_{254}$	$SUVA_{280}$	$SUVA_{365}$	$SCoA_{436}$	SFI_{syn}
ROC_{m1}, initial					
0.45 ff	10.8	9.34	4.47	2.34	7.08
100 kDa	5.64	4.67	1.81	0.82	6.82
30 kDa	11.6	9.46	3.45	1.52	21.1
10 kDa	16.1	13.5	5.45	2.96	27.0
3 kDa	7.51	6.10	2.19	1.17	18.9
1 kDa	5.94	4.78	1.66	0.85	18.1
ROC_{m1}, UVC photodegradation λ: 254 nm, I_o: 1.80×10^{17} quanta/sec, t_{irr}: 90 min					
0.45 ff	11.0	9.47	4.32	2.23	8.55
100 kDa	8.25	6.82	2.61	1.18	10.5
30 kDa	10.1	8.36	3.09	1.36	17.1
10 kDa	9.13	7.39	2.50	1.02	21.4
3 kDa	9.18	7.50	2.77	1.42	22.7
1 kDa	6.90	5.39	1.77	0.84	17.0
ROC_{m1}, solar photodegradation λ: 290-700 nm, I_o: 1.60×10^{16} quanta/sec, t_{irr}: 90 min					
0.45 ff	9.16	7.70	3.28	1.57	6.90
100 kDa	9.03	7.48	2.89	1.35	7.02
30 kDa	9.20	7.58	2.85	1.31	8.19
10 kDa	9.41	7.69	2.76	1.33	13.9
3 kDa	8.07	6.68	2.60	1.47	12.3
1 kDa	7.97	6.62	2.64	1.53	10.8

Table H.5. Specified UV-vis and fluorescence parameters of MSD of ROC_{m2} prior to and following photodegradation.

	$Color_{436}$	UV_{365}	UV_{280}	UV_{254}	UV_{250}	NPOC	FI_{syn}
ROC_{m2}, initial							
0.45 ff	0.442	0.899	2.009	2.344	2.381	23.2	95.7
100 kDa	0.197	0.430	1.117	1.356	1.390	14.7	90.3
30 kDa	0.065	0.141	0.401	0.496	0.509	7.28	90.4
10 kDa	0.043	0.096	0.291	0.367	0.378	4.21	77.8
3 kDa	0.023	0.049	0.153	0.194	0.200	2.72	48.6
1 kDa	0.012	0.027	0.081	0.104	0.107	2.15	31.1
ROC_{m2}, UVC photodegradation λ: 254 nm, I_o: $1.80x10^{17}$ quanta/sec, t_{irr}: 90 min							
0.45 ff	0.325	0.682	1.605	1.901	1.944	18.08	283
100 kDa	0.129	0.293	0.775	0.945	0.970	10.46	278
30 kDa	0.080	0.194	0.550	0.678	0.697	7.58	268
10 kDa	0.052	0.131	0.399	0.497	0.511	5.65	175
3 kDa	0.022	0.055	0.173	0.219	0.226	2.66	89.0
1 kDa	0.018	0.035	0.097	0.121	0.125	1.57	70.4
ROC_{m2}, solar photodegradation λ: 290-700 nm, I_o: $1.60x10^{16}$ quanta/sec, t_{irr}: 90 min							
0.45 ff	0.270	0.595	1.376	1.631	1.668	15.4	79.0
100 kDa	0.149	0.333	0.882	1.079	1.106	12.1	66.5
30 kDa	0.095	0.222	0.624	0.773	0.794	8.77	65.8
10 kDa	0.037	0.099	0.323	0.411	0.423	6.77	61.9
3 kDa	0.021	0.055	0.189	0.242	0.250	5.34	45.4
1 kDa	0.016	0.039	0.135	0.173	0.179	4.78	32.2

Table H.6. Specific UV-vis and fluorescence parameters of MSD of ROC_{m1} prior to and following photodegradation.

	$SUVA_{254}$	$SUVA_{280}$	$SUVA_{365}$	$SCoA_{436}$	SFI_{syn}
ROC_{m2}, initial					
0.45 ff	10.1	8.66	3.87	1.90	4.13
100 kDa	9.20	7.58	2.92	1.34	6.13
30 kDa	6.81	5.50	1.94	0.89	12.4
10 kDa	8.71	6.91	2.28	1.03	18.5
3 kDa	7.13	5.62	1.82	0.85	17.9
1 kDa	4.82	3.76	1.24	0.54	14.5
ROC_{m2}, UVC photodegradation λ: 254 nm, I_o: $1.80x10^{17}$ quanta/sec, t_{irr}: 90 min					
0.45 ff	10.5	8.87	3.77	1.80	15.6
100 kDa	9.03	7.41	2.80	1.23	26.6
30 kDa	8.95	7.25	2.56	1.06	35.4
10 kDa	8.79	7.05	2.32	0.92	30.9
3 kDa	8.23	6.50	2.05	0.83	33.5
1 kDa	7.73	6.18	2.20	1.12	44.9
ROC_{m2}, solar photodegradation λ: 290-700 nm, I_o: $1.60x10^{16}$ quanta/sec, t_{irr}: 90 min					
0.45 ff	10.6	8.93	3.86	1.76	5.13
100 kDa	8.91	7.28	2.75	1.23	5.49
30 kDa	8.82	7.12	2.53	1.08	7.50
10 kDa	6.07	4.77	1.46	0.55	9.15
3 kDa	4.53	3.53	1.03	0.40	8.50
1 kDa	3.62	2.82	0.81	0.32	6.73

Table H.7. Specified UV-vis and fluorescence parameters of MSD of ROC_{ECm1} prior to and following photodegradation.

	$Color_{436}$	UV_{365}	UV_{280}	UV_{254}	UV_{250}	NPOC	FI_{syn}
ROC_{ECm1}, initial							
0.45 ff	0.252	0.505	1.474	1.752	1.782	18.1	84.9
100 kDa	0.098	0.216	0.925	1.133	1.150	13.4	78.5
30 kDa	0.074	0.165	0.811	0.999	1.014	11.9	76.4
10 kDa	0.039	0.086	0.610	0.753	0.763	9.42	69.6
3 kDa	0.019	0.038	0.458	0.555	0.562	7.16	39.6
1 kDa	0.016	0.027	0.390	0.452	0.460	6.16	20.8
ROC_{ECm1}, UVC photodegradation λ: 254 nm, I_o: $1.80x10^{17}$ quanta/sec, t_{irr}: 90 min							
0.45 ff	0.295	0.576	1.462	1.637	1.713	15.4	59.5
100 kDa	0.097	0.220	0.783	0.854	0.914	11.5	72.4
30 kDa	0.094	0.209	0.753	0.817	0.874	10.8	70.8
10 kDa	0.062	0.133	0.556	0.579	0.626	7.82	64.4
3 kDa	0.045	0.085	0.409	0.397	0.435	5.84	41.1
1 kDa	0.043	0.078	0.378	0.363	0.396	5.21	32.1
ROC_{ECm1}, solar photodegradation λ: 290-700 nm, I_o: $1.60x10^{16}$ quanta/sec, t_{irr}: 90 min							
0.45 ff	0.176	0.369	1.240	1.506	1.531	14.7	80.7
100 kDa	0.087	0.200	0.910	1.129	1.149	13.8	61.0
30 kDa	0.070	0.169	0.841	1.049	1.067	12.7	61.8
10 kDa	0.035	0.087	0.630	0.791	0.804	9.60	54.4
3 kDa	0.016	0.036	0.466	0.576	0.586	7.60	33.5
1 kDa	0.014	0.031	0.445	0.554	0.562	7.39	29.0

Table H.8. Specific UV-vis and fluorescence parameters of MSD of ROC_{ECm1} prior to and following photodegradation.

	$SUVA_{254}$	$SUVA_{280}$	$SUVA_{365}$	$SCoA_{436}$	SFI_{syn}
ROC_{ECm1}, initial					
0.45 ff	9.68	8.14	2.79	1.39	4.69
100 kDa	8.48	6.92	1.61	0.74	5.87
30 kDa	8.40	6.82	1.39	0.62	6.42
10 kDa	8.00	6.47	0.91	0.41	7.39
3 kDa	7.75	6.39	0.53	0.26	5.54
1 kDa	7.33	6.33	0.43	0.25	3.37
ROC_{ECm1}, UVC photodegradation λ: 254 nm, I_o: $1.80x10^{17}$ quanta/sec, t_{irr}: 90 min					
0.45 ff	10.7	9.52	3.75	1.92	3.87
100 kDa	7.43	6.82	1.91	0.84	6.30
30 kDa	7.58	6.98	1.94	0.88	6.57
10 kDa	7.41	7.10	1.70	0.79	8.23
3 kDa	6.79	7.01	1.45	0.76	7.03
1 kDa	6.96	7.26	1.49	0.83	6.16
ROC_{ECm1}, solar photodegradation λ: 290-700 nm, I_o: $1.60x10^{16}$ quanta/sec, t_{irr}: 90 min					
0.45 ff	10.2	8.44	2.51	1.19	5.49
100 kDa	8.16	6.58	1.44	0.63	4.41
30 kDa	8.27	6.64	1.33	0.56	4.87
10 kDa	8.23	6.56	0.90	0.36	5.67
3 kDa	7.58	6.13	0.47	0.21	4.41
1 kDa	7.50	6.02	0.42	0.19	3.92

Table H.9. Specified UV-vis and fluorescence parameters of MSD of ROC_{ECm2} prior to and following photodegradation.

	$Color_{436}$	UV_{365}	UV_{280}	UV_{254}	UV_{250}	NPOC	FI_{syn}
ROC_{ECm2}, initial							
0.45 ff	0.385	0.809	2.169	2.567	2.594	28.1	81.3
100 kDa	0.153	0.348	1.267	1.571	1.598	18.6	91.1
30 kDa	0.105	0.249	1.039	1.299	1.321	15.5	87.1
10 kDa	0.050	0.126	0.726	0.918	0.933	11.0	84.4
3 kDa	0.022	0.052	0.500	0.626	0.635	8.50	52.4
1 kDa	0.011	0.026	0.387	0.463	0.470	6.72	26.4
ROC_{ECm2}, UVC photodegradation λ: 254 nm, I_o: $1.80x10^{17}$ quanta/sec, t_{irr}: 60 min							
0.45 ff	0.351	0.741	1.962	2.232	2.310	25.5	85.3
100 kDa	0.142	0.330	1.101	1.254	1.315	16.8	81.2
30 kDa	0.110	0.267	0.965	1.095	1.154	15.2	78.8
10 kDa	0.061	0.160	0.696	0.772	0.822	12.2	66.5
3 kDa	0.027	0.073	0.448	0.462	0.503	8.55	59.3
1 kDa	0.015	0.038	0.333	0.319	0.353	6.22	34.5
ROC_{ECm2}, solar photodegradation λ: 290-700 nm, I_o: $1.60x10^{16}$ quanta/sec, t_{irr}: 60 min							
0.45 ff	0.348	0.737	2.067	2.463	2.490	27.2	67.0
100 kDa	0.145	0.334	1.240	1.541	1.573	18.3	69.9
30 kDa	0.105	0.249	1.041	1.306	1.331	15.6	65.7
10 kDa	0.050	0.127	0.728	0.925	0.942	11.7	65.6
3 kDa	0.021	0.053	0.498	0.629	0.640	8.35	42.0
1 kDa	0.012	0.029	0.384	0.466	0.475	5.94	21.8

Table H.10. Specific UV-vis and fluorescence parameters of MSD of ROC_{ECm2} prior to and following photodegradation.

	$SUVA_{254}$	$SUVA_{280}$	$SUVA_{365}$	$SCoA_{436}$	SFI_{syn}
ROC_{ECm2}, initial					
0.45 ff	9.14	7.72	2.88	1.37	2.89
100 kDa	8.43	6.80	1.87	0.82	4.89
30 kDa	8.39	6.71	1.61	0.68	5.63
10 kDa	8.38	6.63	1.15	0.46	7.70
3 kDa	7.36	5.89	0.61	0.26	6.17
1 kDa	6.88	5.75	0.38	0.17	3.92
ROC_{ECm2}, UVC photodegradation λ: 254 nm, I_o: $1.80x10^{17}$ quanta/sec, t_{irr}: 60 min					
0.45 ff	8.75	7.69	2.91	1.38	3.35
100 kDa	7.46	6.55	1.96	0.84	4.83
30 kDa	7.21	6.35	1.76	0.72	5.18
10 kDa	6.35	5.72	1.31	0.50	5.47
3 kDa	5.40	5.23	0.85	0.32	6.94
1 kDa	5.12	5.35	0.61	0.25	5.55
ROC_{ECm2}, solar photodegradation λ: 290-700 nm, I_o: $1.60x10^{16}$ quanta/sec, t_{irr}: 60 min					
0.45 ff	9.07	7.61	2.71	1.28	2.47
100 kDa	8.42	6.78	1.82	0.79	3.82
30 kDa	8.36	6.67	1.59	0.67	4.21
10 kDa	7.89	6.22	1.09	0.43	5.60
3 kDa	7.53	5.96	0.63	0.25	5.04
1 kDa	7.84	6.47	0.48	0.21	3.68

Table H.11. Specified UV-vis and fluorescence parameters of MSD of ROC_{m1} prior to and following solar photocatalytic degradation.

	$Color_{436}$	UV_{365}	UV_{280}	UV_{254}	UV_{250}	NPOC	FI_{syn}
Initial							
0.45 ff	0.311	0.595	1.245	1.442	1.468	13.3	94.2
100 kDa	0.095	0.210	0.543	0.656	0.672	11.6	79.3
30 kDa	0.058	0.131	0.358	0.438	0.450	3.79	80.1
10 kDa	0.080	0.147	0.364	0.433	0.443	2.69	72.5
3 kDa	0.024	0.045	0.124	0.152	0.157	2.03	38.3
1 kDa	0.014	0.027	0.077	0.096	0.099	1.61	29.2
TiO_2 Concentration: 0.25 mg/mL, t_{irr}: 40 min							
0.45 ff	0.028	0.071	0.213	0.286	0.297	4.61	14.2
100 kDa	0.027	0.069	0.212	0.286	0.296	4.45	14.5
30 kDa	0.027	0.069	0.212	0.286	0.296	4.32	14.5
10 kDa	0.028	0.068	0.207	0.278	0.289	4.12	14.3
3 kDa	0.024	0.055	0.164	0.218	0.226	3.32	11.2
1 kDa	0.016	0.033	0.096	0.128	0.132	3.03	5.40
N-TiO_2 Concentration: 0.25 mg/mL, t_{irr}: 60 min							
0.45 ff	0.095	0.187	0.499	0.619	0.636	6.97	53.8
100 kDa	0.073	0.159	0.444	0.555	0.571	6.30	53.0
30 kDa	0.049	0.119	0.360	0.461	0.476	5.36	47.5
10 kDa	0.035	0.087	0.271	0.351	0.362	3.82	41.6
3 kDa	0.012	0.031	0.108	0.145	0.151	2.05	23.6
1 kDa	0.006	0.014	0.048	0.065	0.068	1.41	10.6
ZnO Concentration: 0.25 mg/mL, t_{irr}: 80 min							
0.45 ff	0.072	0.157	0.436	0.551	0.568	7.78	38.7
100 kDa	0.058	0.135	0.379	0.481	0.497	6.11	35.7
30 kDa	0.046	0.119	0.354	0.451	0.467	6.04	32.9
10 kDa	0.034	0.090	0.269	0.348	0.360	4.17	29.6
3 kDa	0.018	0.045	0.134	0.175	0.182	2.25	17.4
1 kDa	0.013	0.029	0.075	0.099	0.103	1.63	7.58
TiO_2/ZnO Concentration: 0.25 mg/mL, t_{irr}: 70 min							
0.45 ff	0.094	0.185	0.493	0.602	0.617	5.96	58.2
100 kDa	0.093	0.185	0.491	0.599	0.615	5.72	55.9
30 kDa	0.066	0.150	0.412	0.510	0.523	5.54	56.9
10 kDa	0.079	0.149	0.399	0.490	0.504	4.18	53.2
3 kDa	0.057	0.098	0.246	0.302	0.311	3.48	34.7
1 kDa	0.039	0.065	0.157	0.194	0.200	2.75	22.8

Table H.12. Specific UV-vis and fluorescence parameters of MSD of ROC_{m1} prior to and following solar photocatalytic degradation.

	$SUVA_{254}$	$SUVA_{280}$	$SUVA_{365}$	$SCoA_{436}$	SFI_{syn}
Initial					
0.45 ff	10.8	9.34	4.47	2.34	7.08
100 kDa	5.64	4.67	1.81	0.82	6.82
30 kDa	11.6	9.46	3.45	1.52	21.1
10 kDa	16.1	13.5	5.45	2.96	27.0
3 kDa	7.51	6.10	2.19	1.17	18.9
1 kDa	5.94	4.78	1.66	0.85	18.1
TiO_2 Concentration: 0.25 mg/mL, t_{irr}: 40 min					
0.45 ff	6.22	4.63	1.54	0.61	3.08
100 kDa	6.42	4.77	1.56	0.61	3.27
30 kDa	6.62	4.91	1.59	0.61	3.37
10 kDa	6.76	5.04	1.66	0.68	3.48
3 kDa	6.57	4.94	1.66	0.72	3.36
1 kDa	4.22	3.17	1.09	0.51	1.78
N-TiO_2 Concentration: 0.25 mg/mL, t_{irr}: 60 min					
0.45 ff	8.89	7.16	2.68	1.37	7.72
100 kDa	8.81	7.04	2.53	1.16	8.41
30 kDa	8.60	6.71	2.22	0.91	8.87
10 kDa	9.18	7.09	2.26	0.91	10.9
3 kDa	7.06	5.25	1.49	0.56	11.5
1 kDa	4.63	3.43	0.97	0.41	7.54
ZnO Concentration: 0.25 mg/mL, t_{irr}: 80 min					
0.45 ff	7.09	5.61	2.01	0.92	0.91
100 kDa	7.96	6.21	2.22	0.95	1.32
30 kDa	7.39	5.86	1.97	0.76	1.21
10 kDa	8.35	6.46	2.16	0.82	2.00
3 kDa	7.79	5.95	2.00	0.81	3.46
1 kDa	6.04	4.58	1.77	0.82	3.70
TiO_2/ZnO Concentration: 0.25 mg/mL, t_{irr}: 70 min					
0.45 ff	10.1	8.27	3.10	1.57	9.77
100 kDa	10.5	8.59	3.24	1.62	9.78
30 kDa	9.20	7.44	2.71	1.19	10.3
10 kDa	11.7	9.56	3.56	1.88	12.7
3 kDa	8.67	7.08	2.80	1.64	10.0
1 kDa	7.05	5.71	2.37	1.42	8.30

Table H.13. Specified UV-vis and fluorescence parameters of MSD of ROC_{m2} prior to and following solar photocatalytic degradation.

	$Color_{436}$	UV_{365}	UV_{280}	UV_{254}	UV_{250}	NPOC	FI_{syn}
Initial							
0.45 ff	0.442	0.899	2.009	2.344	2.381	23.2	95.7
100 kDa	0.197	0.430	1.117	1.356	1.390	14.7	90.3
30 kDa	0.065	0.141	0.401	0.496	0.509	7.28	90.4
10 kDa	0.043	0.096	0.291	0.367	0.378	4.21	77.8
3 kDa	0.023	0.049	0.153	0.194	0.200	2.72	48.6
1 kDa	0.012	0.027	0.081	0.104	0.107	2.15	31.1
TiO_2 Concentration: 0.25 mg/mL, t_{irr}: 50 min							
0.45 ff	0.137	0.315	0.873	1.100	1.133	13.6	68.2
100 kDa	0.072	0.193	0.611	0.795	0.821	11.2	71.2
30 kDa	0.070	0.188	0.601	0.784	0.810	10.6	70.2
10 kDa	0.040	0.116	0.398	0.529	0.548	7.39	60.3
3 kDa	0.015	0.046	0.171	0.234	0.244	4.55	35.3
1 kDa	0.022	0.042	0.119	0.156	0.161	2.60	19.8
N-TiO_2 Concentration: 0.25 mg/mL, t_{irr}: 120 min							
0.45 ff	0.149	0.359	0.995	1.228	1.261	13.6	105
100 kDa	0.075	0.208	0.667	0.867	0.896	11.2	58.8
30 kDa	0.074	0.205	0.670	0.864	0.893	10.6	58.5
10 kDa	0.038	0.115	0.409	0.545	0.564	7.38	50.4
3 kDa	0.020	0.061	0.234	0.317	0.329	4.55	35.6
1 kDa	0.010	0.028	0.113	0.152	0.159	2.60	18.4
ZnO Concentration: 0.25 mg/mL, t_{irr}: 100 min							
0.45 ff	0.220	0.471	1.173	1.424	1.459	16.1	41.5
100 kDa	0.081	0.204	0.598	0.758	0.780	9.22	45.1
30 kDa	0.071	0.183	0.549	0.700	0.721	8.51	44.3
10 kDa	0.041	0.110	0.360	0.468	0.483	6.09	40.0
3 kDa	0.024	0.058	0.196	0.257	0.266	3.52	24.5
1 kDa	0.043	0.074	0.189	0.234	0.241	2.19	17.6
TiO_2/ZnO Concentration: 0.25 mg/mL, t_{irr}: 150 min							
0.45 ff	0.156	0.345	0.906	1.110	1.139	12.7	119
100 kDa	0.106	0.226	0.657	0.847	0.875	12.0	59.0
30 kDa	0.088	0.199	0.610	0.787	0.813	10.6	60.2
10 kDa	0.090	0.184	0.534	0.690	0.714	7.62	50.9
3 kDa	0.043	0.083	0.245	0.319	0.330	4.42	28.3
1 kDa	0.046	0.081	0.216	0.276	0.285	3.57	22.3

Table H.14. Specific UV-vis and fluorescence parameters of MSD of ROC_{m2} prior to and following solar photocatalytic degradation.

	$SUVA_{254}$	$SUVA_{280}$	$SUVA_{365}$	$SCoA_{436}$	SFI_{syn}
Initial					
0.45 ff	10.1	8.66	3.87	1.90	4.13
100 kDa	9.20	7.58	2.92	1.34	6.13
30 kDa	6.81	5.50	1.94	0.89	12.4
10 kDa	8.71	6.91	2.28	1.03	18.5
3 kDa	7.13	5.62	1.82	0.85	17.9
1 kDa	4.82	3.76	1.24	0.54	14.5
TiO_2 Concentration: 0.25 mg/mL, t_{irr}: 50 min					
0.45 ff	8.09	6.42	2.32	1.00	5.01
100 kDa	7.07	5.44	1.72	0.64	6.34
30 kDa	7.41	5.68	1.78	0.66	6.64
10 kDa	7.16	5.39	1.57	0.54	8.17
3 kDa	5.15	3.77	1.01	0.34	7.76
1 kDa	5.99	4.57	1.62	0.85	7.59
N-TiO_2 Concentration: 0.25 mg/mL, t_{irr}: 120 min					
0.45 ff	9.02	7.31	2.64	1.09	7.69
100 kDa	7.72	5.94	1.85	0.66	5.23
30 kDa	8.16	6.34	1.94	0.70	5.53
10 kDa	7.38	5.54	1.56	0.52	6.82
3 kDa	6.96	5.15	1.34	0.44	7.83
1 kDa	5.86	4.35	1.09	0.37	7.07
ZnO Concentration: 0.25 mg/mL, t_{irr}: 100 min					
0.45 ff	8.83	7.27	2.92	1.37	2.57
100 kDa	8.23	6.49	2.21	0.88	4.89
30 kDa	8.22	6.45	2.14	0.83	5.21
10 kDa	7.68	5.92	1.81	0.67	6.58
3 kDa	7.30	5.57	1.64	0.68	6.96
1 kDa	10.7	8.62	3.38	1.95	8.03
TiO_2/ZnO Concentration: 0.25 mg/mL, t_{irr}: 150 min					
0.45 ff	8.76	7.15	2.73	1.23	9.41
100 kDa	7.03	5.46	1.88	0.88	4.90
30 kDa	7.46	5.78	1.89	0.84	5.71
10 kDa	9.05	7.00	2.41	1.18	6.68
3 kDa	7.22	5.55	1.89	0.96	6.41
1 kDa	7.71	6.04	2.26	1.28	6.25

Table H.15. Specified UV-vis and fluorescence parameters of MSD of ROC_{ECm1} prior to and following solar photocatalytic degradation.

	$Color_{436}$	UV_{365}	UV_{280}	UV_{254}	UV_{250}	NPOC	FI_{syn}
Initial							
0.45 ff	0.252	0.505	1.474	1.752	1.782	18.1	84.9
100 kDa	0.098	0.216	0.925	1.133	1.150	13.4	78.5
30 kDa	0.074	0.165	0.811	0.999	1.014	11.9	76.4
10 kDa	0.039	0.086	0.610	0.753	0.763	9.42	69.6
3 kDa	0.019	0.038	0.458	0.555	0.562	7.16	39.6
1 kDa	0.016	0.027	0.390	0.452	0.460	6.16	20.8
TiO_2 Concentration: 0.25 mg/mL, t_{irr}: 90 min							
0.45 ff	0.044	0.127	0.594	0.784	0.822	12.2	22.6
100 kDa	0.036	0.118	0.576	0.763	0.799	12.0	20.9
30 kDa	0.036	0.114	0.567	0.753	0.788	11.6	20.6
10 kDa	0.031	0.101	0.527	0.697	0.730	11.2	18.8
3 kDa	0.020	0.066	0.419	0.548	0.575	9.10	13.6
1 kDa	0.013	0.040	0.315	0.397	0.418	7.43	7.64
N-TiO_2 Concentration: 0.25 mg/mL, t_{irr}: 80 min							
0.45 ff	0.088	0.207	0.891	1.088	1.113	12.4	90.3
100 kDa	0.049	0.125	0.718	0.894	0.917	11.5	50.6
30 kDa	0.043	0.116	0.701	0.876	0.898	11.4	48.9
10 kDa	0.026	0.077	0.593	0.742	0.760	9.87	44.9
3 kDa	0.013	0.038	0.464	0.572	0.586	8.11	29.5
1 kDa	0.006	0.018	0.365	0.426	0.438	6.02	14.3
ZnO Concentration: 0.25 mg/mL, t_{irr}: 170 min							
0.45 ff	0.108	0.245	0.954	1.198	1.231	14.8	35.2
100 kDa	0.046	0.123	0.691	0.890	0.914	11.7	31.1
30 kDa	0.043	0.118	0.679	0.873	0.898	11.6	31.1
10 kDa	0.026	0.079	0.579	0.751	0.771	10.4	26.3
3 kDa	0.012	0.038	0.439	0.562	0.577	8.46	15.5
1 kDa	0.007	0.021	0.367	0.453	0.465	7.31	8.72
TiO_2/ZnO Concentration: 0.25 mg/mL, t_{irr}: 90 min							
0.45 ff	0.092	0.217	0.863	1.032	1.060	14.8	100
100 kDa	0.035	0.102	0.636	0.786	0.812	13.6	45.6
30 kDa	0.034	0.101	0.633	0.782	0.808	11.7	50.6
10 kDa	0.021	0.065	0.515	0.628	0.650	10.9	44.7
3 kDa	0.014	0.040	0.424	0.503	0.520	10.4	35.8
1 kDa	0.008	0.021	0.343	0.389	0.402	6.78	32.9

Table H.16. Specific UV-vis and fluorescence parameters of MSD of ROC_{ECm1} prior to and following solar photocatalytic degradation.

	$SUVA_{254}$	$SUVA_{280}$	$SUVA_{365}$	$SCoA_{436}$	SFI_{syn}
Initial					
0.45 ff	9.68	8.14	2.79	1.39	4.69
100 kDa	8.48	6.92	1.61	0.74	5.87
30 kDa	8.40	6.82	1.39	0.62	6.42
10 kDa	8.00	6.47	0.91	0.41	7.39
3 kDa	7.75	6.39	0.53	0.26	5.54
1 kDa	7.33	6.33	0.43	0.25	3.37
TiO_2 Concentration: 0.25 mg/mL, t_{irr}: 90 min					
0.45 ff	6.43	4.88	1.04	0.36	1.85
100 kDa	6.37	4.81	0.98	0.30	1.75
30 kDa	6.49	4.89	0.99	0.31	1.78
10 kDa	6.25	4.72	0.91	0.28	1.69
3 kDa	6.02	4.60	0.73	0.22	1.49
1 kDa	5.35	4.24	0.54	0.17	1.03
N-TiO_2 Concentration: 0.25 mg/mL, t_{irr}: 80 min					
0.45 ff	8.75	7.17	1.67	0.71	7.27
100 kDa	7.80	6.26	1.09	0.43	4.41
30 kDa	7.68	6.14	1.02	0.37	4.29
10 kDa	7.52	6.01	0.78	0.26	4.55
3 kDa	7.05	5.72	0.47	0.17	3.64
1 kDa	7.08	6.06	0.30	0.11	2.37
ZnO Concentration: 0.25 mg/mL, t_{irr}: 170 min					
0.45 ff	8.11	6.46	1.66	0.73	2.38
100 kDa	7.58	5.88	1.04	0.39	2.65
30 kDa	7.54	5.86	1.02	0.37	2.68
10 kDa	7.19	5.54	0.76	0.24	2.52
3 kDa	6.64	5.18	0.45	0.14	1.84
1 kDa	6.19	5.02	0.29	0.09	1.19
TiO_2/ZnO Concentration: 0.25 mg/mL, t_{irr}: 90 min					
0.45 ff	6.98	5.84	1.47	0.62	6.80
100 kDa	5.80	4.69	0.75	0.26	3.36
30 kDa	6.71	5.43	0.87	0.30	4.34
10 kDa	5.79	4.74	0.60	0.20	4.12
3 kDa	4.83	4.07	0.39	0.13	3.43
1 kDa	5.74	5.06	0.31	0.11	4.85

Table H.17. Specified UV-vis and fluorescence parameters of MSD of ROC_{ECm2} prior to and following solar photocatalytic degradation.

	$Color_{436}$	UV_{365}	UV_{280}	UV_{254}	UV_{250}	NPOC	FI_{syn}
Initial							
0.45 ff	0.385	0.809	2.169	2.567	2.594	28.1	81.3
100 kDa	0.153	0.348	1.267	1.571	1.598	18.6	91.1
30 kDa	0.105	0.249	1.039	1.299	1.321	15.5	87.1
10 kDa	0.050	0.126	0.726	0.918	0.933	11.0	84.4
3 kDa	0.022	0.052	0.500	0.626	0.635	8.50	52.4
1 kDa	0.011	0.026	0.387	0.463	0.470	6.72	26.4
TiO_2 Concentration: 0.25 mg/mL, t_{irr}: 100 min							
0.45 ff	0.065	0.193	0.841	1.075	1.123	17.3	50.1
100 kDa	0.056	0.179	0.813	1.044	1.090	16.4	45.7
30 kDa	0.055	0.177	0.803	1.030	1.076	15.6	45.5
10 kDa	0.046	0.148	0.707	0.903	0.943	13.9	40.5
3 kDa	0.031	0.097	0.537	0.673	0.704	10.8	29.8
1 kDa	0.026	0.080	0.475	0.587	0.614	9.48	24.9
N-TiO_2 Concentration: 0.25 mg/mL, t_{irr}: 200 min							
0.45 ff	0.125	0.307	1.142	1.416	1.468	17.3	86.6
100 kDa	0.067	0.199	0.922	1.174	1.222	16.0	49.9
30 kDa	0.065	0.194	0.911	1.161	1.208	14.8	50.4
10 kDa	0.043	0.136	0.731	0.929	0.969	13.2	43.2
3 kDa	0.019	0.065	0.490	0.608	0.634	9.09	27.7
1 kDa	0.012	0.040	0.384	0.458	0.479	7.15	18.2
ZnO Concentration: 0.25 mg/mL, t_{irr}: 220 min							
0.45 ff	0.141	0.332	1.167	1.464	1.505	17.2	41.5
100 kDa	0.076	0.208	0.920	1.181	1.217	15.6	45.1
30 kDa	0.069	0.196	0.886	1.140	1.176	15.0	44.3
10 kDa	0.040	0.124	0.686	0.887	0.915	11.8	40.0
3 kDa	0.017	0.055	0.457	0.582	0.600	7.82	24.5
1 kDa	0.013	0.038	0.374	0.464	0.478	6.29	17.6
TiO_2/ZnO Concentration: 0.25 mg/mL, t_{irr}: 250 min							
0.45 ff	0.122	0.313	1.212	1.503	1.559	20.0	101
100 kDa	0.059	0.187	0.970	1.235	1.289	19.6	60.3
30 kDa	0.061	0.187	0.964	1.226	1.280	19.2	58.9
10 kDa	0.046	0.139	0.801	1.015	1.059	15.4	54.4
3 kDa	0.024	0.076	0.589	0.734	0.767	11.2	41.4
1 kDa	0.013	0.039	0.423	0.498	0.521	8.35	32.9

Table H.18. Specific UV-vis and fluorescence parameters of MSD of ROC_{ECm2} prior to and following solar photocatalytic degradation.

	$SUVA_{254}$	$SUVA_{280}$	$SUVA_{365}$	$SCoA_{436}$	SFI_{syn}
Initial					
0.45 ff	9.14	7.72	2.88	1.37	2.89
100 kDa	8.43	6.80	1.87	0.82	4.89
30 kDa	8.39	6.71	1.61	0.68	5.63
10 kDa	8.38	6.63	1.15	0.46	7.70
3 kDa	7.36	5.89	0.61	0.26	6.17
1 kDa	6.88	5.75	0.38	0.17	3.92
TiO_2 Concentration: 0.25 mg/mL, t_{irr}: 100 min					
0.45 ff	6.22	4.86	1.12	0.38	2.90
100 kDa	6.36	4.95	1.09	0.34	2.79
30 kDa	6.60	5.14	1.14	0.35	2.92
10 kDa	6.49	5.08	1.06	0.33	2.91
3 kDa	6.26	4.99	0.90	0.29	2.77
1 kDa	6.19	5.01	0.85	0.28	2.63
N-TiO_2 Concentration: 0.25 mg/mL, t_{irr}: 200 min					
0.45 ff	8.20	6.61	1.78	0.72	5.01
100 kDa	7.32	5.75	1.24	0.42	3.11
30 kDa	7.86	6.17	1.32	0.44	3.42
10 kDa	7.06	5.55	1.03	0.32	3.28
3 kDa	6.68	5.38	0.72	0.21	3.05
1 kDa	6.41	5.37	0.55	0.17	2.55
ZnO Concentration: 0.25 mg/mL, t_{irr}: 220 min					
0.45 ff	8.49	6.77	1.92	0.82	2.40
100 kDa	7.58	5.91	1.34	0.49	2.89
30 kDa	7.58	5.89	1.30	0.46	2.95
10 kDa	7.54	5.83	1.05	0.34	3.40
3 kDa	7.45	5.84	0.70	0.22	3.13
1 kDa	7.37	5.95	0.60	0.20	2.80
TiO_2/ZnO Concentration: 0.25 mg/mL, t_{irr}: 250 min					
0.45 ff	7.50	6.05	1.56	0.61	5.03
100 kDa	6.30	4.95	0.95	0.30	3.08
30 kDa	6.40	5.03	0.98	0.32	3.08
10 kDa	6.58	5.20	0.90	0.30	3.53
3 kDa	6.59	5.28	0.68	0.22	3.71
1 kDa	5.96	5.07	0.46	0.15	3.93